MATERIAL DEGRADATION STUDIES IN MOLTEN HALIDE SALTS

BRENDAN D'SOUZA

Dissertation submitted to the faculty of the Virginia Polytechnic Institute and State University in partial fulfillment of the requirements for the degree of

Doctor of Philosophy

In

Nuclear Engineering

Jinsuo Zhang, Chair

Mark Pierson

Yang Liu

Xianming Bai

5th March, 2021

Blacksburg, Virginia

Keywords: Molten Salt Purification, Molten Salt Corrosion, Nickel-Based Alloys, Ferrous-Based Alloys, Boriding/Boronizing

MATERIAL DEGRADATION STUDIES IN MOLTEN HALIDE SALTS

BRENDAN D'SOUZA

ABSTRACT

This study focused on molten salt purification processes to effectively reduce or eliminate the corrosive contaminants without altering the salt's chemistry and properties. The impurity-driven corrosion behavior of HAYNES® 230® alloy in the molten KCl-$MgCl_2$-NaCl salt was studied at 800 ºC for 100 hours with different salt purity conditions. The H230 alloy exhibited better corrosion resistance in the salt with lower concentration of impurities. Furthermore, it was also found that the contaminants along with salt's own vaporization at high temperatures severely corroded even the non-wetted surface of the alloy. The presence of Mg in its metal form in the salt resulted in an even higher mass-loss possibly due to Mg-Ni interaction. The study also investigated the corrosion characteristics of several nickel and ferrous-based alloys in the molten KCl-$MgCl_2$-NaCl salt. The average mass-loss was in the increasing order of C276 < SS316L < 709-RBB* < IN718 < H230 < 709-RBB < 709-4B2. The corrosion process was driven by the outward diffusion of chromium. However, other factors such as the microstructure of the alloy i.e. its manufacturing, refining, and heat-treatment processes have also shown to influence the corrosion process. Lowering the Cr content and introducing W and Mo in the alloy increased its resistance to corrosion but their non-uniform distribution in the alloy restricted its usefulness. To slow-down the corrosion process, and enhance the material properties, selected alloys were boronized and tested for their compatibility in the molten KCl-$MgCl_2$-NaCl salt. The borided alloys exhibited better resistance to molten salt attack, where the boride layer in the exposed alloy was still intact, non-porous, and strongly adhered to the substrate. The alloys also did not show any compensation in their properties (hardness). It was also found that the boride layer always composed of an outermost silicide composite layer, which is also the weakest and undesired layer as it easily cracks, breaks, or depletes under mechanical and thermal stresses. Various different grades of "virgin" nuclear graphites were also tested in the molten KF-UF_4-NaF salt to assist in the selection of tolerable or impermeable graphites for the MSR operational purposes. It was found that molten salt wettability with graphite was poor but it still infiltrated at higher pressure. Additionally, the infiltration also depended on the pore-size and porosity of the graphite. The graphite also showed severe degradation or disintegration of its structure because of induced stresses.

MATERIAL DEGRADATION STUDIES IN MOLTEN HALIDE SALTS

BRENDAN D'SOUZA

GENERAL AUDIENCE ABSTRACT

Molten salts are considered as potential fuel and coolant candidates in MSRs because of their desirable thermophysical properties and heat-transfer capabilities. However, they pose grave challenges in material selection due to their corrosive nature, which is attributed to the impurities and their concentration (mostly moisture and oxygen-based) in the salt. This study focused on purifying the salt to reduce these contaminants without compromising its composition and properties. The influence of purification processes on the corrosion behavior of HAYNES® 230® alloy was studied in the molten chloride salt with different purity conditions. Various nickel and ferrous-based alloys were also studied for their compatibility in the molten chloride salt. This will assist in expediting the material selection process for various molten salt applications. It was observed that several factors such as alloy composition, its microstructure, impurities in the salt attribute to molten salt corrosion. It was also quite evident that corrosion in molten salts is inevitable and hence, the focus was shifted on slowing down this process by providing protective barriers in the form of coatings (i.e. boronization). The borided (coated) alloys not only improved the corrosion resistance but also enhanced and retained their properties like hardness after exposure to molten salts. Since these studies were conducted under static conditions, a more detailed investigation is needed for the selected alloys by subjecting them to extreme flow-conditions and for longer a duration of time. To achieve this objective, a forced circulation molten salt loop was designed and fabricated to conduct flow corrosion studies for alloys in molten chloride salt. Graphite is another critical component of the MSR where it is used as a moderator or reflector. Generally, molten salts exhibit poor wettability with graphite, but they can still infiltrate (graphites) at higher applied pressures, and result in the degradation or disintegration of graphite's structure, and eventually its failure in the reactor. This study provides infiltration data, and understanding of the degradation of various 'virgin' nuclear graphite grades by the molten fluoride salt. This should assist in the selection of tolerable or impermeable graphite grades for MSR operational purposes.

ACKNOWLEDGEMENTS

I would like to express my sincere gratitude to my advisor Dr. Jinsuo Zhang for his patience, guidance, and encouragement throughout my PhD program. His willingness to give time, provide valuable insights and useful critiques, share his immense knowledge, and support new ideas has been very much appreciated. I would also like to express great appreciation to my committee members Dr. Mark Pierson, Dr. Yang Liu, and Dr. Xianming Bai for their time, patience and valuable suggestions.

I would like to acknowledge the United States Department of Energy (DOE) for partially funding this study. I wish to thank Dr. Kevin Robb from Oak Ridge National Lab (ORNL), Dr. Sham Sam and Dr. Xuan Zhang from Argonne National Lab (ANL), Mr. Stephen Lyle from Precision Ceramics USA, Mr. Tom Gosling and Mr. Aria Khalili from Gosco Valves, Dr. Tom Staley from X-ray Characterization Lab, Mr. Stephen McCartney from Nanoscale Characterization and Fabrication Laboratory, Dr. Jeffrey Parks from Inductively Coupled Plasma Mass Spectrometry Metals Analysis Service Center, Mr. Mac McCord from Busting Lab, Dr. Xu Feng from Surface Analysis Lab, Dr. Wenjun Cai, and Mr. Jia Chen, at the Virginia Tech University for their contributions in this study. I also thank my colleagues Ms. Qiufeng Yang, Ms. Amanda Leong, Mr. Weiqian Zhuo and Mr. Jaewoo Park for their time and assistance with the analyses.

A special thanks to Mr. Brenton Davis, Mr. Mingyang Zhang and Dr. Huali Wu, for their constant motivation, support and assistance throughout my study. Finally, I wish to thank my family, it is because of their support, prayers, patience and motivation that I was able to complete my graduate school.

TABLE OF CONTENTS

LIST OF TABLES

LIST OF FIGURES

LIST OF ABBREVIATIONS

ANL	Argonne National Lab
AOD	Argon-Oxygen-Decarburization
BWR	Boiling Water Reactor
CSP	Concentrated Solar Power
CVD	Chemical Vapor Deposition
CVR	Chemical Vapor Reaction
DSC	Differential Scanning Calorimetry
DOE	Department of Energy
DI	De-Ionized
ECCS	Emergency Core Cooling System
EDS	Energy Dispersive X-ray Spectroscopy
ESR	Electro-Slag-Remelting
GFT	Gas-Cooled Fast Reactor
HTGR	High Temperature Gas-Cooled Reactor
HTF	Heat-Transfer-Fluid
HP	High-Purity
IAEA	International Atomic Energy Agency
ICP-MS	Inductively Coupled Plasma-Mass Spectroscopy
ICL	Israel Chemicals Limited
LWR	Light Water Reactor
LOCA	Loss of Coolant Accident
LFR	Lead-Cooled Fast Reactor
MSR	Molten Salt Reactor
ORNL	Oak Ridge National Lab
PWR	Pressurized Water Reactor
SFR	Sodium-Cooled Fast Reactor
SCWR	Supercritical Water-Cooled Reactor
SEM	Scanning Electron Microscopy
TES	Thermal-Energy-Storage
USA	United States of America
VHTR	Very High Temperature Reactor
VIM	Vacuum Induction Melting
VAR	Vacuum Arc Remelting
XPS	X-ray Photo-electron Spectroscopy
XRD	X-ray Diffraction
psig	pounds-square-inch-gauge

i.e.	that is
viz.	which is
g/mg	gram/milli-gram
cm/m	centimeter/meter
ccm	cubic-centimeter
µm	micro-meter
mm	milli-meter
mol	moles
K	Kelvin
^{o}C	degree-celsius
J	Joules
N	Newton
MPa	Mega-Pascal
mL	milli-liter
abs	absolute
fps	foot-per-second
wt.%	weight-percent
s/sec.	seconds
mA	milli-amphere
V	volts
mV	milli-volts
µV	micro-volts
ppm	parts-per-million
(s)	solid
(g)	gas
(l)	liquid
(v)	vapor
Ø	diameter
e.g.	example

CHAPTER 1

1 INTRODUCTION

The global energy demand is expected to increase by 45% in the next twenty years. As per the International Atomic Energy Agency (IAEA), coal remained the dominant source of electricity production around the world in 2018 followed by hydropower and renewables, which significantly increased to 25.8%, while the share of electricity production from natural gas and nuclear energy remained at about 23% and 10.2% respectively [1]. However, with rapid increase in the demand for electricity, and reduced dependence on fossil fuels, there is a need for nuclear energy to be the fastest growing energy source. This will also assist in achieving the climate goals by reducing the carbon footprints. Currently, most of the nuclear fleets operating around the world are solid fuel light water reactors (LWRs) i.e. pressurized water reactors (PWRs) and boiling water reactors (BWRs). Though efficient, they still pose grave challenges in terms of safety during an accident, and during the handling and disposal of radioactive waste that is generated over the reactor operating cycle. During the loss of coolant accident (LOCA) i.e. caused by large or small pipe break, reactors are designed with advanced safety features like the Emergency Core Cooling System (ECCS), and the passive nuclear safety system, which prevents fuel-meltdown by shutting down and cooling the reactor safely, and in a timely manner. But, with human intervention there is always a risk as also observed at Fukushima Daiichi Nuclear Power Plant, Okuma, Fukushima, Japan in 2011 [2], where the loss of coolant accident resulted in severe consequences on the surrounding life-forms, and the environment.

In response to these issues, and in an effort to address climate change, a consortium i.e. the Generation IV International Forum, led by a group of nine nations (Argentina, Brazil, Canada, France, Japan, the Republic of Korea, the Republic of South Africa, the United Kingdom and the United States) was created to initiate the development and faster deployment of innovative nuclear reactor systems [3]. These include (1) Gas-Cooled Fast Reactors (GFRs), (2) Very-High Temperature Reactors (VHTRs), (3) Sodium-Cooled Fast Reactors (SFRs), (4) Lead-Cooled Fast Reactors (LFRs), (5) Supercritical Water-Cooled Reactors (SCWRs), and (6) Molten Salt Reactors (MSRs). Some of these reactor concepts could be commercially realized within the next decade (as early as 2030). These modern reactor concepts are beneficial in terms of energy efficiency,

better waste management, reduced greenhouse emissions, lower capital and maintenance costs, enhanced safety features, and lower risk of nuclear weapon proliferation.

Among them, the MSR concept has sparked renewed interest among the nuclear community due to its "inherent safety" and flexibility. It has a long history with the early works being carried out by the Oak Ridge National Lab (ORNL) under their molten salt program from 1950s–1970s [4]. The MSRs use molten halide (chlorides and fluorides) salts as liquid fuel, and coolant due to their desirable thermo-physical properties like lower melting-point, higher boiling-point, low density, low viscosity, low vapor pressure, etc., good neutronic properties, and excellent heat transfer capabilities [5, 6].

The molten salt specifically chloride salts are also used in other applications like solar energy, baths for various alloy heat-treatments like annealing and martempering of steel, for surface modifications of steels like carburizing and nitro-carburizing [7, 8, 9], etc. In the Concentrated Solar Power (CSP) plant technology, they are selected as a potential coolant candidate for the thermal-energy-storage (TES), and heat-transfer-fluid (HTF) systems, where they are expected to replace the existing nitrate salts due to good stability at high temperatures (above 500 ºC). This will increase the plant's operating temperatures, and its overall efficiency. However, the molten halide salts also pose grave challenges with material selection because of its aggressive behavior at high temperatures [7, 10, 11].

Numerous studies [12, 13, 14, 15, 16, 17, 18] have shown that nickel-based alloys exhibit better resistance to corrosion than ferrous-based alloys in different molten halide salts. Corrosion in these alloys are attributed to the preferential attack on chromium (Cr) by the molten salt with the severity of the attack depending on its concentration in the alloy. This is because as the formation of passive layer becomes thermodynamically unfavorable in the molten salt, corrosion proceeds as active metal dissolution. The voids formed by the depletion of the less noble elements will severely depreciate the physical and mechanical properties (i.e. tensile strength, hardness, wear and fatigue resistance, etc.) of the alloy. As shown in **Figure 1**, the corrosion kinetics at the material interface is governed by a three-step process.

1) Dissolution
2) Mass Transfer via Convection

3) Mass Transfer via Diffusion

Generally, the molten salt corrosion is driven by impurities in the salt, which are mostly oxygen-based and water-based [13]. Depending on the salt's stability, they can react (i.e. undergo hydrolysis during heating) with the salt to form soluble and/or insoluble oxide, hydroxide, oxyhalide compounds, and the corrosive halide gas. The impurities accelerate the corrosion in metals and alloys by oxidation, chlorination, etc. Thus, this requires developing purification processes for the molten salts in order to eliminate or reduce these impurities without compensating the salt chemistry (i.e. its composition), and its properties.

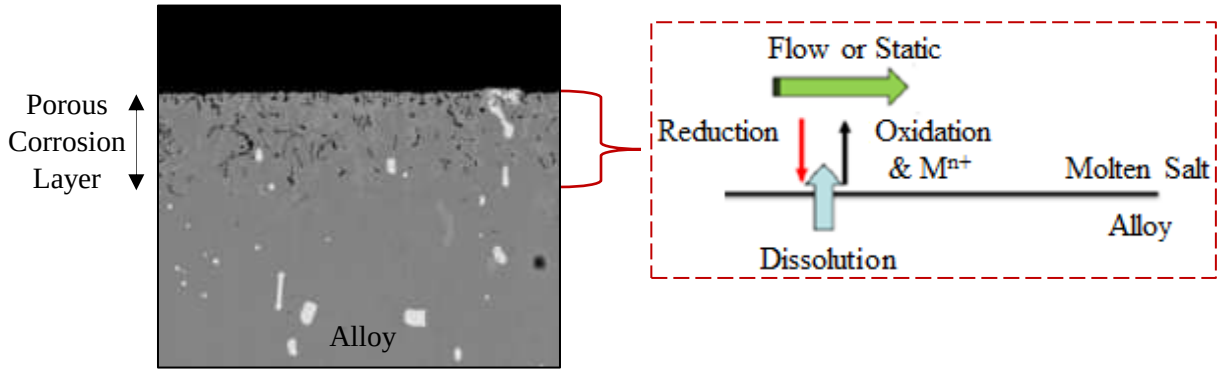

Figure 1. Molten chloride salt corrosion in HAYNES® 230® alloy, and the corrosion kinetics in molten halide salt.

It is quite evident from most of the past, recent and ongoing studies that material corrosion in molten salts is inevitable; so the focus now should shift on slowing-down this process by providing protective barriers in the form of coatings and other surface treatments. Numerous studies have already investigated different types of coatings like MCrAlX (M: Ni and/or Co and X: Y, Ta, Hf, and/or Si) coating [19], castable silica-based cement with boron nitride addition [20], Ni20Cr coating [21], NiCrFeNbMoTiAl coating [22], etc., and their effects on the corrosion resistance of alloys and super-alloys in molten salts. Some of these are metal-based overlay coatings, which exhibit poor thermal stability, thus resulting in its peeling, spalling and/or cracking because of thermal mismatch.

Other coating techniques like boronization has not yet been studied in molten salts. Boron being a neutron-poison cannot be considered for materials in the nuclear reactors (i.e. the primary (core) system of the reactor) as they will interfere in the nuclear chain reaction due to its high neutron

absorption cross-section, but they can still be used in the secondary (steam) system of the reactor in critical components like the pump impellors, valve balls and seats, etc., which are usually subjected to extreme flow-conditions. Unlike conventional coatings, boronization is a surface hardening diffusion coating process, where the boron atoms are diffused into the alloy surface at high temperatures, and for required time duration to form various different metal-borides. The resultant borided material exhibits increased hardness, wear and fatigue resistance [23, 24]. The effectiveness of boronization process depends on the thickness and the composition of the boride layer. If the thickness increases, the volume increases which generates surface tensile stresses and make the alloy more susceptible to stress corrosion cracking at high temperatures [25]. Furthermore, the concentration of the alloying element also affects the growth kinetics of the boride layer, where increased concentration of chromium, nickel, molybdenum and vanadium in the alloy have shown to inhibit the growth of the boride layer [24]. The morphology, composition, properties and stability of boride layers in various different nickel-based and ferrous-based alloys has already been extensively studied. However, the effect of this surface modification on the alloy's capabilities to resist "tribo-corrosion" i.e. resistance against wear and chemical attack under certain environments also needs to be studied.

Graphite is another critical component in the thermal-MSRs, where it acts as a good neutron moderator and reflector because of its low neutron absorption cross-section and high neutron scattering cross-section, high-purity, high-strength (i.e. ability to withstand high temperatures, and fast neutron irradiation), etc. [26, 27, 28]. The graphites commonly used in nuclear reactors are the polygranular types with pore-size ranging from few nanometers to several micrometers. Graphites are inert, and exhibit very poor wetting characteristics with molten salts [29]. However, at pressures and temperatures above the threshold values they could still be infiltrated by the molten salt [30, 31, 32]. The infiltration can cause graphite degradation and microstructural changes in graphite possibly due to molten salt interaction, and induced-stresses. It may also change the graphite's properties such as thermal expansion coefficient, and its irradiation behavior [33, 34], and will increase the damage-rate. Eventually, this would result in the failure of the graphite component in the reactor system.

The causes of degradation could be due to fluorination of graphites in molten fluoride salts caused by the replacement of certain 'C-H' bonds viz. a residual from the graphitization process, with 'C-

F' bonds, thermal-induced stresses by temperature gradient, internal stresses induced by salt crystallization or solidification, external stresses induced by gas pressure, and/or mechanical-induced stresses from manufacturing processes [35, 36, 37, 38]. Considering its importance in the nuclear reactor system, it is necessary to select suitable (which exhibits impermeability in molten salts and resists any form of interaction, and also capable of withstanding high irradiation doses) graphite grades and pore-sizes for the MSR operational purposes.

Most of the past, recent and ongoing corrosion studies in molten salts are based on static conditions in small-scale environments. It must be noted that the corrosion process in such environments is heavily influenced by various different factors like the area (exposed material surface) to volume (molten salt) ratio, where the corrosion process will depend on the solubility limit (as a function of temperature) of various metal-oxide and metal-halide species in the molten salt, hydrodynamic parameters like the pressure gradient effects, shear stress effects, and viscosity effects, which depend on the fluid properties like density, viscosity, solid particles (insoluble impurities) in the fluid, etc., and its flow-velocity. Several molten salt flow systems (natural and forced circulation) have already been designed by ORNL [39], the University of Wisconsin [40], etc. to study the effects of flow-controlled-molten salt corrosion in various different alloys. Some of these systems have only worked with molten fluoride salts. Furthermore, several issues have also been found in these systems which were related to valves, seals, pumps, salt purification, instrumentations, etc. It is necessary to address these issues as they can also transpire during the MSR operation. Furthermore, there is also a need to develop a flow system to study the corrosion characteristics of candidate alloy (which is selected from the static corrosion tests for various different alloys) in the selected molten chloride salt for the MSRs, and also for the CSP plants.

1.1 Research Objectives

The objective of this study is to understand the influence of various different factors (i.e. impurities in the salt, effect of alloying elements, and microstructure) on the corrosion behavior of alloys/superalloys (nickel and ferrous-based alloys) in molten halide salts. Any compromise in the mechanical properties of the materials due to molten salt corrosion is also evaluated. Efforts are made to mitigate corrosion using the diffusion coating process (boronization). The virgin nuclear grade graphites are also studied for their compatibility in molten salts which includes understand the infiltration behavior of molten salt in these materials as a function of temperature and pressure, and material changes (degradation) caused by salt-material interaction or stresses (salt infiltration, pressure, thermal or/and mechanical). This study should assist with material selection for molten salt applications.

The study comprises of four sections, the first section involves purification of molten chloride (KCl-$MgCl_2$-NaCl) and fluoride (KF-UF_4-NaF) salts, and evaluating the effectiveness of these purification processes in eliminating or reducing the corrosive contaminants in the salt. Additionally, the influence of these impurities on the corrosion behavior is also studied by testing Haynes® 230® alloy in the molten KCl-$MgCl_2$-NaCl salt using different salt-purity conditions, under static conditions, in an inert environment, at 800 ºC for 100 hours.

The second section involves testing (immersion and vapor corrosion) various material in molten halide salts again under static conditions, in an inert environment, at 800 ºC for 100 hours. Different nickel-based alloys (Haynes® 230®, Hastelloy® C276 and Inconel® 718), ferrous-based alloys (Stainless Steel 316L and 709), boronized nickel-based alloys (Hastelloy® C276, Inconel® 718), boronized ferrous-based alloy (Stainless Steel 316L) are selected and tested for their corrosion characteristics in the molten KCl-$MgCl_2$-NaCl salt. The corroded alloys are also studied to understand the effects of microstructural changes (grain-boundary examination) caused during the alloy's manufacturing, and/or refinement processes, heat-treatments, etc. on their corrosion behavior in molten salts. The alloys are also examined for any changes in their mechanical properties (i.e. hardness and wear resistance) due to molten salt corrosion.

The third section involves testing different grades and pore-sizes of "virgin" nuclear grades of graphite in the molten (KF-UF_4-NaF) salt at different temperatures and pressures, to select suitable

tolerable graphites for the MSRs operational purposes. The infiltrated graphites are studied to detect and measure salt infiltration, and identify the cause of degradation (possibly salt-graphite interaction and/or induced stresses).

Based on the static corrosion test results suitable materials will be selected for longer duration flow corrosion tests for which a high temperature forced circulation molten salt system is designed and built at the Virginia Tech University, and will be introduced in the fourth section.

CHAPTER 2

2 REVIEW OF LITERATURE

2.1 Fundamentals of Molten Salt Corrosion

Molten halide salts are ionic compounds i.e. chemical compounds held together by ionic bonds usually between a metal (electron donor) and a non-metal (electron acceptor). The ionic bonds depend on the electronegativity difference (large) between the ions. More electronegative the element is (e.g. Fluorine), more attraction its shows towards electrons. Unlike covalent bonds, ionic bonds are stronger (requires greater energy to break the bond), and polar. Polarity of ionic compounds defines its solubility in solvent (water), where it could dissociate into ions.

Selection of corrosion-resistant material is a major challenge for the molten salt applications. When a metal/alloy/superalloys contacts the molten salt, the soluble contaminants extensively reacts with the least noble elements in the alloy like chromium, nickel, iron, etc. to form various metal-oxide and metal-halide compounds [41, 42]. The order of interaction depends on thermodynamic favorability of the reactions in the molten salt. The compounds are highly unstable, and based on their solubility in the molten salt will eventually dissolve in it. The corrosion cycle continues until the molten salt saturates with these oxide/chloride species, or exhausts the impurities. Generally, the corrosion process in molten salt is governed by [43],

1) Impurities or contaminants i.e. presence of oxidants like dissolved O_2, H_2O, and its concentration in the molten salt.
2) Solubility of metal-oxide and metal-halide compounds in the molten salt.
3) Galvanic interaction because of dissimilar metal contact in the electrolytic molten salt medium.
4) Erosion corrosion because of flow-induced stresses i.e. combined effects of molten salt density and flow-velocity.
5) Material degradation because of thermal-induced stresses i.e. temperature-gradient effects.
6) Intergranular attack caused by molten salt diffusion or infiltration through the grain-boundaries (specifically if the grain-boundaries are enriched with active elements like Cr-rich regions).

There are various different types of molten salts like the molten chloride salts, molten fluoride salts, molten nitrate salts, molten sulphate salts, molten carbonate salts, etc., and they occur in different forms as binary, ternary or quaternary salts. The selection of candidate salt depends on the application (solar energy where it will be used as coolant, nuclear where it will be used as fuel or coolant or both), and the desirable thermophysical properties (low vapor pressure, good stability at low and high temperatures, high boiling-point, low melting-point), heat-transfer capabilities (good specific heat, good thermal conductivity), nuclear related properties (non-interference in the nuclear chain reaction, good moderator, effective removal of decay heat, better negative reactivity feedback, and efficient dissolution of fissile material to maintain the criticality), hydrodynamic properties (low density, low viscosity), and compatibility with the containment and structural materials [44, 45].

2.1.1 Molten Salt Selection

Molten chloride salts are considered as a potential coolant candidate for the CSP plant technologies, where they are expected to replace the existing nitrate salts due to good stability at higher temperature thus enhancing the thermal efficiency of the plant [7, 8]. On the other hand, for the MSRs, molten chloride salts can be used as fuel-coolant in the primary system (reactor system), or/and just as coolant in the secondary system (steam system), or/and for pyro-processing (fluoride and chloride volatility methods) of spent nuclear fuel (extract fissile material from the waste for recycling thus reducing the volume of high-level wastes) [46]. Molten fluoride salts are the ideal choice for thermal-spectrum-MSRs because of lower thermal neutron absorption cross-section. Another core-issue with chloride salts is the production of long-live radio-isotope, chlorine-36 (^{36}Cl), which is a beta-emitter and highly soluble in water [47]. Large production of this isotope will create problems with the radioactive waste disposal. Furthermore, unlike fluoride salts where fluorine has a single oxidation state (-1), chlorine in chloride salts have several oxidation states (+7, +5, +3, +1 and -1) thus making the corrosion process more complicated because of the possibility to form different complex bonding configurations [47]. However, the molten chloride salts can still be used and are considered for fast-spectrum-MSRs [47, 48].

2.1.2 Effects of Non-Metallic Impurities

The impurities commonly found in molten salts are metallic impurities like Fe, Ni, Cr, etc., and non-metallic impurities which are mostly oxygen-based and water-based. These impurities exist in the salts (pure compounds), possibly introduced during its synthesis/production, exposure to air during storage, handling and transportation, or by the hydrolysis of salt during its dehydration process (on heating the salt will react with water) or by thermolysis or thermal decomposition (chemical decomposition caused by heat). Most salts are stable at room temperatures (the water does not bond with the salt and stays as hydrates), however, when heated they can undergo hydrolysis to form the soluble or/and insoluble oxide, hydroxide and oxy-halide compounds and the hydrogen halide (hydrogen chloride or hydrogen fluoride) gas [[49], [50]]. Both these gases are toxic and aggressive in nature. Prolonged exposure to these gases is highly detrimental to the contacting materials.

They will react with the most active elements by "single displacement reaction" or "single replacement reaction" to form metal-halide compounds (it depends on the order of the elements in the "activity series" or "reactivity series" i.e. metals with activity higher than hydrogen are easily displaced by it in the reaction). Just like metal-oxides, the metal-halides are also unstable in molten salts. They are not self-sustaining, and do not provide any form of protection against molten salt attack, and depending on their solubility in the molten salt will eventually dissolve in it. Additionally, the molten salt corrosion process also depends on the Gibbs free energy of formation (ΔG) for the driving reactions that form metal-oxides (chromium oxide, nickel oxide, iron oxide), and metal-chlorides (chromium chloride, nickel chloride, iron chloride) or metal-fluorides (chromium fluoride, nickel fluoride, iron fluoride). At a given temperature,

- If $\Delta G < 0$ (negative), the driving reaction is spontaneous, or thermodynamically favorable.
- If $\Delta G = 0$, the system is in equilibrium.
- If $\Delta G > 0$ (positive), the driving reaction is non-spontaneous, or not thermodynamically favorable.

Figure 2 shows the corrosion process in alloys by molten salt, which is a combination of dissolution, oxidation and chlorination processes, generally occurs through electron transfer at the alloy surface.

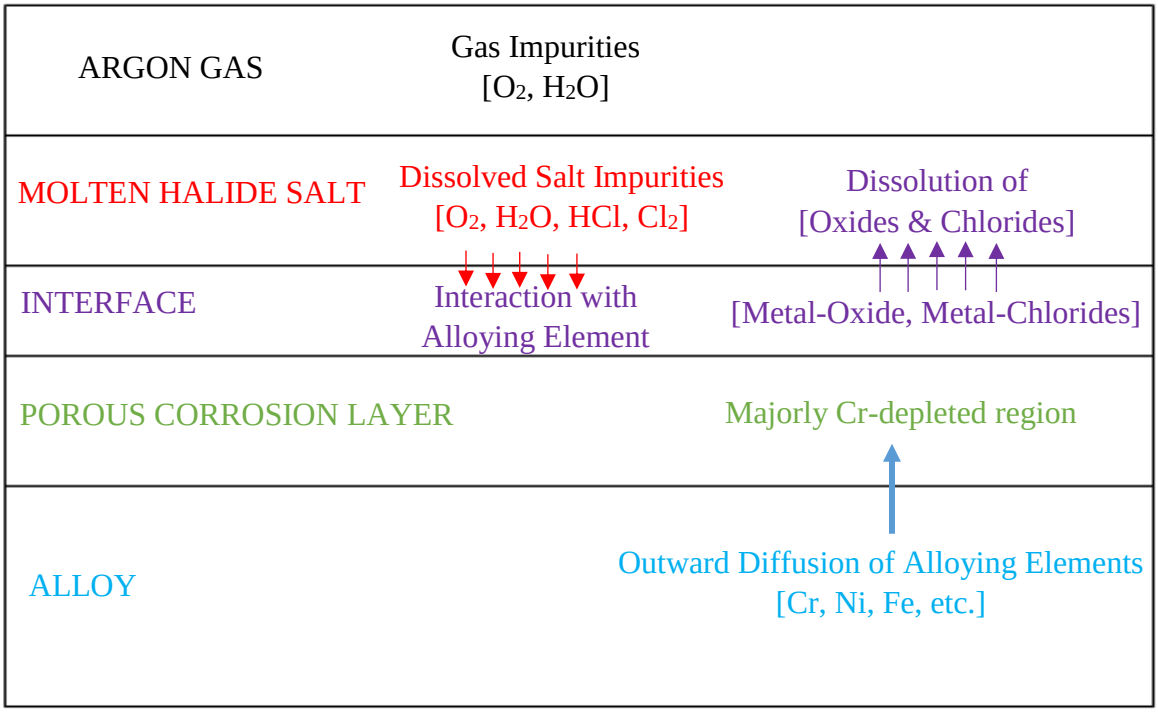

Figure 2. Schematic representation of corrosion mechanism in alloys by molten halide salt with non-metallic impurities.

The corrosion-rate have shown linear dependence on the concentration of corrosive impurities in the molten salt. Ding, W. et. al. [13], proposed the modified "impurity-driven" ($MgOH^+$) corrosion-rate formulation for [Fe-Ni-Cr] based alloys in molten chloride salt ($MgCl_2$/KCl/NaCl), which depends on the exposure temperature and the $MgOH^+$ concentration.

$$CR = k(T) \cdot c(MgOH^+)^a \quad \textbf{(1)}$$

CR = corrosion-rate (µm/year)

K(T) = reaction constant in µm/year/(ppm), dependent on the temperature of the melt

$c(MgOH^+)^a$= concentration of impurity in the salt (ppm) with a as the reaction order

Just like in aqueous solution (H^+ ions), the acidity-basicity of molten salt is determined from the oxide (O^{2-}) ion concentration [Lux-Flood acid-base model] i.e. low O^{2-} ion concentration indicates basicity of the molten salt and vice-versa [43]. This assists in identifying the corrosion pathway (i.e. dissolution of metal-oxide via acidic or basic pathway) in the molten salts. For instance, if the oxide ion concentration in the molten salt is low, then the metal-oxide dissolution happens via acidic pathway, where it dissociates to form O^{2-} ions and metal ions (M^{z+}), which might be soluble

in the molten salt. In other words, in an acidic melt (with low oxide ion concentration) the corrosion is cathodic controlled and in a basic melt (with high oxide ion concentration) is anodic controlled.

Step I: Passivation layer [43]

$$yM + \left(\frac{x}{2}\right) O_2 = M_yO_x \quad \textbf{(2)}$$

M: Cr, Ni, Fe, etc.

Step II-A: Metal-oxide dissolution via acidic pathway [43]

$$M_yO_x = xM^{z+} + O^{2-} \quad \textbf{(3)}$$

M: Cr, Ni, Fe, etc.

If the molten salt has excess oxide ion concentration, then the metal-oxide dissolution happens via basic pathway, where the metal-oxide accepts the O^{2-} ions to form the metal-oxide anions.

Step II-B: Metal-oxide dissolution via basic pathway [43]

$$M_yO_x + zO^{2-} = M_xO_{y+z}^{-2} \quad \textbf{(4)}$$

M: Cr, Ni, Fe, etc.

Analogous to Pourbaix diagram in aqueous corrosion, the pO^{2-} phase diagrams are used for molten salt corrosion which helps define the dissolution pathway for metal species in molten salts under equilibrium conditions at given temperatures [51].

2.1.3 Effects of Alloying Elements

Numerous studies have been conducted to investigate the compatibility of various different metals/alloys/superalloys in molten halide salts. It was found that nickel-based alloys exhibit good corrosion resistance in molten salts than ferrous-based alloys. Even among nickel-based alloys, the corrosion resistance was in the increasing order of [Ni-Mo-Cr] > [Ni-W-Cr] > [Ni-Fe-Cr], thus indicating significant influence of alloying elements [52]. One of the cheapest, easiest and quickest way to check the compatibility of various different materials (metals/alloys/superalloys) in molten salts, is by conducting small-scale short duration static corrosion tests. The performance of materials in molten salts is predicted from the weight-changes (weight-loss), which is used to estimate the average corrosion-rates from the following formulation [53],

$$CR = \frac{K\Delta W}{ATD} \quad \textbf{(5)}$$

CR = average corrosion-rate (µm/year)

K = conversion factor for µm/year, 8.76 X 10^7

ΔW = weight loss (g)

A = exposed area (cm^2)

T = exposure time (hours)

D = density of the material (g/cm^3)

However, even with good corrosion-resistant properties, the nickel-based alloys still do not meet the requirements [viz. CR must be <10 µm/year (limiting value)] of materials for commercial applications. The chromium (Cr) content in the alloy is one of the critical factors that drives and controls molten salt corrosion in alloys. This is because of its strong electro-motive-force (EMF) in the molten salts [[13], [54]]) causing it to readily react with O_2, HX (halide gases, X: HCl or HF) to form chromium-oxide and chromium-halide (chloride or fluoride) compounds. Instability and dissolution of these compounds in the molten salt drives out more Cr from the alloy and creates a near-uniform porous corrosion layer in the region close to the alloy interface. The outward diffusion rate of Cr also depends on the solubility limit of the chromium species in the molten salt or the impurity concentration in the salt i.e. if the solubility reaches or exceeds the critical saturation limit, or if the impurities in the salt are completely consumed, the corrosion process will either slow down or cease.

There is limited information available in the literatures on the solubility limit for metal-oxides, metal-halides (chlorides/fluorides), and halide gases in the molten salts [[55], [56]]. Studies conducted by Goods, S. H. et. al. [[57]], also showed that the Cr content (from the exposed alloy) in molten salt (nitrate salt, at 570 ºC) increases initially (up to 846 hours), after which it reaches equilibrium and remains constant for the remainder of the test (up to 7000 hours) thus acting as a corrosion inhibitor. It must also be noted that impurities in the molten salt could alter the salt-chemistry (eutectic composition), and affect its properties (thermophysical properties, heat-transfer capabilities, etc.).

Some studies have also shown adding elements like molybdenum (Mo) and tungsten (W) in the alloy can increase its resistance against the molten salt attack [58, 59, 60, 61]. This because both these elements are inert (most noble elements) to molten salts i.e. the Gibbs free energy of formation for all possible interactions with the molten salt is more positive, and thus thermodynamically unfavorable. Furthermore, the larger atomic size of tungsten also makes it difficult to be diffused through the alloy thus protecting the alloy by forming a barrier and preventing any further outward-diffusion of Cr. However, it should also be noted that the content of these inert elements in the alloy is very small, and is usually scattered across the alloy in the form of rich-regions thus severely undermining their effects.

Also, the corrosion studies in static conditions do not account for other influential factors such as temperature gradient effects and flow-effects (refer **Figure 3**), where the corrosion process is initially instantaneous and governed by the impurities and its concentration in the salt. However, as time progresses (impurities are completely consumed), the corrosion (slowly increases) is driven by other factors (thermal stresses and/or flow-induced shear stresses).

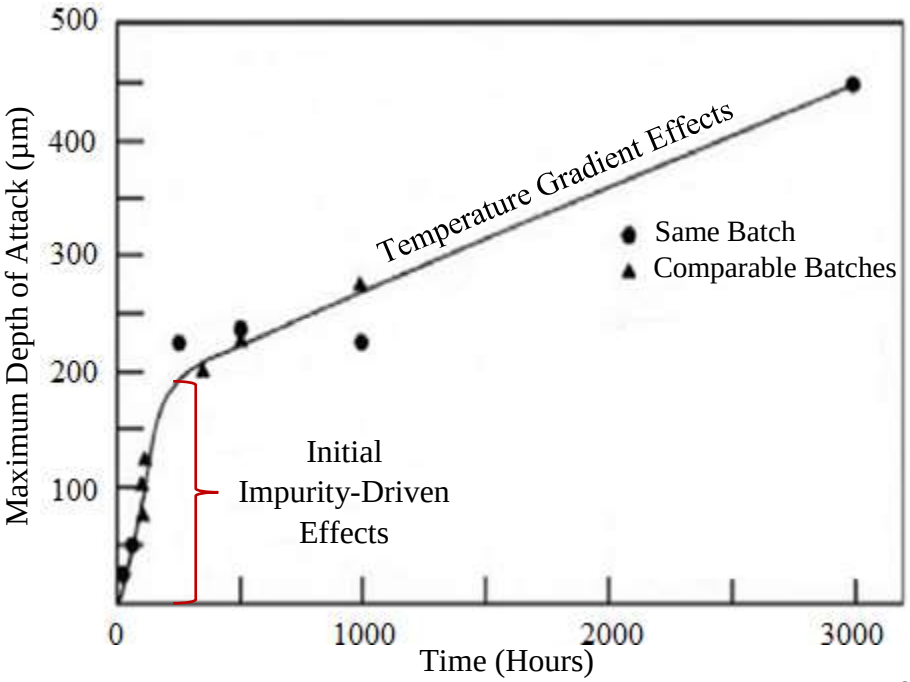

Figure 3. Flow-induced corrosion in molten salts (reproduced from [62]).

2.1.4 Intergranular Corrosion

All manufactured alloys undergo some form of heat-treatment also known as "age-hardening" process, where the alloy is heated and cooled (annealing process) under controlled conditions which includes considering proper temperatures, heating and cooling rates, and holding time. This is done to refine the alloy (i.e. to reduce impurities from the manufacturing process), relieve residual stresses, and strengthen the material. However, depending on the carbon content in the alloy, it can also undergo sensitization which involves carbide precipitation in the grain-boundaries, when exposed to sensitizing temperatures [63, 64]. The carbides formed are mostly chromium carbides and in some cases molybdenum or tungsten carbides, which precipitate in the grain-boundaries, while depleting in the region adjacent to the grain-boundaries [52]. This makes the alloy more susceptible to intergranular corrosion or intergranular stress corrosion cracking as the presence of Cr in the grain boundaries makes it the most preferential site for the onset of molten salt corrosion.

Studies have confirmed grain-boundary attack in molten salts for ferrous-based alloys as well as nickel-based alloys [52, 65, 66]. It leads to the formation of voids in the grain-boundaries because of the depleting Cr which reacts with the molten salt by fluorination or chlorination, and oxidation. As the voids continue to grow, it will result in total collapse of the grain-boundaries. Sun et. al. [65] noted that, the differences in the corrosion of nickel-based alloys [Ni-Mo-Cr], [Ni-W-Cr], etc. was also attributed to the influence of Mo and W on the diffusion kinetics of Cr in Ni. It can be estimated from the following equation [59],

$$x = (Dt)^{1/2} \quad \textbf{(6)}$$

x = diffusion distance (m)

D = diffusion coefficient ($/m^2s^{-1}$)

t = immersion time (sec)

Generally, the diffusion coefficient for Cr in Ni in the lattice and the grain-boundaries is estimated from the following equation [59, 67],

$$\delta D_z = D_0 e^{-Q/RT} \quad \textbf{(7)}$$

z = lattice (l) or grain boundary (gb)

D = diffusion coefficient (/m^2s^{-1})

δ = grain boundary width (m), and is not applicable for lattice

D_o = constant for a given diffusion system

T = temperature (K)

Q = activation energy ($J \cdot mol^{-1}$)

R = gas constant (J/mol/K)

As shown in **Figure 4**, the lattice and grain-boundary diffusion coefficients are temperature dependent, and increases with temperature. The grain-boundary diffusion coefficient is always larger than the lattice diffusion coefficient thus accelerating the corrosion process [65]. However, since most of the corrosion tests are conducted at constant temperature, this reduces the influence of temperature and increases its (diffusion coefficient) dependency on D_o and Q, which changes with alloy composition and its microstructure.

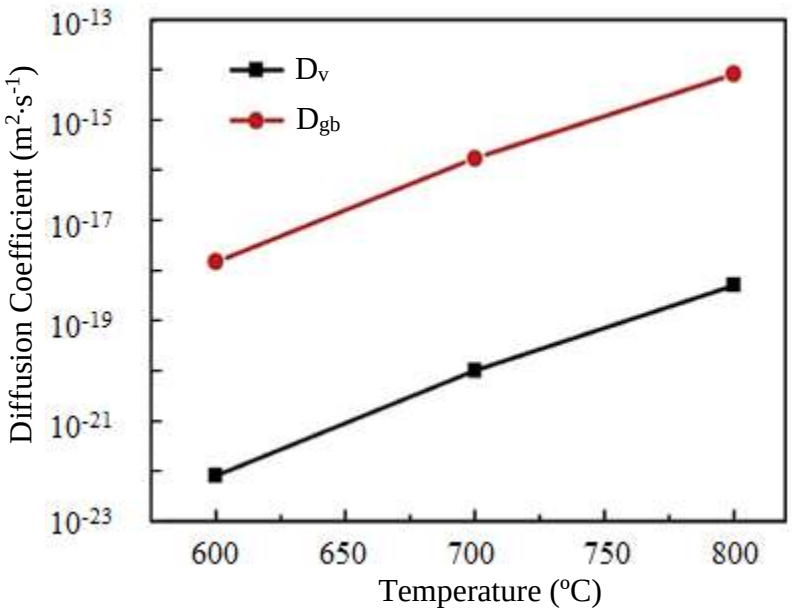

Figure 4. Lattice and grain boundary diffusion coefficient as a function of temperature (reproduced from [65]).

2.1.5 Flow Corrosion

Flow-velocity is another critical factor which affects the corrosion kinetics (erosion corrosion) of alloys in molten salts. There are four types of flow corrosion (1) mass transport controlled

corrosion, (2) phase transport controlled corrosion, (3) erosion corrosion, and (4) cavitation corrosion [68].

2.1.5.1 Mass Transport Controlled Corrosion

Mass transport controlled corrosion is a type of material attack which is caused by convective mass-transfer at the material-fluid interface. For turbulent flow conditions, the mass-transport correlations are defined using combination of dimensionless groups [68],

Sherwood number (Sh)

$$Sh = \frac{kL}{D} \quad \textbf{(8)}$$

k = convective mass transfer coefficient ($m \cdot s^{-1}$)

L = hydraulic diameter (m)

D = mass diffusivity ($m^2 \cdot s^{-1}$)

Reynolds number (Re)

$$Re = \frac{uL}{\nu} \quad \textbf{(9)}$$

u = flow-velocity ($m \cdot s^{-1}$)

ν = kinematic viscosity ($m^2 \cdot s^{-1}$)

Schmidt number (Sc)

$$Sc = \frac{\nu}{D} \quad \textbf{(10)}$$

Mass transport co-relation

$$Sh = aSc^b Re^c \quad \textbf{(11)}$$

a, b and c = constants

The above the co-relation can be re-written to obtain the corrosion-rate as a function of flow-velocity,

$$CR = constant \cdot u^c \quad \textbf{(12)}$$

It must be noted that the above correlation is applicable when only the mass-transfer is the rate determining step. It cannot be used if the corrosion process involves other processes like electrochemical process or chemical process. In such cases, the corrosion will be defined as mixed controlled corrosion. Shemilt, L. W. et. al. [69], developed another model for unsteady state mass-transfer rate based on a two-step process,

Step I: Mass-transfer rate through the diffusion sub-layer in liquid phase

$$\frac{dm}{dt} = K_L(C_b - C_i) \quad \textbf{(13)}$$

Step II: Mass-transfer rate through the porous solid corrosion layer

$$\frac{dm}{dt} = K_s(C_i - C_s) \quad \textbf{(14)}$$

Step III: Resultant mass-transfer rate

$$\frac{dm}{dt} = \frac{(C_b - C_s)}{\left(\frac{1}{K_L} + \frac{1}{K_s}\right)} = K_o(C_b - C_s) \quad \textbf{(15)}$$

$\frac{dm}{dt}$ = mass-transfer rate

K_L = mass-transfer coefficient in liquid sublayer

K_s = mass-transfer coefficient in porous solid layer

C_b = bulk concentration of the diffusing species

C_i = concentration of the diffusing species at interface

C_s = concentration of the diffusing species in the porous layer

K_o = overall mass-transfer coefficient

2.1.5.2 Erosion Corrosion

Erosion corrosion is also a type of material attack which is caused by the relative motion of the corrosive fluid and the material surface. It facilitates the removal of material or its passivation layer because of the moving fluid which generates shear stresses on the material surface when the flow-velocity exceeds the critical limiting value. The erosion-rates increases if the fluid contains any solid particles (e.g. impurities in the molten salt), or phases changes (unlikely in the molten salts), or surface modifications like pits, shallow caters or roughness formed during the corrosion

process or coating process as it disturbs the smooth (laminar) flow-pattern causing localized turbulence zones.

2.1.5.3 Hydrodynamic Parameters

The molten salts are Newtonian fluids, where the velocity field is defined by the Navier-Stokes equation. Generally, the are different types of flow-patterns i.e. laminar, transition from laminar to turbulent, turbulent, which are governed by the laws of hydrodynamics. Based on the flow conditions, different types of interactions (mostly viscosity, and pressure gradient effects) can occur on the material because of the moving fluid.

Pressure Gradient Effects [68]

In turbulent flow conditions, if the surface roughness exceeds the thickness of the laminar sub-layer, the pressure variations convert to shear stress at the surface which adds up to the total shear stress to cause significant damage to the material.

Viscosity Effects [70]

Viscosity of the fluid is another influential factor that affects the flow shear stresses at the material surface. This is because as shown in **Figure 5**, at higher flow-velocities or higher Reynolds number, the fluid moves faster producing a much thinner boundary layer and a larger velocity gradient near the wall thus resulting in higher flow shear stresses.

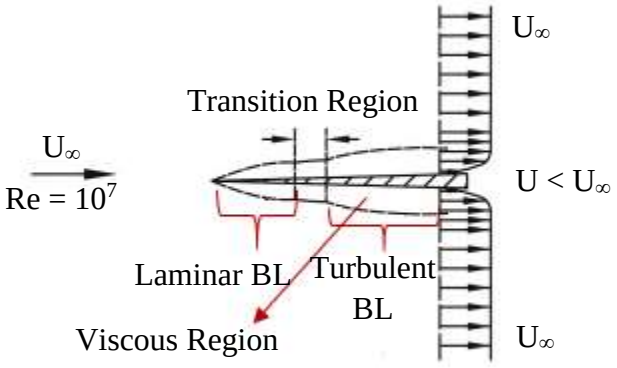

Figure 5. Viscosity effects at higher flow velocities (reproduced from [70]).

Material degradation due to flow corrosion can be averted by ensuring the values of these hydrodynamic parameters do not exceed the critical limiting values. Several efforts have been

made to understand the flow-induced effects in molten salt corrosion with the earliest studies starting in 1972 by the ORNL, where a forced circulation loop was designed and built to evaluate the compatibility of Hastelloy® N in $NaBF_4$-NaF salt at temperatures of 454 ºC and 620 ºC, and flow-velocities of 10.9 fps and 20.8 fps respectively [39]. Other works include University of Wisconsin, which has also designed and built high temperature forced circulation systems for flow corrosion studies in molten FLiNaK, KCl-$MgCl_2$, and nitrate salts [40].

2.2 Molten Salt Purification

Studies have already confirmed that corrosion of metals/alloys/superalloys in molten salts is an impurity-driven process. The contaminants are mostly oxygen-based and moisture-based and depend on the nature of the salt i.e. hygroscopic salts can easily and readily attract and absorb water without bonding. These impurities are undesirable in the molten salt, and can introduce several soluble and insoluble species (oxides, hydroxides, oxyhalides, hydrogen halide gases, etc.) through its hydrolysis, thermal decomposition (thermolysis) and chemical decomposition. Molten salt purification is a complex and a complicated process and involves numerous challenges like, it cannot completely remove the impurities, difficulty in handling toxic and corrosive gases used in the purification processes, possibility of changing the salt chemistry (composition) and its properties due to chemical reaction with the existing impurities or by introducing new impurities from the purification processes, the salt can easily re-contaminate after purification during handling, storage and transportation, etc.

2.2.1 Molten Chloride Salt

The molten chloride salt selected is the potassium chloride-magnesium chloride-sodium chloride (KCl-$MgCl_2$-NaCl) salt. It is the US Department of Energy's (DOE) candidate salt for the CSP plant technologies. In the KCl-$MgCl_2$-NaCl salt, $MgCl_2$ is the prime-source of contamination because of its highly hygroscopic nature [49] which as discussed earlier allows the salt to actively attract water without bonding when exposed to air. However, the KCl, $MgCl_2$ and NaCl salts in its purest form are stable compounds at room temperatures i.e. the water absorbed by the salt does not react with it and stay as "hydrates" ($\cdot\, nH_2O$; for the $MgCl_2$ salt, n is $1, 2, 4, 6, 8$ and 12 [49], for the KCl salt, n is 1, and for the NaCl salt, n is 1).

The dehydration of $MgCl_2 \cdot 6H_2O$ involves the following six-step process [49],

$$MgCl_2 \cdot 6H_2O(s) \rightarrow MgCl_2.4H_2O(s) + 2H_2O(v) \quad \textbf{(16)}$$

$$MgCl_2 \cdot 4H_2O(s) \rightarrow MgCl_2.2H_2O(s) + 2H_2O(v) \quad \textbf{(17)}$$

$$MgCl_2 \cdot 2H_2O(s) \rightarrow MgCl_2.H_2O(s) + H_2O(v) \quad \textbf{(18)}$$

$$MgCl_2 \cdot H_2O(s) \rightarrow MgCl_2(s) + H_2O(v) \quad \textbf{(19)}$$

On heating, most of the water in the salt vaporizes, however, there is still a possibility that $MgCl_2 \cdot 2H_2O$ and $MgCl_2 \cdot H_2O$ could undergo partial-hydrolysis and complete-hydrolysis and form magnesium chloride hydroxide (MgOHCl) compound and hydrogen chloride (HCl) gas.

$$MgCl_2 \cdot 2H_2O(s) \rightarrow MgOHCl(s) + +HCl(g) + H_2O(v) \quad \textbf{(20)}$$

$$MgCl_2 \cdot H_2O(s) \rightarrow MgOHCl(s) + HCl(g) \quad \textbf{(21)}$$

There are concerns with the stability of the magnesium chloride hydroxide compounds, which can thermally decompose to form magnesium oxide (MgO) and HCl gas as shown in the following **Reaction (22)**. The decomposition-rate is temperature-dependent, and accelerates at higher temperatures ≥553 ºC [71].

$$MgOHCl(s) \rightarrow MgO(s) + HCl(g) \quad \textbf{(22)}$$

Magnesium chloride ($MgCl_2$) can also directly react with water at high temperatures and form magnesium oxide (MgO) and magnesium hydroxide ($Mg(OH)_2$) compounds as shown in **Reactions (23) and (24)** [HSC Chemistry® 10 Software],

$$MgCl_2(s) + H_2O(l) \rightarrow MgO(s) + 2HCl(g) \quad \textbf{(23)}$$

$$MgCl_2(s) + 2H_2O(l) \rightarrow Mg(OH)_2(s) + 2HCl(g) \quad \textbf{(24)}$$

Kipouros, et. al. [49] noted that complete dehydration of $MgCl_2$ without hydrolysis is possible and achievable by providing a blanket of chlorine (Cl_2) or chlorine-based gases (HCl) with proper partial pressure ratios $(P_{HCl}: P_{H_2O})$. **Figure 6** shows the vapor pressures of H_2O and HCl as a function of temperature over different hydrates of $MgCl_2$. This data can be used to calculate the minimum ratio of partial pressures of HCl to H_2O that is required to prevent the hydrolysis of $MgCl_2$ salt.

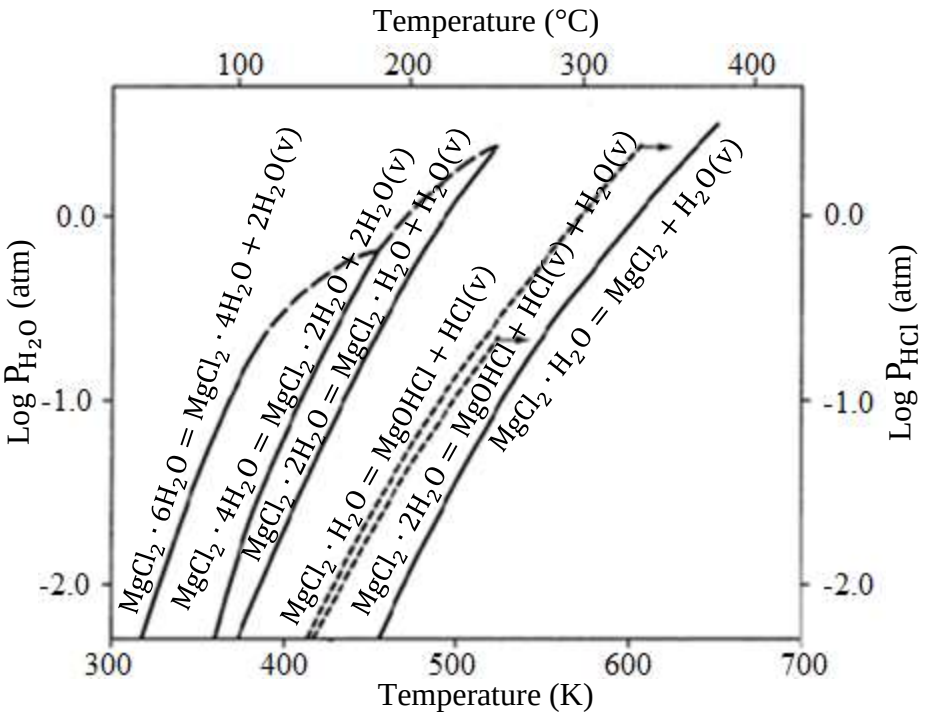

Figure 6. Vapor pressure of H_2O and HCl as a function of temperature for different hydrates of $MgCl_2$ salt (reproduced from [49]).

Over the years, numerous different purification processes have been proposed and used with moderate to great success, to dehydrate (remove water) molten chloride salt (specifically to produce anhydrous magnesium chloride salt), and also to reduce or remove other metallic and non-metallic contaminants.

2.2.1.1 Thermal and Chemical Heat-Treatment [72]

The thermal heat-treatment involves slowly heating the hydrated $MgCl_2$ salt below its hydrolysis temperatures. The hydrolysis temperatures can be estimated by calculating the Gibbs free energy of formation for the driving reactions (i.e. if ΔG is more negative for a particular reaction at a given temperature, the reaction is more favorable at that temperature). However, as discussed earlier in **Section 2.2.1.**, in the absence of proper blanket gas, the mono-hydrate magnesium chloride salt could still undergo hydrolysis.

ORNL proposed to chemically treating the salt during heat-treatment using ammonium chloride (NH_4Cl) to facilitate complete removal of water without hydrolysis as shown in **Reaction (25)**.

$$MgCl_2 \cdot nH_2O + NH_4Cl \xrightarrow{\Delta} MgCl_2 + NH_3(g) + HCl(g) + H_2O\,(v) \quad \textbf{(25)}$$

This process involves several challenges associated with the safety of the reactor caused by the reformation of NH_4Cl in the cold-zones, which could clog the exhaust system of the reactor and result in its catastrophic failure. Furthermore, the process is also inefficient in reducing the oxide content (MgO) in the salt [73].

2.2.1.2 Chlorination

ORNL also proposed using carbo-chlorination process (using chlorine-based gases) to deal with magnesium oxide in the magnesium chloride salt.

(a) Carbon Monoxide (CO) and Chlorine (Cl_2) [74]

$$MgO\,(s) + CO(g) + Cl_2(g) \rightarrow MgCl_2(s) + CO_2(g) \quad \textbf{(26)}$$

(b) Phosgene ($COCl_2$) [75]

$$MgO\,(s) + COCl_2(g) \rightarrow MgCl_2(s) + CO_2(g) \quad \textbf{(27)}$$

(c) Carbon Tetrachloride (CCl_4) [76]

$$MgO\,(s) + \frac{1}{2}CCl_4(g) \rightarrow MgCl_2(s) + \frac{1}{2}CO_2(g) \quad \textbf{(28)}$$

$$MgO\,(s) + CCl_4(g) \rightarrow MgCl_2(s) + \frac{1}{2}CO_2(g) + \frac{1}{2}C(s) + Cl_2(g) \quad \textbf{(29)}$$

$$MgO\,(s) + CCl_4(g) \rightarrow MgCl_2(s) + CO(g) + Cl_2(g) \quad \textbf{(30)}$$

It is observed from the above reactions that carbo-chlorination process not only facilitates the removal of magnesium oxide, but also assists in the recovery of magnesium chloride salt. However, the process is still associated with safety risks from handling the toxic gases i.e. carbon monoxide (CO), chlorine (Cl_2), and phosgene ($COCl_2$).

2.2.1.3 Chemical Heat-Treatment using Magnesium

In this method, small concentration of solid magnesium (Mg) pieces are added to the chloride salt to consume oxygen-based impurities. Mg being an oxygen-scavenger reacts with oxygen and water at high temperatures to form magnesium oxide and magnesium hydroxide compounds as shown in the following reactions.

$$2Mg(s) + O_2(g) \rightarrow 2MgO(s) \quad \textbf{(31)}$$

$$Mg(s) + 2H_2O(l) \rightarrow Mg(OH)_2(s) + H_2(g) \quad \textbf{(32)}$$

The denser insoluble MgO sludge easily separates at the bottom of the salt. Because of its capability to attract impurities in the molten salt, it is also used as a corrosion-inhibitor. However, since Mg is also a reactive element, any contact with the exposed material in the molten salt must be avoided as it could intensify degradation in materials due to possible metal-Mg interaction to form various different complex unstable phases (the type of phases will depend on the metal-Mg binary phase diagrams).

2.2.1.4 Electrochemical Method [77]

MgOHCl compound is formed during the dehydration process by hydrolysis of $MgCl_2$, and is highly undesirable because of its high solubility in the $MgCl_2$ melt. Earlier inventions have considered sparging the salt melt with HCl gas or other chlorine-based gases to recover $MgCl_2$. However, complete removal of MgOHCl will require a large amount of gas and is practically not feasible because of the toxicity of the HCl gas.

The electrolysis process was invented to produce high-purity anhydrous $MgCl_2$ salt. The inventors determined the direct-current voltage (2.75 volts) required to successfully electrolyze a small amount of $MgCl_2$ salt in an electrolyte to produce Mg droplets. The Mg reacts with MgOHCl and recovers $MgCl_2$ as shown in **Reaction (33)**. The electrolyte is the carrier salt (KCl-$MgCl_2$-NaCl), and contains sufficient concentration (15–45 wt.%) of $MgCl_2$ to produce Mg.

$$Mg(s) + 2MgOHCl \rightarrow MgCl_2(s) + 2MgO(s) + H_2(g) \quad \textbf{(33)}$$

Alternatively, another approach involves using a two-electrode set-up in the electrolyte (molten salt), where a direct-current is passed between the two electrodes (both carbon electrodes) to facilitate the removal of MgOHCl. The minimum applied voltage is 2 volts which will destroy MgOHCl at the anode, while producing off-gases like Cl_2, HCl and O_2, which reacts with the carbon electrode to form carbon dioxide (CO_2) and carbon monoxide (CO) gases.
Electrochemical methods though effective in reducing the molten salt impurities involves difficulties in implementing them outside laboratory environments.

2.2.2 Molten Fluoride Salt

The molten fluoride salt selected is potassium fluoride-uranium tetrafluoride-sodium fluoride (KF-UF_4-NaF) salt, and is a potential fuel/coolant candidate for MSRs. Just like the chloride salt, UF_4 in the prime-source of impurities in the fluoride salt because of its hygroscopic nature. However, it is less stable at room temperatures where it can dissolve (hydrolyze) in water to form several uranium-based compounds, though the process is slow and time-consuming.

Analogous to chloride salts, water absorbed by fluoride salts also stay as "hydrates" i.e. no bonding ($\cdot nH_2O$; for the UF_2 salt, n is $0.5-2.5$ [78], for the KF salt, n is 1,2 and 4 [79], and for the NaF salt, n is 1). On heating, these compounds can undergo hydrolysis and form several oxide, hydroxide and oxyfluoride species and the corrosive hydrogen fluoride (HF) gas. Similar to chloride salts, different purification processes have also been proposed and used for the fluoride salts to reduce or remove the corrosive impurities in the salt.

2.2.2.1 Thermal Heat-Treatment

This is the most common method of drying the hydrated salt which involves slowly heating it below the salt's hydrolysis temperatures. The hydrolysis temperatures can be estimated using the thermochemical data of pure fluoride compounds (refer **Table 1**).

Table 1. Hydrolysis temperature for KF, NaF and UF_4 salt [HSC Chemistry® 10 Software].

Reaction	Temperature (°C)
$UF_4 + 2H_2O(g) \rightarrow UO_2 + 4HF\ (g)$	660
$UF_4 + H_2O(g) \rightarrow UOF_2 + 2HF\ (g)$	680
$2NaF + H_2O(g) \rightarrow Na_2O + 2HF\ (g)$	3000
$NaF + H_2O(g) \rightarrow NaOH + HF\ (g)$	1500
$2KF + H_2O(g) \rightarrow K_2O + 2HF\ (g)$	4700
$KF + H_2O(g) \rightarrow KOH + HF\ (g)$	1900

Even with proper heat-treatment, there is always a possibility that in the absence of a proper blanket gas, the salt could hydrolyze to form oxide, hydroxide and oxyfluoride species which can be removed only chemical-treatment. For the UF_4 salt, the commonly occurring impurities are uranium oxide (UO_2), and uranium oxyfluoride (UOF_2). It should be noted that the impurities

including uranyl fluoride (UO_2F_2) could already be present in the starting salts, introduced during its synthesis or production process.

2.2.2.2 Hydrofluorination [80]

This process involves sparging the UF_4 salt-containing UO_2 with HF gas, to convert UO_2 to UF_4 as shown in **Reaction (34)**,

$$UO_2(s) + HF(g) \rightarrow UF_4(s) + H_2O(v) \quad \textbf{(34)}$$

It is carried out either in a "Fluidized-Bed Reactor" (refer **Figure 7a**) or a "Moving-Bed Furnace" (refer **Figure 7b, Section A-A**), and at temperatures ranging between 300 °C to 500 °C. Both dry and aqueous HF gas can be used for the hydrofluorination process. However, the UF_4 produced using aqueous HF gas will require drying. The method though efficient and economical requires a large quantity of HF gas (at least 10–25 mol.% excess gas than the salt) to completely convert UO_2 to UF_4 thus making it highly unsafe and practically infeasible process.

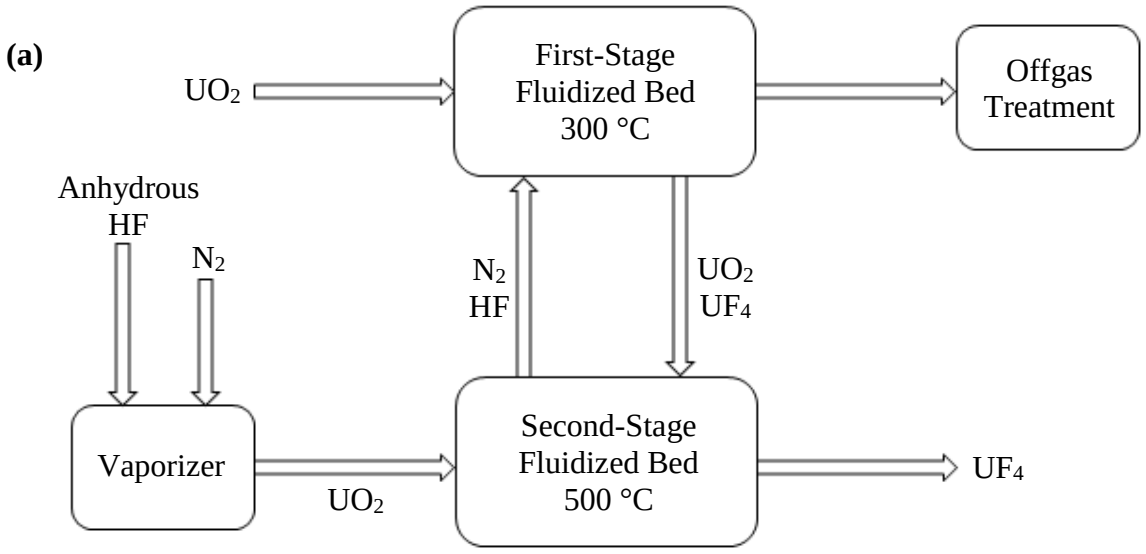

(b)

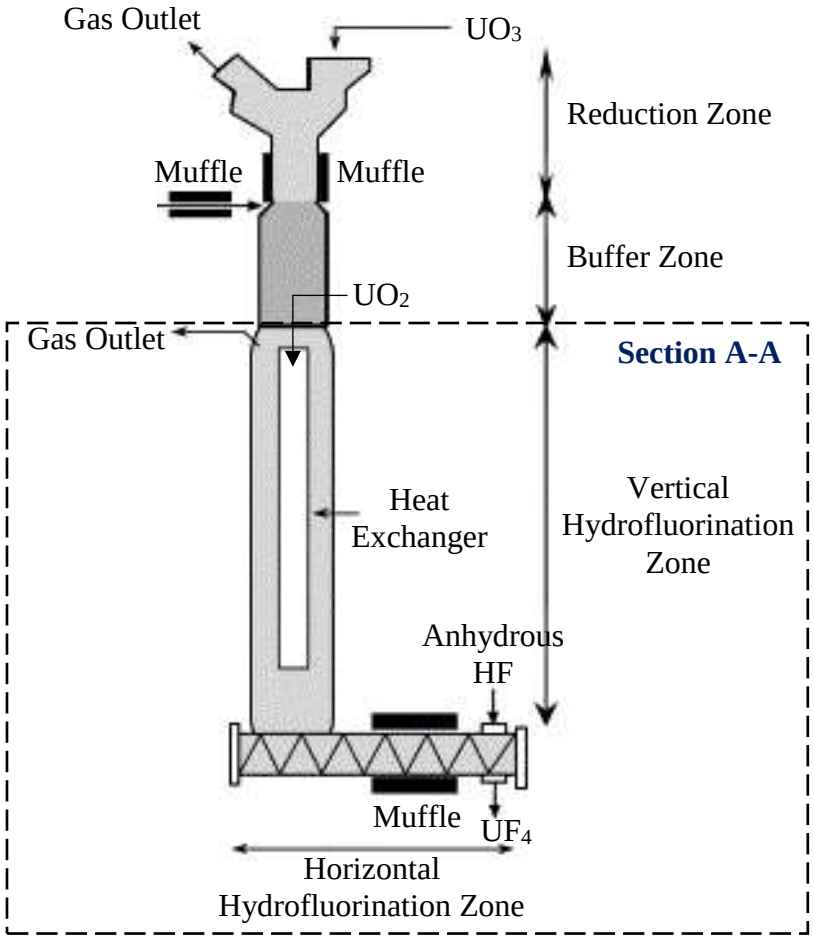

Figure 7. Schematic diagram showing the hydrofluorination process using the **(a)** "Fluidized-Bed Reactor" (reproduced from [80, 81]), and **(b)** "Moving-Bed Furnace" (reproduced from [82]).

2.2.2.3 Chemical Treatment using Fluorinated Ionic Liquid [83]

This method is an alternate approach to the hydrofluorination process, and involves direct conversion of UO_2 to UF_4 under ionothermal conditions i.e. using an ionic liquid ([Bmim][PF_6], hexafluorophosphate), which acts as both solvent and the structure directing agent for the conversion process (refer **Figure 8**). Comparatively, it is safer and non-volatile with low vapor pressure and good stability (ionic liquid). The conversion mechanism is based on the "one-pot reaction" process as shown in **Reactions (35) and (36)**.

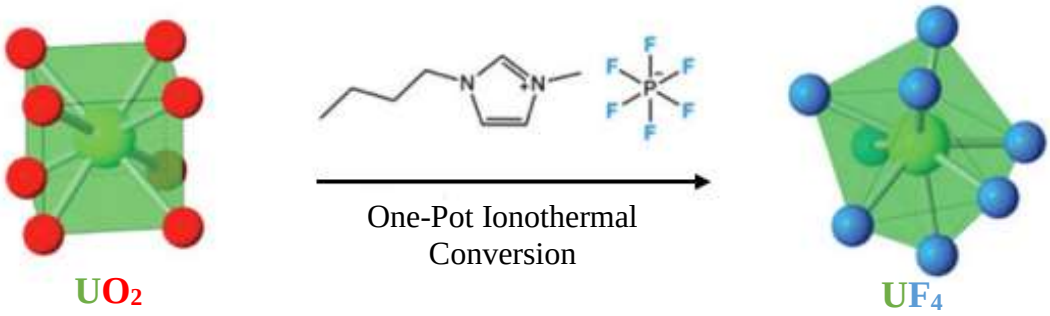

Figure 8. Schematic diagram of conversion of UO_2 to UF_4 using an ionic liquid [Bmim][PF_6] [83].

It initiates with the hydrolysis of the ionic liquid, PF_6 with trace amounts of water that is initially present in it to form difluorophosphate (PO_2F_2) and HF. The HF produced is the driving force for the conversion of UO_2 to UF_4.

$$PF_6 + 2H_2O \rightarrow PO_2F_2 + 4HF \quad \textbf{(35)}$$

$$UO_2 + 4HF \rightarrow UF_4 + 2H_2O \quad \textbf{(36)}$$

The H_2O produced during this conversion process becomes the new source of water required for the hydrolysis of PF_6. However, the process also involves slow dissolution of the resultant UF_4 into UF_5. Thus, the stabilization of $U_{(V)}$ fluorides in [Bmim][PF_6] can affect the efficiency of the conversion process by limiting the ionic liquid's hydrolysis or condensation. Also, as long as the production rate of HF equals its consumption rate, there should not be any safety-related risks associated with this process.

2.3 Conventional and Non-Conventional Approaches to Mitigate Corrosion in Molten Salts

2.3.1 Boronization of Ferrous and Nickel-Based Alloys

Several past, recent and ongoing studies have shown corrosion in molten halide salts is inevitable so the focus now shifts on slowing down this process by modifying the material surface using coatings to avoid direct contact between the substrate and the molten salt. These could include overlay coatings or thermo-chemical diffusion coatings like carburizing, boronizing, nitriding, chromizing, aluminizing, siliciding, etc.

Mahdavi, A. et.al. [84] studied the effects of diffusion treatments on low carbon steel and stainless steel, 316 in salt solution at low and high temperatures, and found that the coated steels exhibited better corrosion resistance with no visible indications of surface degradation like pitting. Furthermore, the coatings also showed good thermal stability i.e. no peeling occurred due to thermal mismatch. Selection of coating materials for molten salt application depends on several factors like thermal stability, chemical stability, properties (physical, mechanical). Elements like chromium, nickel or iron, etc. cannot be considered for coatings in molten salts because they can easily react with the salt by oxidation, chlorination or fluorination to form various metal-compounds like chromium (III) oxide (Cr_2O_3), chromium (II/III) chloride, ($CrCl_2$, $CrCl_3$), chromium (II/III) fluoride (CrF_2, CrF_3); nickel (II) oxide (NiO), nickel (II/III) chloride ($NiCl_2$, $NiCl_3$), nickel (II/III) fluoride (NiF_2, NiF_3)…. These species have high solubility in the molten salt (they will dissolve in the molten salt at high temperatures), and cannot provide any form of protection against the molten salt attack.

Different coatings like MCrAlX coatings, castable silica-based cements with boron nitride addition, Ni20Cr coatings, C22 laser clad coatings, NiCrFeNbMoTiAl coatings, and ceramic coatings were developed for metals/alloys/superalloys and evaluated for their performance in molten alkali chloride salts [19, 20, 21, 22]. It was observed that these coatings provided some form of protection against the molten salt attack, however, their thermal stability was a cause of concern, where it peeled, spalled or cracked due to thermal mismatch because of differences in the thermal expansion coefficient. This will expose the substrate i.e. the metal/alloy/superalloys underneath the coating layer, to the molten salt which will diffuse inwards through the pores or cracks, and

degrade the material. Though different diffusion coating techniques have been developed over the last century, boronization also known as boriding is preferred over others for nickel-based alloys because of ease of use, reliability, consistency and low cost. Furthermore, unlike carburizing and nitriding, where the carbon and nitrogen atoms have limited solubility in nickel, the boron atoms form strong intermetallic compounds with nickel thus resulting in a harder boride layer with a longer wear life [85, 86].

2.3.1.1 Boronization Process

Boronization is a thermo-chemical case hardening process, where boron atoms are diffused into the material surface to form complex metal-boride phases. The boronization process can be used for ferrous, nickel, cobalt, and titanium-based alloys. There is no mechanical interface between the boride layer and the substrate thus indicating a true diffusion process. The microstructure, the composition and the growth kinetics of the boride layer depends on the chemical composition of the alloy; for instance, ferrous alloys will form iron borides, FeB/FeB_2, nickel alloys will form nickel borides, NiB/Ni_2B/Ni_3B/Ni_4B_3, cobalt alloys will form cobalt borides CoB/Co_2B/Co_3B, and titanium alloys will form titanium borides, TiB/TiB_2. Also, depending on the type of alloy, the boride layer can comprise of (1) a single uniform solid "compound layer", or (2) a double layer with an outer solid "compound layer" and an inner "dispersed layer", or (3) a double layer with an outer solid "compound layer", an inner "dispersed layer" and a "grain precipitation zone" at the bottom [24]. In some cases, depending on the boronizing agent, these boride layers could also accompany an outermost thin metal-silicide-metal-boride composite layer (refer **Figure 9**).

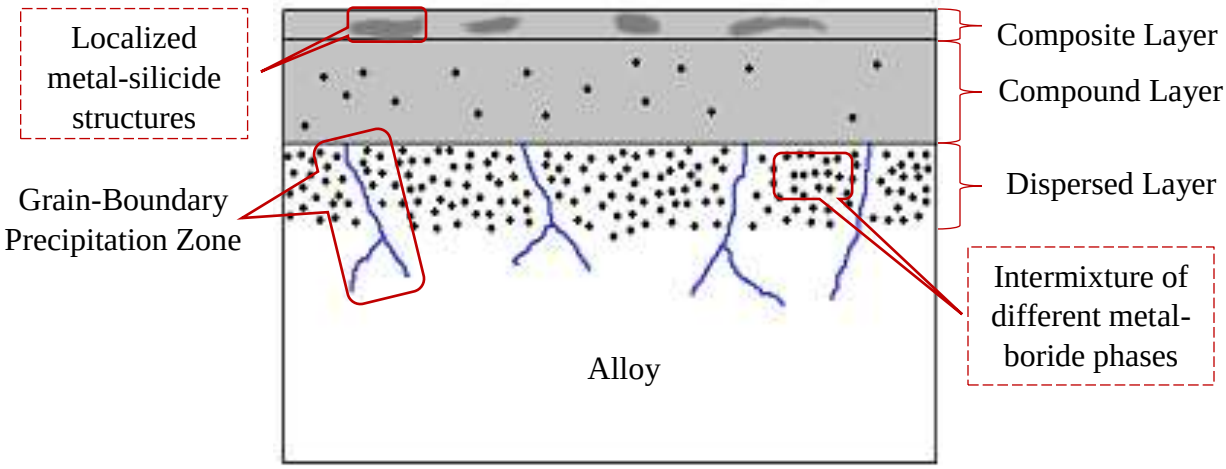

Figure 9. Schematic diagram of the boride layer structure [24].

The boronization process (i.e. pack-boronizing process) involves a boronizing agent viz. a powder comprising of (1) boron-yielding substance, (2) an activator viz. a boron containing compound that facilitates the diffusion process, and (3) a diluent or filler material viz. a silicon containing compound that controls the diffusion kinetics [87]. The metal/alloy surface to be boronized is cleaned, covered in the boronizing powder, and transferred into a sealed container, where it is heated to boronizing temperatures and time in an inert environment (argon, helium or nitrogen) to form the boride layer. Generally, the boride layer formation involves the following three steps [87, 88],

Step I: Boron Diffusion and Silicide Formation

At boronizing temperatures, the activator decomposes and reacts with the boron-yielding substance to form boron-halide gas, which transfers the boron atoms on to the surface of the substrate via gaseous-diffusion process. On the other hand, the diluent i.e. the silicon containing compound, oxidizes to form silicon oxide (SiO_2) on the surface, which also reacts with the boron-halide gas to form silicon-halide gas. The silicon-halide gas reacts with metal to form metal-silicide compounds. As the boronizing time increases, the silicide layer thickness also increases, which slows down the boron diffusion- rate thus limiting the boride layer thickness.

Step II: Boride Formation

The boron atom diffuses into the substrate via solid-state-diffusion process. Based on the Gibbs free energy of formation (refer **Figure 10**), the boron atom will react with the (alloying) elements in the order of chromium, nickel, iron, etc. to form various different complex metal-borides.

Step III: Growth of Borides

As time progresses, the boron concentration along the cross-section will decrease causing the already formed metal-borides to intermix and fill the gaps or voids created by the depleting boron atoms to form a solid thick uniform boride layer.

Boronizing ferrous-based alloys is slightly complicated than nickel-based alloys. Unlike in nickel-based alloys, where the boride layer is composed of Ni-B phases i.e. single phase, NiB, Ni_2B, Ni_3B, Ni_4B_3 etc., the boride layer in ferrous-based alloys is composed of Fe-B phases i.e. single phase FeB and/or FeB_2, and/or double phase FeB-FeB_2. The final composition of the boride layer depends on the activity (i.e. the effective concentration) of the boride species in the mixture. The

dual phase FeB-FeB_2 is highly undesirable in the boride layer because of the different thermal expansion coefficient of FeB and FeB_2, which can cause the layer to crack or spall by thermal mismatch. Surface preparation like shot-blasting of the base material before boronizing has also shown to influence the diffusion process by creating surface deformations that leads to atom dislocation thus resulting in a thicker boride layer [89].

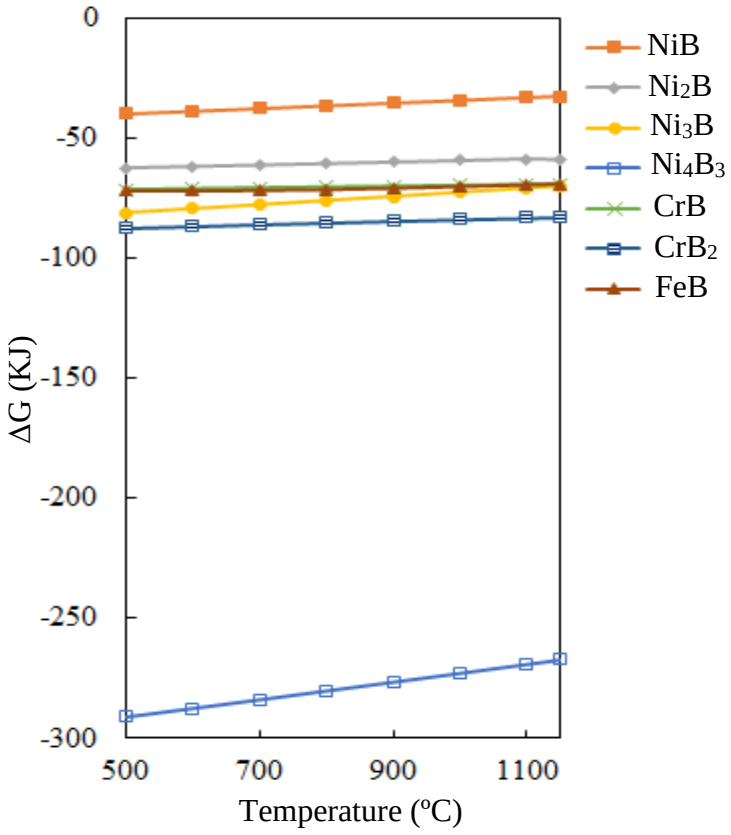

Figure 10. Gibbs free energy of formation for metal-borides as a function of temperature [HSC Chemistry® 10 Software].

It should also be noted as discussed in the boronizing process, there is a possibility of formation of Ni-silicide (Ni_2Si, etc.) layer as the outer-most layer in nickel-based alloys. It is also not desired in the boride layer because of its lower hardness (i.e. it is softer than the boride layer), instability (poor adhesion properties with the boride layer, and different thermal expansion coefficient with the boride layer), and also compromises the wear resistance of the boride layer (the layer can be easily removed in mechanical application) [87].

2.3.1.2 Hardness and Wear Properties

The boride layer enhances the material properties with increased hardness, wear and fatigue resistance [24, 90]. Furthermore, it also increases the material's resistance to "tribo-corrosion" viz. a material degradation process caused by the combined effects of corrosion and wear. The thickness of the boride layer depends on the diffusion rate of boron atoms, its solubility, properties of boronizing powder, exposure temperature and time. Matsuda, F, et.al. [24] evaluated different boronized Ni-binary alloys and found that titanium (Ti), vanadium (V), niobium (Nb), chromium (Cr) and molybdenum (Mo) are the most effective elements for increasing the hardness possibly caused due to substitution of Ni_2B and Ni_3B with $(Ni, X)_2B$ and $(Ni, X)_3B$, where X is the alloying element. However, the hardness of boronized nickel-based alloys cannot be simply estimated or compared against the hardenability of boronized Ni-binary alloys [24]. In case of boronized nickel-based alloys, the hardenability depends on the content of the alloying element and the preferability over the formation of metal-borides in the boride layer.

The boride layer also improves the wear resistance of the material. The wear-resistant property of the borided alloy depends on the boride layer thickness and the residual stresses in the boride layer. The residual stresses are those stresses which remain in the material after it is relieved of all other external stresses except for gravity. The stresses could be either tensile or compressive in nature. The magnitude of these stresses determines the material's capability to with-stand wear, and is affected by temperature gradient, thermal expansion coefficient of the coating and the substrate, and the geometry of the material. Campos-Silva, I., et. al. [90] showed that increasing the boride layer thickness develops residual compressive stresses, which then increases the wear resistance of the boride layer. It was observed, Inconel® 718 with a thicker boride layer (thickness 50 ± 5 µm) showed two to three fold less wear than with a thinner boride layer (thickness 19 ± 2 µm). Effects of boronizing temperature and time on the boride layer thickness are shown in **Figure 11** and **Figure 12**, where the boride layer thickness non-linearly increases with boronizing temperature and time.

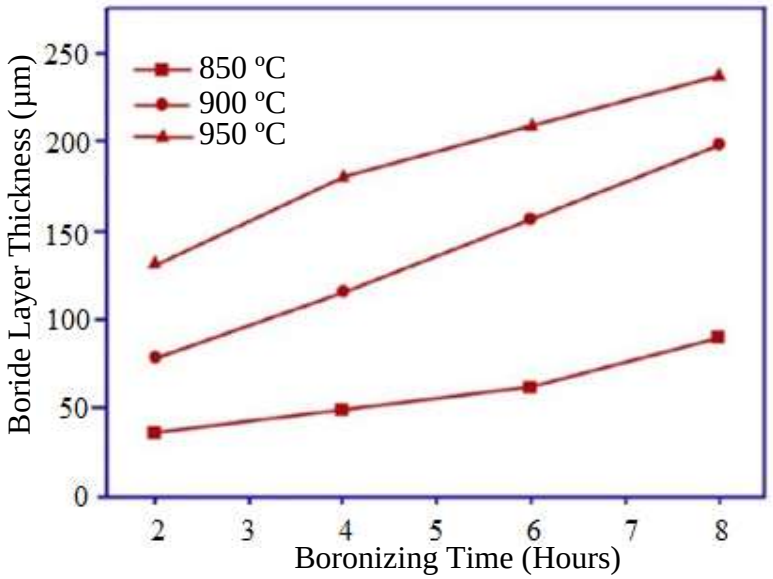

Figure 11. Effects of temperature and time on the boride layer thickness in nickel-based alloys (reproduced from [91]).

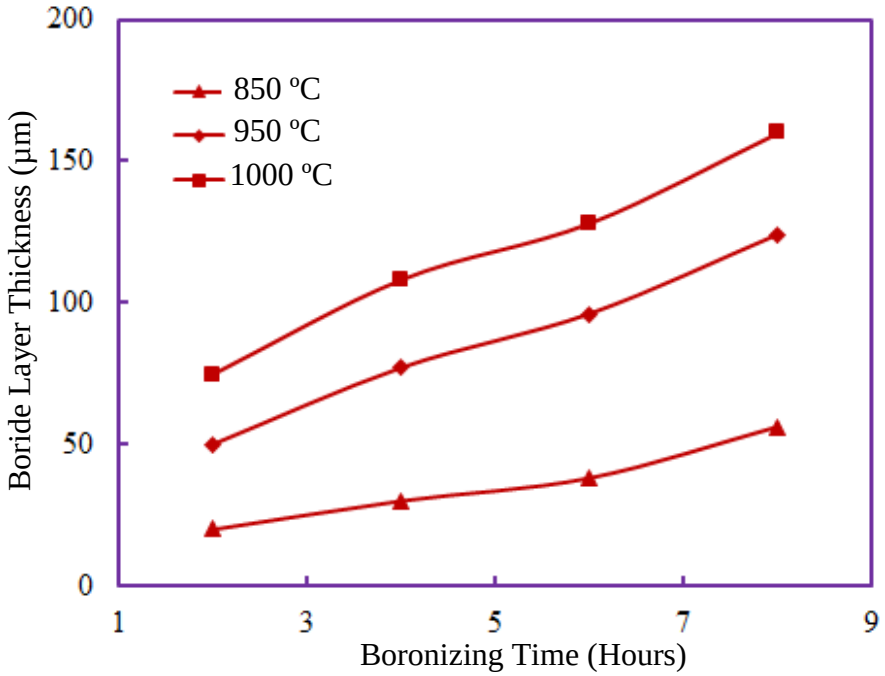

Figure 12. Effects of temperature, and time on the boride layer thickness in ferrous-based alloys [92].

However, it must also be noted that boronizing at very high temperatures and for longer time duration makes the boride layer unstable thus resulting in flaking, which ultimately reduces its thickness and compromises the material properties (hardness and wear resistance).

2.3.1.3 Effects of Heat-Treatment on Boride Layer Structure and Properties

Heat-treatment of alloys also shown to influence the growth kinetics of the boride layer (composition, microstructure and thickness), and the properties like wear resistance, which is quite evident from the studies conducted by Deng, D., et. al. [93]. In the study, the nickel-based alloy, Inconel® 718 produced by Vacuum Induction Melting (VIC) and Vacuum Arc Remelting (VAR) technologies and subjected to standard heat-treatment process (viz. (1) solution treatment: heating the alloy to 1050 °C for 1 hours followed by air cooling, (2) aging treatment: re-heating the alloy to 720 °C for 8 hours then furnace cooling to 620 °C for 8 hours followed by air cooling [93]), was borided using the paste-boriding process.

It was found that the heat-treatment increased the boron diffusion-rate into the substrate thus resulting in the formation new (unexpected) boride phases. The thickness of the boride layer increased by two-fold and showed presence of Fe_2B and CrB in the diffusion zone of the boride layer. However, the heat-treated borided Inconel® 718 alloy still exhibited excellent wear resistance with slight difference (positive) in the wear-rates in comparison to the untreated borided Inconel® 718 alloy (refer **Figure 13**).

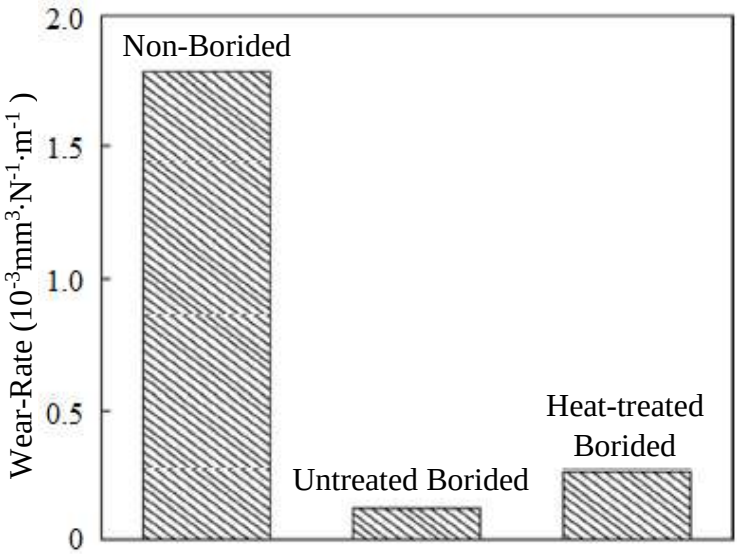

Figure 13. Wear-rates of non-borided, untreated borided, heat-treated borided Inconel® 718 alloy (reproduced from [93]).

2.4 Molten Salt Infiltration in Graphites

Graphite is an important material in historical and modern nuclear reactors such as Light Water Reactors (LWRs), High Temperature Gas Cooled Reactors (HTRs), and Molten Salt Reactors (MSRs), where it is used as neutron moderator or reflector due to low thermal neutron absorption cross-section and high neutron scattering cross-section [26]. But, being the life limiting component in the reactor severely restricts its usefulness. Several challenges associated with graphite include [10],

1) Interaction (i.e. fluorination) with the fuel/coolant (i.e. molten salt).
2) Microstructural changes due to irradiation.
3) Infiltration by molten salt.
4) Degradation because of oxidation, thermal stresses, mechanical stresses, external stresses by applied pressures, internal stresses by salt crystallization or condensation.
5) Carburization of metals/alloys/superalloys.

These bring about significant changes in the graphite's behavior, its properties; and is strongly influenced by graphite's purity, and its microstructure i.e. irradiated microstructure or "virgin" microstructure. Over the years, extensive research and development (R&D) has led to the development of several "impermeable" nuclear grade graphites. The inertness of these graphite in molten salts is one important feature which is needed and which helps maintains its integrity (i.e. the graphite will neither corrode or interact) in the MSRs (molten salts) during their normal operation, or in case of an accident scenario.

The wettability in porous media is determined by measuring the contact angle (θ) the fluid makes with the solid surface (refer **Figure 14**), where $\theta >> 90°$ indicates poor wetting characteristics while $\theta << 90°$ indicates good wetting characteristics [94]. There are several methods to measure the contact angle like (1) the conventional telescope-goniometer method, (2) the Wilhelmy balance method, and (3) the drop-shape analysis method [94]. The contact angle is influenced by the graphite's surface morphology like roughness, porosity and its distribution, heterogeneity, etc. [94].

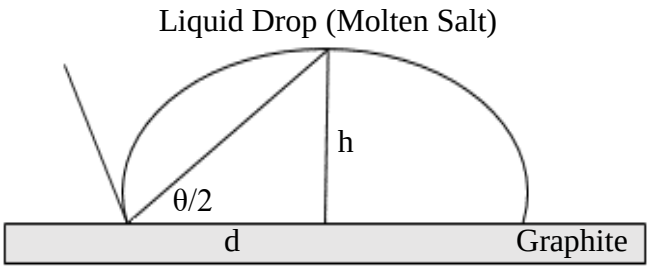

$$\frac{\theta}{2} = \tan^{-1}\left(\frac{h}{d}\right) \quad \textbf{(37)}$$

θ = contact angle

h = apex height

d = drop diameter

Figure 14. Contact angle at the liquid-solid interface (based on assumption that the liquid drop is small and spherical shaped) by drop-shape analysis method [94].

The liquid infiltrates into the solid pores because of the capillary suction created by the applied pressure. Early studies conducted by ORNL were focused on selecting suitable "impermeable" graphite grades for the MSR operations [4]. It was found that the infiltration of graphite (ZXF-5Q from Poco Inc. and IG-110 from Toyo Tanso Co. Ltd.) by the molten salt (lithium fluoride-beryllium fluoride-uranium tetrafluoride, LiF-BeF_2-UF_4 or FLiNaK) was dependent on the pressure, and pore-characteristics i.e. pore-size and its distribution, while being restricted by the surface tension. There is a strong co-relation between the neck diameter of the graphite's pores and the infiltration behavior of molten salt. Studies have also shown the infiltration resistance of graphite increases with reduction in pore-size or pore entrance diameter (i.e. less than 1 μm) [95]. Furthermore, the infiltration can also be averted by if the applied pressure is below the threshold pressure for infiltration. The threshold pressure can be determined experimentally or calculated using the Washburn equation [96],

$$P = -\left(\frac{4\gamma\cos(\theta)}{\delta}\right) \quad \textbf{(38)}$$

θ = contact angle

γ = surface tension (N/m)

δ = pore-size (m)

P = threshold pressure (MPa)

Xu, H. et. al. [97] evaluated the effects of pressure on the infiltration behavior of graphite (64% natural flake graphite-16% graphitized coke-20% phenol resin binder, pore-size less than 1 μm) in the molten lithium fluoride-beryllium fluoride salt ($2LiF\text{-}BeF_2$, FLiBe) and found the threshold pressure to be 7 bar (abs) which was in good agreement with the value (6.57 bar (abs)) predicted by the Washburn equation.

Numerous techniques have been explored to prevent molten salt infiltration such as (1) sealing, closing or filling the open pores by coating the graphite's surface, (2) modifying the graphite's microstructure. Tang, H. et. al. [98] showed that ultra-fine grained (NG-CT-50 from Chengdu Carbon Co. Ltd.) graphite exhibits higher resistance to molten salt infiltration than the medium (NBG-18 from SGL Carbon Group) and fine grained graphites (NG-CT-10 from Chengdu Carbon Co. Ltd. and IG-110 from Toyo Tanso Co. Ltd.). Other efforts involved coating the graphite (IG110 from Toyo Tanso Co. Ltd) with silicon carbide (SiC) and silicon carbide-glass carbon composite using the Chemical Vapor Deposition (CVD) process and the Chemical Vapor Reaction (CVR) process [99]. It was found that the CVR process was superior than the CVD process as it creates a strong bond between the SiC coat and the graphite thus increasing the graphite's strength. The SiC coatings provided protection to graphite by increasing its resistance to infiltration by the molten salt. Furthermore, it also exhibited good thermal stability because of similar thermal expansion coefficient with the substrate (graphite), while retaining the neutronic properties of graphite. It was able to reduce the infiltration from 14.8 wt.% to 1.2 wt.% at pressures under 6 bar (abs.), however, it is still higher than the required value (<0.5 wt.%) proposed for MSRs (refer **Figure 15**). In comparison, the SiC-glassy carbon composite coating showed even better resistance to infiltration with the values measured at 0.26 wt.% . It was observed that the surface morphology of the graphite may affect the coating properties i.e. any defects on the untreated graphite surface will lead to poor adhesion between the coating and the substrate, and thus resulting in its peeling/cracking/spalling during heat-treatment, and shortening its life.

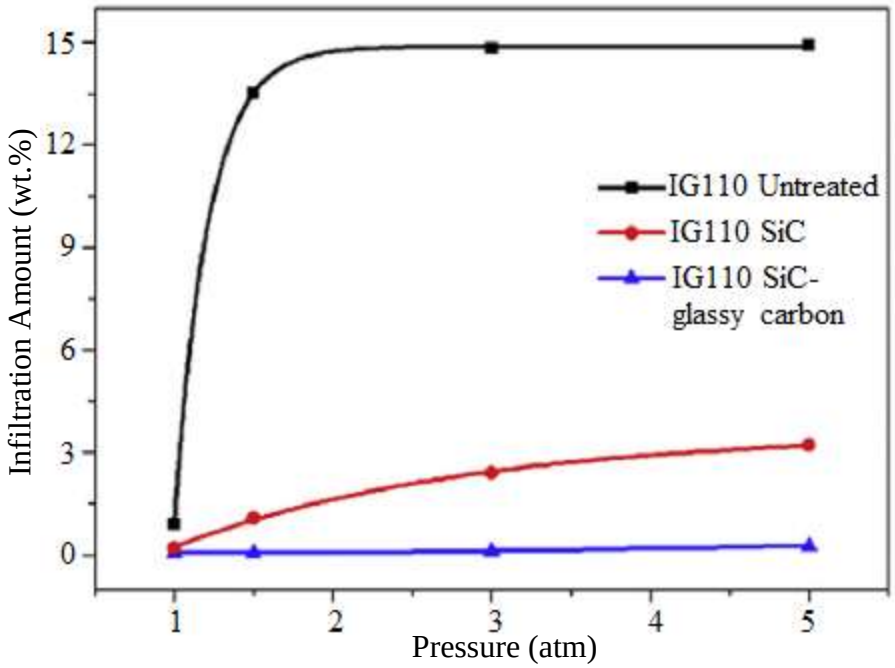

Figure 15. Molten salt infiltration in IG110 graphite untreated, SiC coated, and SiC-glassy carbon composite coated (reproduced from [99], under Creative Commons license).

Graphites exhibit high strength at high temperatures (above 2500 °C), and is inert to all, but the strongest oxidizing agents like oxygen (O_2), water (H_2O), hydrogen (H_2) and carbon dioxide (CO_2) (refer **Table 2**) [28].

Table 2. Graphite reactions with O_2 (g), H_2O (g), CO_2 (g) and H_2 (g) [28].

Graphite Reaction	Temperature (°C)
$2C(s) + O_2(g) \rightarrow 2CO(g)$	>380
$C(s) + H_2O(v) \rightarrow CO_2(g) + H_2(g)$	>625
$C(s) + H_2(g) \rightarrow CH_4(g)$	>750
$C(s) + CO_2(g) \rightarrow 2CO(g)$	>750

Chemical reactions between graphite and molten salts is not thermodynamically favorable. Studies conducted by ORNL for graphites (National Carbon Company) in molten LiF-BeF_2-UF_4 salt showed negligible to very small changes in the dimensions (<0.02%) and weights (<0.03%) with no evidence of erosion [4]. However, Yang, X. et. al. [37] reported fluorination of graphite in lithium fluoride-sodium fluoride-potassium fluoride salt (LiF-NaF-KF) at 500 °C under vacuum which

showed evidence of replacement of certain 'C-H' bonds with 'C-F' bonds. This is because of higher dissociation energy of 'C-F' bonds, which makes it more stable in graphite than 'C-H' bonds i.e. the interaction between graphite and fluorine is more favorable [[100]].

Another possible cause of degradation could be the stresses generated due to the repulsive force between the salt and the pore surface during salt solidification or crystallization [[37], [38]]. Under equilibrium conditions, high stresses will be exerted only in the small pores where the crystals are surrounded by the film of solution. However, the high stresses can also be exerted in the larger pores when the film becomes discontinuous during drying or solidification.

Microstructural changes in graphite due to fast neutron irradiation is another cause of concern in the nuclear reactors. It has been extensively studied, and is a well-understood process. The virgin nuclear graphite is a polycrystalline, and has honeycomb hexagonal lattice structure and basal planes as shown in **Figure 16** [[101], [102]].

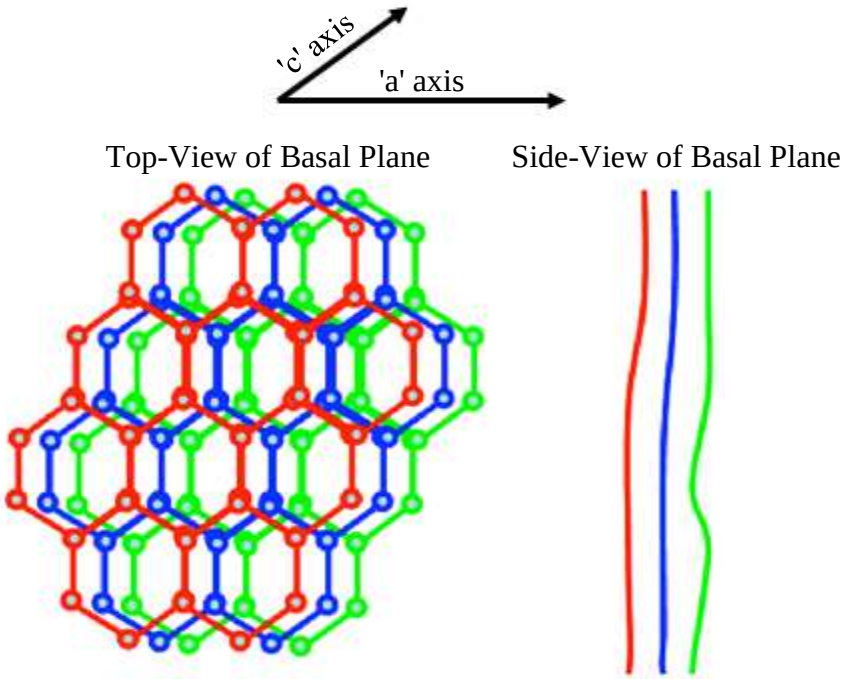

Figure 16. Schematic diagram showing the microstructure of a virgin nuclear graphite (reproduced from [[102]]).

The microstructure of the graphite heavily depends on the raw material, the binder, and the manufacturing process. The microstructure of the manufactured graphite will always show

cracks/pores on its surface formed during the heat-treatment processes like baking or graphitization (i.e. "Mrozowshi" cracks formed during the cool-down from the graphitization temperatures) [103]. Generally, graphites have strong basal planes but weaker bonding between those planes. The cracks in the 'c' direction will increase the graphite's thermal shock resistance by accommodating the thermal expansion without causing any destruction to its structure. Furthermore, the pores in the 'c' and 'a' direction will also accommodate stresses from the irradiation-induced changes.

As demonstrated in **Figure 17**, when graphite is bombarded with high energy fast neutrons, these neutron would dislodge or displace the carbon atoms from its equilibrium position resulting in two possibilities (i) creation of vacancies, and (ii) creation of a cluster of carbon atoms [102, 104]. The displaced carbon atom will recoil and displace other neighboring carbon atoms thus creating a "cascade" effect.

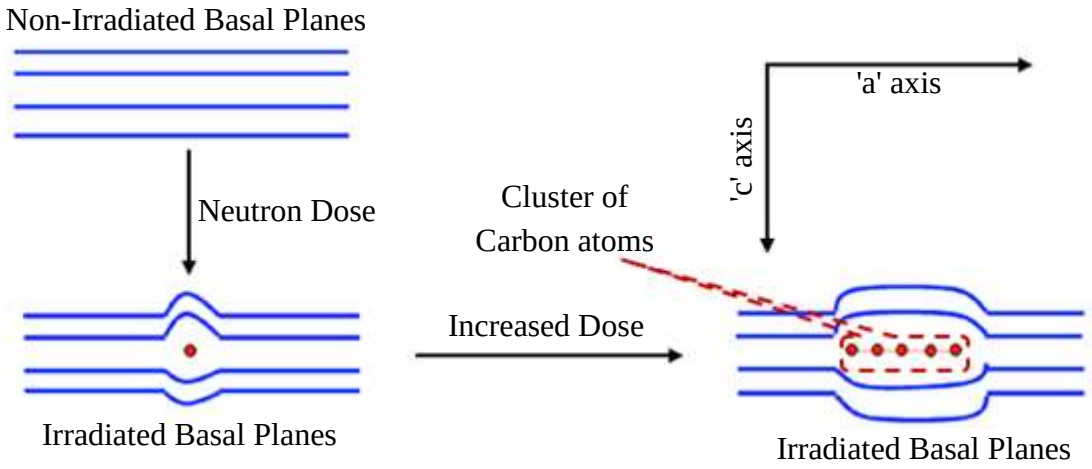

Figure 17. Schematic diagram showing the radiation induced changes in the virgin nuclear graphite microstructure (reproduced from [102]).

The displacement of carbon atoms will create multiple vacancy sites within the basal planes, while its accumulation between the basal planes will cause 'c' direction swelling. The original microstructure of the graphite (i.e. the thermal shrinkage cracks and pores formed during the manufacturing process) will accommodate this initial 'c' direction expansion and 'a' direction shrinkage. As the dose-rate increases, the graphite's capabilities to accommodate these changes will decrease. However, the swelling along the 'c' direction will continue to grow generating new cracks and pores, and result in the total destruction of graphite.

CHAPTER 3

3 EXPERIMENTAL

3.1 Materials

3.1.1 Molten Chloride Salt

The anhydrous KCl-$MgCl_2$-NaCl salt (48-47-5 mol.%) was supplied by Israel Chemicals Ltd., Israel (ICL). The high-purity sodium chloride (NaCl, >99.999%) and potassium chloride (KCl, >99%) salts were purchased from Sigma Aldrich, USA, while magnesium chloride ($MgCl_2$, >98%, <2% moisture) was purchased from VWR International, USA.

3.1.2 Molten Fluoride Salt

Sodium fluoride (NaF, ≥99.0%) and potassium fluoride (KF, ≥99.5%) salts were purchased from Sigma-Aldrich, USA, while natural uranium tetrafluoride (UF_4) salt was purchased from IBILABS, USA.

The salts received from the suppliers were analyzed to verify its purity by performing the X-ray Photoelectron Spectroscopy (XPS), Differential Scanning Calorimetry (DSC), X-Ray Diffraction (XRD) and Inductively Coupled Plasma-Mass Spectroscopy (ICP-MS) analyses. The purities measured were found to be in agreement with the certificates of analysis provided by the suppliers. The salt-mixtures were prepared to the required composition by separately measuring the pure compounds using the analytical balance (Mettler Toledo, USA, ± 0.1 mg), and effectively mixing them in the crucible using a clean spatula.

3.1.3 Alloys

3.1.3.1 Ferrous-Based Alloys

Stainless Steel Grade 316L

Alloy 316L is a dual certified austenitic stainless steel, and was purchased from McMaster Carr. SS 316L is the most popular material because it is easily available, economical, and exhibits excellent machining and welding characteristics, good stability at high temperatures. The innumerable properties (corrosion resistance, oxidation resistance, etc.) makes it an ideal choice

for nuclear applications. However, the high Cr content could severely restricts its usefulness in the molten halide salts. The chemical composition of SS 316L is provided in **Table 3**.

Table 3. The chemical composition of SS 316L.

Alloy Type	Chemical Composition (wt.%)					
	C	Si	Mn	P	S	Cr
SS 316L	0.025	0.47	1.49	0.030	0.0019	16.56
	Mo	Ni	N	Cu	Fe	
	2.02	10.08	0.039	0.42	Bal.	

The SS 316L alloy was annealed at 1040 °C followed by air and water quenching.

Alloy 709 - Grade 4B2/RBB/RBB*

Alloy 709 is a high strength advanced austenitic stainless steel developed by ORNL. However, for this study, the alloy was supplied by Argonne National Lab (ANL). Alloy 709 Grade 4B2 was refined by Argon-Oxygen-Decarburization (AOD) process. AOD is an advanced refinement technology. It is a three-step process which involves,

Step I: Decarburization

Decarburization reduces the amount of carbon in the steel, however, during this process it could also oxidize some of the elements in the alloy.

Step II: Reduction

To decrease the oxides and retrieve critical elements like Cr, strong reducers like aluminum (Al) and silicon (Si) are added during the reduction process.

Step III: Desulfurization

Desulfurization is achieved by introducing high concentration of lime in the slag to dilute the sulfur content in the alloy.

Alloy 709 Grade RBB was refined by Electro-Slag-Remelting (ESR) process. It involves a electrode (the alloy)-molten slag (calcium fluoride, lime and alumina) set-up. As the tip starts to melt, the liquid droplet refines through the slag after which it solidifies. The technology is highly effective in removing the non-metallic inclusions like oxides, sulfides, etc. from the alloy, and also ensures rapid and efficient desulfurization of the alloy.

Both these grades of alloy 709 (4B2 and RBB) were solution annealed to 1100 ºC viz. a heat-treatment process employed to alter the microstructural characteristics of the material to relieve stress, improve its ductility and machinability.

Alloy 709 Grade RBB* follows the same refinement process as of Grade RBB, and was age-hardened also known as precipitation hardening viz. a heat-treatment process employed to produce carbonitrides and carbides, and also improve the yield strength of the alloy. The chemical composition of alloy 709 is provided in **Table 4**.

Table 4. The chemical composition of SS 709 alloy.

Alloy Type	Chemical Composition (wt.%)					
	C	Cr	Ni	Mn	Mo	N
SS 709	0.066	19.93	24.98	0.91	1.51	0.148
	Nb	B	Fe	Si	P	Ti
	0.2	0.0045	Bal.	0.44	0.014	0.04

The alloy consists of high Cr content to enhance its corrosion resistance properties, while nickel (Ni) is added as an austenitic stabilizer, and to counter the ferritic stabilizing effects of Cr.

3.1.3.2 Nickel-Based Alloys

Inconel® 718

Inconel® 718 is a nickel-chromium superalloys. It exhibits good thermal stability, high hardness, good corrosion resistance, high tensile strength, high fatigue strength, high creep strength and high rupture strength. The alloy was purchased from Rolled Alloys Inc., USA. The alloy was manufactured using the Vacuum Induction Melting-Electroslag Remelting (VIM-ESR) processes, and was also pickled and annealed. The chemical composition of Inconel® 718 is provided in **Table 5**.

Table 5. The chemical composition of Inconel® 718.

Alloy Type	Chemical Composition (wt.%)						
	C	Mn	Fe	S	Si	Cu	Ni
IN718	0.03	0.09	17.59	0.001	0.09	0.16	53.55
	Ti	Co	Mo	Nb	Ta	B	P
	0.98	0.23	2.88	5.10	0.004	0.002	0.009

The IN718 alloy was pickled, and normalized annealed up to 982 °C for 3.2 minutes and air-cooled.

Haynes® 230®

Haynes® 230® is a nickel-chromium superalloys with small additions of tungsten and molybdenum. It exhibits good oxidation resistance up to 1149 ºC, high strength, and good thermal stability. Additional features include lower thermal expansion, and good resistance to grain growth at high temperatures. The chemical composition of Haynes® 230® is provided in **Table 6**.

Table 6. The chemical composition of Haynes® 230®.

Alloy Type	Chemical Composition (wt.%)						
	C	Mn	Fe	La	Si	Ni	Cr
H230	0.1	0.5	3 max.	0.02	0.4	57 Bal.	22
	W	Al	Ti	Nb	B	Co	Mo
	14	0.3	0.1 max.	0.5 max.	0.015 max.	5 max.	2

Hastelloy® C276

Hastelloy® C276 is a nickel-molybdenum-chromium alloy with good corrosion resistant properties in aggressive environments. The high concentration of nickel and molybdenum improves the alloy's resistance to pitting and crevice corrosion in reducing environments, while chromium presence makes the alloy oxidation resistant. The chemical composition of Hastelloy® C276 is provided in **Table 7**.

Table 7. The chemical composition of Hastelloy® C276.

Alloy Type	Chemical Composition (wt.%)					
	C	Mn	P	S	Si	Ni
C276	0.01 max.	1.00 max.	0.04 max.	0.03 max.	0.08 max.	Bal.
	V	W	Mo	Co	Fe	
	0.35 max.	3.0–4.5	15.0–17.0	2.5 max.	4.0–7.0	

Haynes® 230® and Hastelloy® C276 was supplied by ORNL. The test specimens were cut to dimensions of 25 mm length, 13 mm width, and 1.6 mm thick either using the water-jet machine or the Electrical Discharge Machining (EDM) machine. The machined surface was abraded using 600–800 grit silicon carbide (SiC) paper, followed by ultrasonic cleaning in de-ionized (DI) water, rinsing in ethanol and air drying. The specimens were then weighed and measured for its

dimensions before the corrosion test using the analytical balance (Mettler Toledo, USA, ±0.1 mg) and the vernier caliper (Mitutoyo, USA, ±0.0010 mm).

3.1.4 Nuclear Graphites

The details of "virgin" (non-irradiated) nuclear graphites selected for the infiltration test are provided in **Table 8**.

Table 8. Details of graphite selected for the infiltration test.

Grade	Supplier	Pore Size (µm)	Porosity (%)	Raw Coke Material	Notes
R7710	SGL, Germany	0.6	10	Coke	Isotropy Ratio: 1.09 Density: 1.88 g/cm^3 Process: Iso-Moulding
R7650	SGL, Germany	1.1	10	Coke	Isotropy Ratio: 1.07 Density: 1.84 g/cm^3 Process: Iso-Moulding
HPG-830	Toyo Tanso, Japan	0.6	16	Not Available to Public	Isotropy Ratio: 1.03 Density: 1.77 g/cm^3 Process: Iso-Moulding
HPG-510	Toyo Tanso, Japan	1.2	16	Not Available to Public	Isotropy Ratio: - Density: 1.78 g/cm^3 Process: Iso-Moulding
2175	Mersen, France	0.9	13.5	Pitch	Isotropy Ratio: 0.955 Density: 1.88 g/cm^3 Process: Iso-Moulding
T6	Ibiden, Japan	0.6	9	Coal	Isotropy Ratio: 1.05 Density: 1.9 g/cm^3 Process: CIP
FGM19	Ibiden, Japan	1.02	12	Coal	Isotropy Ratio: - Density: 1.89 g/cm^3 Process: CIP
TM	Entegris, USA	1.5	85	Pet Coke	Isotropy Ratio: - Density: 1.82 g/cm^3 Process: Iso-Moulding

3.2 Boronization Process

The nickel-based alloys (Inconel® 718 and Hastelloy® C276) and ferrous-based alloys (SS 316L) were boronized using the Gosco Valves proprietary boronizing process. It is a thermo-chemical surface-hardening process, where the boron atoms are diffused into the alloy surface by covering it in the powdered boronizing medium, and heating to 982 ºC for 10 hours in a sealed box furnace to form a case-hardened layer. Specimen preparation for the boronization process involves the following six-steps,

1) Rough machining
2) Stress relieving
3) Finish machining
4) Grinding
5) Four levels of lapping

The prepared specimens are boronized by employing the following four-step process,

1) Specimen is cleaned to remove any residue or debris.
2) Boronization of the specimen using the Gosco Valves proprietary boronizing process.
3) Finish lapping of the boronized specimens.

The resultant material (borided alloy) is harder, and exhibits good corrosion, wear and fatigue resistant properties, and is also capable of withstanding high temperature shocks.

3.3 Equipment

Figure 18 shows the static system assembly used for salt purification, corrosion and infiltration test. It comprises of a autoclave-chamber made of SS 316L, and is designed with capabilities to operate at temperatures up to 900 °C and pressures up to 11 bar (abs). The chamber houses the nickel crucible containing either the salt for the purification process or the salt and the alloys or the graphite specimens for the corrosion/infiltration test.

It is provided with 5 ports for a $^1/_4$ in. vacuum line, $^1/_4$ in. ultra-high-purity argon gas inlet line into the chamber, a $^1/_8$ in. ultra-high-purity argon gas inlet line for purging the salt, a $^1/_2$ in. vent line and a $^1/_8$ in. K-type thermocouple. The argon gas supply and its pressure entering into the system is controlled at the inlet using the 2-stage gas pressure regulator with a built-in purifier

(McMaster Carr, 0–18.3 bar (abs)). A variable-area-gas flowmeter (Airgas, 0–500 ccm, accuracy: ±10% full-scale) is also provided at the inlet to monitor and control the gas flowrate. The pressure in the system is controlled using the back-pressure regulator (Swagelok, 0–35.5 bar (abs)) provided at the exit of the vent line. A 304 stainless steel chamber with in-line particle filter (Swagelok, 0.5 µm element pore-size) is provided at the end of the vent line to capture contaminants and protect critical instrumentations like pressure transmitter and back-pressure regulator. The system is also provided with a vacuum pump (Kozyvacu) and a compound gauge (McMaster Carr, vacuum: -1–0 bar, pressure: 0–20.7 bar) at the exit of the vacuum line to reduce the O_2 and H_2O levels in the chamber before the purification process, the corrosion and the infiltration test. The system is effectively sealed using VR-X mica gasket (Mercer Gasket & Shim, 950 °C, 749.8 bar (abs)) for the flanged connection and Deacon 8875-Thin sealant (Jet-Lube, 982 °C, 345.8 bar (abs)) for the threaded connections. Both these materials are rated for extreme conditions, and suited for aggressive environments.

The system heating is provided and controlled using the ceramic fiber radiant heater (Watlow, 1121 °C), the EZONE-PM681CJ-B controller (Watlow), and a weld pad thermocouple (Watlow, 0–1070 °C) clamped to the outer surface of the chamber. An additional long probe K-type thermocouple (Omega Engineering, 0–1070 °C, special limits of error: greater of ±0.5 °C or 0.4%) is inserted into the chamber, close to the crucible to measure the salt temperature.

To minimize heat loss, the system is completely insulated with at least two to three layers of high density one-inch thick ceramic insulation. The pressure in the system is measured using the pressure transmitter (Prosense, 4–20 mA, 0–500 psig, accuracy: greater than ±0.5% of full-range) provided at the exit of the vent line. The temperature and pressure readings are monitored and recorded using the DI-245 data-logger and the Windaq software (DATAQ Instruments, Inc., temperature: -180–1360 °C, accuracy: ±(0.1% of span + 2) °C, voltage: ±10 mV, ±25 mV, ±50 mV, ±100 mV, ±250 mV, ±500 mV, ±1 V, ±2.5 V, ±5 V, ±10 V, ±25 V and ±50 V, accuracy: ±(0.05% of range + 10) µV).

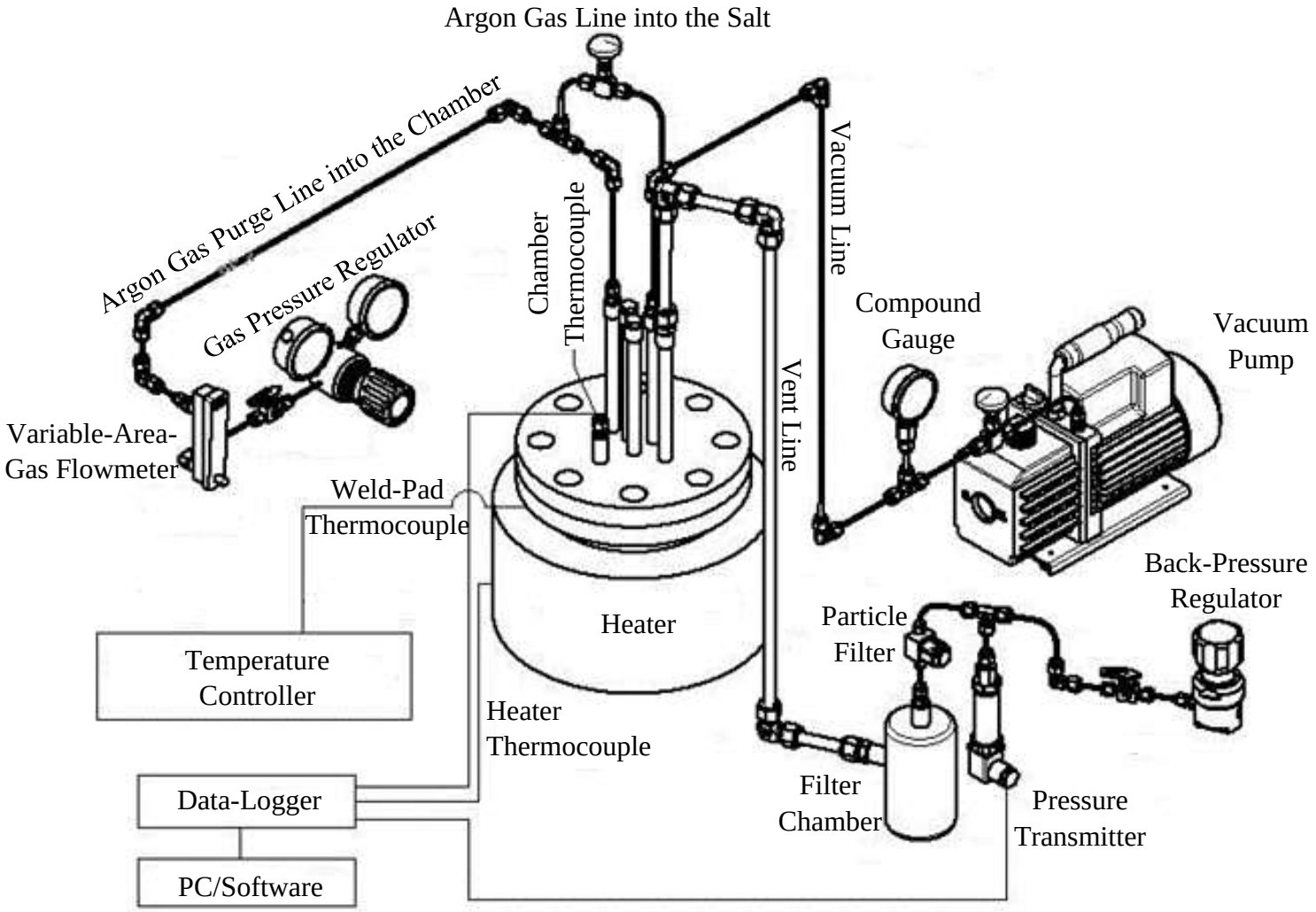

Figure 18. The static system assembly.

3.4 Methodology

3.4.1 Purification Processes

3.4.1.1 Thermal Purification

For the thermal purification process, the salt is heated slowly and sequentially (refer **Table 9**) to temperatures below the hydrolysis temperatures of pure compounds (starting salts). The process was carried out under continuous argon gas flow to enhance the movement of water vapors, and corrosive off gases like HCl, etc. away from the salt surface and towards the exhaust where it is vented out from the system.

Table 9. Heating schedule for thermal purification.

Temperature (ºC)	Ramp Rate (ºC/min)	Hold Time (Hours)	Gas Flowrate & Pressure	Notes
RT-117	10	8	>150 ccm, 15–20 psi	Purge the powdered salt with ultra-high-purity argon gas using nickel tube
117-180	2-5	8	>150 ccm, 15–20 psi	
180-240	2-5	2	>40 ccm, 15–20 psi	
240-400	2-5	1	>40 ccm, 15–20 psi	
400-600	2-5	1	>40, <150 ccm, 15–20 psi	
600-RT	Naturally	N/A	>40 ccm, 15–20 psi	

3.4.1.2 Chemical Purification

For the chemically purification process, <1.7 wt.% of solid pure Mg pieces were added to the thermally purified salt. The salt was then reheated slowly and sequentially (refer **Table 10**) under continuous argon gas flow. Mg being an oxygen scavenger will react with O_2 and H_2O at high temperatures to form the insoluble MgO (dark sludge) and the slightly soluble $Mg(OH)_2$ compounds. MgO being denser than the salt separates out along with other metallic impurities at the bottom of the crucible.

Table 10. Heating schedule for chemical purification.

Temperature (ºC)	Ramp Rate (ºC/min)	Hold Time (Hours)	Gas Flowrate & Pressure
RT-117	10	2	>150 ccm, 15–20 psi
117-850	2	1	>40 ccm, 15–20 psi
850-RT	Naturally	N/A	>40 ccm, 15–20 psi

For the fluoride salt, only thermal purification was performed owing to complexities and challenges associated with handling the toxic and corrosive HF gas.

3.4.2 Static Corrosion Test

The corrosion tests were conducted for various different alloys and ceramics in the purified molten salt, under static conditions, in an inert argon environment. The alloys (borided and non-borided, nickel-based and ferrous-based alloys) were tested in the molten chloride salt (KCl-$MgCl_2$-NaCl) at 800 ºC for 100 hours, while the ceramics (boron nitride and silicon carbide) were tested in the molten fluoride salt (KF-UF_4-NaF) at 900 ºC for 100 hours.

The influence of impurities on the molten salt corrosion behavior was investigated by testing Haynes® 230® alloy in the molten chloride salt with different salt conditions at 800 ºC for 100 hours. The salt conditions is depends on the processes used to purify the salt, (a) high-purity salt purified only by heat-treatment (without Mg), (b) high-purity salt thermally and chemically purified, (c) ICL salt not purified, (d) ICL salt thermally and chemically purified, and (e) ICL salt thermally and chemically purified and the purified salt intentionally appended with Mg.

As shown in **Figure 19a**, the test specimens (three) were held in the nickel crucible from its cover using high-purity Ø1 mm wire (material same as that of the test specimen). The specimen-wire and crucible-cover were isolated using high-purity alumina tubes (99.8%, Coorstek, USA). The crucible was wrapped in a heat-treatable stainless steel bag to prevent salt loss due to vaporization. After the corrosion test, the specimens were careful retrieved, ultrasonically cleaned in DI water for at least 8 minutes to remove any salt debris or residue from the surface, followed by rinsing in ethanol and air drying.

3.4.3 Static Infiltration Test

Figure 19 shows the different approaches that were used for arranging the graphite specimens in the crucible and ensuring they remained in the liquid salt.

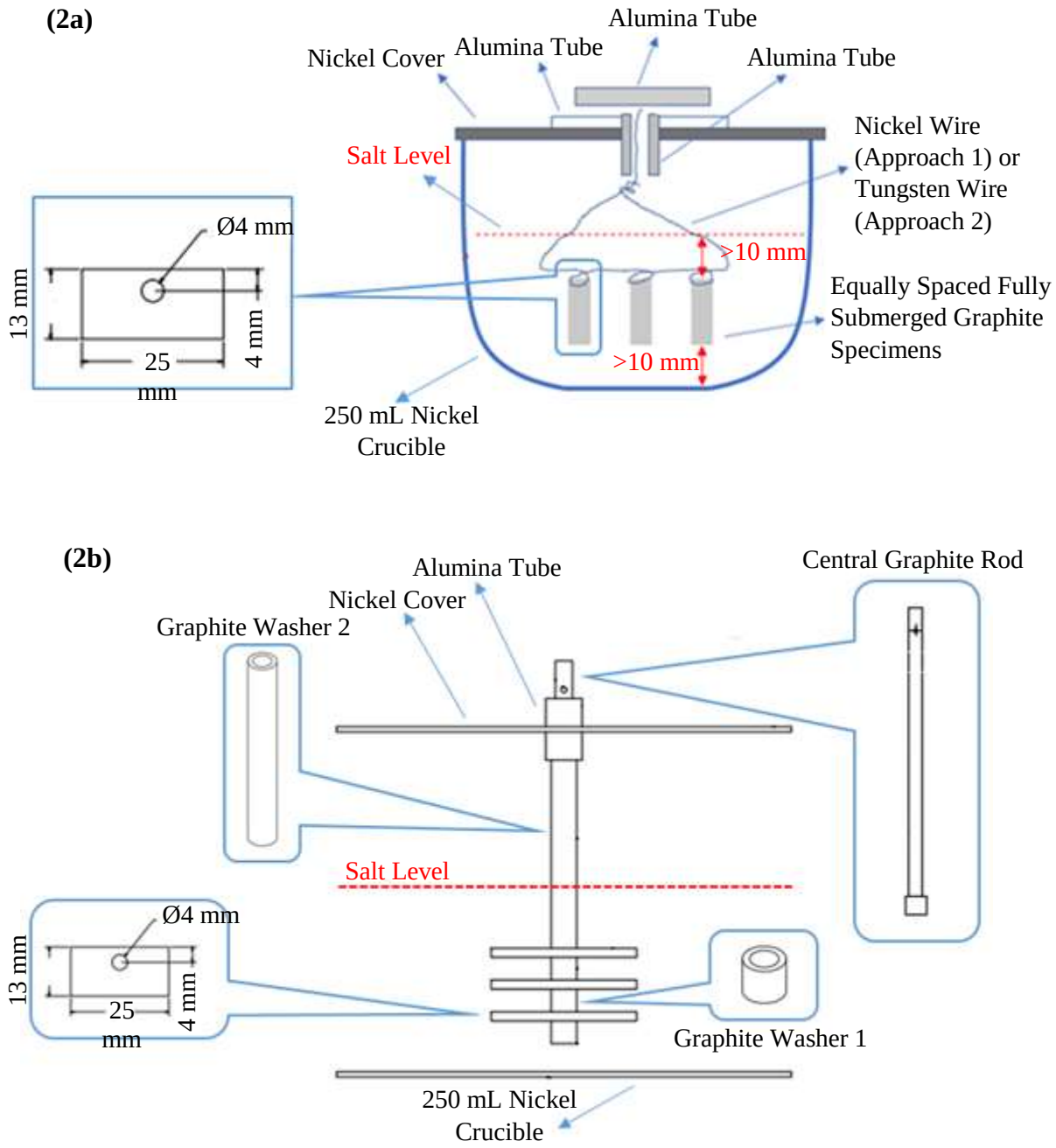

Figure 19. (a) "Approach 1" and "Approach 2", **(b)** "Approach 3" used as graphite specimen set-up for the infiltration test.

For "Approach 1" (refer **Figure 19a**), high-purity nickel wire, for "Approach 2" (refer **Figure 19b**), high-purity tungsten wire and for "Approach 3" (refer **Figure 19c**), high-purity graphite rod and washers were used to hold the graphite specimens. "Approach 1" and "Approach 2" were initially used and were replaced with "Approach 3" because the nickel and tungsten wire underwent severe degradation due to dissimilar metal contact with the graphite specimens in the electrolytic molten salt medium. The infiltration tests (refer **Table 11**) were carried out in the static system at the required pressures, temperatures and time duration.

Table 11. Details of static infiltration tests.

Graphite Supplier & Grade	Pore-Size (μm)	Test Conditions			
		Temperature (ºC)	Pressure (bar (abs))	Duration (Hours)	Specimen Set-Up
Graphite-Molten Salt Interaction Studies					
SGL & R7710	0.6	700	6	24	Approach 1
SGL & R7710	0.6	700	6	100	Approach 1
Toyo Tanso & HPG-830	0.6	700	6	200	Approach 2
Mersen & 2175P	0.9	850	10	100	Approach 3
Mersen & 2175P	0.9	850	10	200	Approach 3
Effects of Applied Pressure on Molten Salt Infiltration					
Mersen & 2175P	0.9	850	10	200	Approach 3
			11		
Microstructural Effects on Molten Salt Infiltration					
Mersen & 2175P	0.9	850	11	200	Approach 3
Ibiden & T6	0.3				
SGL & R7650	1.1				
Toyo Tanso & HPG 510	1.2	850	8	200	Approach 3
Ibiden & FGM19	1.02				
Entegris & TM	1.5				

Before the infiltration test, the specimens were ultrasonically cleaned in DI water for 4 minutes to unclog the closed pores, followed by rinsing in DI water, air drying and baking at 600 ºC for 8 hours in the argon-filled glovebox using the electric melt furnace. After the infiltration test, the specimens were carefully retrieved and gently cleaned using a clean soft bristle brush to remove any salt debris, residue or deposits from the surface.

3.4.4 Characterization Techniques

Several different characterization techniques were employed to analyze the molten salt, corroded specimens and the infiltrated graphite specimens. The instruments and associated softwares used for these techniques are as follows,

- DSC (TA Instruments, SDT Q600, and Universal Analysis software, version 5.5.22)
- ICP-MS (Thermo Scientific™ iCAP™ RQ ICP-MS, and Qtegra™ Intelligent Scientific Data Solution™ software)
- XPS (PHI VersaProbe III Scanning XPS Microscope, and PHI MultiPak software, version 9.7.0.1)
- XRD (Panalytical, Single Crystal X-ray Diffraction System)
- SEM-EDS (FEI Quanta 600 FEG Environment SEM equipped with EDS Bruker QUANTAX 400, High-Speed Silicon Drifted Detector, and ESPRIT software, version 2.0)
- Hardness tester (Vickers Microhardness Tester, LECO V-100-A2)
- Wear tester (RTEC Instruments, Tribometer MFT).

Salt Purity Measurement

Molten salt after purification was analyzed to check its purity, and to verify its composition. This was done by performing DSC analysis to measure the melting-point temperature of salt and compare it with the eutectic melting-point temperature for any deviations. Any impurities in the salt will lower its melting-point or broaden the melting-point range as less energy will be required to break the intermolecular bonds. Additional analysis involved ICP-MS, XPS, XRD and SEM-EDS to check, identify and quantify the presence of any metallic and non-metallic impurities in the salt.

Boride Layer Analysis

The borided specimens were morphologically examined for the boride layer structure and its composition (metal-borides) using SEM-EDS and XRD.

Corrosion or Degradation Measurement

The corrosion-rate (mg/cm^2) was determined by measuring weight-loss in the corroded specimens (before and after corrosion) using the analytical balance. The surface and cross-section of the

corroded specimens was characterized using SEM-EDS to identify the type of attack (pitting), examine the corrosion layer (depletion of alloying elements) and to measure the depth of attack.

Microstructural Evaluation

The microstructural effects on molten salt corrosion was investigated by examining the microstructure (grain-boundaries) of the corroded specimens using SEM-EDS for any changes because of corrosion, or for any indications of intergranular-driven corrosion. The grain-boundaries of the corroded specimens were revealed by etching its cross-section (polished) with the Adlers reagent ((hydrochloric acid, ammonium copper chloride, ferric chloride, water).

Infiltration Measurement

The molten salt infiltration in graphites was measured using SEM-EDS, and verified using XPS. The infiltrated specimens were also analyzed using XPS to check for any possible molten salt-graphite interaction.

Property Measurement

Any compromise in the mechanical properties of the materials due to corrosion was studied by measuring the hardness of the alloys before and after the corrosion test using the Vickers Microhardness Tester.

CHAPTER 4

4 RESULTS AND DISCUSSION

4.1 Effectiveness of Purification Processes for Molten Salts

4.1.1 Molten Chloride Salt

Figure 20 shows the DSC analysis results of the non-purified KCl-$MgCl_2$-NaCl salt that was supplied by Israel Chemicals Limited.

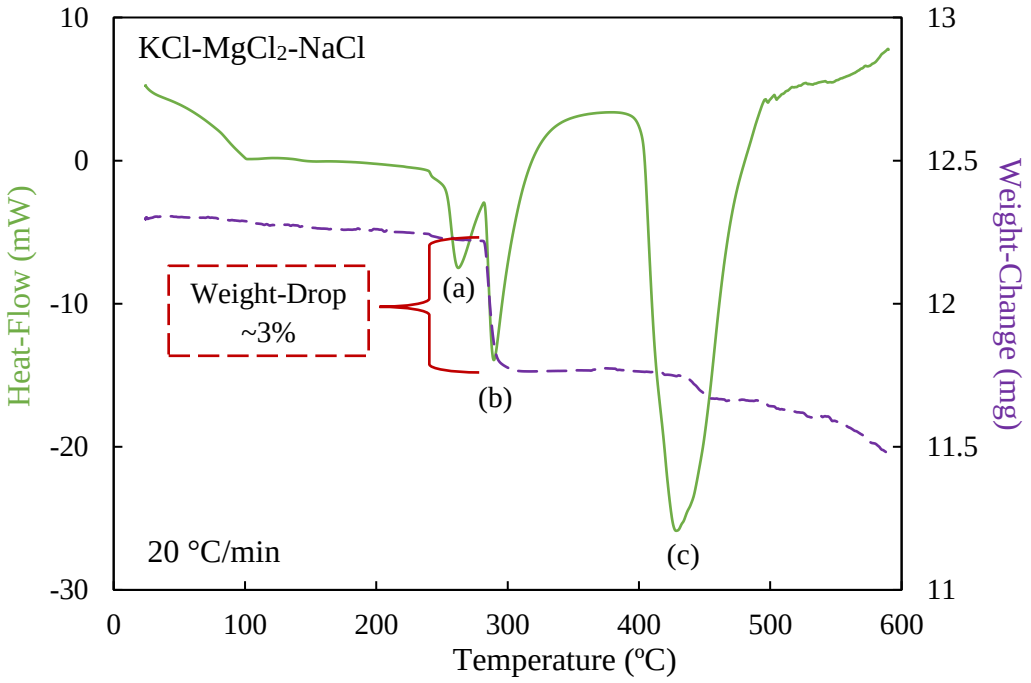

Peak Identification	Onset Temperature (ºC)	Weight-Change (mg)
(a)	253.69	-0.0812
(b)	283.17	-0.4532
(c)	403.65	-0.1252

Figure 20. DSC analysis of the non-purified dehydrated KCl-$MgCl_2$-NaCl, ICL salt.

Three peaks were observed, peak (a) at 253.69 °C, peak (b) at 283.17 °C, and peak (c) at 403.65 °C. Peaks (a) and (b) could represent a possible phase transition in the salt, however this cannot be confirmed as it is not is observed in the subsequent heating cycle. It also showed weight-loss (~3%) in the salt, thus indicating moisture presence in the salt owing to the hygroscopic nature of $MgCl_2$.

As temperature increases, the moisture in the salt vaporizes; the increased vapor pressure can rupture the aluminum crucible lid, thus generating an endothermic peak with its intensity depending on the amount of vapor pressure released from the salt sample. Peak (c) represents the onset melting temperature of the chloride salt, which was measured as 403.7 °C.

Figure 21a and **Figure 21b** show the XRD analysis results for the ICL, KCl-$MgCl_2$-NaCl salt before, and after purification. The non-purified salt (refer **Figure 21b**) showed the presence of moisture in the form of hydrates ($KMgCl_3 \cdot 6H_2O$), and magnesium oxychloride (MgOHCl). Since, the salt was already dehydrated by the supplier, the moisture must have introduced in the salt during its handling, storage, and/or transportation, while the MgOHCl could be the by-product of the dehydration process, formed from the hydrolysis of the (hydrated) salt. However, the source of these impurities cannot be confirmed due to limited knowledge on the salt's history involving its synthesis, and dehydration process.

Generally, $MgCl_2$ salt blends always exhibit high avidity for moisture because of its highly hygroscopic nature, and hence, is the major contributor or source of impurities (mostly non-metallic) in the molten salts. **Figure 21b** shows that the purification (i.e. thermal and chemical treatment) processes were highly effective in reducing the moisture and oxygen based contaminants in the salt. Also, no new impurities (i.e. metallic or non-metallic) were introduced in the salt during the purification processes. As slow heat-treatment during thermal purification dries the salt by vaporization of moisture, Mg addition during chemical purification reduces the oxygen content in the salt. This is because Mg being an active element and an oxygen scavenger will react with oxygen and/or any residual moisture in the salt at high temperatures to form insoluble magnesium oxide (MgO, formed as dense sludge) and slightly soluble magnesium hydroxide ($Mg(OH)_2$) compounds (refer **Figure 25**). The MgO sludge along with other insoluble dense metallic contaminants such as non-consumed Mg pieces, nickel from the crucible, etc.) easily separates out from the salt at the bottom of the crucible as shown in **Figure 22a**, **Figure 22b-1**, and **Figure 22b-2**).

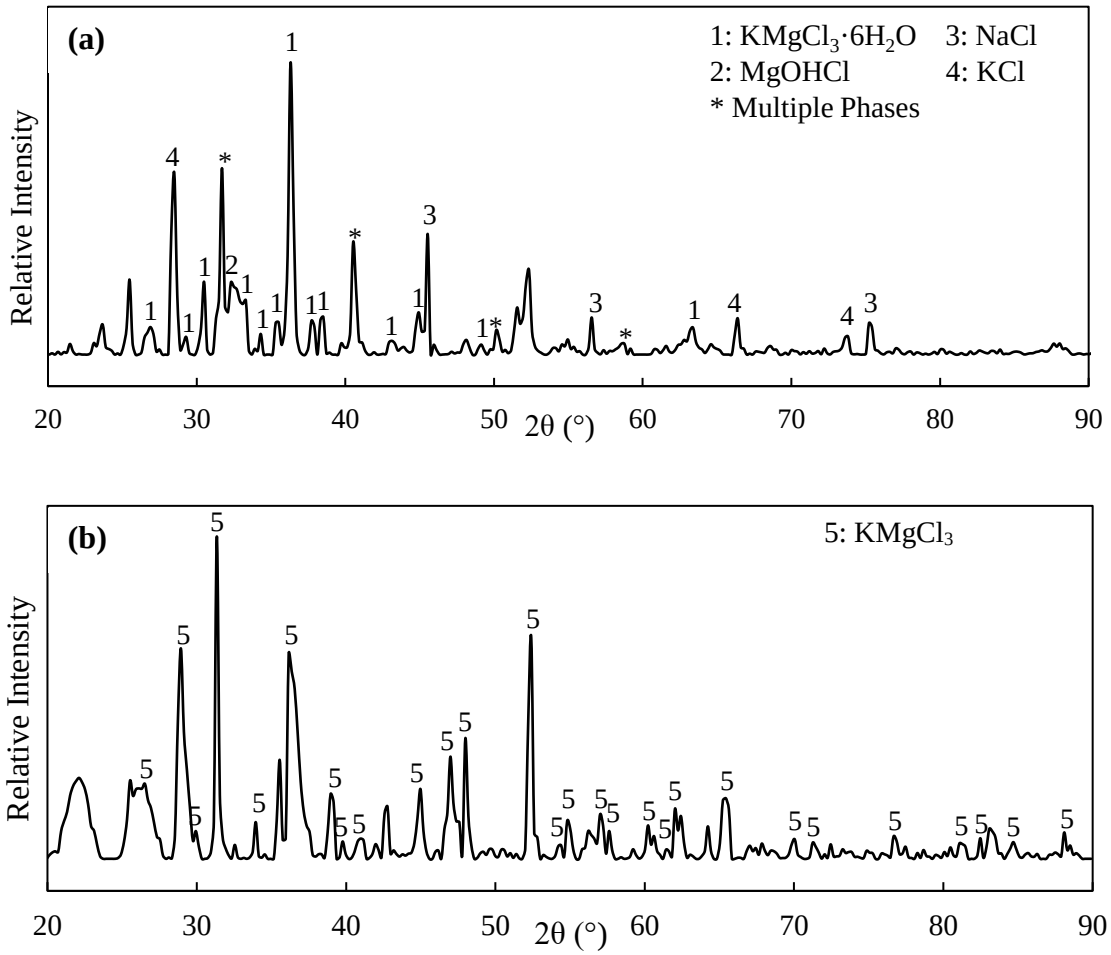

Figure 21. XRD analysis of the KCl-$MgCl_2$-NaCl, ICL salt **(a)** purified, and **(b)** non-purified.

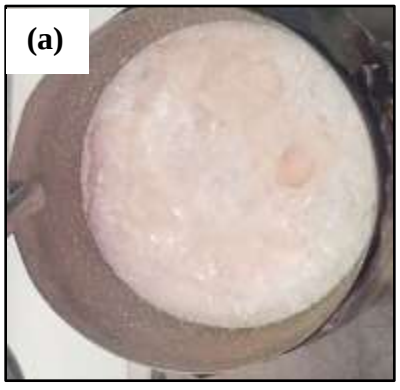

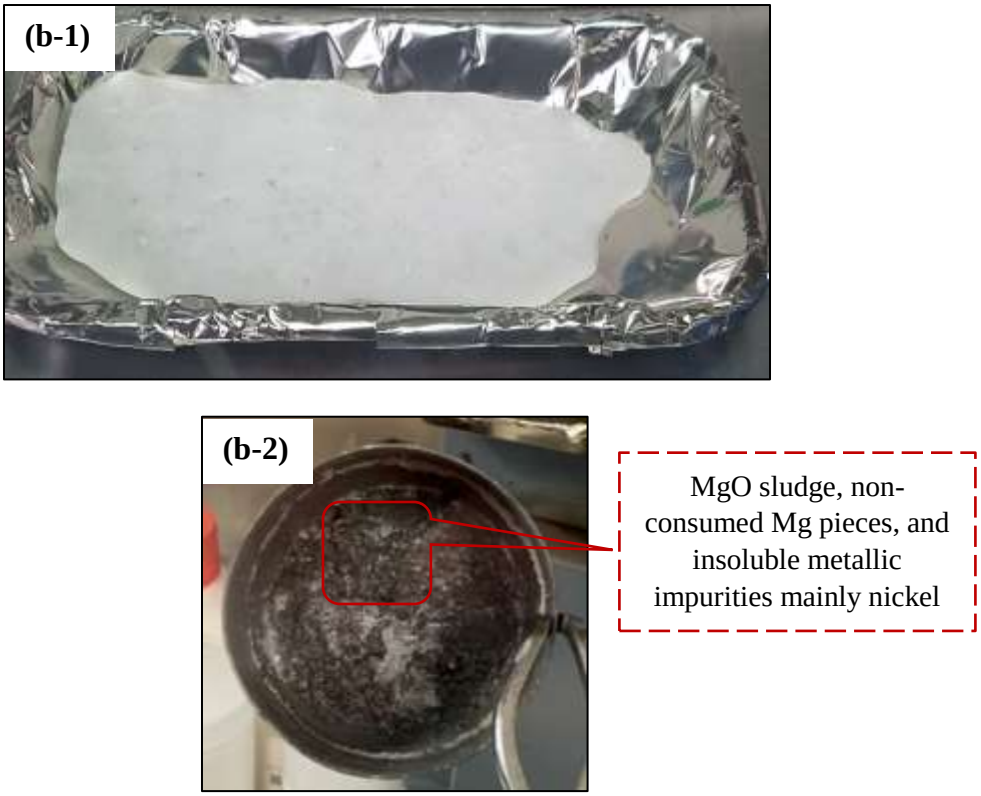

Figure 22. (a) Salt after thermal purification, salt after chemical purification **(b-1)** clean part, and **(b-2)** the contaminants comprising of MgO sludge, non-consumed Mg pieces, and insoluble metallic impurities.

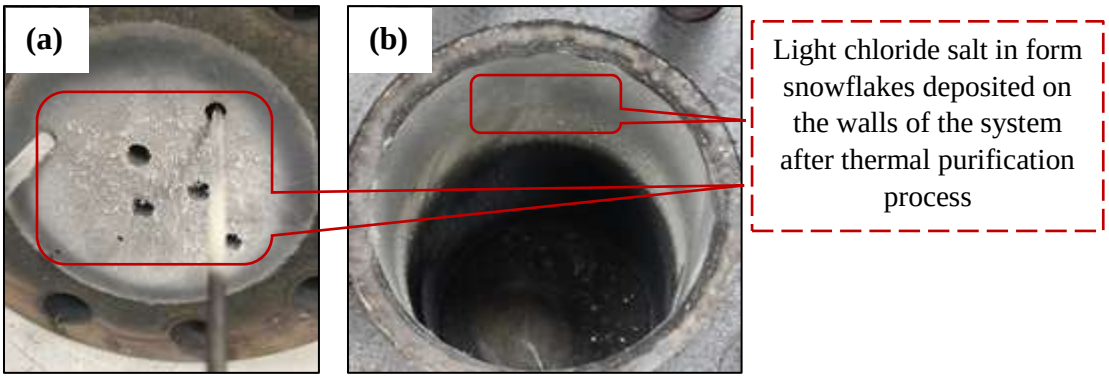

Figure 23. The static system images after the thermal purification process **(a)** inner-wall of the static-chamber, and **(b)** bottom surface of the blind flange.

In the absence of a proper blanket gas (viz. Cl_2 gas or Cl_2 blend gas), the hydrolysis of $MgCl_2$ is inevitable [105]. Some studies have even shown that the hydrolysis in carnallite salt ($KMgCl_3$) is significantly lower than bischofite salt ($MgCl_2$), and hence, is more preferred for the molten chloride salts. There are several negative characteristics associated with the hydrolysis of $MgCl_2$

such as, (a) formation of magnesium oxychloride (MgOHCl) compound [50, 52], (b) alteration in the salt chemistry, and its properties like melting-point temperature, heat capacity, etc., due to loss of $MgCl_2$, and (c) formation of toxic and corrosive off-gases like hydrogen chloride (HCl) gas.

MgOHCl presence in the salt in undesirable as it can thermally decompose to form MgO and HCl gas. Studies related to decomposition kinetics of MgOHCl have shown that the decomposition commences at 376 °C and completes at 600 ± 50 °C without any intermediate steps. The reaction is greatly influenced by the removal rate of HCl gas from the salt interface, thus making this process the "rate-determining" or "rate-limiting" step of the reaction. Kashani-Nejad et. al. [106] found that the decomposition kinetics is also linearly dependent on the initial concentration of MgOHCl in the chloride salt.

Furthermore, prolonged exposure of HCl gas is also highly detrimental to metals and alloys because of its corrosive nature. Based on its solubility in the chloride salt melt at given temperatures, it can dissolve to form a saturated solution and react with the least noble metals and alloying elements by the displacement reaction, thus accelerating corrosion in these materials. Some studies [106] have shown purging or sparging the salt with argon gas with proper flow-rates can facilitate the removal of HCl gas from the salt's interface.

In this study, the MgOHCl compound was not present in the purified salt indicating one of two, or both the possibilities (refer **Figure 25**),

1. Mg will react with MgOHCl to recover some of the $MgCl_2$ salt and form MgO and H_2 gas as byproducts,

$$Mg + 2MgOHCl = MgCl_2(s) + 2MgO(s) + H_2(g) \quad \textbf{(39)}$$

2. MgOHCl will thermally decompose at higher temperatures to form MgO and HCl gas,

$$MgOHCl = MgO(s) + HCl(g) \quad \textbf{(40)}$$

Additional analyses using ICP-MS (refer) and XPS (refer **Figure 24a** and **Figure 24b**) also verified the purity of the salt, except for some contaminations (possibly hydrates, $\cdot nH_2O$), which could have introduced in the salt during its transportation from the glovebox (the salt was prepared in a sealed chamber) to the XPS facility. However, the intensity measured for the O (1s) peak (i.e. MgO) was relatively lower. This indicates also that there could always be a possibility, trace

amounts of MgO formed during the chemical purification process will always be present in the purified salt.

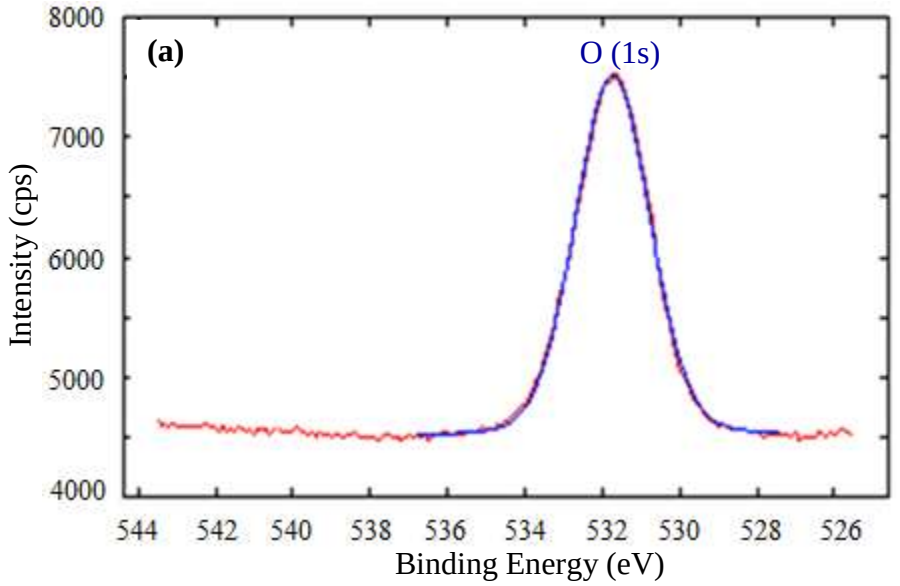

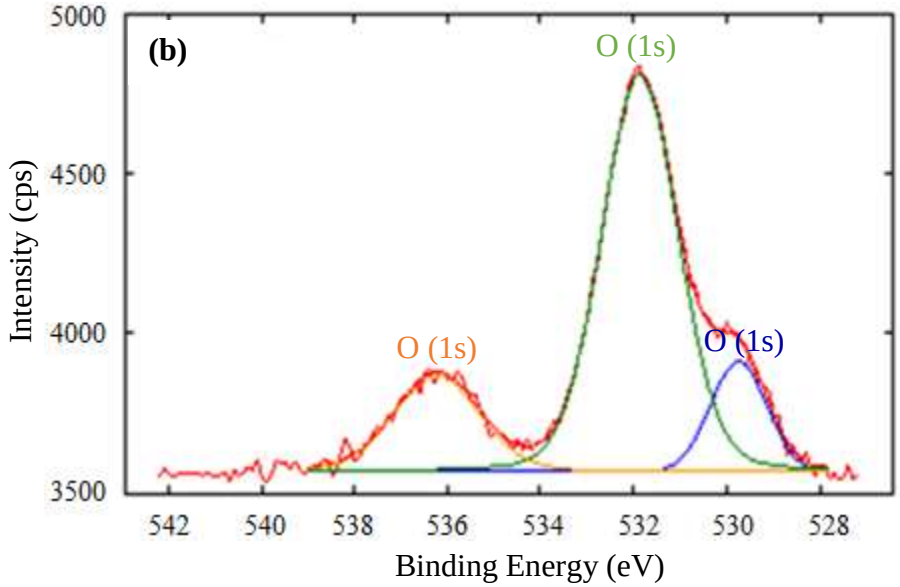

Peak Details	Measured Position (eV)	NIST Database or Literature Values (eV)	Peak Assignment	Area (%)
Non-Purified Salt (refer **Figure 24a**)				
O (1s)	531.7	Not Available	$\cdot nH_2O$ (Hydrates)	100
Purified Salt (refer **Figure 24b)**				

O (1s)	531.9	Not Available	·nH_2O (Hydrates)	68.05
O (1s)	529.7	529.6 [107]	MgO	13.04
O (1s)	536.2	~536.0	Na (KLL)	18.92

Figure 24. XPS high-resolution spectra for O (1s) peaks obtained from **(a)** non-purified salt, and **(b)** purified salt.

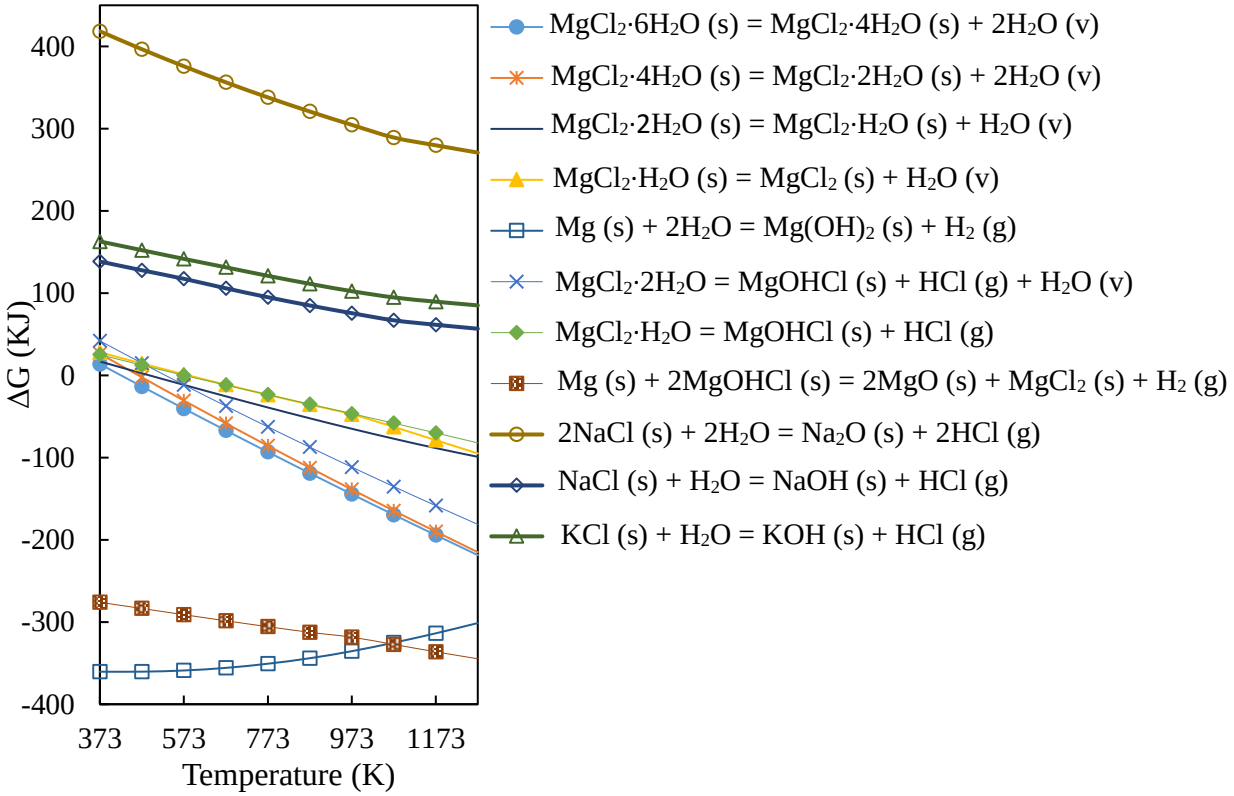

Figure 25. Gibbs free energy of formation as a function of temperature for all possible hydrolysis reactions in molten KCl-$MgCl_2$-NaCl salt [HSC Chemistry® 10 Software].

As shown in **Figure 23a** and **Figure 23b**, salt crystals in the form of light flake like structures was found deposited on the inner walls of the static chamber (only after the thermal purification process). The ICP-MS analysis showed the deposits were majorly composed of the chloride salt, and metallic impurities like iron, chromium, etc. due to corrosion of non-wetted stainless steel (316L) components. This phenomenon possibly occurs due to moisture in the salt, and/or salt vaporization (cause by salt creeping). The salt will dissolve in the liquid water (moisture) to form ionic solution of Cl^- (aq), K^+ (aq), Na^+ (aq), Mg^+ (aq). As the temperature increases and approaches the boiling point of water, the aqueous ionic solution will start evaporating and become less dense.

The denser argon gas (during purging) will raise these vapors and push them towards the vent line of the system. However, during this process, when these vapors contact the surface (non-wetted) of the system (which are comparatively at a slightly lower temperature than the salt); due to temperature gradient effects, it will flash out on the exposed surface, thus leaving a trace of salt precipitates.

4.1.2 Molten Fluoride Salt

For the molten fluoride salt, only thermal purification was performed i.e. salt drying using heat-treatment to remove moisture. **Figure 26a** and **Figure 26b** show the XPS high-resolution spectra for the U peaks obtained from the UF_4 salt before purification, and from the KF-UF_4-NaF salt after purification. **Figure 27a** and **Figure 27b** show the XPS high-resolution spectra for the O peaks from the UF_4 salt before purification, and from the KF-UF_4-NaF salt after purification. The individual compounds (KF, NaF and UF_4 salts) used for the salt preparation were of high-purity, and showed no major metallic and non-metallic impurities except for moisture, which was present in the salt in the form of hydrates ($M \cdot nH_2O$, M: UF_4 and n: 0.5–2.5 [108]; M: NaF and n: 1; M: KF and n: 1, 2 and 4 [79]). The XPS analysis (refer **Figure 27**) of the UF_4 salt also showed the presence of uranium oxide (UO_2). The oxide compound could have been introduced during the synthesis of UF_4 as an intermediate compound in the conversion of UF_6 to UO_2 or U metal, which also cannot be confirmed due to limited knowledge on the salt's history involving its synthesis, handling, storage and transportation. Unlike NaF and KF salt, the UF_4 salt can slowly hydrolyzes even at room temperature to form different oxide and oxyfluoride compounds.

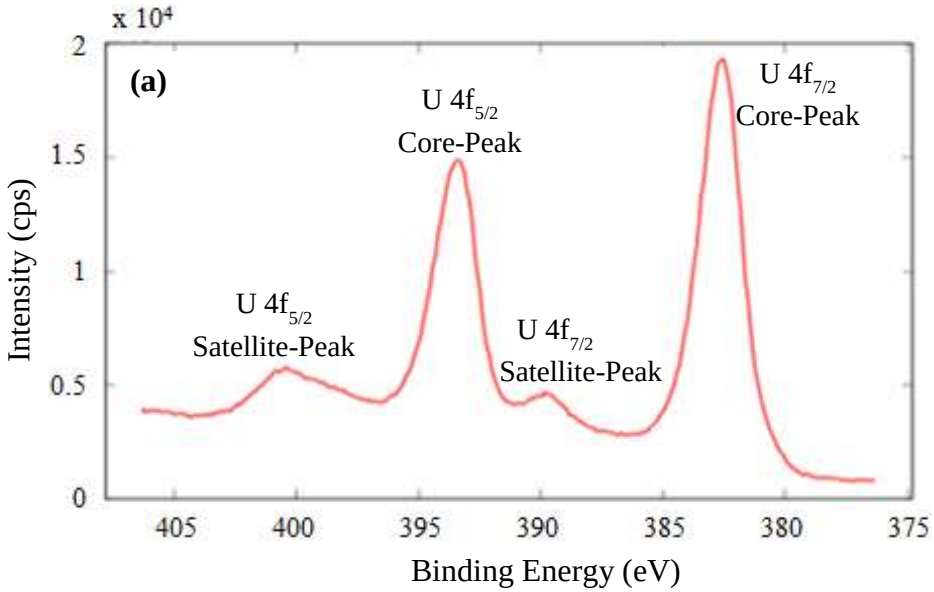

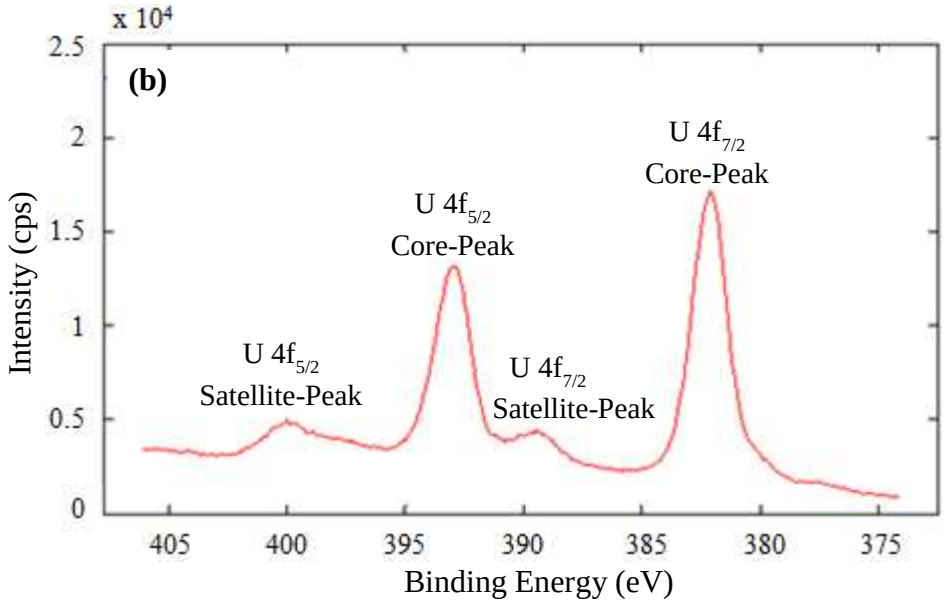

Peak Details	Measured Position (eV)	NIST Database or Literature Values (eV)	Peak Assignment
Non-Purified UF_4 Salt (refer **Figure 26a)**, and Purified KF-UF_4-NaF Salt (refer **Figure 26b**)			
U ($4f_{7/2}$) - Core-Peak	382.6	382.3 [109]	UF_4
U ($4f_{7/2}$) - Satellite-Peak	389.7	Not Available	UF_4
U ($4f_{5/2}$) - Core-Peak	393.4	393.2 [109]	UF_4
U ($4f_{5/2}$) – Satellite-Peak	400.4	Not Available	UF_4

Figure 26. XPS high-resolution spectra for U peaks obtained from **(a)** UF_4 salt before purification, and **(b)** KF-UF_4-NaF salt after purification.

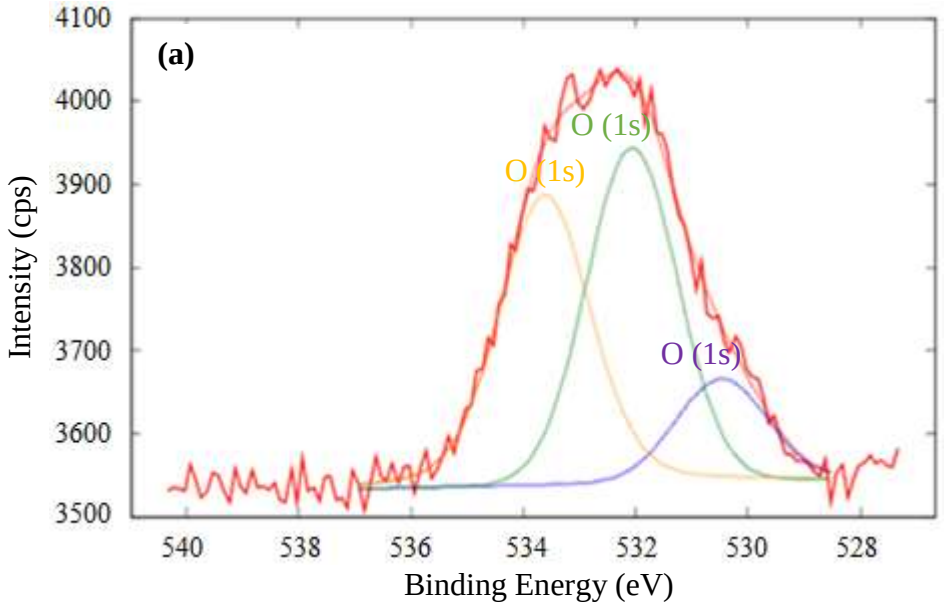

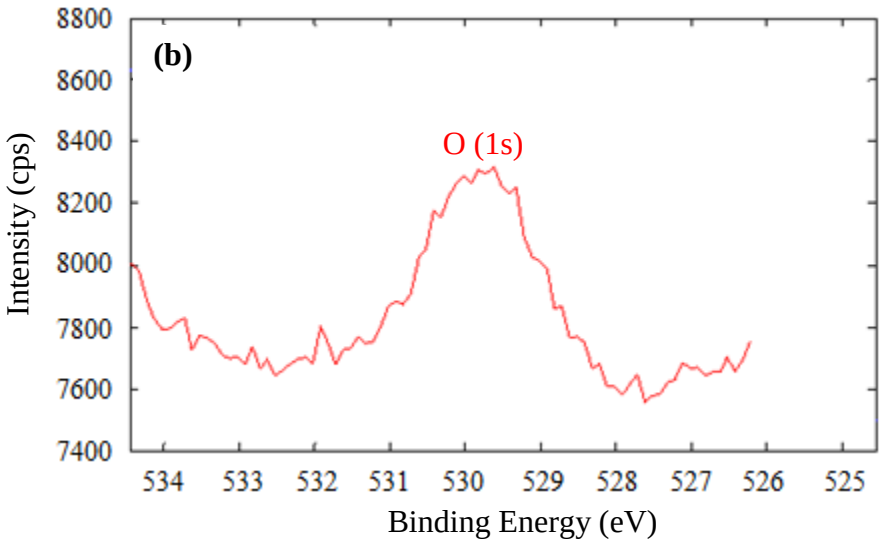

Peak Details	Measured Position (eV)	NIST Database or Literature Values (eV)	Peak Assignment	Area (%)
Non-Purified UF_4 Salt (refer **Figure 27a**)				
O (1s)	530.5	530.4 [110]	UO_2	13.54
O (1s)	532.1	Not Available	$\cdot nH_2O$ (Hydrates)	44.42
O (1s)	533.6	533.3 [111]	H_2O	42.04
Purified KF-UF_4-NaF Salt (refer **Figure 27b**)				
O (1s)	529.8	530.4 [110]	UO_2	100

Figure 27. XPS high-resolution spectra for O (1s) peaks from **(a)** UF_4 salt before purification, and **(b)** KF-UF_4-NaF salt after purification.

Figure 28 shows the Gibbs free energy of formation for the hydrolysis reactions of KF, NaF and UF_4 salts as a function of temperature. It indicates that the selected temperatures for the thermal purification process should safely dry the salt without forming any oxide, hydroxide, and/or oxy-fluoride compounds. This is also evident from the XPS analysis done on the purified salt, which confirmed complete removal of moisture from the fluoride salt. However, uranium oxide was still present in the salt, since, it already exists in the salt provided by the supplier. Although, it is possible to completely convert UO_2 to UF_4 by hydro-fluorination (using hydrogen fluoride gas, refer **Chapter 2**), this was not done considering the difficulties and complexities involved with handling the toxic and corrosive gas [112].

Additional analyses using ICP-MS, DSC and SEM-EDS also confirmed the purity, composition (no change in salt chemistry) and homogeneity of the salt. During the DSC analysis, it was also

found that at lower ramp-rates between 1 to 5 ºC/min, the onset melting-point peak exhibited double-peaks, or peak-splitting, or shoulder-peaks, where the highest/largest peak represented the salt's onset melting-point temperature, while the smallest/shortest peak could represent a secondary phase or a structural change.

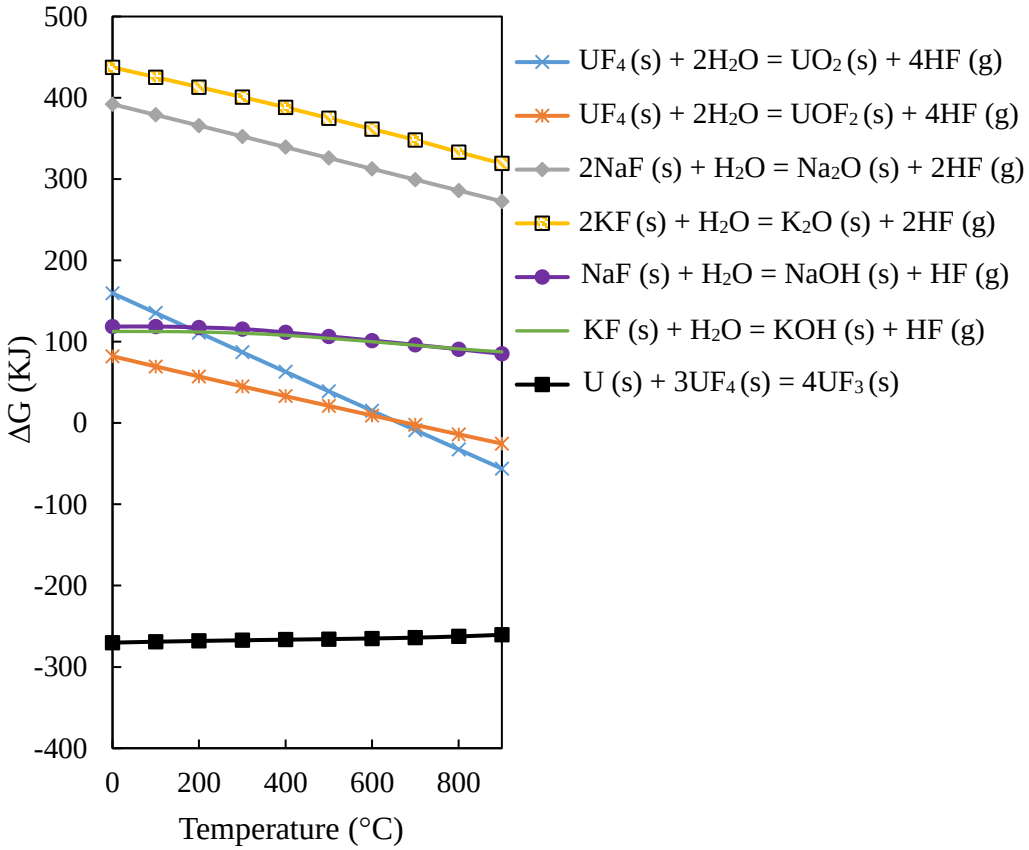

Figure 28. Gibbs free energy of formation as a function of temperature for all possible hydrolysis reactions in molten KF-UF_4-NaF salt [HSC Chemistry® 10 Software].

Also, from the SEM analysis (refer **Figure 29**), uranium was detected in the purified salt, which could be either pure uranium metal (U) or uranium-oxide (UO_2) compound. There is always a possibility that U metal could be present in the UF_4 salt from its production process. However, from **Figure 28**, it can be interpreted that U metal if present in the salt should be entirely consumed during the thermal purification process by reacting with UF_4 to form UF_3. If it is not consumed entirely then being denser it should separate out at the bottom of crucible or react with the nickel crucible during the graphite impregnation test for form various different Ni-U binary phases (NiU_6,

Ni_9U_7, Ni_7U_5 and Ni_2U) at temperatures above 668 ºC (based on the phase diagram of U-Ni system [113]).

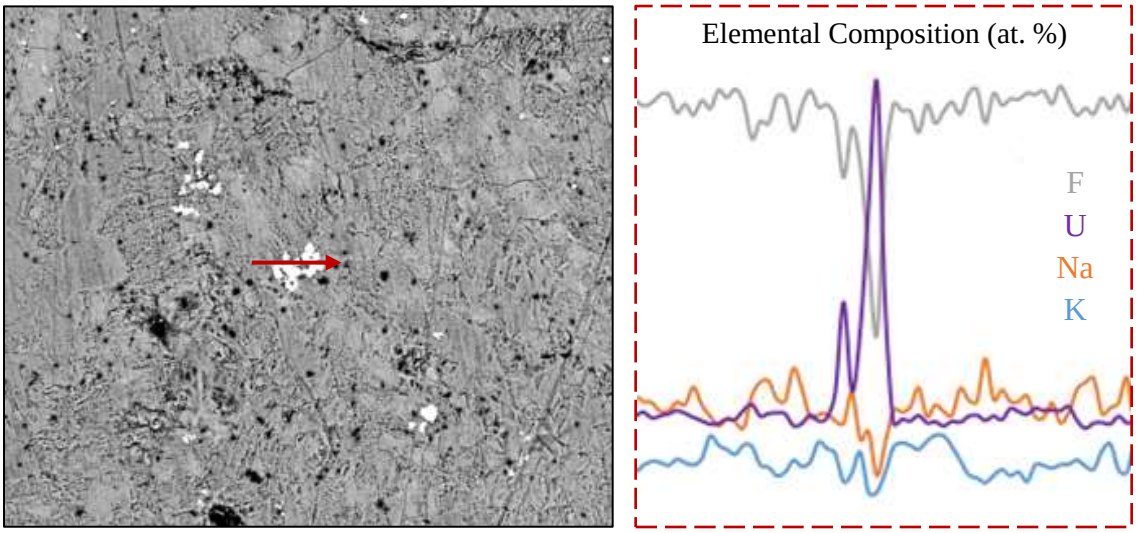

Figure 29. SEM-EDS surface characterization of the purified KF-UF_4-NaF salt.

But these compounds or phases were not visibly detected on the walls of the nickel crucible after the graphite impregnation test. Furthermore, U metal was also not seen floating on the salt or at the bottom of nickel crucible after the purification process. The high-resolution spectra obtained for the U ($4f_{7/2}$) peaks also did not show any presence of U metal in the UF_4 salt, and U metal and UF_3 compound in the salt after purification. Thus, this confirms that the U detected in the salt after purification is UO_2.

The analyses showed that the purification processes adopted for the chloride and fluoride salts were effective in reducing the corrosive contaminants in the salt without altering its chemistry (i.e. composition). However, it must also be noted that considering the large batches of salt purchased for these tests, it will always be difficult to completely remove the pre-existing impurities in the salt, which can also escape detection during analysis.

4.2 Impurity-Driven Molten Chloride Salt Corrosion in HAYNES® 230® Alloy

The effects of impurities in the molten chloride salt on the corrosion rate of HAYNES® 230® alloy was studied by exposing the alloy in different salt (KCl-$MgCl_2$-NaCl) conditions (refer **Table 12**) such as (a) high-purity salt that was thermally purified (just involves heat treatment) without adding Mg, (b) high-purity salt that was thermally and chemically purified by adding Mg, (c) ICL salt that was not purified, (d) ICL salt that was thermally and chemically purified by adding Mg and (e) ICL salt that was thermally and chemically purified by adding Mg and the purified salt was intentionally appended with Mg; and at 800 ºC for 100 hours. For salt condition (c), the alloy was not immersed in the molten chloride salt (i.e. corrosion in non-wetting surface); and for salt condition (e), the effects of Mg addition (corrosion inhibitor) in molten chloride salt, on the corrosion of 230 alloy was studied (here, the solid Mg pieces added to the purified salt were contacted with the alloy to understand its influence on the corrosion behavior of H230 alloy).

Table 12. Details of different salt (KCl-$MgCl_2$-NaCl) conditions, (a)–(e).

Salt Condition	Details	Major Impurities*
(a): High Purity Salt	▪ Thermally purified ▪ Three specimens-immersed in the salt	▪ No metallic impurities ▪ MgO ▪ H_2O** (possibly in the form of hydrates)
(b): High Purity Salt	▪ Thermally purified ▪ Chemically purified ▪ Three specimens-immersed in the salt	▪ No metallic impurities ▪ MgO (concentration lower than condition (a) and (d)) ▪ H_2O** (possibly in the form of hydrates)
(c): ICL Salt	▪ Not purified ▪ Three specimens-not immersed in the salt	▪ No metallic impurities ▪ $\cdot nH_2O$; n: 1, 2, 4, 6 ▪ MgOHCl
(d): ICL Salt	▪ Thermally purified ▪ Chemically purified ▪ Three specimens-immersed in the salt	▪ No metallic impurities ▪ MgO (concentration lower than condition (a)) ▪ H_2O** (possibly in the form of hydrates)
(e): ICL Salt	▪ Thermally purified ▪ Chemically purified ▪ Two specimens-immersed in the salt	▪ Impurities: Same as salt condition (d) ▪ >0.5 wt.% solid Mg pieces added to the purified salt ▪ Mg piece positioned in close proximity or in contact with the specimens

* ICP-MS, XPS and/or XRD analyses

** The presence of moisture (possibly surface contamination) is due to hygroscopic nature of $MgCl_2$ and could have been introduced during transfer of salt from the glovebox to the XPS facility

Figure 30 shows the average mass-loss in mg/cm^2 measured for alloy 230 after exposure to the molten KCl-$MgCl_2$-NaCl salt at 800 ºC for 100 hours in different salt conditions ("a"–"e").

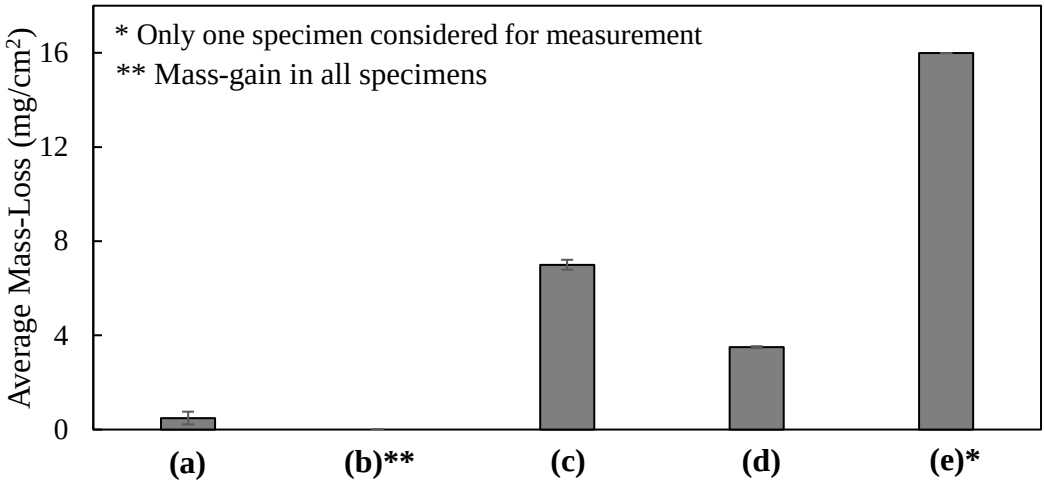

Figure 30. Average mass-loss (mg/cm^2) in H230 alloy after exposure to molten KCl-$MgCl_2$-NaCl salt at 800 ºC for 100 hours, **(a)** HP salt purified without Mg, **(b)** HP salt purified with Mg, **(c)** ICL salt not purified, **(d)** ICL salt purified with Mg, and **(e)** ICL salt purified with Mg and appended with Mg.

The average mass-loss (mg/cm^2) was found to be in the increasing order of (b) 0 mg/cm^2 < (a) 0.77 mg/cm^2 < (d) 3.55 mg/cm^2 < (c) 7.21 mg/cm^2 < (e) 15.99 mg/cm^2. The corrosion-rate in 230 alloy increased in salt with higher concentration of corrosive impurities. **Figure 31** and **Figure 32** show the SEM-EDS surface and cross-sectional analysis of the corroded specimens. The surface analysis (refer **Figure 31**) of the corroded specimens showed extensive pitting except for salt condition (b), where no pitting or any other form of surface degradation was observed. The pits were irregular in shape and non-uniform across the surface. The surface also did not show any presence of metal-oxide and metal-chloride layer or deposit that could have formed due to interaction of alloying elements with the chloride salt and the impurities.

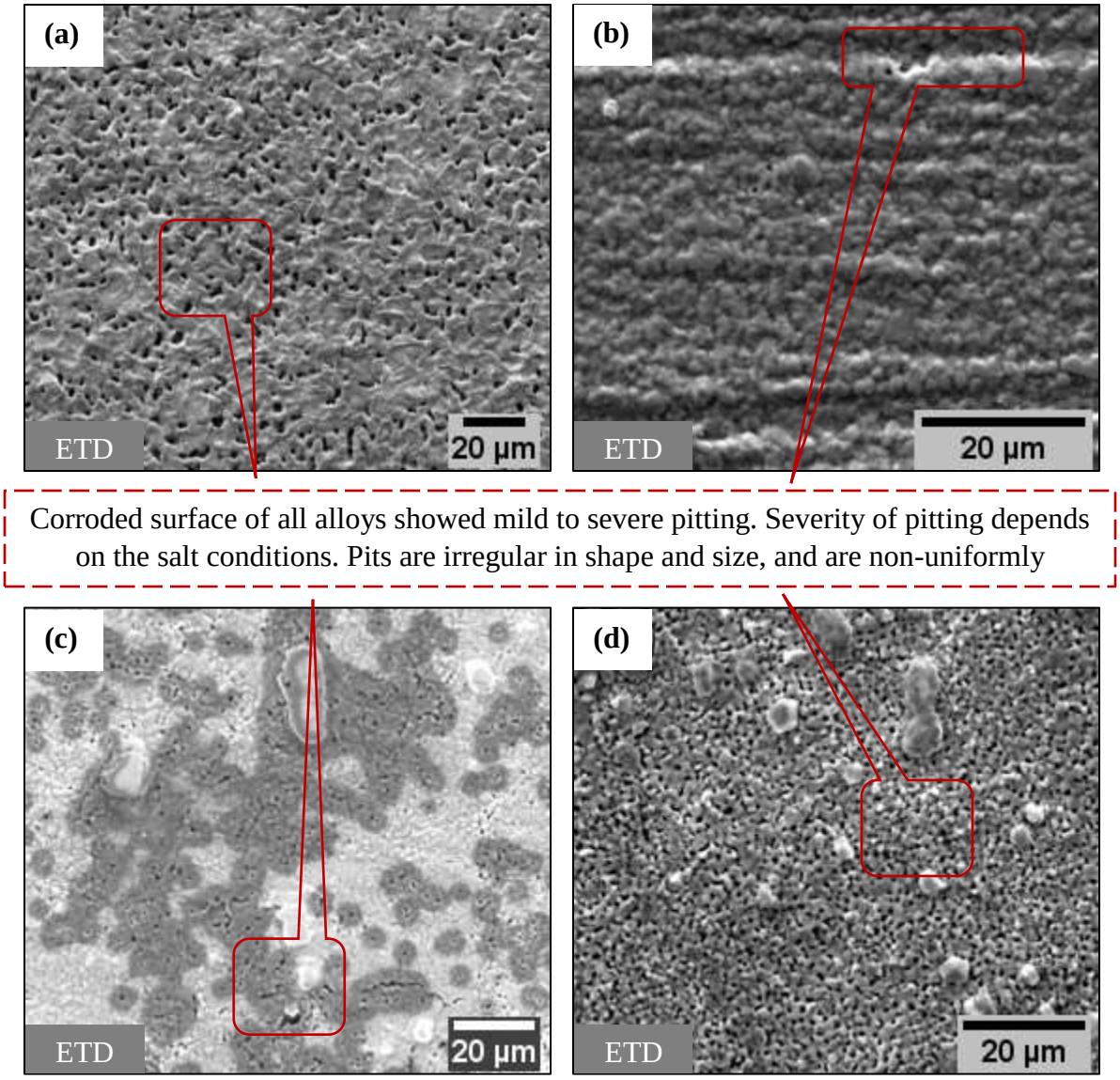

Figure 31. SEM-EDS surface characterization of H230 alloy after exposure to molten KCl-$MgCl_2$-NaCl salt at 800 ºC for 100 hours, **(a)** HP salt purified without Mg, **(b)** HP salt purified with Mg, **(c)** ICL salt not purified and **(d)** ICL salt purified with Mg.

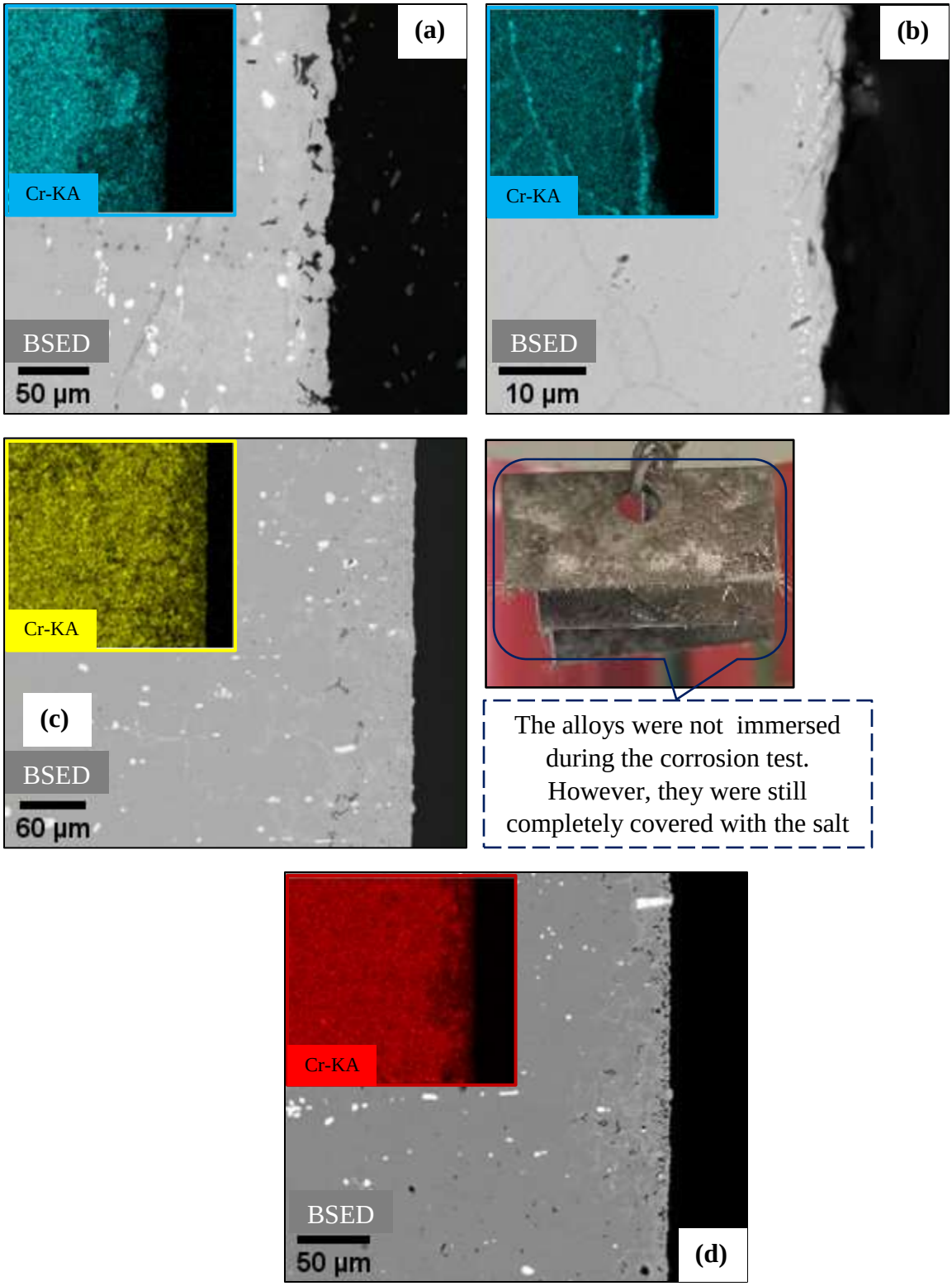

Figure 32. SEM-EDS cross-sectional characterization of H230 alloy after exposure to molten KCl-$MgCl_2$-NaCl salt at 800 ºC for 100 hours, **(a)** HP salt purified without Mg, **(b)** HP salt purified with Mg, **(c)** ICL salt not purified and **(d)** ICL salt purified with Mg.

The cross-sectional analysis (refer **Figure 32**) of the corroded specimens showed a near-uniform porous corrosion layer with severe chromium depletion and minor nickel enrichment in the region near the interface for all salt conditions except salt condition (b).

The corrosion mechanism is impurity driven and its interaction with the alloying elements, and is dependent on the Gibbs free energy of formation [HSC Chemistry® 10 Software, [52], [65]] for the governing reactions (i.e. more negative the Gibbs free energy, more thermodynamically favorable the reaction is for the given temperature ranges). Based on this data, the most active elements in the alloy in the increasing order of Cr, Fe and Ni will react with the soluble HCl or other active impurities like O_2, Cl_2, H_2O and $MgOH^+Cl^-$ through the following **Reactions (41–44)** to form respective chloride ($CrCl_2$) or oxide (Cr_2O_3) species.

$$MgCl_2 \cdot H_2O = MgOHCl(s) + HCl(g) \quad \textbf{(41a)}$$

$$MgOHCl = MgO(s) + HCl(g) \quad \textbf{(41b)}$$

$$Cr + 2HCl = CrCl_2(s) + H_2(g) \qquad \Delta G_{800\,°C} = -62.53\ KJ \quad \textbf{(42)}$$

$$Cr + Cl_2 = CrCl_2(s) \qquad \Delta G_{800\,°C} = -265.18\ KJ \quad \textbf{(43)}$$

$$Cr + O_2 = Cr_2O_3(s) \qquad \Delta G_{800\,°C} = -852.99\ KJ \quad \textbf{(44)}$$

Formation of metal-oxides depends on the O^{2-} concentration (activity) in the salt melt, and can be determined from the E-pO^{2-} diagrams for the alloying elements (Cr, Fe, Ni, etc.) in the molten salt at the required temperatures. Here, the oxide layer formation is highly unlikely because of reduced impurity concentration in the salt after its purification. However, if the oxides are still formed then depending on the solubility of these metal-oxides and metal-chlorides in the liquid chloride melt at given temperatures, they will not sustain or provide any protection, and will eventually dissolve in the molten chloride salt. The results also indicated that corrosion of alloys in molten salt is inevitable even after purifying the salt (salt condition (d)), specifically if it's initial purity is compromised, which further depends on the salt's synthesis/production, storage and transportation. Here, the source of impurities for corrosion could have been moisture ($\cdot nH_2O$) (hydrolyzed the salt during heat-treatment) and/or MgOHCl (formed during the supplier's dehydration process), which were pre-existing in the salt (refer **Reaction 41a** and **41b**).

Adding molybdenum (Mo) and tungsten (W) in the alloy have also shown to influence the corrosion rate by slowing it down owing to its inertness towards the molten halide salts [114]. It can form a protective barrier and prevent the outward diffusion of chromium. The SEM surface and cross-sectional examination of the HAYNES® 230® alloy showed W-enriched regions, where no pitting occurred, thus indicating that these inert elements provide some form protection against the molten chloride salt attack. However, their distribution within the alloy matrix is not uniform thereby restricting its usefulness in controlling the corrosion process.

Figure 33 shows the surface and cross-sectional images of the 230 alloy after exposure to the molten chloride salt appended with Mg (salt condition (e)).

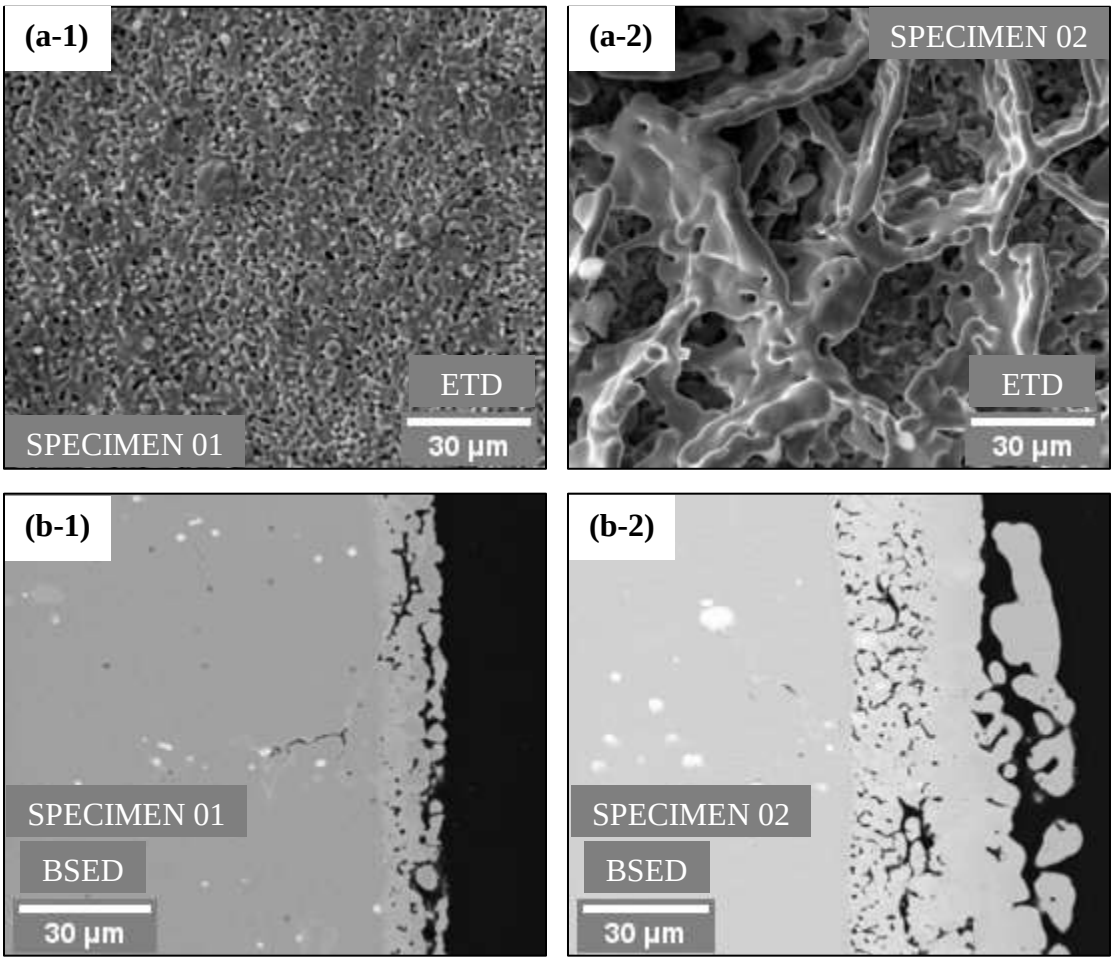

Figure 33. SEM-EDS **(a)** surface, and **(b)** cross-sectional characterization of H230 alloy after exposure to molten KCl-$MgCl_2$-NaCl salt at 800 ºC for 100 hours, ICL salt purified with Mg and appended with Mg (salt condition (e)).

Two specimens were immersed in the same salt (condition (e)), and one possibly contacted the Mg during the corrosion test (the intensity of corrosion in the two specimens was different). Generally, Mg should act as a corrosion inhibitor in the molten chloride (Mg-based) salts, where it is preferred over the alloying elements like Cr, Fe, Ni, etc. to react with the corrosive impurities in the salt like H_2O, Cl_2, O_2, HCl, etc. (refer **Reactions (45–48)**), and thus assisting in slowing down the corrosion in alloys.

$$Mg + 2H_2O = Mg(OH)_2(s) + H_2(g) \qquad \Delta G_{800\,^\circ C} = -325.13\ KJ \qquad \textbf{(45)}$$

$$Mg + Cl_2 = MgCl_2(s) \qquad \Delta G_{800\,^\circ C} = -477.12\ KJ \qquad \textbf{(46)}$$

$$2Mg + O_2 = 2MgO(s) \qquad \Delta G_{800\,^\circ C} = -970.09\ KJ \qquad \textbf{(47)}$$

$$Mg + 2HCl = MgCl_2(s) + H_2(g) \qquad \Delta G_{800\,^\circ C} = -274.48\ KJ \qquad \textbf{(48)}$$

However, in the present study, appending the molten salt with Mg intensified corrosion in 230 alloy. This was because the less dense (freely floating) Mg pieces melted at high temperature and contacted the alloy during the corrosion test (refer **Figure 33a-2** and **Figure 33b-2**), and severely degraded it by possibly forming Mg-Ni phases (Mg-hcp + Mg_2Ni, $MgNi_2$ + Mg_2Ni, Ni-fcc + $MgNi_2$ [115]). These phases are thermally unstable due to the differences in their thermal expansion coefficient with the alloy, and hence are highly undesirable. This requires complete removal of any unconsumed Mg pieces after chemical purification process, and if considered as a corrosion inhibitor then avoid contacting it with the nickel-based alloy. Therefore, if there is excess Mg metal in the salt, the corrosion can be accelerated.

Based on these analyses, it was observed that the salt purity greatly influences the corrosion in alloys, where its severity depends on the concentration of impurities in the salt. The purification processes such as thermal purification (heat-treatment) and chemical purification (heat-treatment with Mg addition) processes developed for the molten KCl-$MgCl_2$-NaCl was efficient in reducing the contaminants and the corrosion-rate in the H230 alloy. However, it must also be noted that any residual Mg pieces from the purification process must be completely removed from the purified salt as any contact with the exposed surface of the alloy (nickel-based alloy) will intensify corrosion due to Mg-Ni interaction.

4.3 Molten Salt Corrosion in Nickel and Ferrous-Based Alloys

Corrosion characteristics of nickel-based alloys such as HAYNES® 230®, Hastelloy® C276 and Inconel® 718, and ferrous-based alloys such as Stainless Steel, 316L and 709-RBB, 709-4B2 and 709-RBB* were studied after exposing these alloys to molten KCl-$MgCl_2$-NaCl salt (salt condition (d)) in an inert (argon) environment at 800 °C for 100 hours.

4.3.1 Nickel-Based Alloys

Figure 34 and **Figure 35** show the SEM-EDS surface and cross-sectional characterization of the corroded nickel-based alloys.

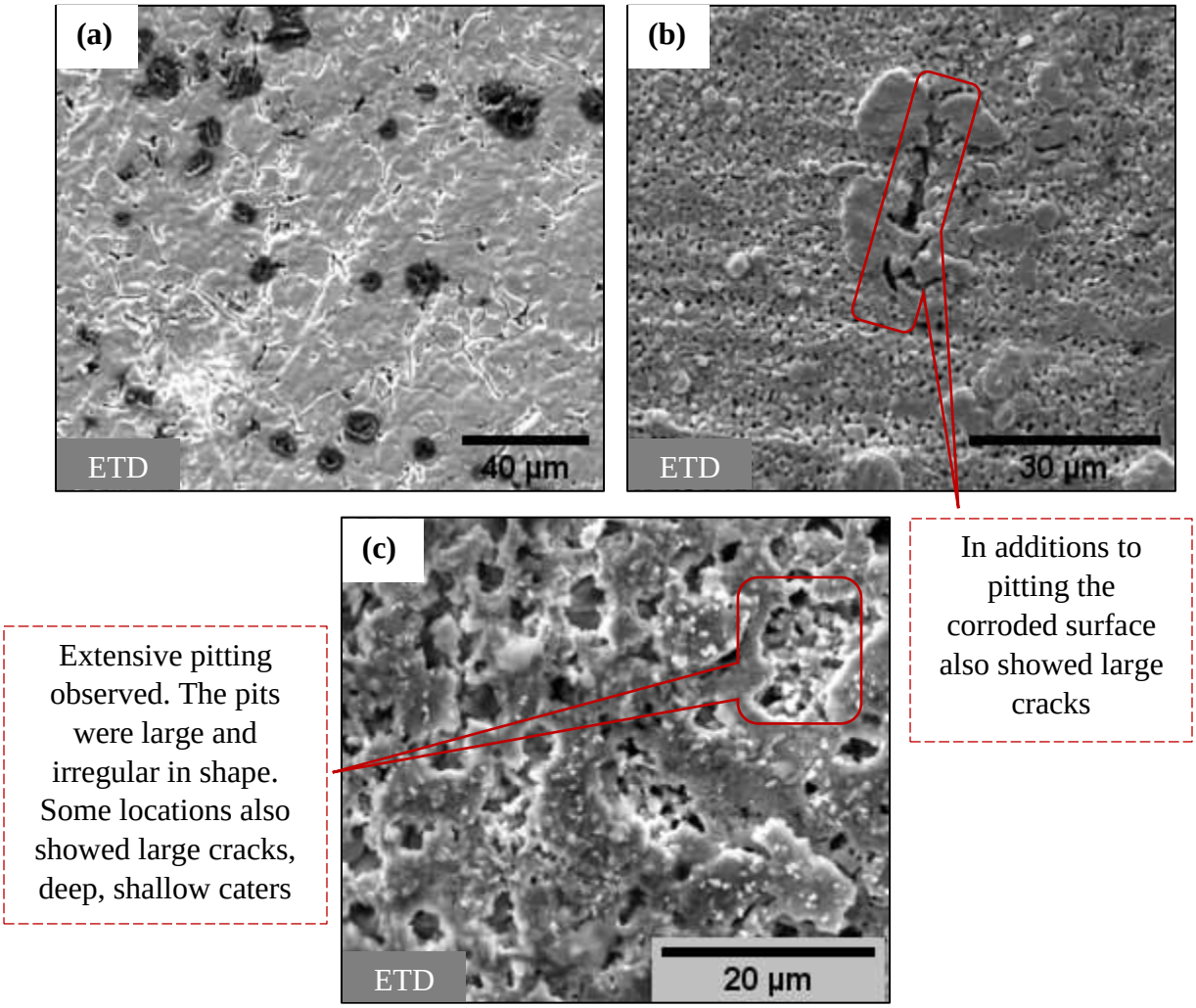

Figure 34. SEM-EDS surface characterization of **(a)** C276, **(b)** H230, and **(c)** IN718 alloys after exposure to molten KCl-$MgCl_2$-NaCl salt at 800 ºC for 100 hours, ICL salt purified with Mg.

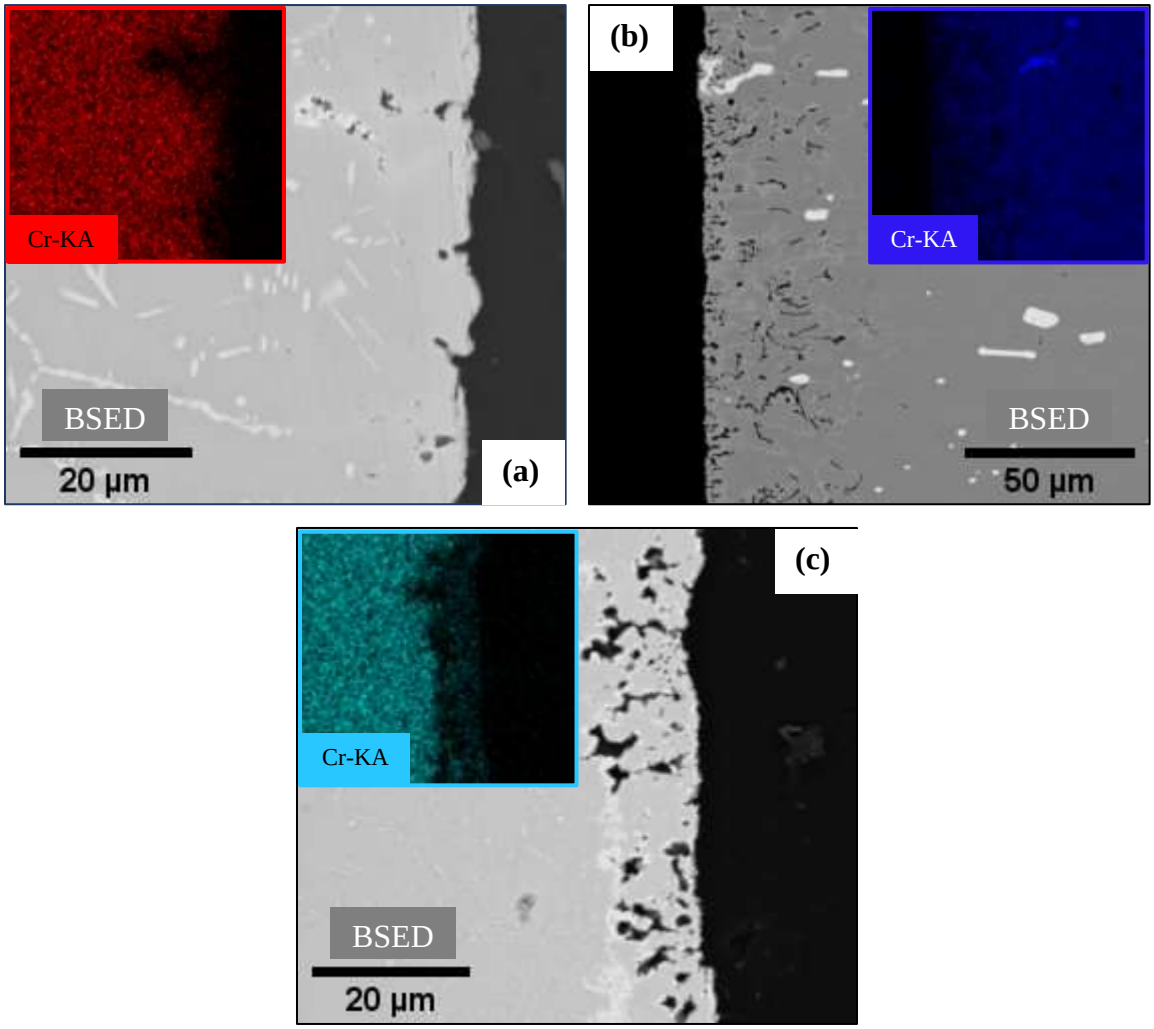

Figure 35. SEM-EDS cross-sectional characterization of **(a)** C276, **(b)** H230, and **(c)** IN718 alloys after exposure to molten KCl-$MgCl_2$-NaCl salt at 800 ºC for 100 hours, ICL salt purified with Mg.

The corroded surface of nickel-based alloys showed mild to severely pitting, while the cross-section showed a near-uniform porous corrosion layer. The pits were irregular in shape and size, and non-uniformly distributed across the surface. At various locations on the surface of H230 and IN718 alloys, cracks, and deep and shallow caters/pits/cavities were observed indicating break-down or disintegration of alloy structure. The corrosion layer showed chromium depletion and nickel enrichment in the region near the interface. The degradation depth was comparatively significant in IN718 and H230 alloys.

4.3.2 Ferrous-Based Alloys

Figure 36 and **Figure 37** show the SEM-EDS surface and cross-sectional characterization of the corroded ferrous-based alloys.

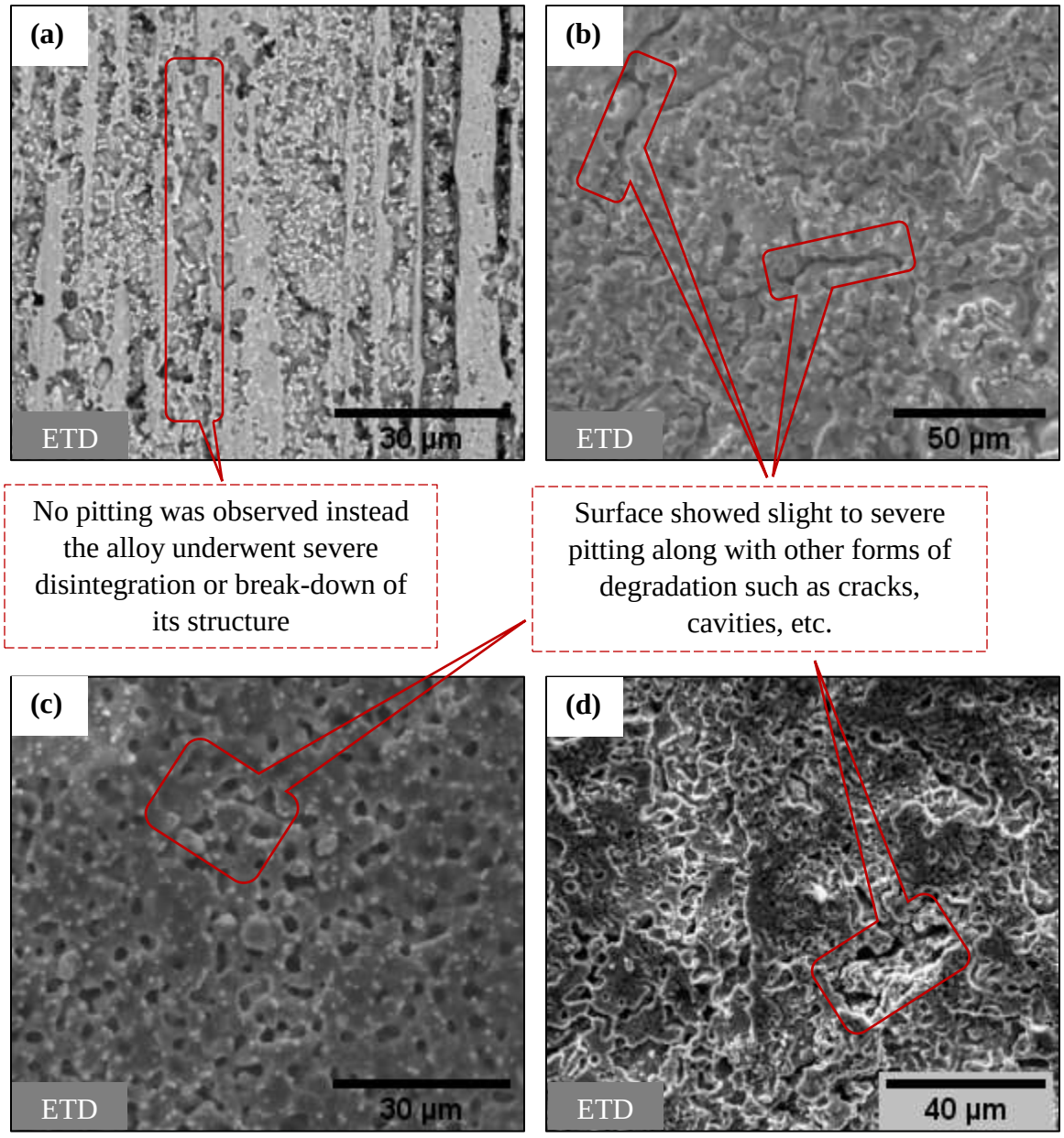

Figure 36. SEM-EDS surface characterization of **(a)** SS316L, **(b)** 709-4B2, **(c)** 709-RBB, and **(d)** 709-RBB* alloys after exposure to molten KCl-$MgCl_2$-NaCl salt at 800 ºC for 100 hours, ICL salt purified with Mg.

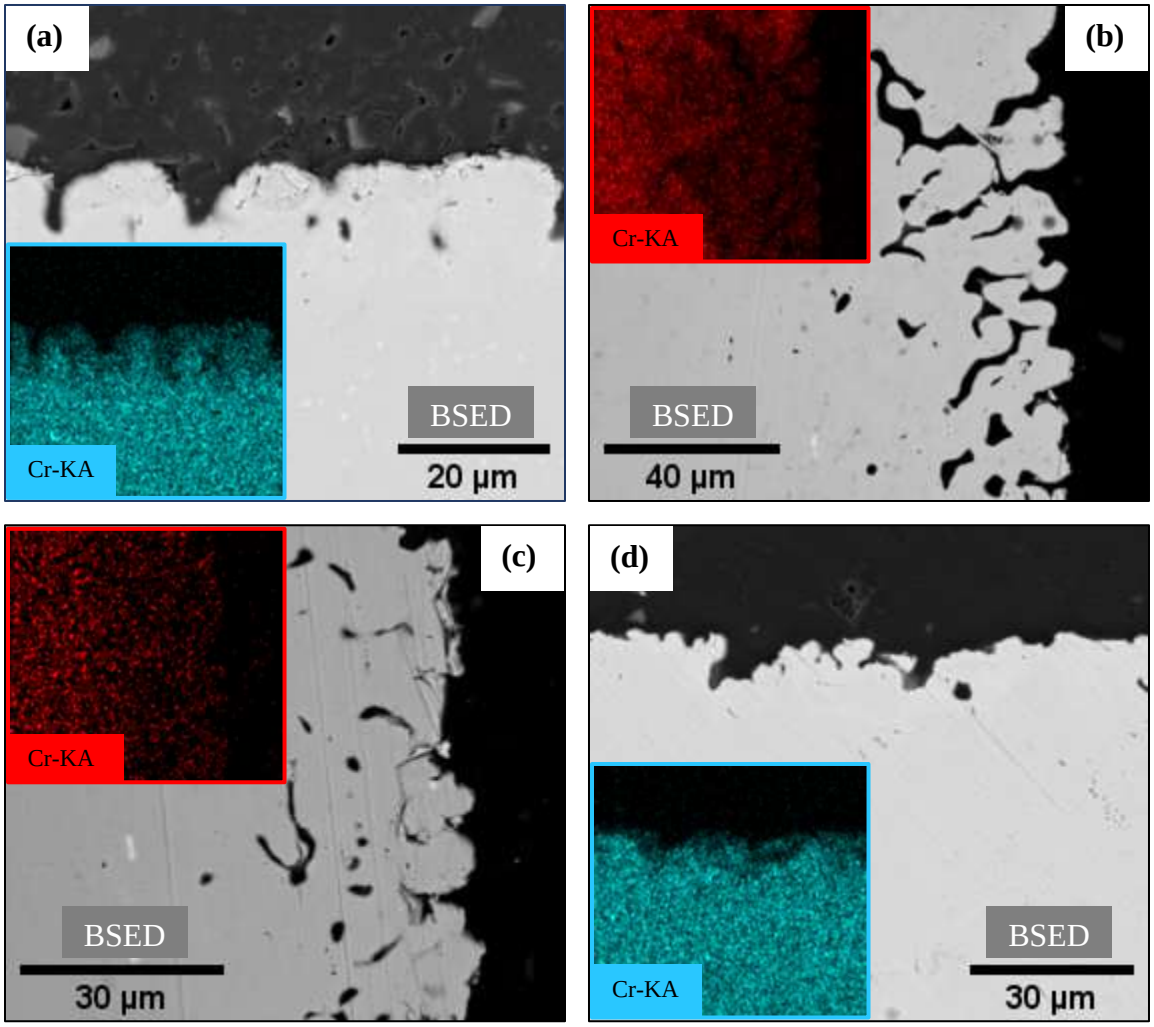

Figure 37. SEM-EDS cross-sectional characterization of stainless steel **(a)** 316L, **(b)** 709-4B2, **(c)** 709-RBB, and **(d)** 709-RBB* alloys after exposure to molten KCl-$MgCl_2$-NaCl salt at 800 ºC for 100 hours, ICL salt purified with Mg.

The corrosion behavior in ferrous-based alloys was quite similar across the surface and throughout the cross-section. For some alloys, there was a total break-down of the corrosion layer possibly because of high iron and chromium content, and its distribution in the alloy. This surface recession was small and not uniform as no significant change in dimensions was observed in the alloys after corrosion. **Figure 38** shows the average mass-loss per unit area (mg/cm^2) in nickel and ferrous-based alloys after exposure to molten KCl-$MgCl_2$-NaCl salt.

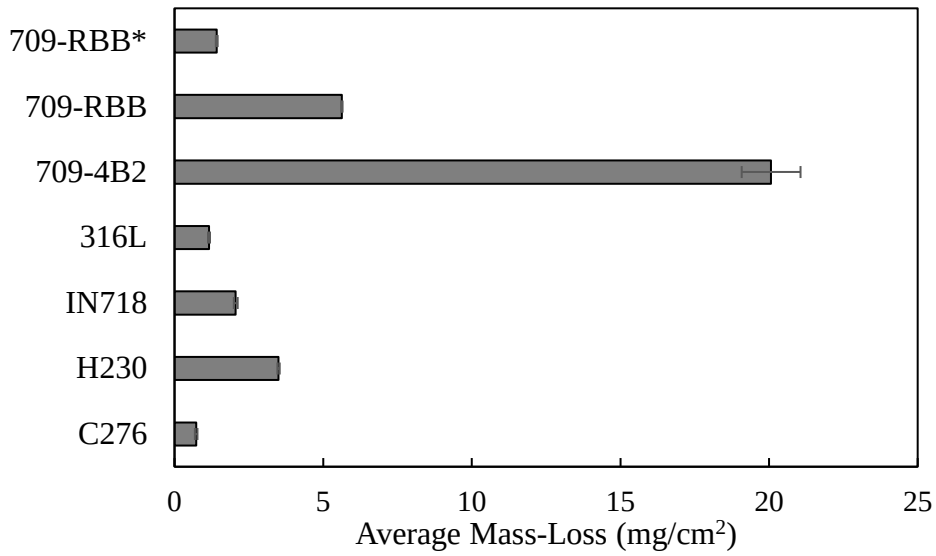

Figure 38. Average mass-loss (mg/cm^2) in nickel and ferrous-based alloys after exposure to molten KCl-$MgCl_2$-NaCl salt at 800 ºC for 100 hours, ICL salt purified with Mg.

It was found to be in the increasing order of C276 (0.73 mg/cm^2) < 316L (0.91 mg/cm^2) < 709-RBB* (1.42 mg/cm^2) < IN718 (2.06 mg/cm^2) < H230 (3.5 mg/cm^2) < 709-RBB (5.63 mg/cm^2) < 709-4B2 (20.07 mg/cm^2). The variations in the corrosion rates can be attributed to,

(1) The differences in the alloying element content, specifically active elements like chromium, iron, nickel, etc., and also the inert elements like tungsten and molybdenum, and their distribution in the alloy matrix. Apart from its inertness in molten chloride salts (i.e. based on the Gibbs free energy of formation which is either least negative or positive, their interactions in the molten chloride salt are not thermodynamically favorable, refer **Figure 39**), the larger atomic size of these elements blocks the open pores or gaps created by the depleting chromium, and prevents any further outward diffusion of chromium from the alloy and inward diffusion of salt and its corrosive impurities into the alloy. However, it must also be noted these low concentration elements are always non-uniformly distributed into alloy in the form enriched regions, thus severely restricting its usefulness in protecting the alloy against the molten salt attack.

(2) Manufacturing (i.e. refinement to reduce the impurities in the alloy), and heat-treatment processes which defines or re-defines the alloy microstructure (like grain-boundaries) even if they have the same composition. In the present study, Stainless Steel 316L and 709-RBB* showed better corrosion resistance than Inconel® 718, HAYNES® 230®, 709-RBB and 709-

4B2 alloys, which indicates that even with higher iron content, there were other factors like alloy manufacturing and refinement processes (to reduce the impurities in the alloy), and heat-treatment processes (to enhance the properties, relieve residual stresses, etc.) could assist in slowing down the corrosion process in these alloys.

(3) Corrosive impurities and their concentration in the molten chloride salt. The purity for different batches of salt used for the corrosion tests will always differ even after using the same purification treatment because of the highly hygroscopic nature of Mg-based salts, and the limitations with the analysis of the salt i.e. measurement techniques and insufficient knowledge on the properties (solubility data) of various impurities in the molten salt.

(4) The surface (exposed alloy surface) to volume (molten salt) ratio required to make the small scale test relevant to an industrial scale system, and also the saturation limit of various metal-oxide and metal-chloride compounds in the molten salt. Some of the corroded alloys also showed presence of magnesium and oxygen (possibly MgO) embedded into the open pores/gaps/voids.

(5) This indicates that molten salt continually infiltrates the alloy through these pores, and allowing the corrosion process will continue until the impurities in the molten salt are completely exhausted or the molten salt is saturated with the oxide and chloride compounds at the given conditions.

Some studies [116] have also shown other refractory elements like cobalt (Co) and tantalum (Ta) increase the corrosion resistance of nickel-based alloys, where the stable spinel formation of these refractory materials and the formation of poorly soluble chloride compounds provide good passivation against the molten chloride salt. It must be noted that none of the corroded alloys showed any metal-oxide or metal-chloride or other corrosion products formed or present or deposited on the surface. This confirms that any oxide layer formed during the corrosion and the self-passivating oxide layer (chromium oxide, Cr_2O_3) of stainless steel exhibits any stability in the molten chloride salt i.e. they are not self-sustaining, and do not form a protective barrier between the alloy interface and the interacting salt, and will eventually dissolve in the liquid salt.

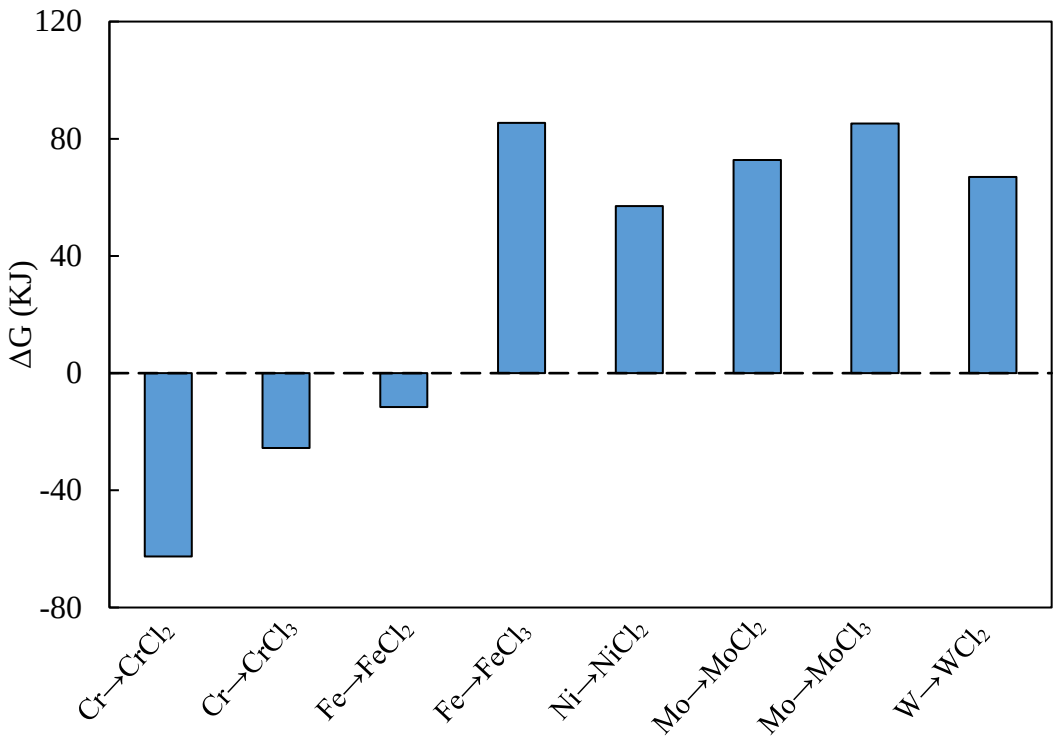

Figure 39. Gibbs free energy of formation for all possible interactions of active alloying elements with HCl (the common corrosive impurity in the molten chloride salt) at 800 °C [HSC Chemistry® 10 Software].

Some of the corroded specimens (refer **Figure 40**) also showed presence of Mg and O deposits (possibly MgO) embedded in the open pits or pores created by the depleting chromium. Unlike the molten chloride salt, the MgO cannot be removed because of its lower solubility in water. The formation of MgO could be due to one of the following possibilities,

(a) The purified salt was re-contaminated with oxygen, which reacts with any residual Mg pieces from the purification process to form MgO.

(b) MgO sludge formed during the purification process cannot be completely separated from the purified salt.

(c) Interaction of residual Mg pieces from the purification process with the alloying element (Cr) to form the thermodynamically unstable Mg-alloying element-oxide compound (Cr_2MgO_4). However, the SEM-EDS images do not show the presence of Cr thus indicating this cannot be a possibility for MgO presence on the alloy surface.

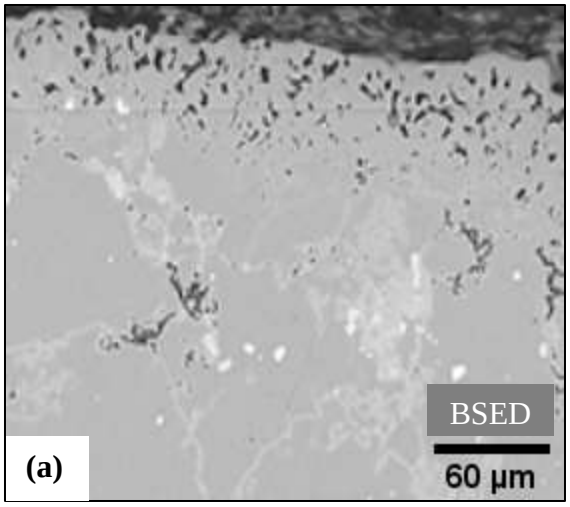
BSED
60 µm
(a)

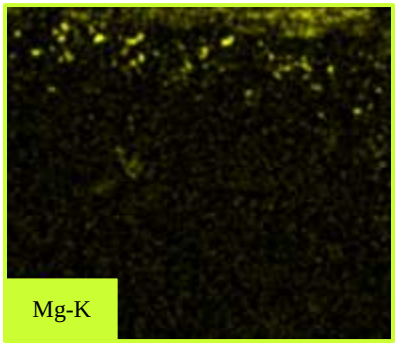
Mg-K

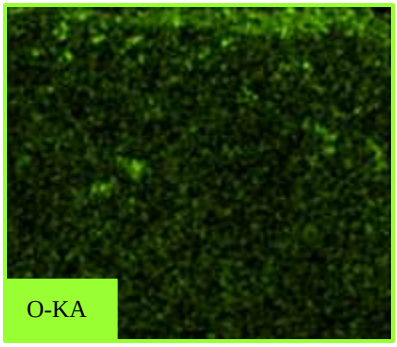
O-KA

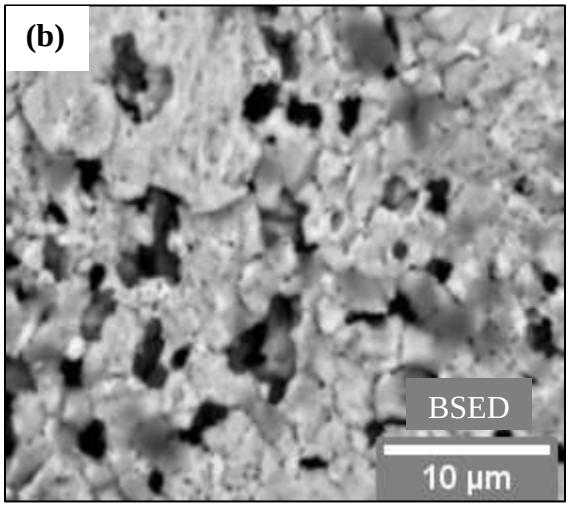
(b)
BSED
10 µm

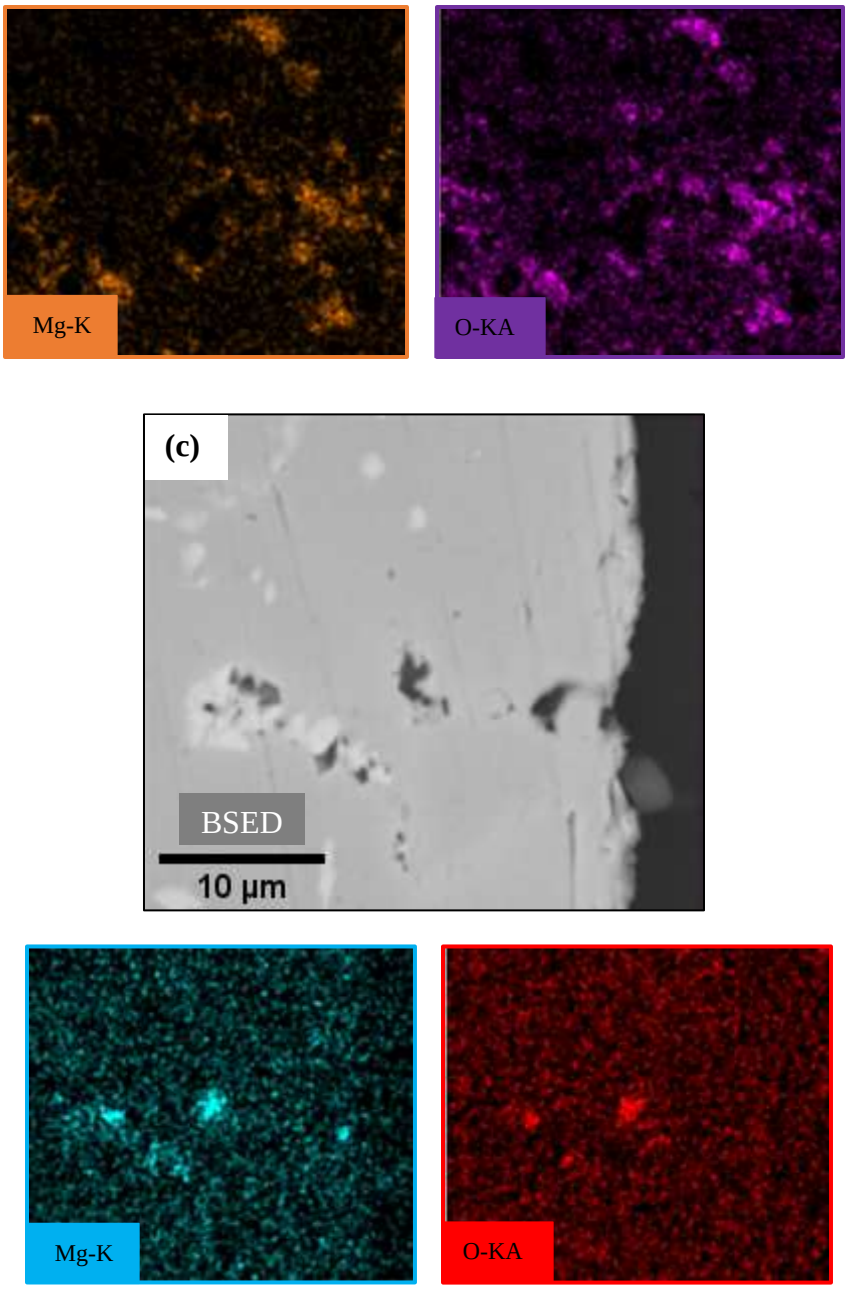

Figure 40. Mg and O deposition in nickel-based alloys, **(a)** H230, **(b)** IN718, and **(c)** C276 alloys after exposure to molten KCl-$MgCl_2$-NaCl salt at 800 °C for 100 hours.

This indicates that the liquid salt will continue to infiltrates into the alloy through its porous structure and attack the base material until either the salt solution is saturated with the respective oxide and chloride species or the salt has exhausted its impurity concentration. It must be noted that presence of these deposits on the alloy surface could affect the materials heat transfer properties, while its presence in the molten salt could interfere with the flow-path (viscous nature) and clog the circulating pumps.

4.4 Effects of Micorstructure on the Molten Salt Corrosion in Nickel and Ferrous-Based Alloys

4.4.1 Nickel-Based Alloys

Figure 41 shows the SEM-EDS grain-boundary characterization in H230 alloy after exposure to molten KCl-$MgCl_2$-NaCl salt (salt condition (d)).

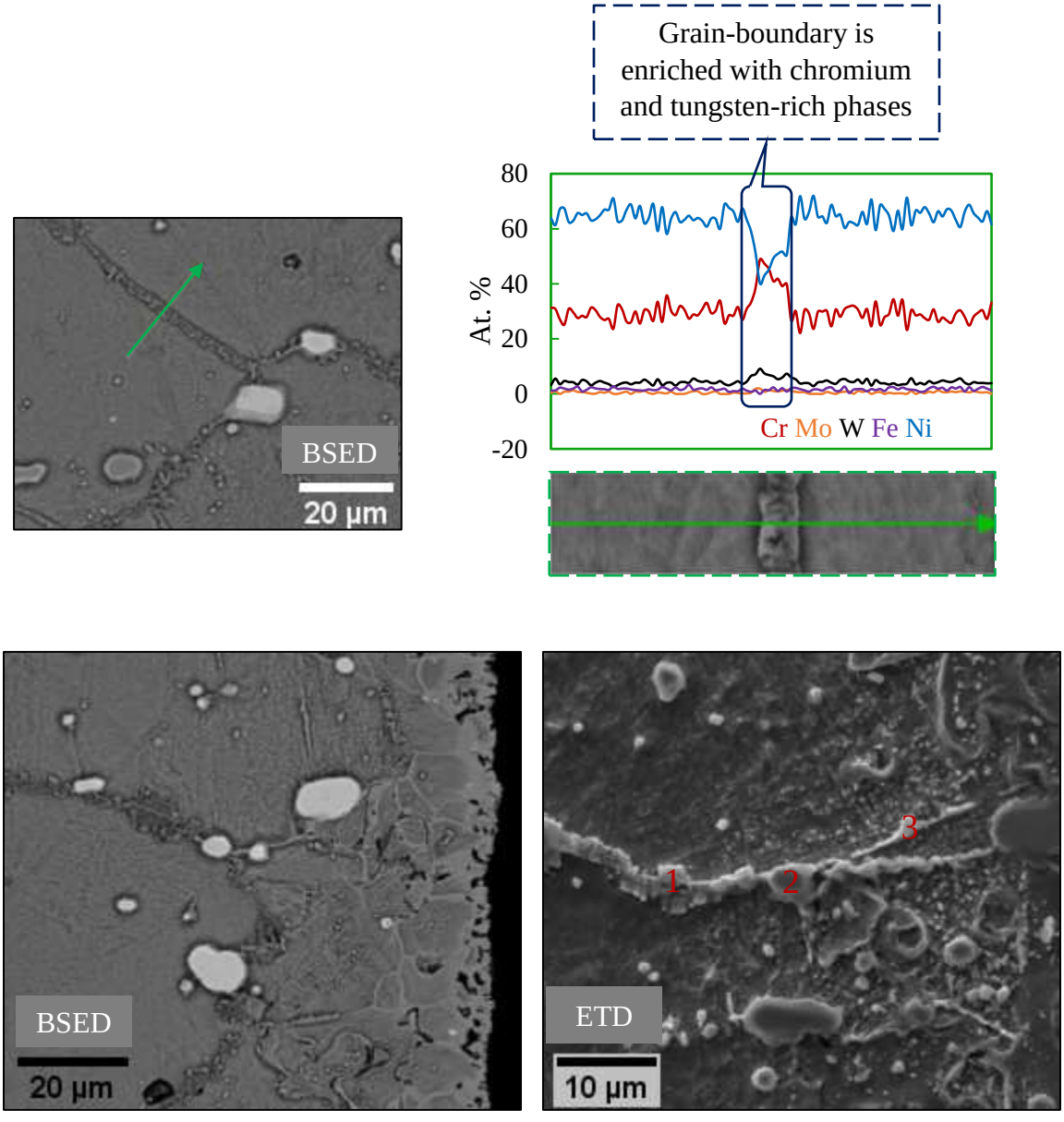

Point Location	Description	Elemental Composition (At. %)				
		Cr	Fe	Ni	Mo	W
1	On the grain-boundary in the alloy	38.03	2.20	51.02	2.70	6.05
2	At the triple point of the grain-boundary in the alloy	57.10	1.32	27.17	5.12	9.30
3	On the grain-boundary near the corrosion layer	51.93	2.50	32.42	5.16	7.99

Figure 41. SEM-EDS microstructural evaluation of H230 alloy cross-section after exposure to molten KCl-$MgCl_2$-NaCl salt at 800 ºC for 100 hours, ICL salt purified with Mg.

The EDS line-scan and point-scans (refer **Figure 41**) along the grain-boundaries showed chromium and tungsten-enrichment in the grain boundaries, and its depletion in the region close to the grain-boundaries. It was also observed that the grain-boundaries in the alloy were comparatively thicker than those close to the corrosion layer, and also had less chromium content in it. In the corrosion layer, the grain-boundaries could not be revealed because of change in the structure of the alloy because of composition (Cr and Fe depletion and Ni enrichment), and/or degradation or disintegration, and/or porosity.

4.4.2 Ferrous-Based Alloys

Figure 42, **Figure 43**, **Figure 44** and **Figure 45** show the SEM-EDS grain-boundary characterization in ferrous-based alloys such as austenitic Stainless Steel 316L, 709-4B2, 709-RBB and 709-RBB* alloys, after exposure to molten KCl-$MgCl_2$-NaCl salt (salt condition (d)).

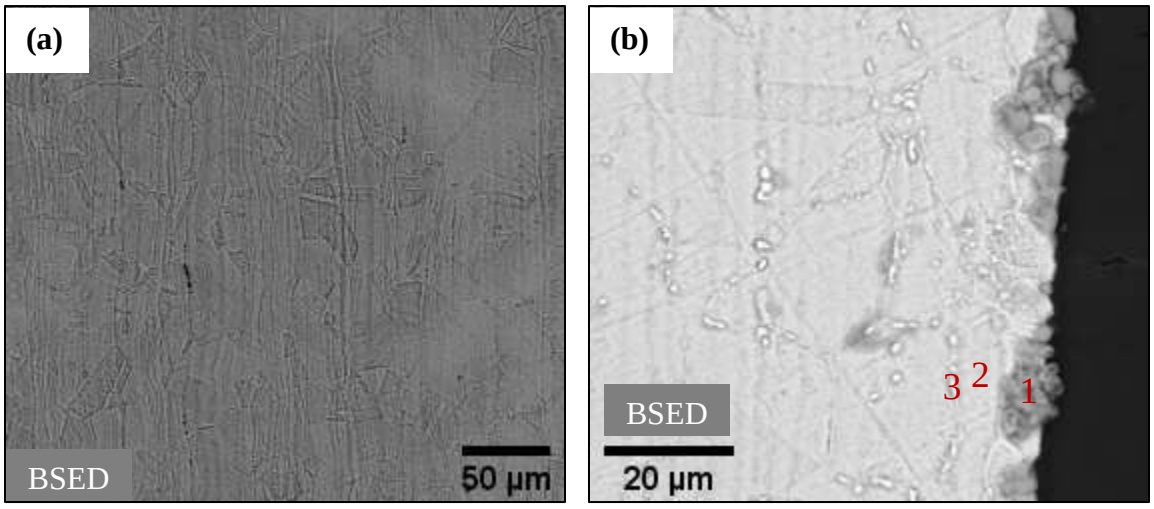

Point Location	Description	Elemental Composition (At. %)					
		O	Cl	Cr	Fe	Ni	Mo
1	On the oxide formed on the corrosion layer	70.98	2.19	0.80	22.05	3.79	0.18
2	On the alloy near the grain-boundary	0.90	0.08	17.31	71.50	8.95	1.25
3	On the grain-boundary	6.17	0.47	42.25	42.40	5.23	3.47

Figure 42. SEM-EDS microstructural evaluation of stainless steel 316L alloy cross-section **(a)** before, and **(b)** after exposure to molten KCl-$MgCl_2$-NaCl salt at 800 ºC for 100 hours, ICL salt purified with Mg.

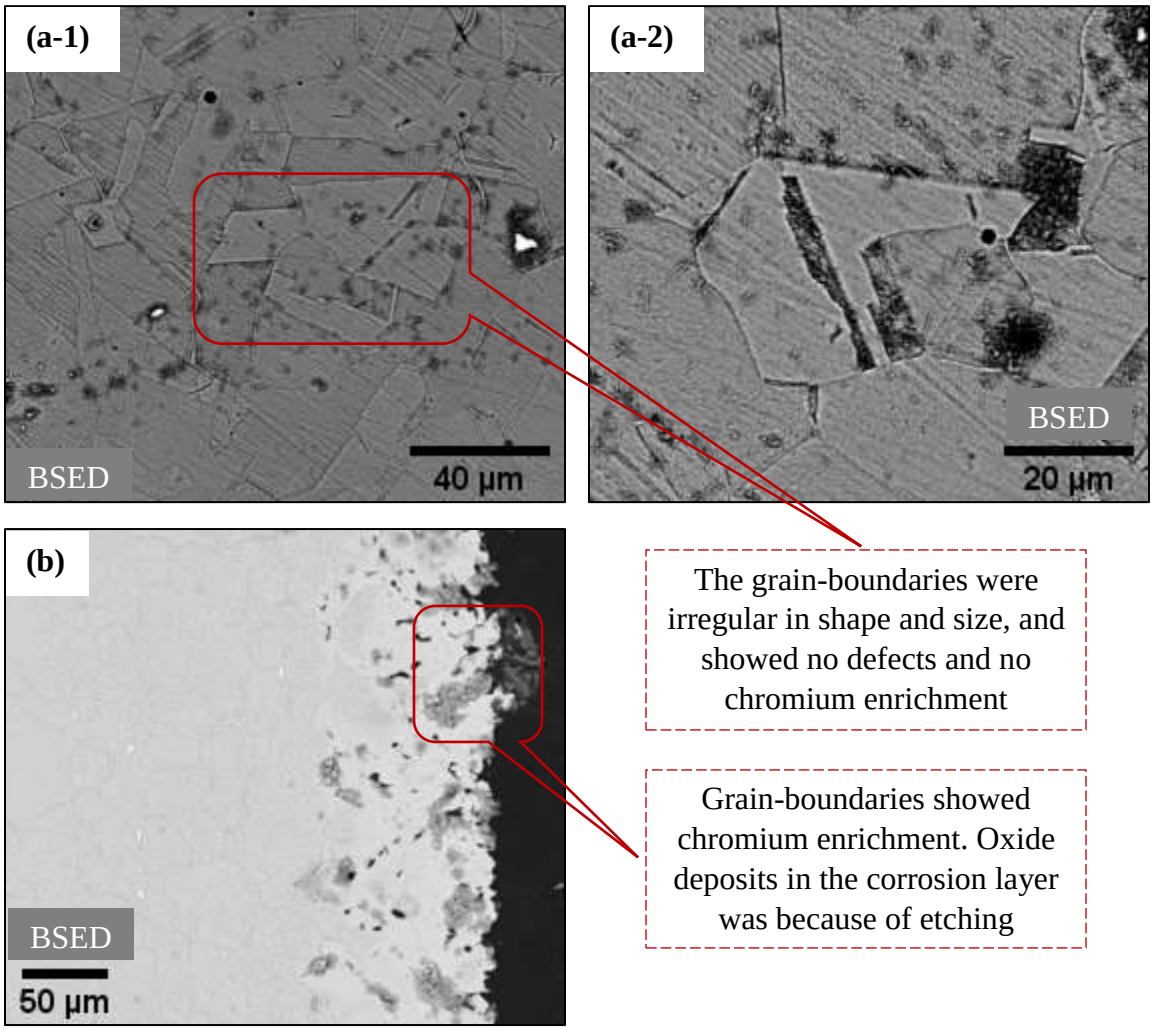

Figure 43. SEM-EDS microstructural evaluation of stainless steel 709-4B2 alloy cross-section **(a-1)**, **(a-2)** before, and **(b)** after exposure to molten KCl-$MgCl_2$-NaCl salt at 800 ºC for 100 hours, ICL salt purified with Mg.

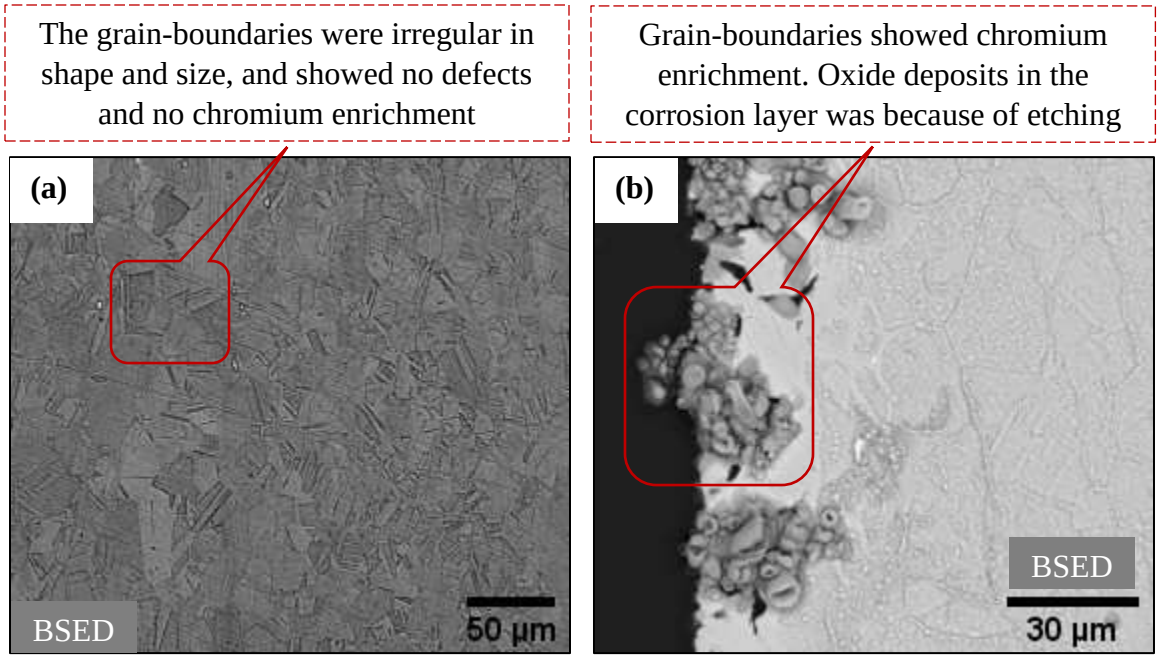

Figure 44. SEM-EDS microstructural evaluation of stainless steel 709-RBB alloy cross-section **(a)** before, and **(b)** after exposure to molten KCl-$MgCl_2$-NaCl salt at 800 ºC for 100 hours, ICL salt purified with Mg.

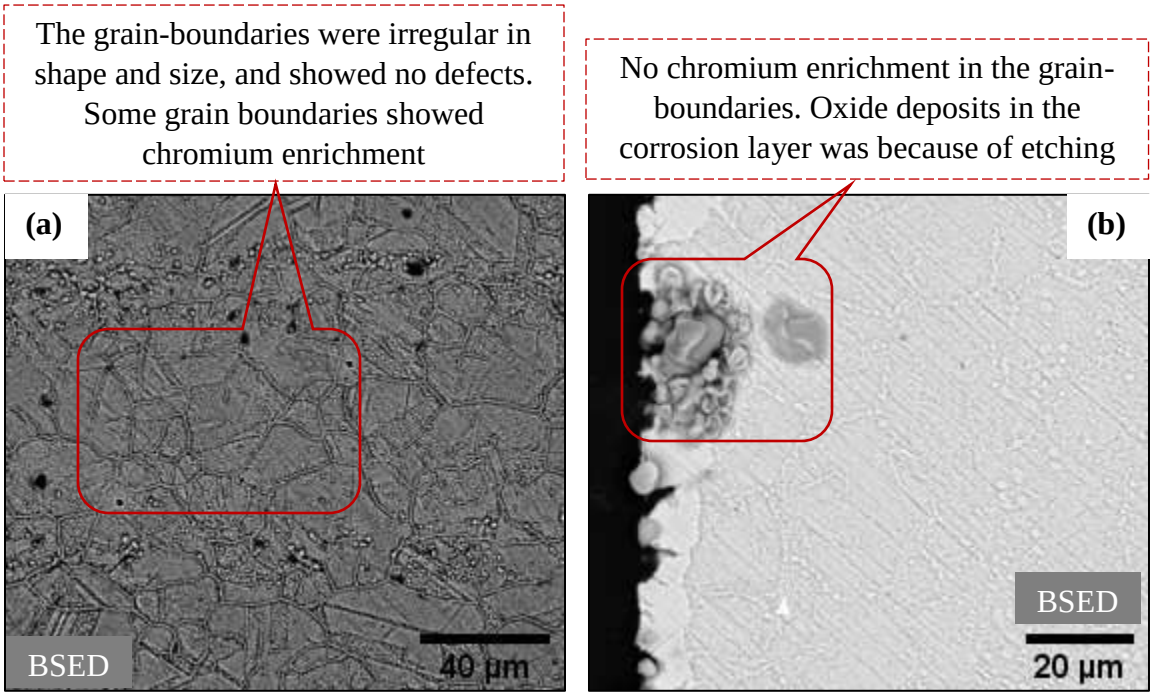

Figure 45. SEM-EDS microstructural evaluation of stainless steel 709-RBB* alloy cross-section **(a)** before, and **(b)** after exposure to molten KCl-$MgCl_2$-NaCl salt at 800 ºC for 100 hours, ICL salt purified with Mg.

The grain-boundaries of the raw specimens (i.e. before exposure to molten chloride salt) were of irregular shape and size, and showed no defects and chromium enrichment except for alloy 709 RBB*, where some grain-boundaries showed increased concentration of chromium. After exposure to molten chloride salt at 800 °C for 100 hours, grain-boundaries of all alloys showed increased concentration of chromium except for alloy 709 RBB*. The cross-section of the corroded alloys also showed presence of metal-oxides (mostly associated with iron and nickel) deposits in the corrosion layer, which were formed during the etching process due to interaction with the etchant. This can also be confirmed from SEM cross-sectional images of the corroded alloys (refer **Figure 37**) which did not show any presence of oxide layer or scales or deposits on the exposed surface.

Here also, in the corrosion layer, the grain-boundaries could not be revealed because of change in the structure of the alloy because of composition (Cr and Fe depletion, and Ni enrichment), and/or degradation or disintegration and/or porosity. However, it can still be predicted from the nature of the attack (i.e. a near uniform porous corrosion layer indicating that the chromium depletion (pathway) is not restricted to the grain-boundaries) that the corrosion in both nickel and ferrous-based alloy was not only driven by the intergranular corrosion but also because of chromium content and its distribution in the alloy.

Galetz, M.C., et. al. [114] reported the formation of Cr, Mo and W-rich carbides, which influenced the corrosion of nickel-based alloys in molten chloride salts. Unlike Mo and W-rich carbides, the Cr-rich carbides do not exhibit inertness towards the molten chloride salt. The enrichment of chromium along the grain-boundaries is due to sensitization, where during the heat-treatment processes, chromium carbides are formed which diffuses towards the grain-boundaries. The high concentration of chromium along the grain-boundaries makes it the most preferable site for the onset of corrosion in the molten chloride salt. Based on the analyses, carbide-enriched regions were only observed in the nickel-based alloy, HAYNES® 230® alloy. Another influencing factor [65] is the diffusion distance of the alloying elements like Cr in Ni which is dependent on the immersion time and the temperature dependent lattice and grain boundary diffusion coefficients. At higher temperatures, the grain boundary diffusion coefficient is greater than the lattice diffusion coefficient [65]. This also causes the chromium to diffuse outwards through the grain-boundaries, and ultimately dissolve in the molten chloride salt, thus resulting in intergranular corrosion. Studies

have also shown that the corrosion rate in alloys is dependent on the grain-sizers, where larger grain-size reduces the grain-boundary area thereby reducing the attack path and making the alloy more resistant to corrosion.

4.5 Corrosion Behavior of Boronized Nickel and Ferrous-Based Alloys in Molten Salts

It is quite evident from the corrosion studies, it is not plausible to complete remove the impurities in the salt even after employing extensive purification processes. Furthermore, irrespective of the alloy type (composition, microstructure, etc.), the corrosion in molten chloride salt is inevitable i.e. it can be slowed down but cannot be avoided. To overcome this issue, selected nickel and ferrous-based alloys such as C276, IN718 and SS316L which exhibited good corrosion resistance were boronized and studied for its (boride layer) corrosion characteristics in the molten chloride salt.

4.5.1 Nickel-Based Alloys

Figure 46 and **Figure 47** show the surface and cross-sectional morphology of the boride layer in the nickel-based alloy, IN718 before and after the corrosion test. The borided specimens exhibited high surface roughness (an uneven surface), and showed presence non-uniformly distributed silicide structures (nickel-silicide). The formation of silicide layer can be attributed to the presence of silicon (silicon carbide) as a diluent in the boronizing agent. The boride layer was solid, homogenous and showed no cracks, gaps or voids indicating strong adhesion with the substrate.

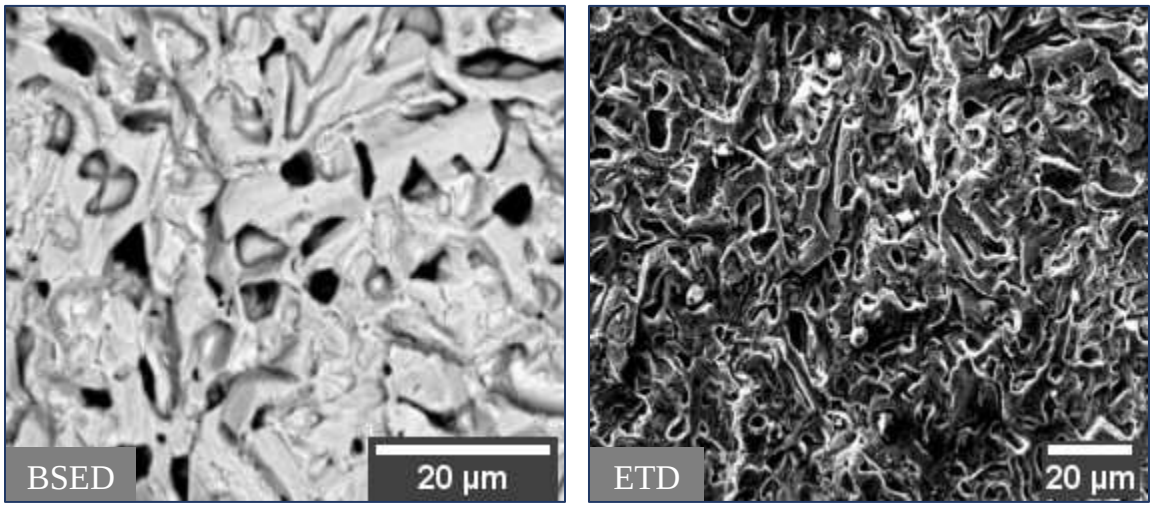

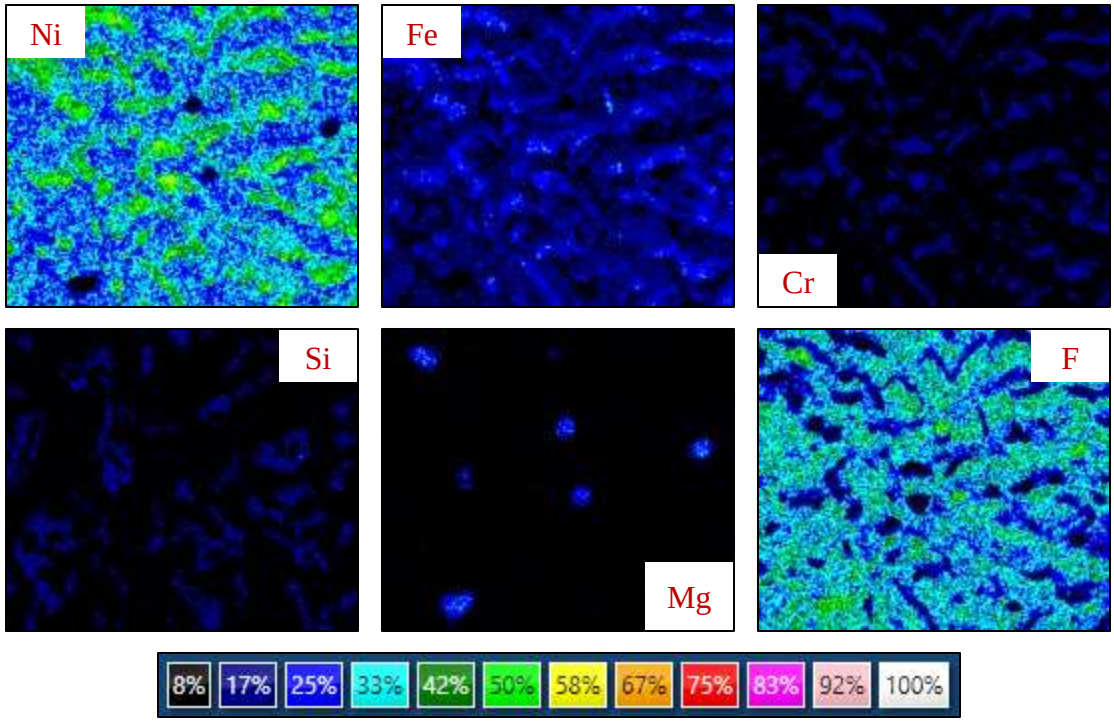

Figure 46. SEM-EDS surface characterization of the boride layer in IN718 alloy.

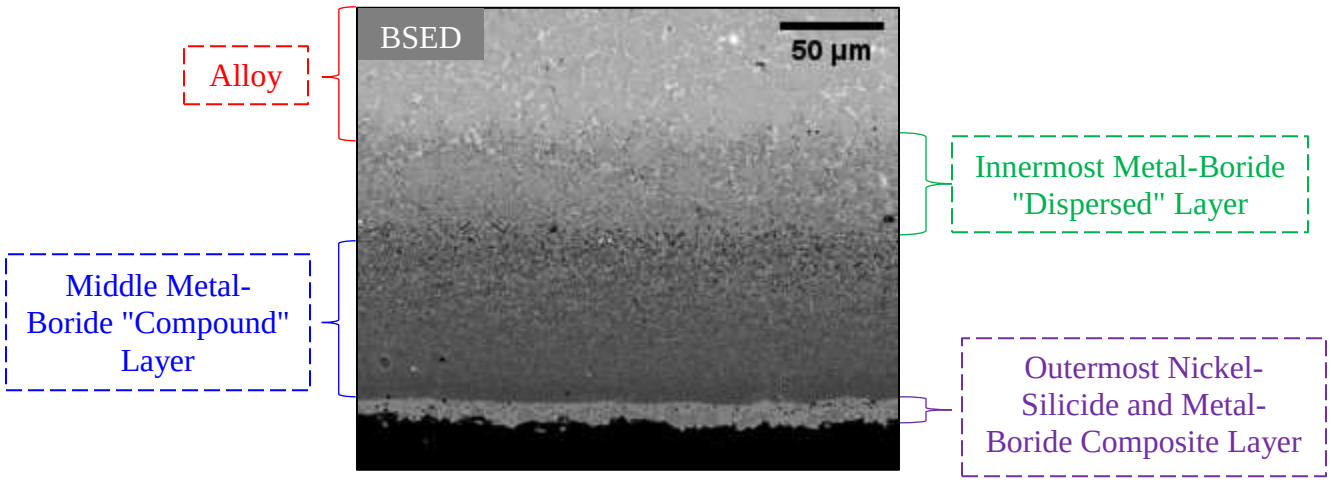

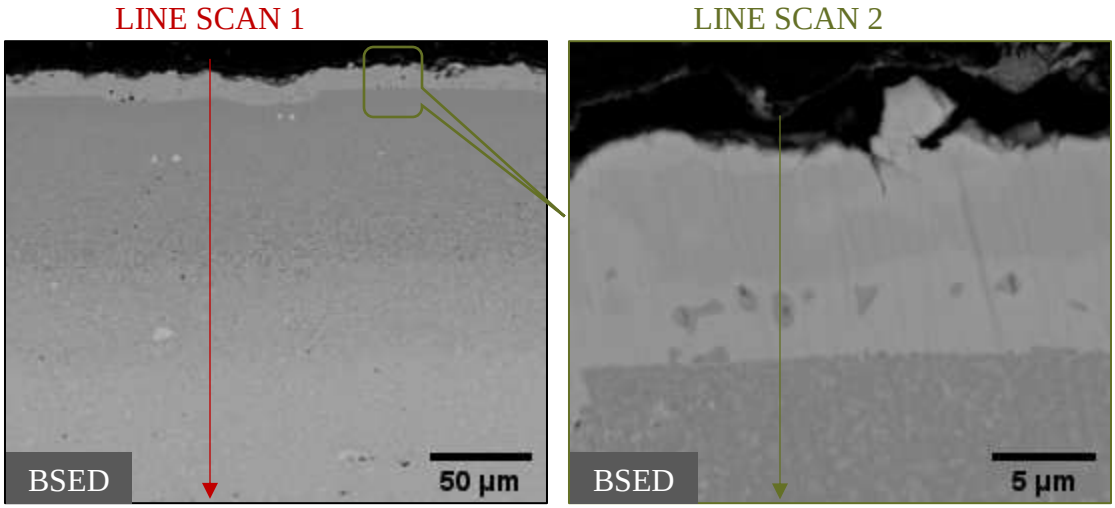
LINE SCAN 1
LINE SCAN 2
BSED
50 µm
BSED
5 µm

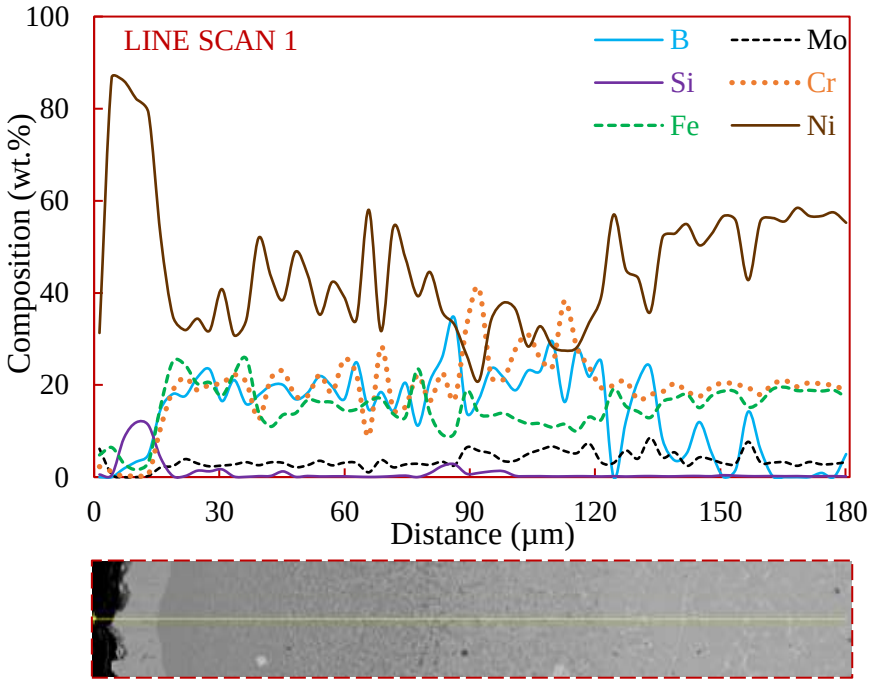
LINE SCAN 1
B
Mo
Si
Cr
Fe
Ni
Composition (wt.%)
100
80
60
40
20
0
0
30
60
90
120
150
180
Distance (µm)

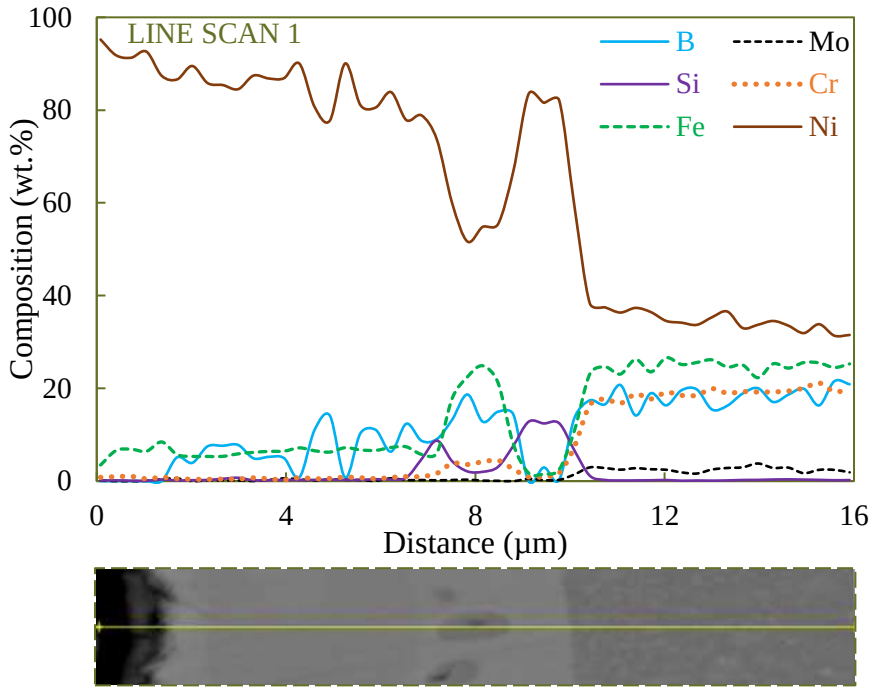

Figure 47. SEM-EDS cross-sectional characterization of the boride layer in IN718 alloy.

The cross-sectional analysis showed the boride layer was comprised of three layers, an outermost solid layer, the middle solid "compound" layer, and an inner solid "dispersed" or "diffusion" layer. No "grain boundary precipitation zone" was seen in either of these alloys. **Figure 48** and **Figure 49** show the XRD analysis on the surface of the borided IN718 alloys before and after the corrosion test, and the borided C276 alloy only after the corrosion test.

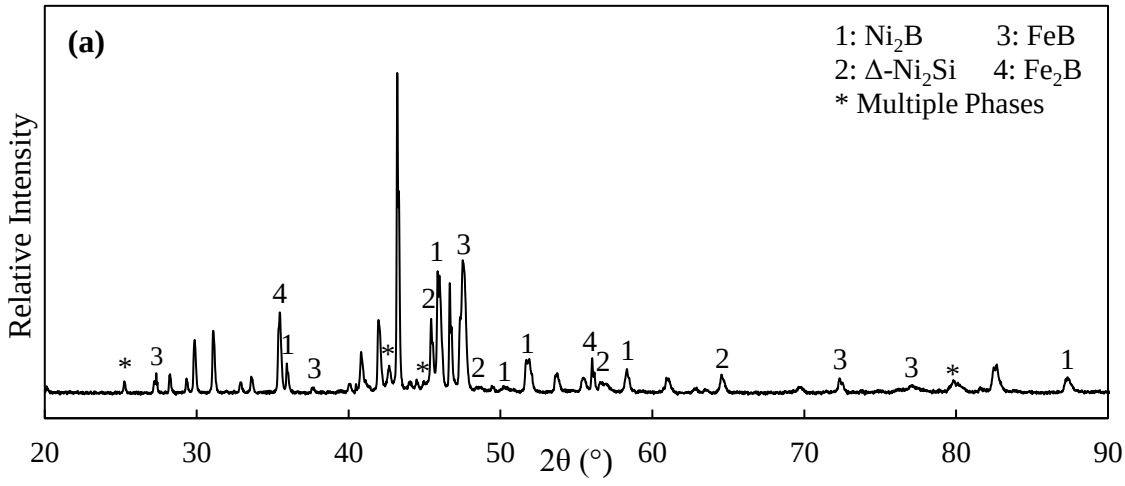

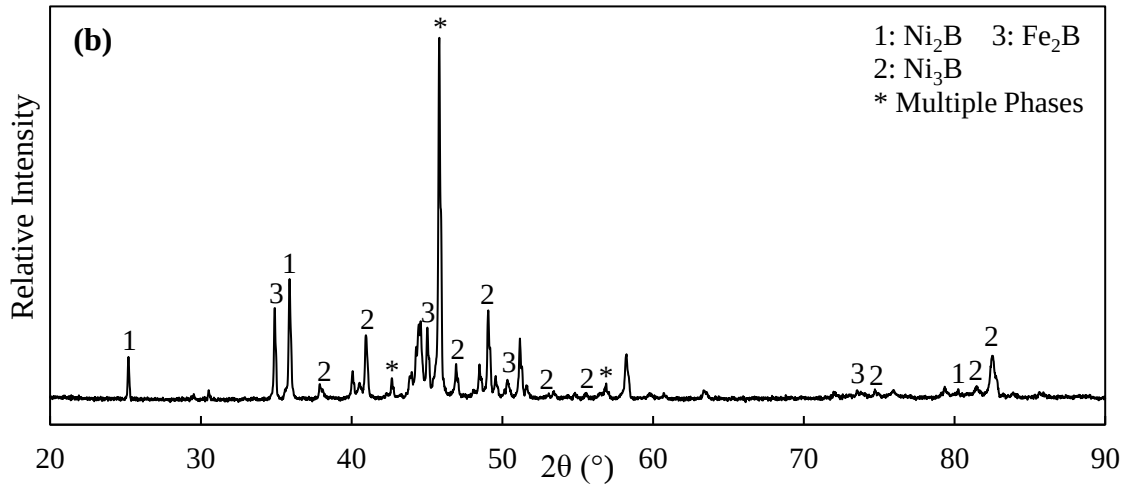

Figure 48. XRD analysis of the outer boride layer in IN718 alloy **(a)** before, and **(b)** after exposure to molten KCl-$MgCl_2$-NaCl salt at 800 ºC for 100 hours.

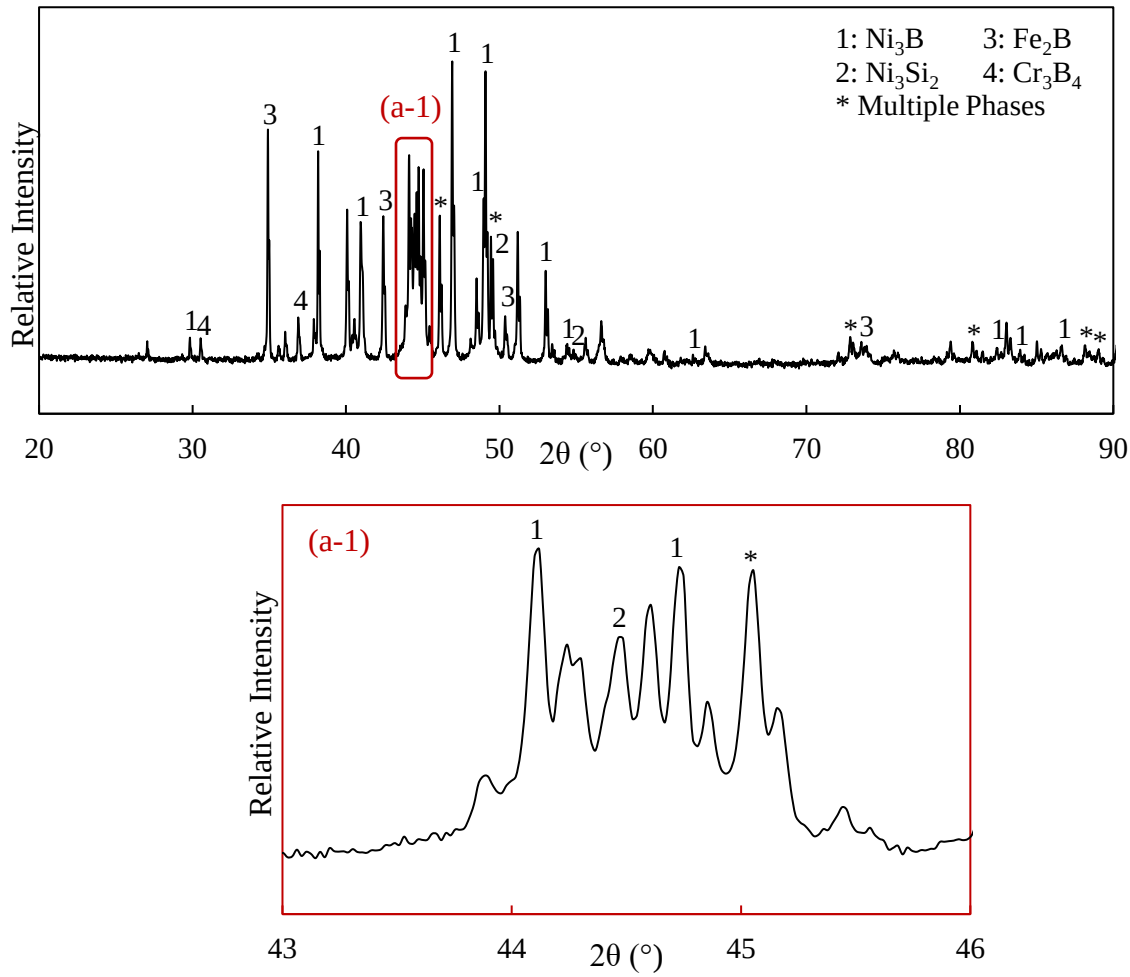

Figure 49. XRD analysis of the outer boride layer in C276 alloy after exposure to molten KCl-$MgCl_2$-NaCl salt at 800 ºC for 100 hours.

The preference for phase formation in the boride layer depends on the Gibbs free energy of the binary and ternary intermetallic borides like chromium-boride (Cr-B), iron-boride (Fe-B), nickel-boride (Ni-B)….etc., Cr-Ni-B, Fe-Ni-B…etc. and usually follows the order of Cr, Fe, Ni [117, 118]. The growth of the intermediate phases also depends on the phase diagram of the metal-boron binary systems, where the phases which exhibit good stability at the diffusion annealing temperatures will form in the boride layer [119]. The SEM-EDS and XRD analyses of the boride layers showed,

For boronized IN718 alloy (refer **Figure 46**, **Figure 47** and **Figure 48**):

The outermost layer was mostly composed of Ni-B (Ni_2B) and Ni-Si (NiSi and Δ-Ni_2Si) phases, and low to very low concentrations of Fe-B (FeB) and Cr-B (Cr_5B_3) phases. The middle "compound" layer was also mostly composed of Ni-B phases, and lower concentrations of Fe-B and Cr-B phases. The "diffusion" zone was an intermixture of Ni-B, Fe-B and Cr-B phases. The surface of the boride layer also showed localized enrichment of magnesium (Mg) and fluorine (F), which was introduced from the boronizing agent during the boronization process.

For boronized C276:

Since, there were no borided C276 specimens (non-exposed) available for the analysis; and the analysis of the borided IN718 alloy showed no change in the composition and morphology of the boride layer after the corrosion test; and the borided C276 alloys also exhibited little to no mass-loss after exposure to molten chloride salt; the boride layer in C276 alloy was characterized from the alloy after the corrosion test. From **Figure 49**, **Figure 51b** and **Figure 52b**, it can be interpreted that the outermost layer was mostly composed of Ni-B (Ni_3B) and Ni-Si (Ni_3Si_2) phases, and low to very low concentrations of Fe-B (Fe_2B) and Cr-B (Cr_3B_4) phases. The middle solid "compound layer" was also mostly composed of Ni-B phases, and lower concentrations of Fe-B, Cr-B and Mo-B phases. The "diffusion" zone was an intermixture of Ni-B, Cr-B and Mo-B phases.

Figure 50 shows the average mass-loss per unit area (mg/cm^2) in the boronized and non-boronized nickel-based alloys after exposure to molten KCl-$MgCl_2$-NaCl salt.

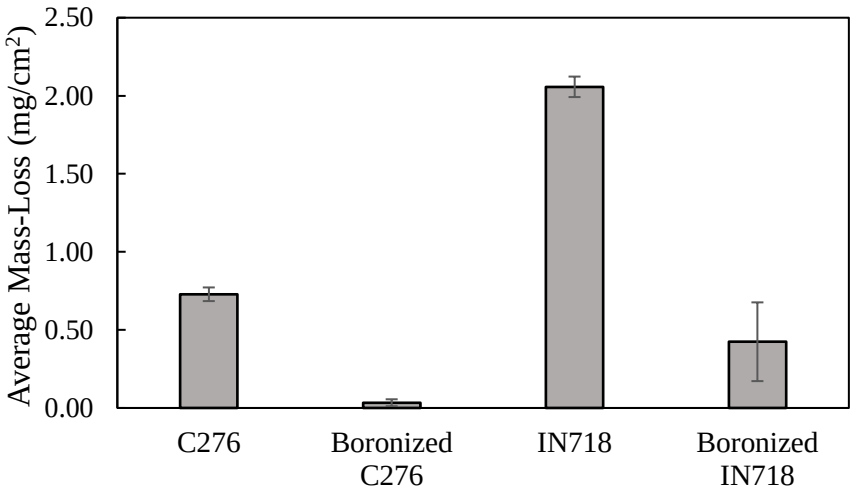

Figure 50. Average mass-loss (mg/cm^2) in the boronized and non-boronized nickel-based alloys after exposure to molten KCl-$MgCl_2$-NaCl salt at 800 ºC for 100 hours.

The average mass-loss was found to be in the increasing order of, boronized C276 (0.03 mg/cm^2) < boronized IN718 (0.42 mg/cm^2) < C276 (0.73 mg/cm^2) < IN718 (2.06 mg/cm^2). The borided nickel-based alloys exhibited better corrosion resistance against the molten chloride salt. **Figure 51** and **Figure 52** show the surface and cross-sectional characterization of the borided nickel-based alloys after the corrosion test.

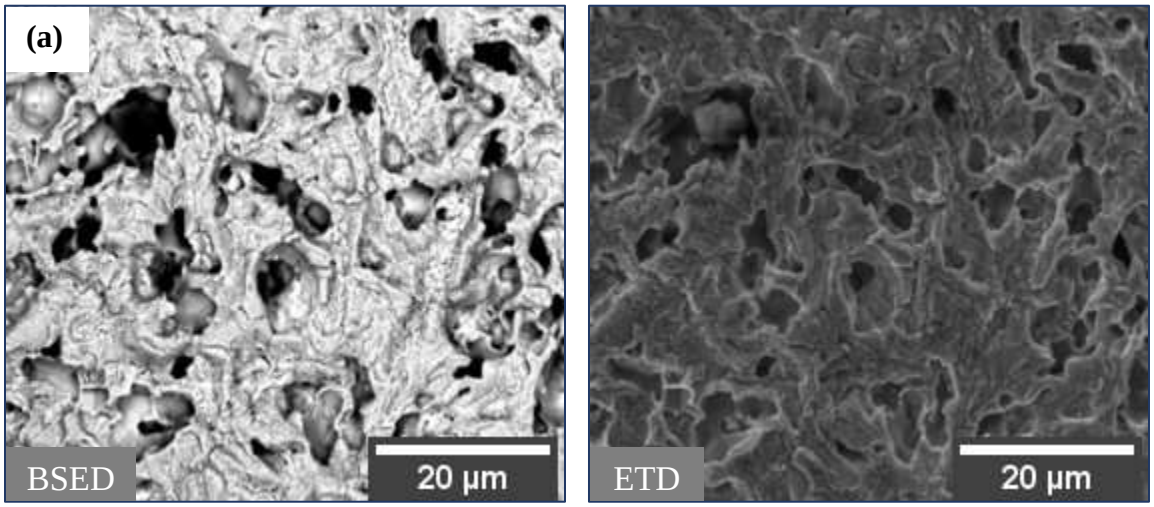

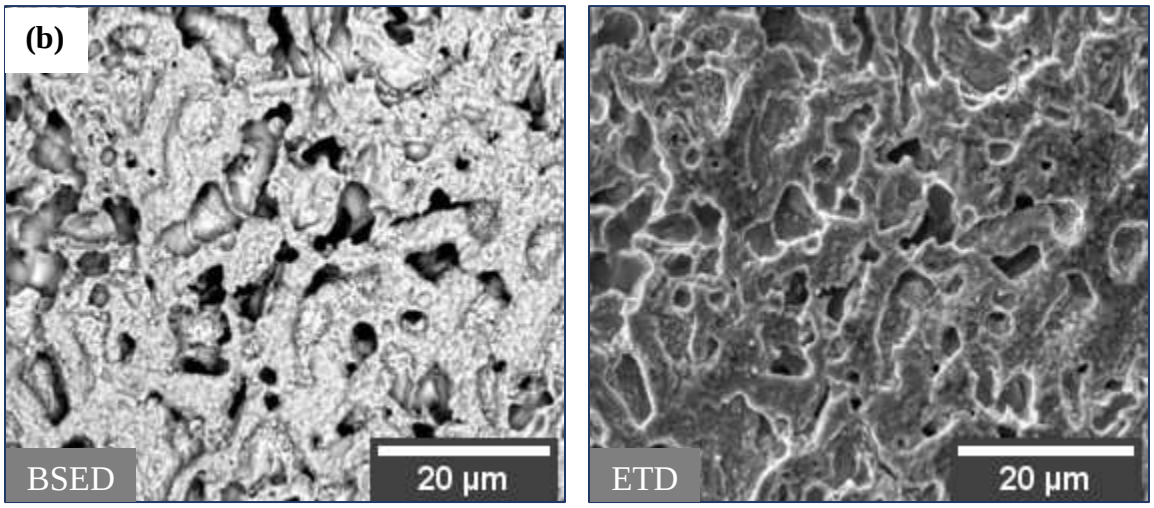

Figure 51. SEM-EDS surface characterization of corroded boronized **(a)** IN718, and **(b)** C276 alloys after exposure to molten KCl-$MgCl_2$-NaCl salt at 800 ºC for 100 hours

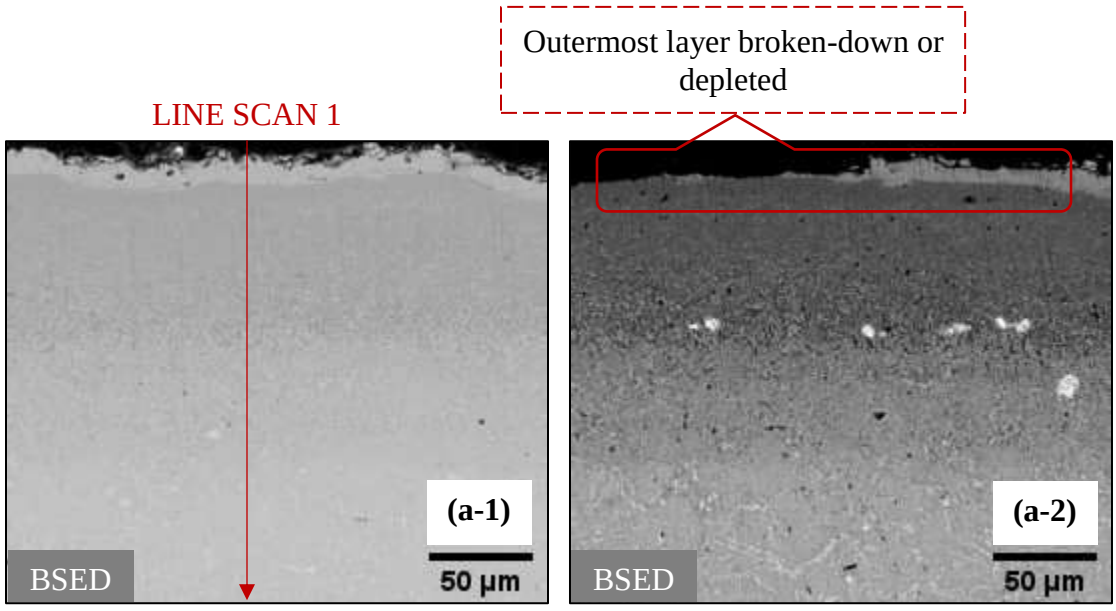

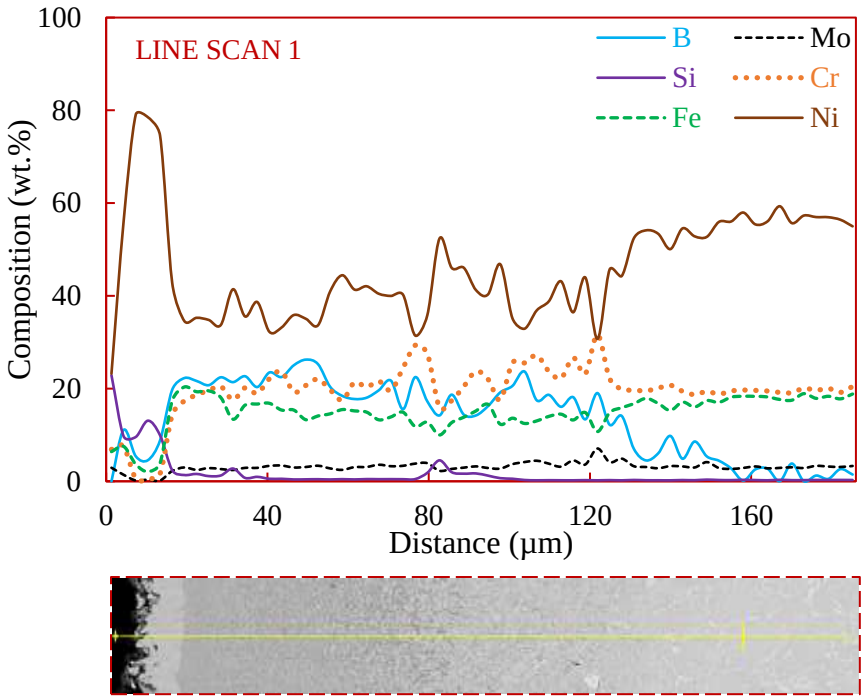

Figure 52a. SEM-EDS cross-sectional characterization of corroded boronized IN718 alloy after exposure to molten KCl-$MgCl_2$-NaCl salt at 800 ºC for 100 hours.

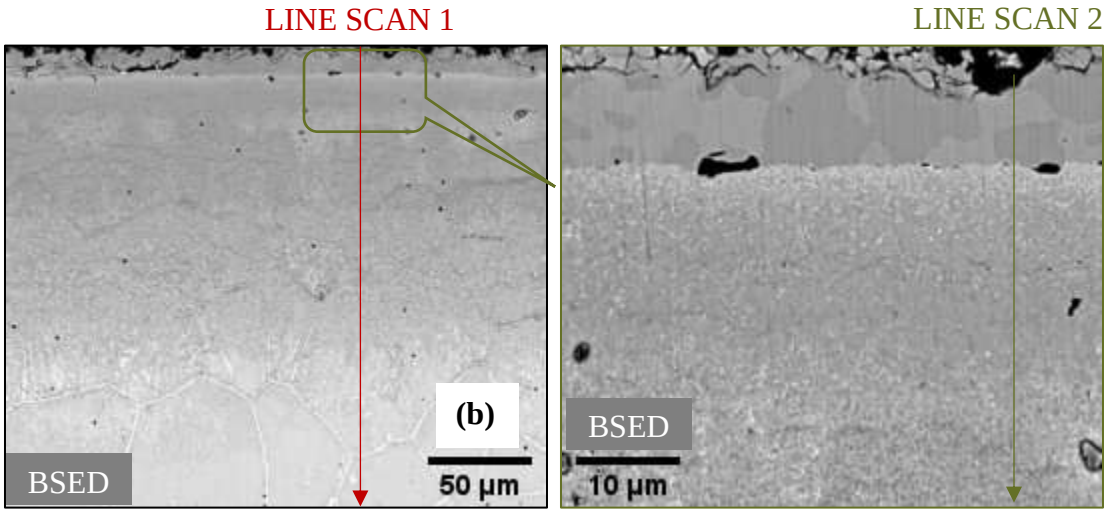

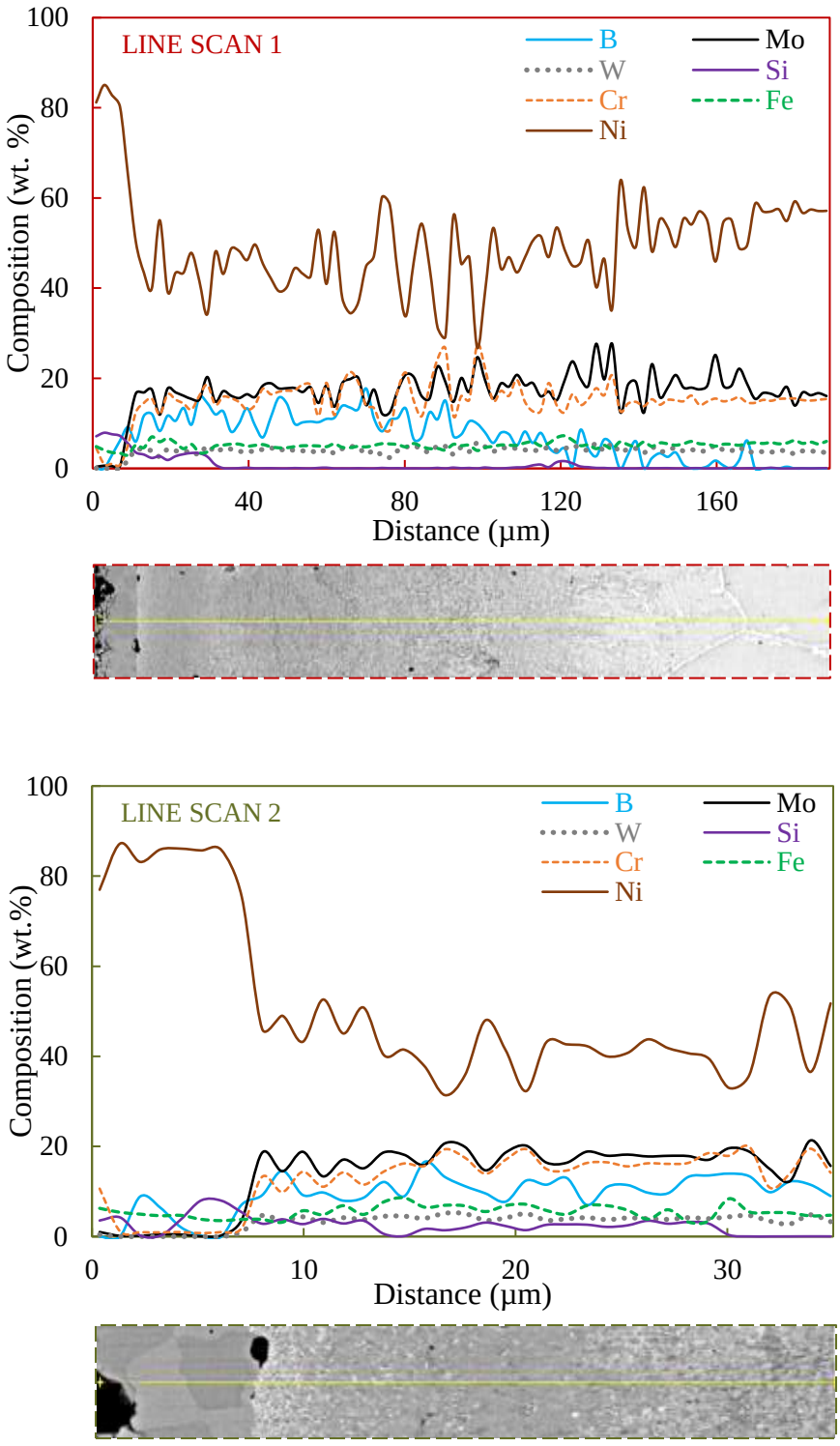

Figure 52b. SEM-EDS cross-sectional characterization of corroded boronized C276 alloy after exposure to molten KCl-$MgCl_2$-NaCl salt at 800 ºC for 100 hours.

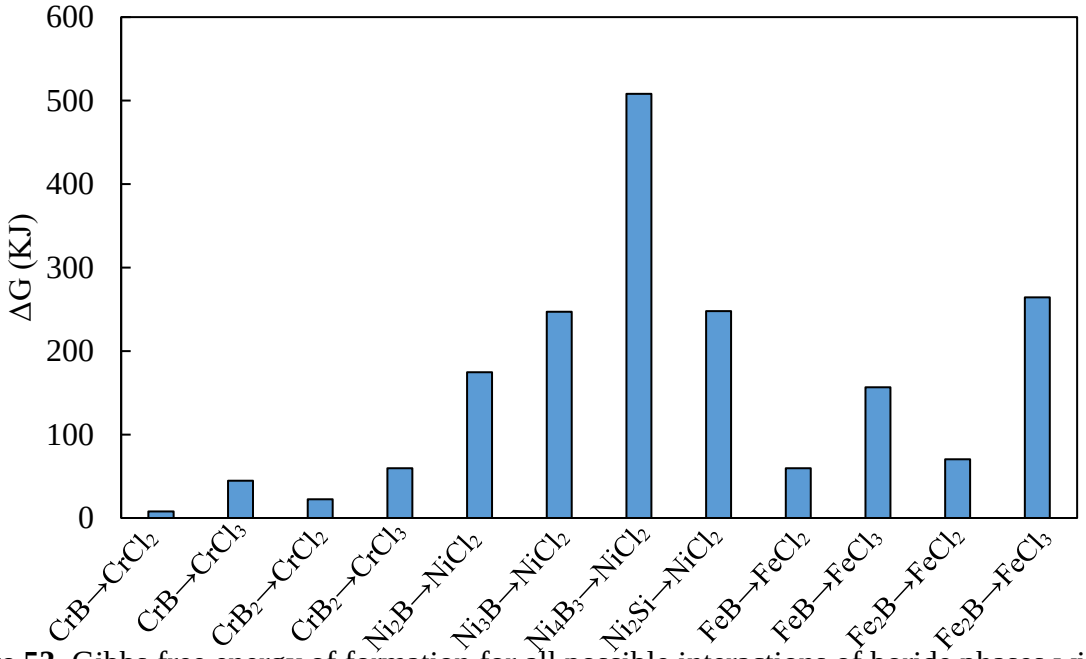

Figure 53. Gibbs free energy of formation for all possible interactions of boride phases with HCl at 800 ºC [HSC Chemistry® 10 Software].

The surface of the borided alloys after the corrosion test showed large voids or cavities caused due to break-down of the outermost layer. Targhi, V.T, et. al. [120] showed silicides by itself can enhance the corrosion resistance of alloys in molten salts. However, in the borided alloys, the outermost layer is non-homogenous, and is composed of both nickel-silicides and metal-borides (primarily nickel boride and low concentration of iron-boride and/or chromium boride), which are in the form of deposits non-uniformly distributed across the surface. The mass-loss in borided nickel-based alloys can be attributed to the break-down of these structures. This can be confirmed from the SEM cross-sectional images, where the outermost layer is still attached to substrate at few locations, while at other locations the layer is peeled or spalled or cracked from the substrate. Furthermore, unlike the intermetallic boride layer, the silicide structures exhibit poor physical properties (i.e. it is brittle, this is observed when preparing (i.e. cutting and polishing) the non-corroded specimens for SEM analysis, where the layer breaks easily under mechanical induced stresses), and has a different thermal expansion coefficient with the metal-borides causing it to crack, peel or spall due to thermal mismatch.

Even among the borided alloys, mass-loss in IN718 was higher than C276 possibly due to high iron content, which can form the undesirable dual iron-boride phases (i.e. FeB-FeB_2) during the

boronization process. The dual phases are unstable and can also crack, peel or spall due to thermal mismatch owing to the differences in their thermal expansion coefficient.

It was found that the intermetallic boride layer (i.e. the middle and the inner layer) was still intact and strongly adhered to the substrate. This demonstrates the stability of the boride layer at high temperatures, and also its chemical compatibility in the molten chloride salt. The stability of the intermetallic borides depends on the strength of the metal-boron and boron-boron bonds. The least stability is usually exhibited by metal-borides with only single boron atoms, while the greatest stability is shown by the borides with increased boron atoms like di-borides, tri-borides, etc. [[121]]. Furthermore, the dissolution rate of the metal-borides will also reduce by its transition to more complex lattice structures like octahedral complexes, etc.

The thermo-chemical data (refer **Figure 53**) shows that the interactions between metal-borides and corrosive impurities like HCl, etc. is thermodynamically unfavorable, which indicates chemical stability metal-borides in molten chloride salt. The thermal decomposition or dissolution of metal-borides to liberate metal ions in the molten salt is not possible because of the stronger metal-boron and boron-boron bonds, which will require large amount of energy to break these bonds. It must be noted that even after the depletion or disintegration of break-down of the outermost layer, the middle and the inner boride layer were sufficiently thick enough to provide adequate protection against the molten salt attack, this preventing any interaction with the alloying elements (Cr, Fe, Ni, etc.). It also needs to note that the outmost layer can be avoided by improve the boronization method.

4.5.2 Ferrous-Based Alloys

Unlike nickel-based alloys, boronization of ferrous-based alloys is more complicated due to the formation of dual iron boride phases (FeB-Fe_2B). These phases exhibit thermal instability due to differences in their thermal expansion coefficient, thus resulting in spalling or peeling or cracking due to thermal mismatch. The boride layer in ferrous-based alloys is comparatively thinner than in nickel-based alloys, and is also influenced by the boronizing agent, boronizing time and temperature. **Figure 54** and **Figure 55** show the surface and cross-sectional characterization of the borided ferrous-based alloy before the corrosion test.

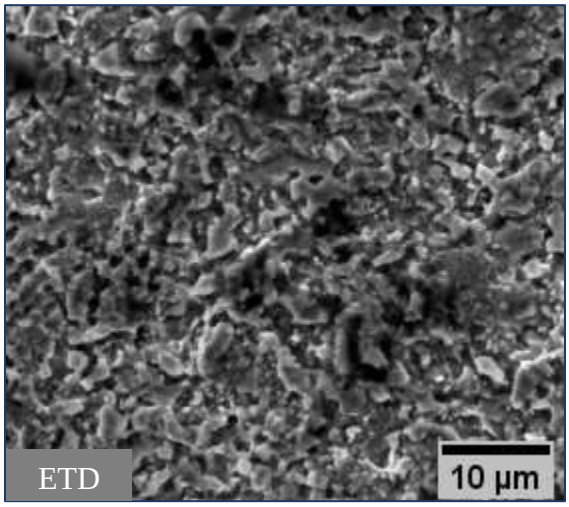

Figure 54. SEM-EDS surface characterization of the boride layer in SS316L alloy before exposure to molten KCl-$MgCl_2$-NaCl salt at 800 ºC for 100 hours.

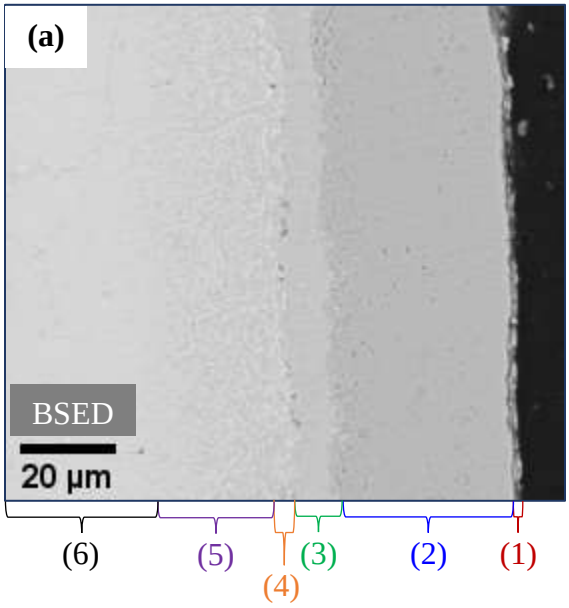

(1) Iron-Silicide and Metal-Boride Composite Layer
(2) Metal-Boride "Compound" Layer
(3) Metal-Boride "Compound" Layer
(4) Metal-Boride Layer with Nickel-Silicide Enrichment
(5) "Dispersed" Layer (Metal-Borides)
(6) Alloy

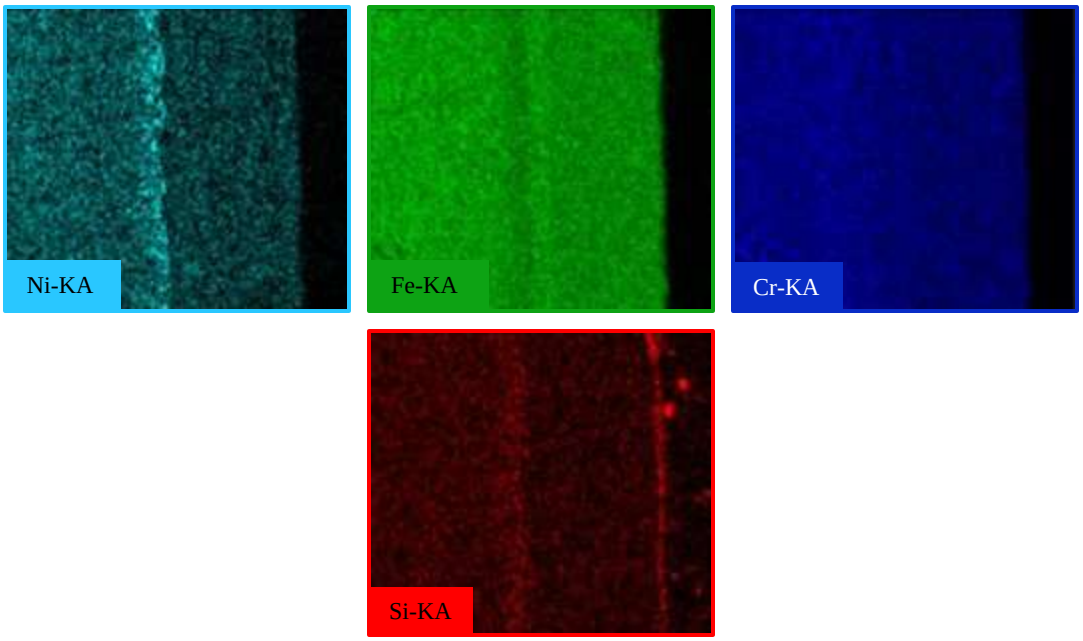
Ni-KA
Fe-KA
Cr-KA
Si-KA

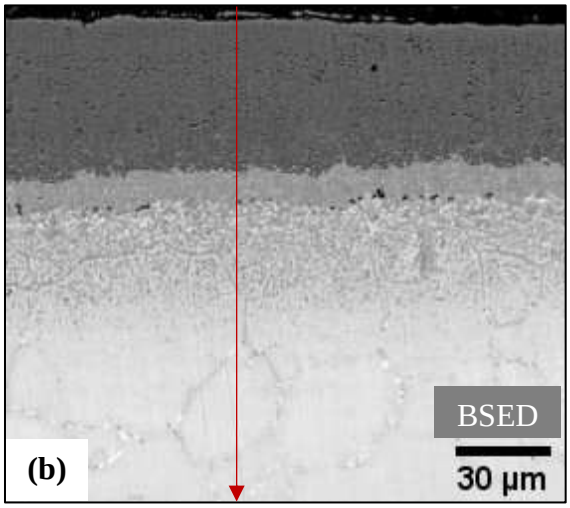
(b)
BSED
30 µm

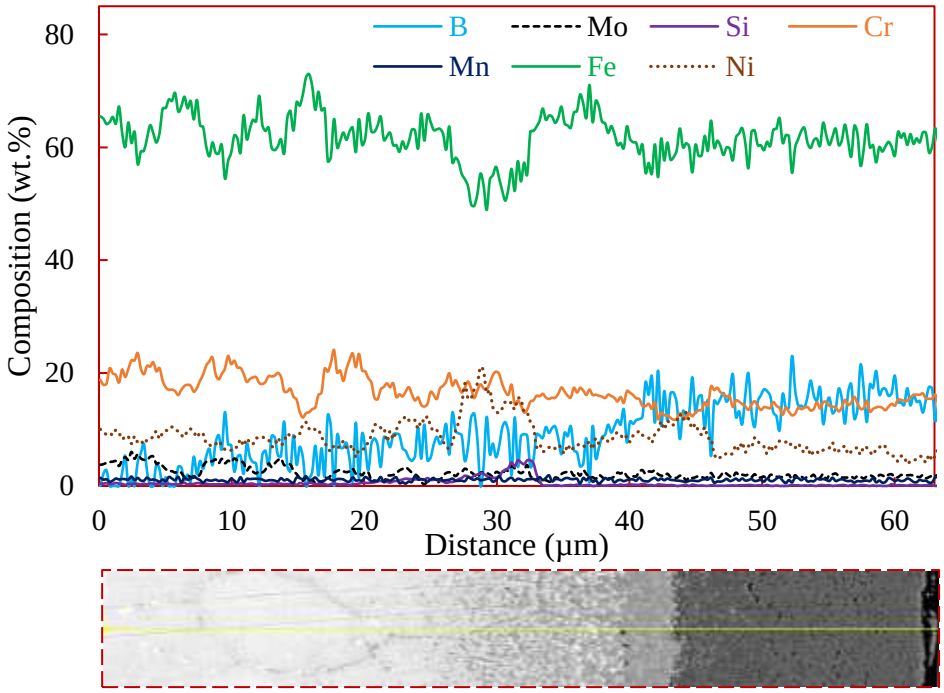

Figure 55. SEM-EDS cross-sectional characterization **(a)** elemental mapping, and **(b)** line-scan of the boride layer in SS316L alloy before exposure to molten KCl-$MgCl_2$-NaCl salt at 800 ºC for 100 hours.

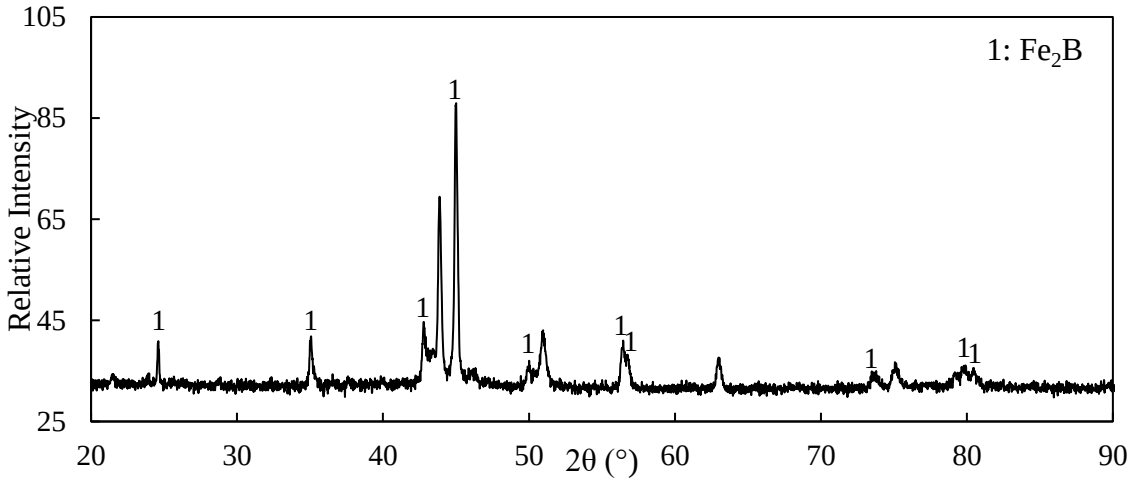

Figure 56. XRD analysis of the outer boride layer in SS316L alloy before exposure to molten KCl-$MgCl_2$-NaCl salt at 800 ºC for 100 hours.

The boronization process for ferrous alloys still need refinement as most of the borided specimens showed mild to severe spalling of the boride layer. The spalling was localized. The SEM cross-sectional characterization (refer **Figure 57**) of the spalled specimens showed the outer layers (1),

(2) and (3) were absent, which could have been due to the boronizing agent and/or the boronizing conditions (i.e. temperature and time, resulting in thicker boride layers).

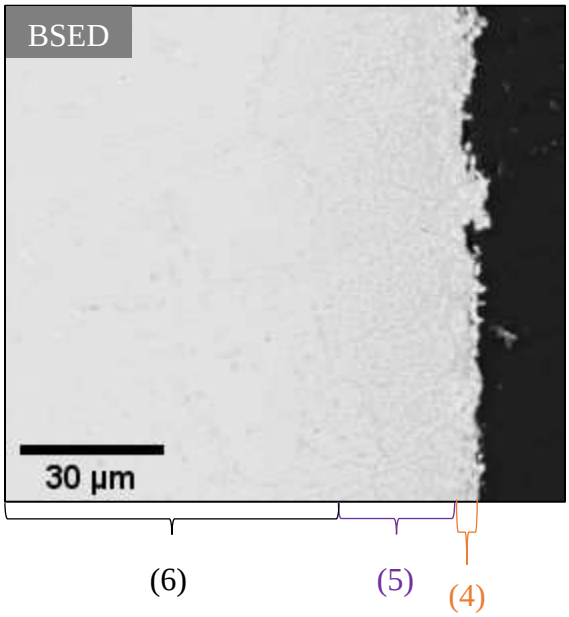

Figure 57. Boride layer spalling in SS316L alloy after boronization.

For the corrosion test, two specimens (one without spalling and one with mild spalling) were considered and exposed to molten KCl-$MgCl_2$-NaCl salt at 800 °C for 100 hours. **Figure 58** shows the average mass-loss per unit area (mg/cm^2) in the boronized and non-boronized ferrous-based alloy after exposure to molten KCl-$MgCl_2$-NaCl salt.

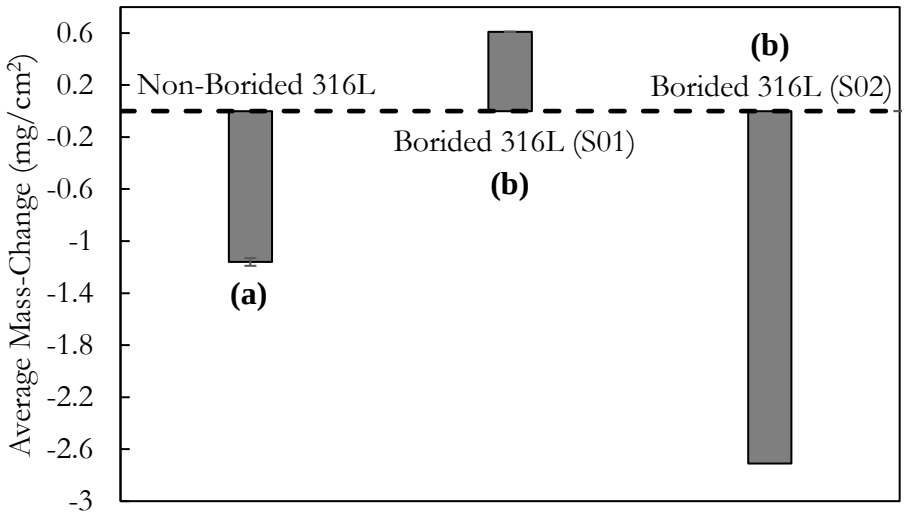

Figure 58. Average mass-change (mg/cm^2) in the **(a)** non-boronized, and **(b)** boronized SS316L alloy after exposure to molten KCl-$MgCl_2$-NaCl salt at 800 ºC for 100 hours.

The average mass-loss per unit area was found to be in the increasing order of, boronized SS316L-S01 (non-spalled, no mass-loss) < non-boronized SS316L (0.91 mg/cm^2) < boronized SS316L-S02 (spalled, 2.71 mg/cm^2). **Figure 59**, **Figure 60** and **Figure 61** shows the surface and cross-sectional characterization of the ferrous-based alloys after exposure to molten KCl-$MgCl_2$-NaCl salt.

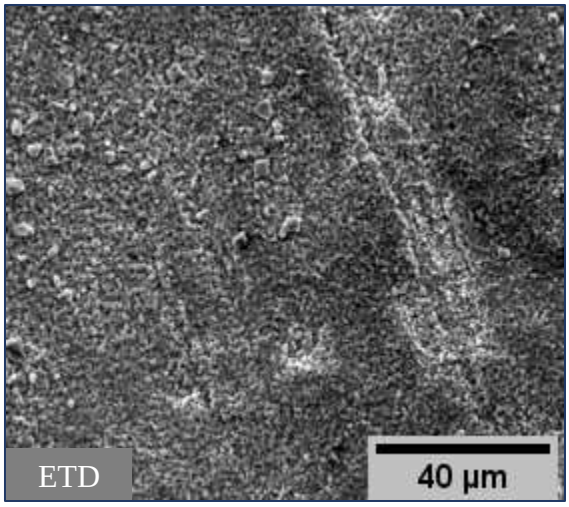

Figure 59. SEM-EDS surface characterization of corroded boronized SS316L alloy after exposure to molten KCl-$MgCl_2$-NaCl salt at 800 ºC for 100 hours.

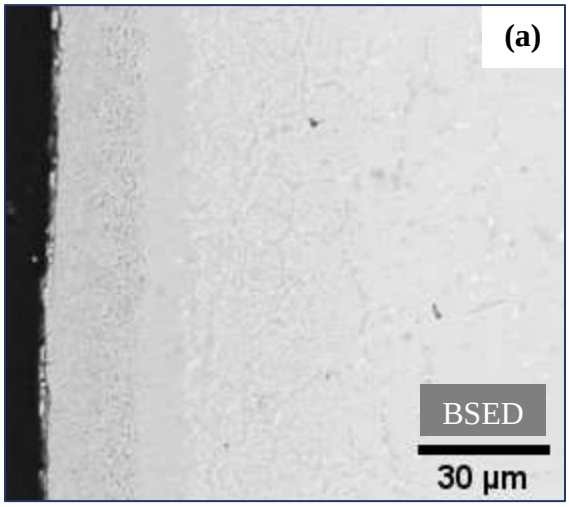

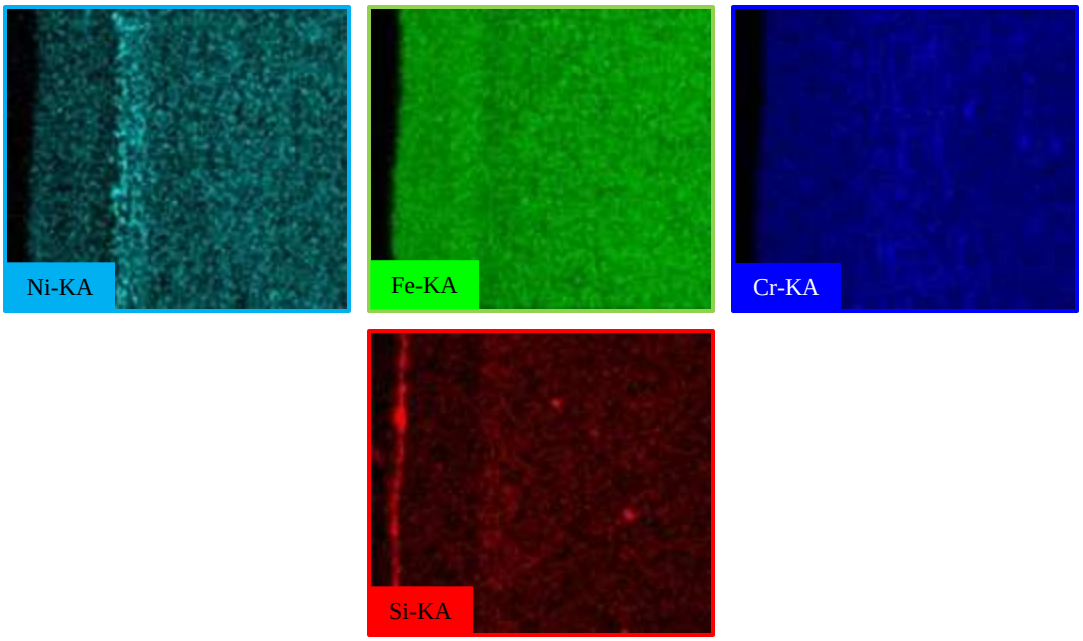
Ni-KA
Fe-KA
Cr-KA
Si-KA
(b)
BSED
30 µm

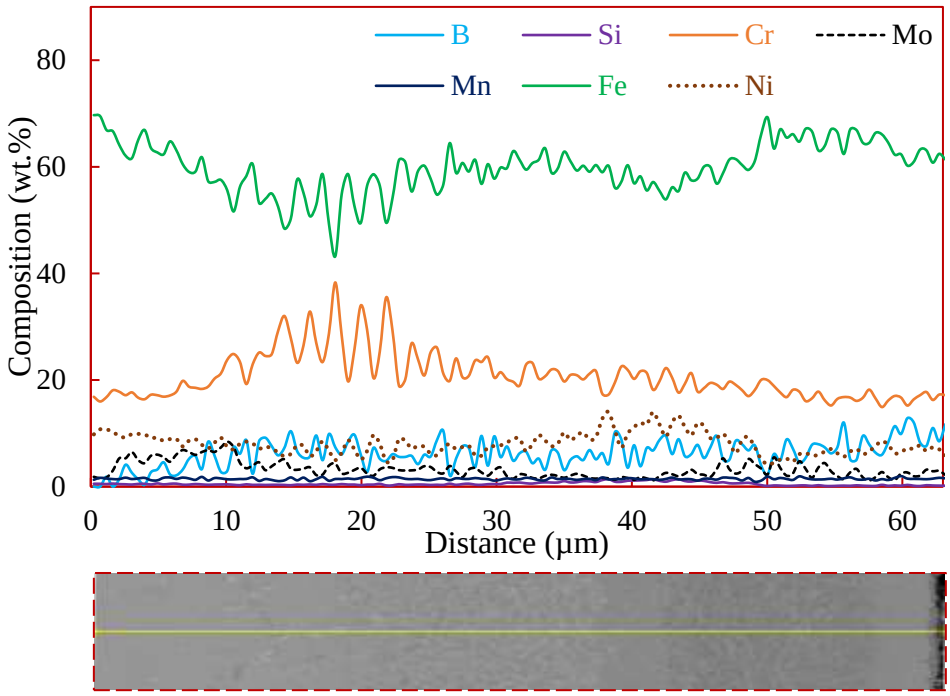

Figure 60. SEM-EDS cross-sectional characterization **(a)** elemental mapping, and **(b)** line-scan of corroded boronized SS316L-S01 alloy after exposure to molten KCl-$MgCl_2$-NaCl salt at 800 ºC for 100 hours.

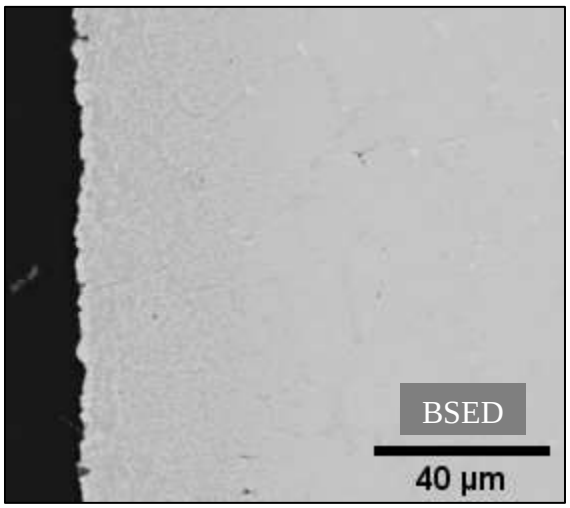

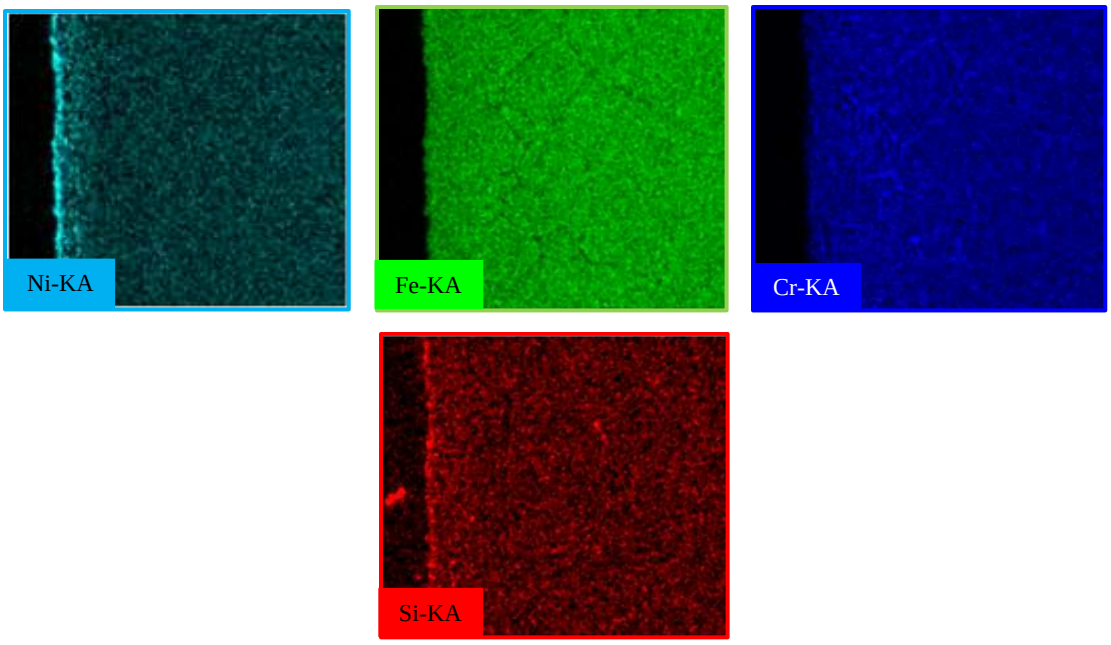

Figure 61. SEM-EDS cross-sectional characterization of corroded boronized SS316L-S02 alloy after exposure to molten KCl-$MgCl_2$-NaCl salt at 800 ºC for 100 hours.

The mass-loss in borided SS316L-S02 (spalled specimen) can attributed to the instability of the (outer) boride layers resulting in its complete break-down during the corrosion test. However, as shown in **Figure 61**, the remaining boride layer still provided some form of resistance against the molten salt attack (i.e. the layer was still solid and intact to the substrate after exposure to molten salt, and there was no chromium depletion from the alloy).

In the present study, the boronizing agent was same as that used for nickel-based alloys. Similar to nickel-based alloys, the borided ferrous-based alloy (SS316L) also exhibited high surface roughness. The boride layer was comprised five layers, the outermost (first) solid layer, the second, third and fourth solid "compound" layer and the fifth solid "dispersed" or "diffusion" layer and was composed of intermetallic borides. No "grain boundary precipitation zone" was seen in these alloys. Based on the SEM and XRD analyses of the boride layer showed that,

For boronized SS316L alloy (refer **Figure 54**, **Figure 55** and **Figure 56**):

The first (outermost) layer was mostly composed of Fe-Si phases and iron boride (Fe_2B) phases, and low to very low concentrations of nickel and chromium boride phases. The second and third layer ("compound" layer) was composed of varying concentrations of various metal-boride phases such as Fe-B, Cr-B, and Ni-B. The fourth layer was also a metal-boride layer with varying

concentration of Fe-B, Cr-B, and Ni-B phases, and also enriched with nickel-silicon phases. The fifth layer ("dispersed" layer) was an intermixture of Fe-B, Cr-B, and Ni-B phases.

The surface roughness of the borided alloy is also an influential factor on the corrosion process in these alloys, specifically in dynamic (flow-induced) conditions. The surface roughness is dependent on the boronizing treatment such as boronizing agent, time and temperature. The surface roughness in the borided alloys is because of the crystalline nature (structures) of the metal-borides and/or silicides formed. Thicker boride layer results in increased volume and generates surface tensile stresses, which pushes the boride and/or silicide structures towards the surface at higher temperatures thus developing a crystalline surface (higher roughness). Studies have shown the boride layer thickness is parabolicaly dependent on the boronizing time, and can be effectively reduced without compensating its stability and properties by reducing the boronizing time. It also depends on the initial surface roughness of the alloy before boronization, where the resultant surface roughness of the borided alloy decreases for higher initial surface roughness [[122]]. Here, the decrease in surface roughness is caused due to filling effects, where the metal-borides and/or silicides structures formed fill into the gaps pre-existing from the alloys initial roughness. In flow conditions, the (increased) surface roughness will increase the corrosion-rate in alloys. This is because, it interferes with the flow-path by increasing turbulence or by forming eddies and also by affecting other hydrodynamic parameters like the mass-transfer boundary layer. This increases the friction between the flowing fluid (molten salt) and the alloy interface under impact and thus intensifying corrosion. As discussed, in borided alloys the outermost layer is the weakest and will provide no protection against this form of attack, however, the inner boride layers are harder and wear resistant and should overcome the effects of flow corrosion.

Based on previous studies [[88]] and the current analysis, the boride layer formation mechanism in nickel and ferrous-based alloys can be summarized as,

a) At boronizing temperatures, the boron atoms are transported to the material surface via gaseous diffusion which then diffuses into the sub-surface region by solid state diffusion.
b) As higher temperatures, the boron atoms will form metal-boride phases with the most active alloying elements.
c) The resulting boride layer formed will comprise of an outermost solid layer, middle solid "compound" layer and an inner "diffusion" layer.

d) The outermost layer is mostly composed of Ni-B (nickel-based alloys)/FeB (ferrous-based alloys) phases, and non-uniformly distributed Ni-Si (nickel-based alloys)/Fe-Si (ferrous-based alloys) phases. The growth of borides and silicides occurs simultaneously. It also shows low to very low concentrations of other metal-boride phases, which depends on the alloy composition.
e) The middle "compound" layer/s is mostly composed of Ni-B (nickel-based alloys) or Fe-B (ferrous-based alloys) phases and varying concentrations of Ni-B, Fe-B, Cr-B phases (for IN718 and SS316L alloys) and Mo-B phase (only for C276 alloy).
f) The "dispersed or diffusion" layer is an inter-mixture of finely dispersed precipitates of metal-boride phases. As the boron concentration gradient along cross-section decreases, the already formed borides will inter-mix to form a thick, non-porous and uniform boride layer.

The composition of the boride layer is dependent on the chemical composition of the alloy, while its thickness is dependent on the boronizing powder, the boronizing temperature and the exposure time and the diffusion rate of boron atoms. The "compound" layer will increase surface hardness and wear resistance of the alloy due to higher metal-B and B-B bonding energies, while the "diffusion" layer with its increased Cr concentration will provide added strength and increased fatigue resistance. Matsuda F., et. al. [24] also showed that Cr, Mo and Nb are the most effective elements in increasing the hardness of the boronized nickel-based alloys due to nickel's substitution with these elements in the Ni_2B and Ni_3B phases. The stability of the boride layer depends on various factors like its morphology in terms of homogeneity, structure (i.e. porous or non-porous), adhesion properties with the substrate, thermal expansion coefficient, etc.

Just like the nickel-based alloys, the boride layer was still intact and strongly adhered to the substrate after the corrosion test. Expect for the outermost layer (silicide and boride) which cracked, peeled or spalled (during or after the corrosion test), the inner boride layers showed no change in its composition or morphology after the corrosion test, and provided an protective barrier against molten salt interaction with the alloying elements. This can be confirmed from the SEM cross-sectional images which showed no depletion in the boride layer, outward diffusion of chromium from the base alloys and infiltration of corrosive impurities into the alloy. The multi-layer (composed of different phases) also did not show any form thermal or chemical instability as the cross-sectional SEM images of these layer did not show any cracks, gaps and/or porosity.

Thus, the analyses show that boronization as a surface treatment/coating option is effective process/technique that could assist in slowing down the corrosion process of nickel and ferrous-based alloys in the molten KCl-$MgCl_2$-NaCl salt, though more studies is still required specifically in non-conventional dynamic conditions before being conclusive on its compatibility in molten salt applications. It must also be noted that since the outermost silicide and boride composite layer is unstable hence, if possible the boronizing treatment could be modified (i.e. using a different agent, reducing the boronizing time, etc.) to prevent its formation. If its formation is unavoidable, the layer must be removed after the boronization process by heat-treatment processes (temperature gradient) and/or by carefully abrading the surface. This is required as break-down of this layer during application will introduce solid contaminants into the molten salt which could increase the corrosion rate in alloys and/or affect the pump performance.

4.6 Molten Salt Corrosion Effects on Mechanical Properties of Nickel-Based Alloys

The properties of the alloys such as hardness value and wear resistance in borided and non-borided nickel and ferrous-based alloys before and after the corrosion test were measured. **Figure 62** and **Figure 63** show the Vickers hardness values and the estimated yield stress for corroded and non-corroded, borided and non-borided nickel and ferrous-based alloys.

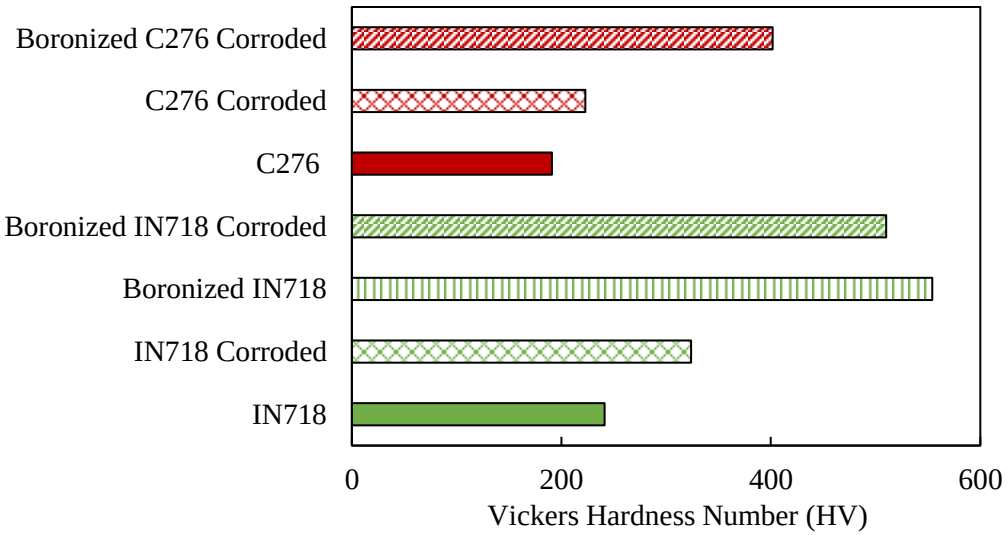

Figure 62. Vickers surface hardness values (HV) of boronized and non-boronized nickel-based alloys before and after exposure to molten KCl-$MgCl_2$-NaCl salt at 800 ºC for 100 hours.

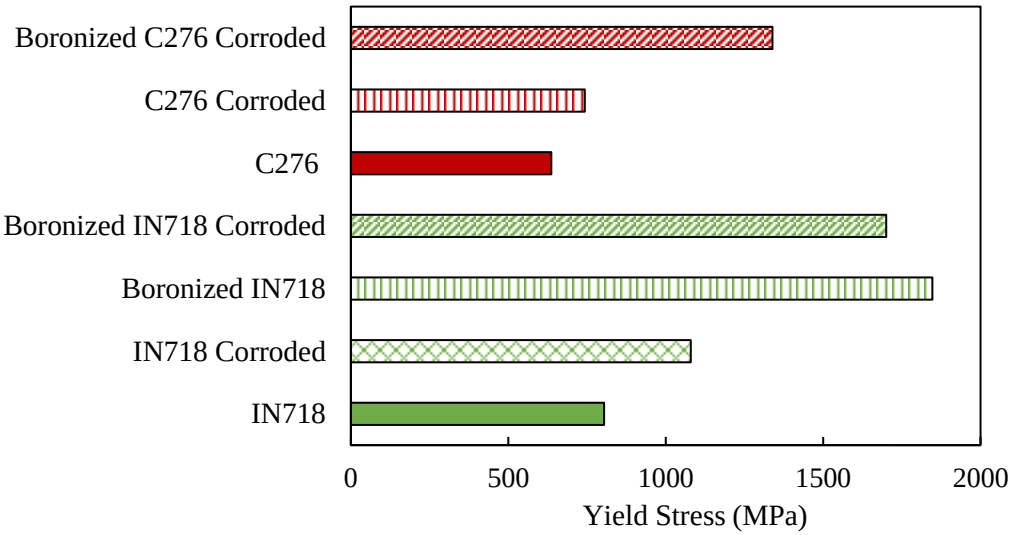

Figure 63. Yield stress values (MPa) of boronized and non-boronized nickel-based alloys before and after exposure to molten KCl-$MgCl_2$-NaCl salt at 800 ºC for 100 hours.

It was found that the hardness value and the estimated yield stress were in the increasing order of C276 (191 HV and 636.67 MPa) < C276 corroded (222.91 HV and 743.01 MPa) < IN718 (241.29 HV and 804.29 MPa) < IN718 corroded (323.87 HV and 1079.58 MPa) < boronized C276 corroded (401.71 HV and 1339.04 MPa) < boronized IN718 corroded (510.13 HV and 1700.42 MPa) < boronized IN718 (554.11 HV and 1847.04 MPa). It must be noted that the hardness values measured for the borided alloys will involve some uncertainties as they were measured from the surface of the alloys viz. the outermost layer, a silicide and boride composite, and which also exhibits high surface roughness. The non-borided nickel-based alloys showed greater hardness and strength after corrosion because of the structure and composition of the corrosion layer which is quite different from the alloy itself i.e. the corrosion layer is depleted of chromium and iron, and enriched with nickel. However, the corrosion layer will not provide any protection against erosion-corrosion because of its porous nature.

4.7 Introduction to Forced Circulation Molten Salt System for Flow Corrosion Studies

4.7.1 Candidate Material of Construction

Generally, for the molten salt applications, the candidate materials must always exhibit high-temperature strength (i.e. high tensile and yield strength), good oxidation resistance, good corrosion resistance, high hardness, high wear and fatigue resistance, etc. However, in flow systems, these materials must also be capable of withstanding erosion-corrosion caused by the relative motion of fluid with the material surface. The rate of erosion is influenced by the flow-induced effect such as hydrodynamic factors, and the mechanical-induced effect like shearing. Furthermore, temperature-gradient (i.e. non-isothermal conditions) effects will also accelerate corrosion in material due to faster dissolution of metal-oxide and metal-chloride layer in the hot-section of the system, and its precipitation in the cold-section of the system.

As discussed in **Chapter 2, s**everal recent and ongoing studies have shown nickel-based alloys are superior over ferrous-based alloys in various different molten halide salts (i.e. chloride and fluoride blends); but higher cost, limited availability, and difficulties involved with its machining and welding makes it less favorable for molten salt applications. In this study, the austenitic stainless steel grade 316L (dual-certified) was selected as the candidate material of construction for the molten salt system. Since, 316L SS has high chromium content, it makes the alloy more susceptible to corrosion in molten salt.

Hence, a higher corrosion allowance (CA) and factor of safety (FOS) were selected when designing the system. The thicknesses of tanks and pipes were calculated using the stringent ASME boiler and pressure vessel and other codes (Section B31.8 for piping, and Section VIII Division 1 for tanks). The pipes and associated fittings (i.e. elbows and tees) in the system were of schedule (SCH) 160. The flanges were Class# 300 Sleep on Raise Face (SORF). For the molten salt pump (Wenesco, United States), the wetted parts (i.e. impellor, suction and discharge line) were made of 316 SS, while the non-wetted parts (i.e. structural and other associated fittings) were made of 304 SS. The system was also provided with several fully metal-seated bi-directional ball valves (Gosco Valves, Canada) to control the flow direction and its velocity. The valves were made of borided Inconel® 718 alloy, ball and seat, and 316 SS Graphoil seals. Boronizing the

alloys enhances its properties with increased hardness, and wear and fatigue resistance, thus making the alloy suitable for extreme temperature, abrasive and corrosive applications. All wetted joints in the system were either butt-welded or flanged connected. For flanged connections, semi-metallic gaskets viz. 316L SS central metallic core lined with Thermiculite 815; Flexitallic Gaskets, United States, were used to provide an effective seal.

4.7.2 Design Configuration and Experimental Set-Up

Figure 64 shows the high temperature forced circulation molten salt loop, which was designed and built at Virginia Tech University to study the flow corrosion in ferrous and/or nickel-based alloys.

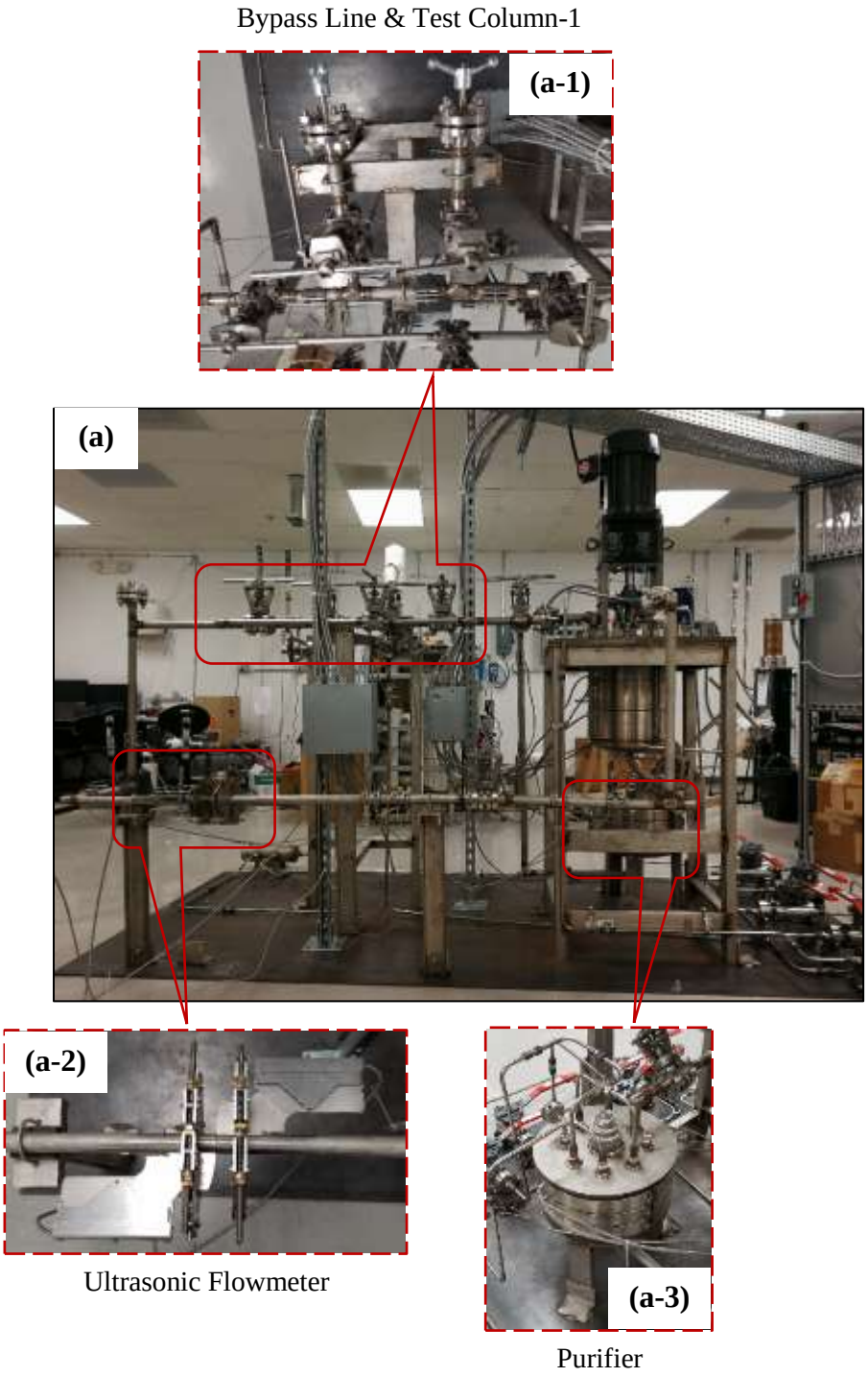

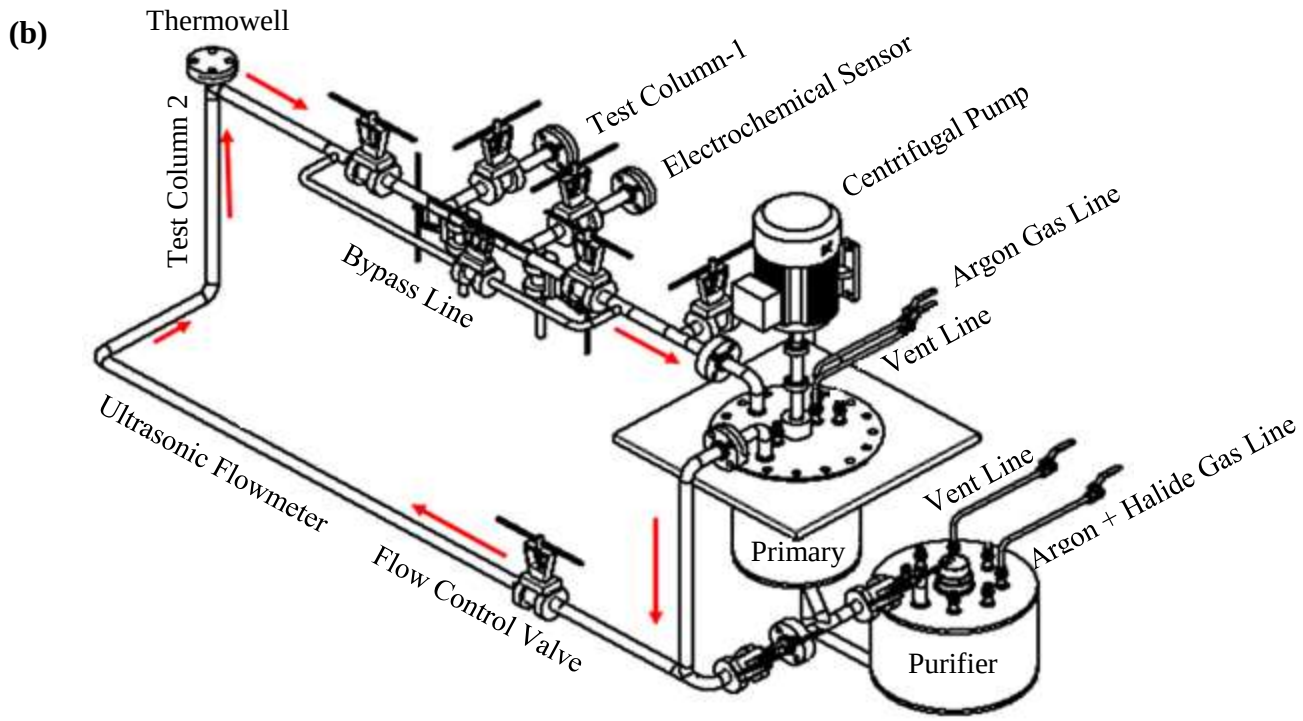

Figure 64. The forced circulation molten salt system **(a)** actual image, and **(b)** schematic representation.

The system is designed with capabilities to operate at high temperatures (up to 700 °C) and high flow-velocities (up to 2 m/s), and to simulate or replicate the MSR operating conditions (i.e. proper selection of exposed surface area to volume ratio). It consists of a primary tank, which houses the three-horsepower submersible centrifugal molten salt pump, and an auxiliary tank (also known as purifier tank), which is used to collect and purify the molten salt before the corrosion test.

4.7.2.1 Flow-Velocity and Temperature Control

The required flow-velocity is generated by the molten salt pump, which is equipped with a Variable-Frequency-Drive (VFD). It is capable of producing 20 to 25 gallons per minute (gpm) flow-rate at 10 feet total head and for molten salts with density less than 2 g/cm^3. The flow-velocity can be fine-controlled using the 90° V-port ball valve positioned just before the ultrasonic flow-meter (refer **Figure 64b**). The flow-velocity will be monitored and recorded using the externally mounted ultrasonic flowmeter (Flexim, Germany). It works on the principle of transient time difference co-relation to measure the average flow-velocity at high temperatures (above 600 °C). The flow-velocity measured is independent of the fluid viscosity and is unaffected by the type of

fluid, pipe materials, pressure losses, etc. Unlike Coriolis or Vortex flowmeters, it will not contact the molten salt, and hence will be less prone to break-down. It consists of wave-injectors which separate the temperature sensitive transducers or probes from the hot pipes. This will not only protects the transducers or probes from damage, but will also provide good acoustic coupling because the flow-velocity depends on the sound waves generated by the molten salt at a given temperatures. The transducers or probes were positioned (i.e. distance separating the two transducers or probes) using the data that has already been measured for different binary molten chloride salts. The process of collecting the flow-velocity data is based on the single beam and single sound path mechanism.

The desired temperature is achieved using the mineral insulated ring type band heaters installed on each tanks, and several pipe band heaters installed on pipes, at various different locations across the system. The heater configurations were selected based on the heating capacity of the molten chloride salt, and the total amount of salt that will be used for the corrosion test. Furthermore, the system is completely insulated with three layers of 1-inch thick high density ceramic insulation followed by wrapping with aluminum foil. The ceramic insulation will minimize heat losses due to conduction and convection, while the foil will minimize radiant heat losses. The heating is controlled by the K-type long probe thermocouples installed in the tanks, and using the Watlow temperature controller (Watlow, United States). The temperatures across the system will be continuously monitored and recorded using the weld pad thermocouples positioned at various different locations across the system, and the Watlow composer software. The heating system will ensure effective heating of the system, and prevent formation of freeze or cold zones (salt solidification) in the system during the corrosion test.

4.7.2.2 Test Column

Figure 65a shows the original retractable test column (Test Column-1) assembly, which is designed to hold the test specimens during the corrosion test. Two disc-shaped specimens will be attached to the test column such that the exposed surface of the specimens aligns with the pipe's inner wall surface. This will eliminate any form of irregularities that could perturb the flow-pattern (caused due to formation of large eddies or patches). The disturbances in the flow affects the surface sub-layer, and influences (intensify or accelerate) the corrosion process. The alumina shaft will isolate the corrosion specimens from the molten salt system, thus preventing galvanic corrosion due to dissimilar metal contact.

(a)

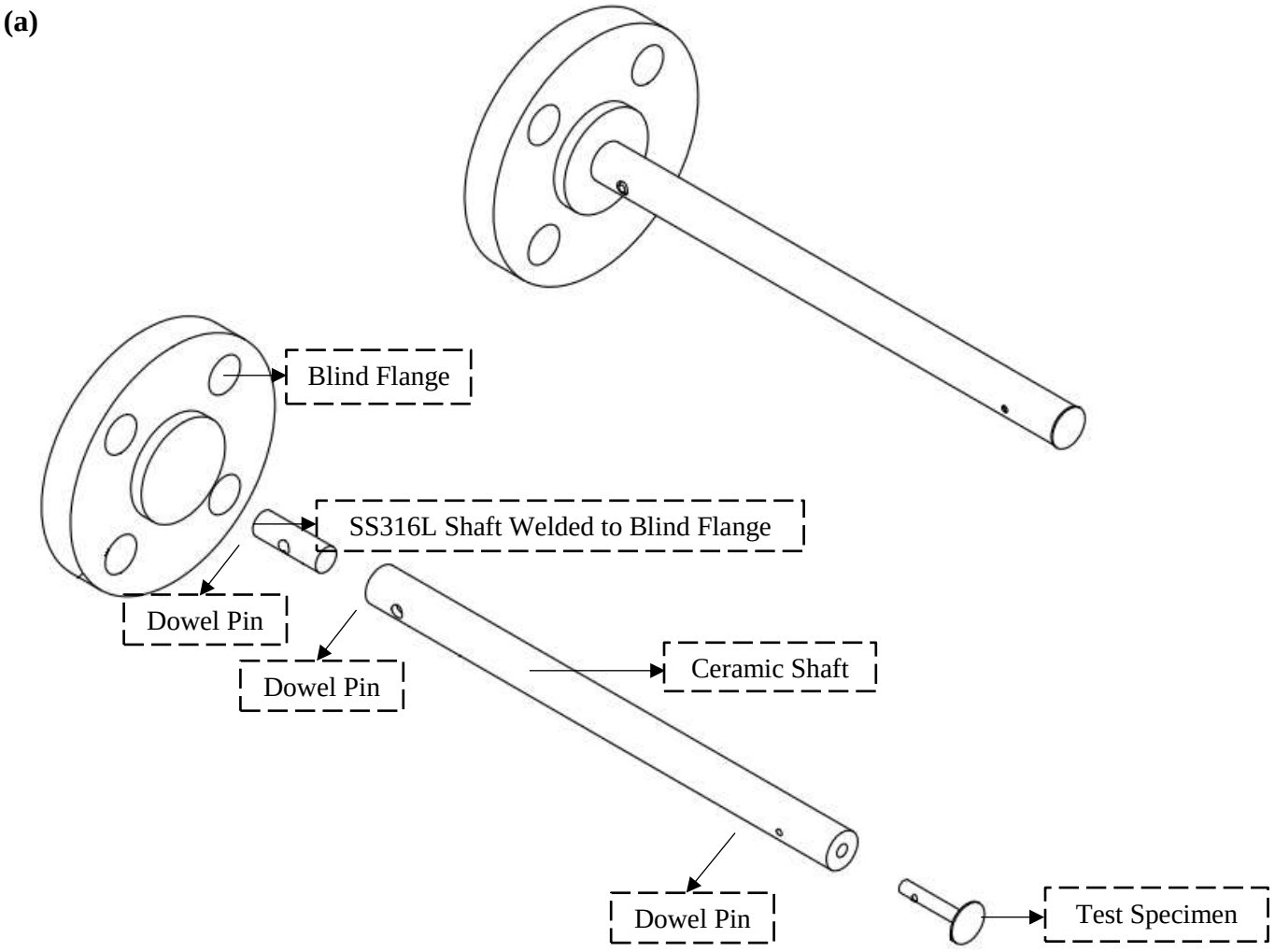

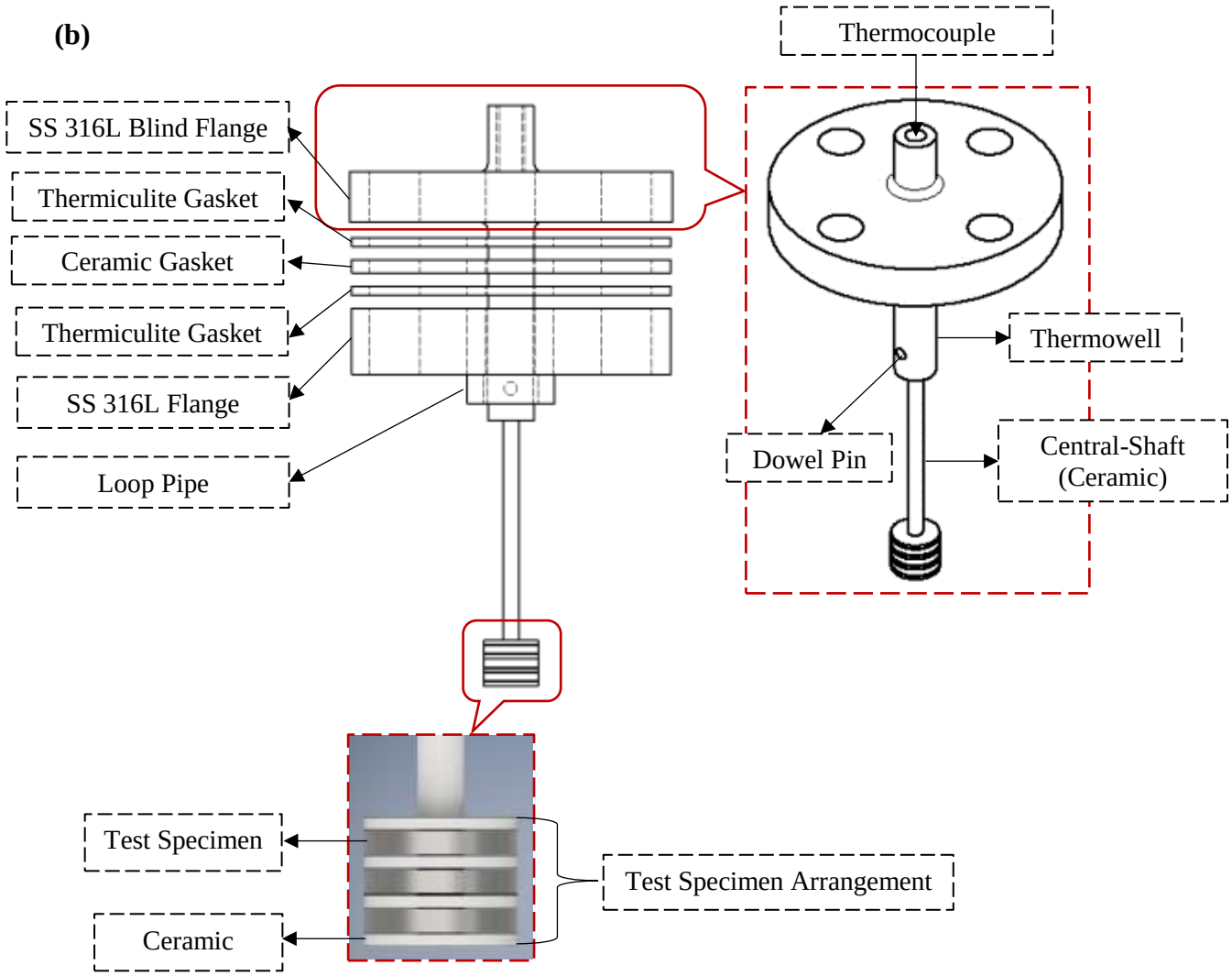

Figure 65. Test specimen holder during the corrosion tests, **(a)** Test Column-1, and **(b)** Test Column-2.

It must be noted that the loop components will also simultaneously corrode during the corrosion test, and introduce solid contaminants (particles and/or compounds) in the molten salt, which will also influence (i.e. introduce uncertainties in the corrosion measurements) the corrosion process.

4.7.3 Proposed Purification and Corrosion Testing Procedure

Before the corrosion test, the molten salt will be purified using thermal (heat-treatment to remove moisture), and chemical treatment (heat-treatment with chlorination or fluorination to remove any residual moisture and oxygen).

For the thermal purification process, the total amount of powdered salt required for the corrosion test will be collected in the purifier tank, and heated slowly and sequentially to temperatures below the hydrolysis temperature of pure halide compounds to remove moisture. During this process, the salt will be continuously sparged with ultra-high-purity argon gas to facilitate the removal of water vapors and any other off-gases (HCl gas) produced from the salt surface, which will be vented out by purging the system with ultra-high-purity argon gas.

For the chemical purification process, the salt will be sparged with halide gas (viz. chlorine-argon mixture for chloride salt, or fluorine-argon mixture for fluoride salt) to remove any residual moisture, and oxygen from the salt, which will be vented out by purging the system with ultra-high-purity argon gas.

After the purification process, liquid salt will be transferred to the primary tank using argon gas. First, the entire primary system will be heated and maintained at the required temperature (to prevent salt solidification during circulation). Now, keeping the by-pass line open, the molten salt will be circulated through the primary system using the molten salt pump. During this time, the test specimens are inserted, and maintained in an inert environment and at the required temperatures. Once the salt conditions (i.e. temperature and flow-velocity) stabilizes, the by-pass line is closed and the molten salt is allowed to make contact with the test specimens for the first time, and the corrosion test is conducted for the required duration of time. At the end of the corrosion test, the test column is isolated by opening the by-pass line, the molten salt in the test column is drained, and the corrosion specimens are carefully retrieved for measurement and analysis.

4.7.4 Challenges and Modifications

Some issues were encountered with the molten salt system related to the test column, and the pump seals.

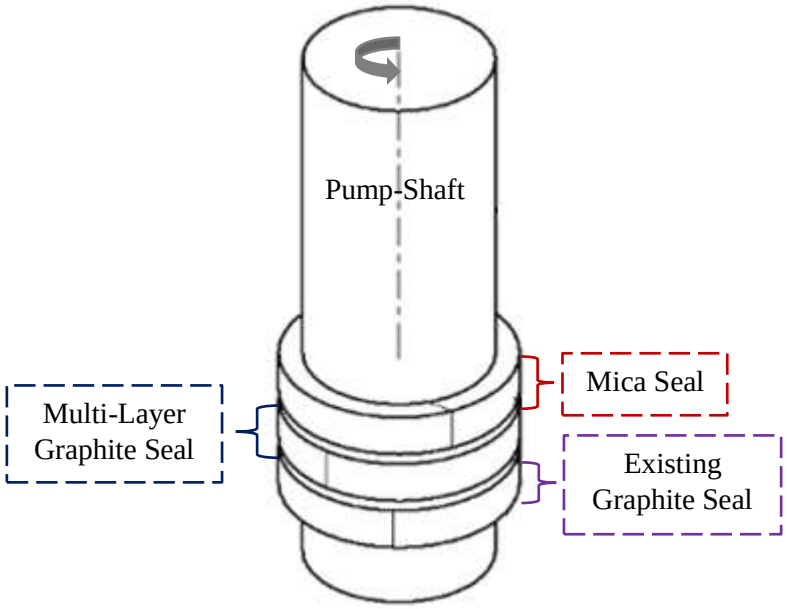

Figure 66. Modified seal design for the molten salt pump.

It was found that the existing test column (Test Column-1) had limitations that it could accommodate only two specimens for each corrosion test. To accommodate more specimens, a new test column (Test Column-2) was proposed and designed for the corrosion test. As shown in **Figure 65b**, the assembly will be positioned in the vertical section of the molten salt system after the ultrasonic flowmeter. The length of the pipe will provide sufficient entrance length required for a fully-developed turbulent flow. The test specimens (which will be hollow circular discs) separated by ceramic discs (to prevent galvanic contact) will be arranged on the central ceramic (viz. a high-purity alumina) shaft. The assembly will be attached to the thermowell (316L SS) using a dowel pin (316L SS). The thermowell flange will be connected to the molten salt system using ceramic gaskets again to isolate the test specimens (to prevent galvanic contact). The thermocouple in the thermowell will control, measure and record the molten salt temperature contacting the test specimens. Also, since with the existing system, the temperature can only be controlled by the thermocouple provided in the primary tank, the temperature in the test column

(Test Column-1 and Test Column-2) could be lower due to losses at the valves, elbows, tees, flowmeter, etc. Hence, to address this issue, the additional heaters will be installed on the Test Column-2, which will be separately controlled using the thermocouple in the thermowell, and the temperature controller.

For the molten salt pump seal, a new seal system was proposed as shown in **Figure 66**, where the existing single seal will be replaced by at least three layers of seals. The bottom two layers will be made of graphite, while the topmost layer will be made of Mica. The mica will protect the graphite seal from oxidation at high temperatures (above 500 °C). The seals will ensure a leak-proof system without compromising the efficiency of the molten salt pump.

4.8 Interaction of Molten Fluoride Salt with Graphite

The contact angle (0º to 180º) measured at the solid-liquid interface yields the wetting characteristics of the liquid with the solid surface. Even if the liquid exhibits good wettability with the solid, the wetting characteristics (i.e. "non-reactive" ("inert") or "reactive" wetting) still needs to be determined. In "non-reactive" wetting, the liquid spreads on the solid surface without reacting with the solid, while in "reactive" wetting, the wetting process is governed by the liquid's interaction with the solid surface. The knowledge of contact angle will assist in the understanding the phenomena such as, the corrosion of materials in molten salts, and mass and heat-transfer properties between the molten salt and the material [29].

Here in this study, the contact angle at the molten KF-UF_4-NaF salt-graphite interface was estimated using the "drop-shape" analysis method (refer **Figure 67**). Generally, this method gives reasonable result as long as the liquid droplet is small and spherical in shape.

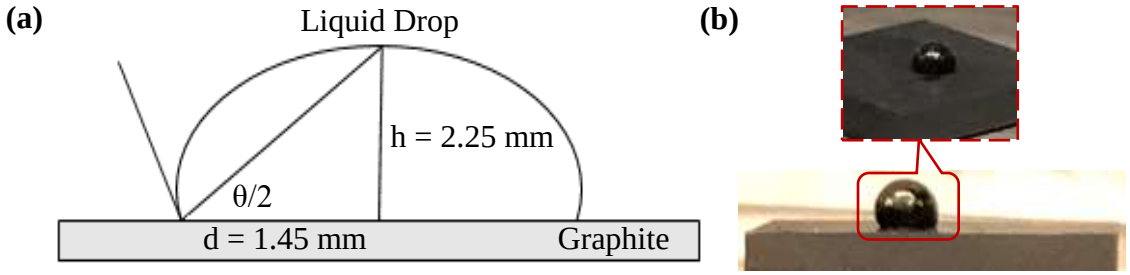

Figure 67. Molten salt-graphite interface **(a)** "drop-shape" analysis method, and **(b)** actual images.

The contact angle was calculated as 114.40º (θ >> 90º, the contact angle is relatively larger) using the **Equation (39)**, thus indicating poor wettability of molten KF-UF_4-NaF salt with the graphite. The liquid drop diameter and the apex height was measured from the images (refer **Figure 67b**) capturing the KF-UF_4-NaF salt droplet on the graphite surface (Ibiden T6 with pore-size 0.6 µm), using the ImageJ software, version 1.52.

It must be noted that the contact angle is greatly influenced by the surface tension of the liquid, where for lower surface tension, the cohesive forces within the liquid are weaker, thus forming a strong adhesion between the liquid and the solid surface i.e. greater wettability and smaller contact angle, and vice-versa. The surface tension is temperature dependent, and it decreases with increase in temperature. Furthermore, it is also affected by other factors like surface roughness, impurities

in the liquid. For soluble impurities, the surface tension value increases, thus resulting in smaller contact angle (good wettability), while for the less soluble impurities the surface tension value decreases, thus result in larger contact angle (poor wettability). Generally, graphite's surface will always exhibit higher surface roughness due to porosity and its non-uniform distribution across the surface, and cracks formed during the manufacturing process. The molten fluoride salt used was of high purity (>99.4%) i.e. it was purified and had very low impurity content (nickel and uranium oxide).

The interaction of molten salt with graphite was studied by testing SGL grade R7710 with pore-size 0.6 µm and porosity 10% at 700 °C and 6 bar (abs) for 24 and 100 hours respectively, Toyo Tanso HPG-830 with pore-size 0.6 µm and porosity 16% at 700 °C and 6 bar (abs) for 200 hours, and Mersen 2175P with pore-size 0.9 µm and porosity 13.5% at 850 °C and 10 bar (abs) for 100 and 200 hours, in molten KF-UF_4-NaF salt. **Figure 68**, **Figure 69**, **Figure 71a** and **Figure 72a** show the SEM-EDS surface and cross-sectional characterization of the infiltrated graphite specimens.

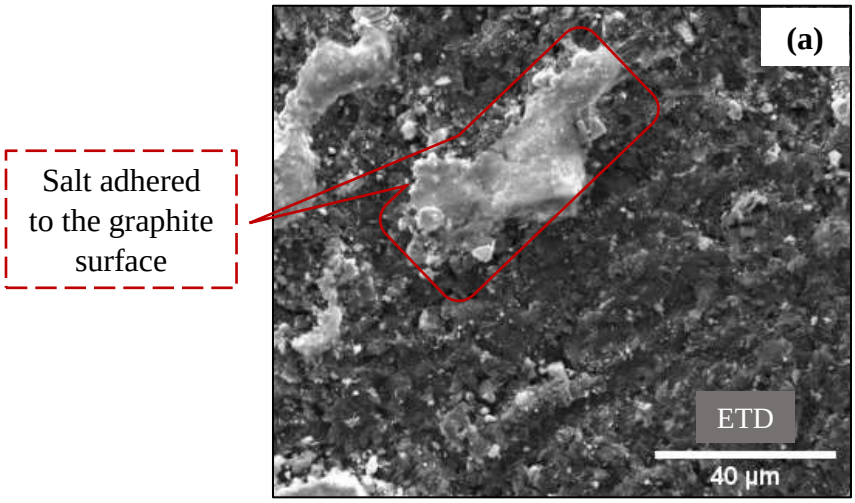

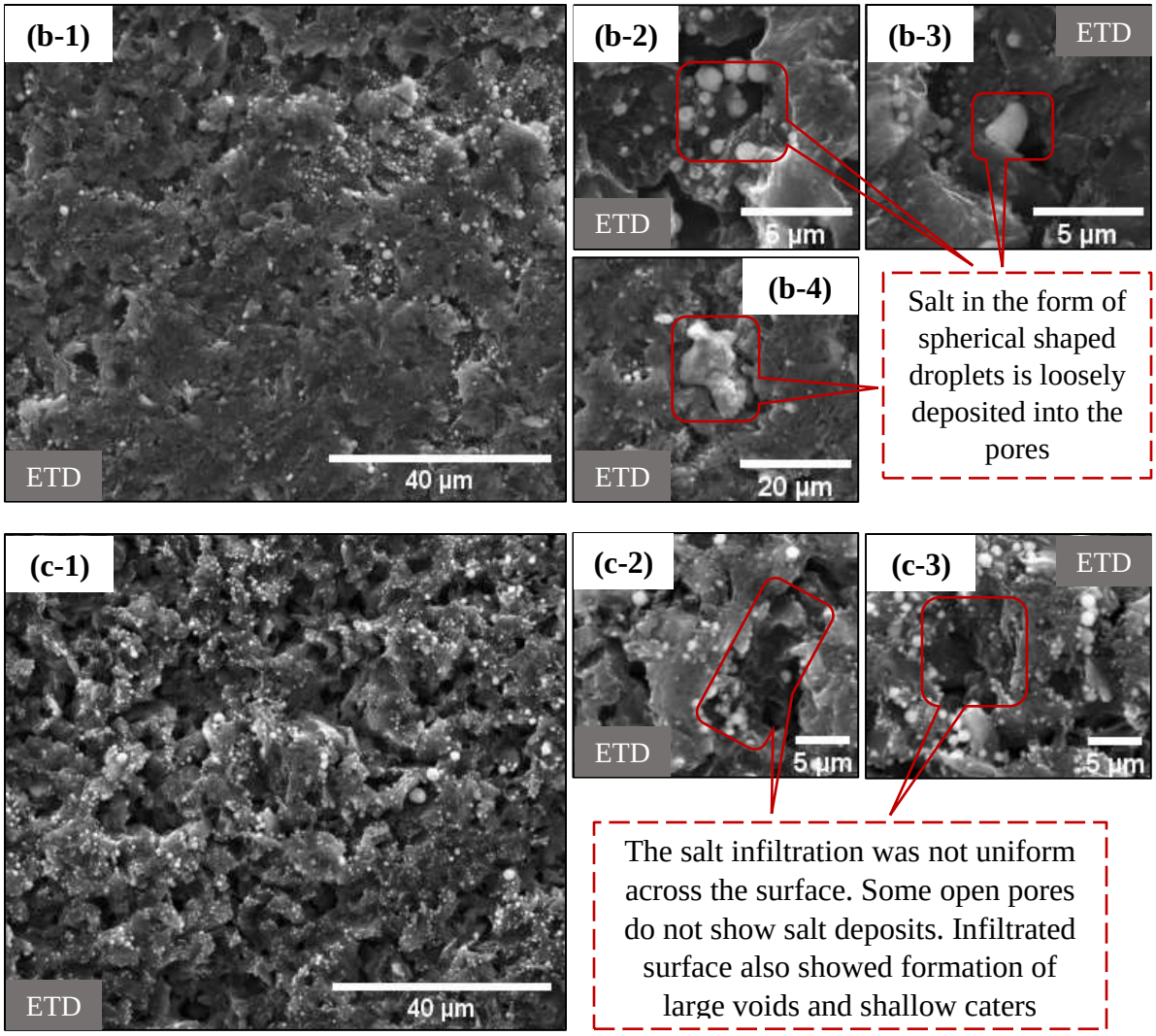

Figure 68. SEM surface characterization of the infiltrated graphites, SGL R7710 after **(a)** 24 hours **(b)** 100 hours, and Toyo Tanso HPG830 after **(c)** 200 hours, by the molten KF-UF_4-NaF salt at 700 °C and 6 bar (abs).

It was observed that after 24 hours, the salt just adhered to the graphite surface (refer **Figure 68a** and **Figure 69a**). However, after 100 and 200 hours, the salt infiltrated the graphite (refer **Figure 68b**, **Figure 68c**, **Figure 68d**, **Figure 69b**, **Figure 69c**, **Figure 69d**, **Figure 71a**, and **Figure 72a**). The infiltration in the graphite was not uniform across the surface, and along the cross-section. Several open pores on the surface showed no salt deposits indicating that either these pores could have been closed before infiltration, and/or the applied pressure was below the threshold pressure required for infiltration.

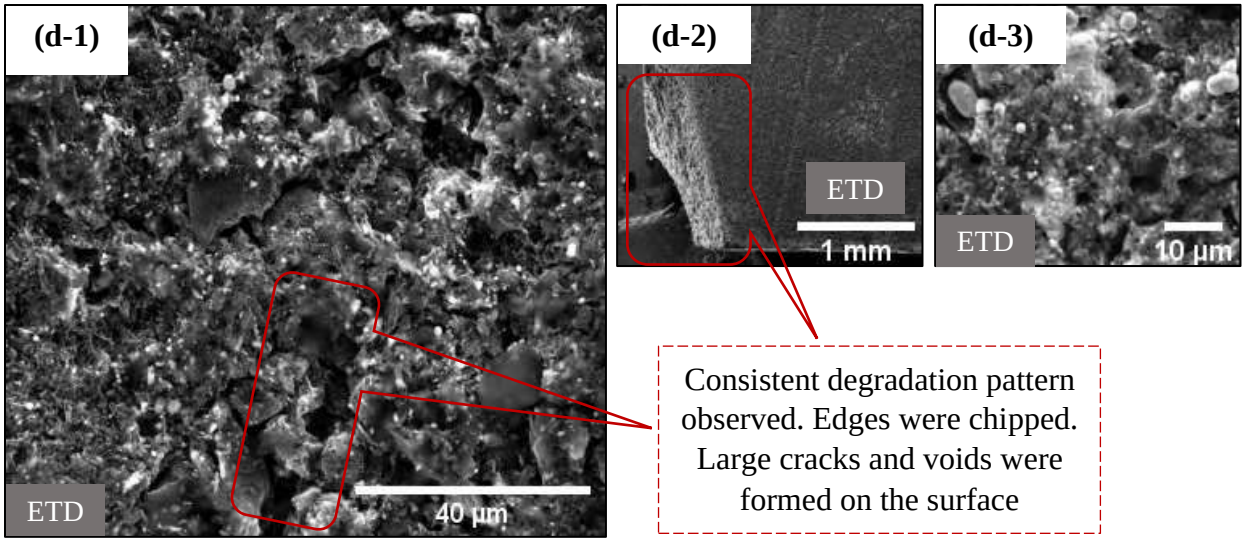

Figure 68d. SEM surface characterization of the infiltrated graphites, Mersen 2175 by the molten KF-UF_4-NaF salt after 100 hours at 850 °C and 10 bar (abs).

The latter cannot be confirmed because the threshold pressure for molten KF-UF_4-NaF salt infiltration in the selected graphite grades at the required conditions is not known. Furthermore, it also cannot be determined using the Washburn equation (refer **Equation 40**) because the surface tension values (as a function of temperature) is also not measured for the molten KF-UF_4-NaF salt. The pores which showed salt deposits, they were in the form of spherical-shaped droplets loosely embedded in the graphite pores owing to molten salt's poor wetting characteristics with the graphite [[29]].

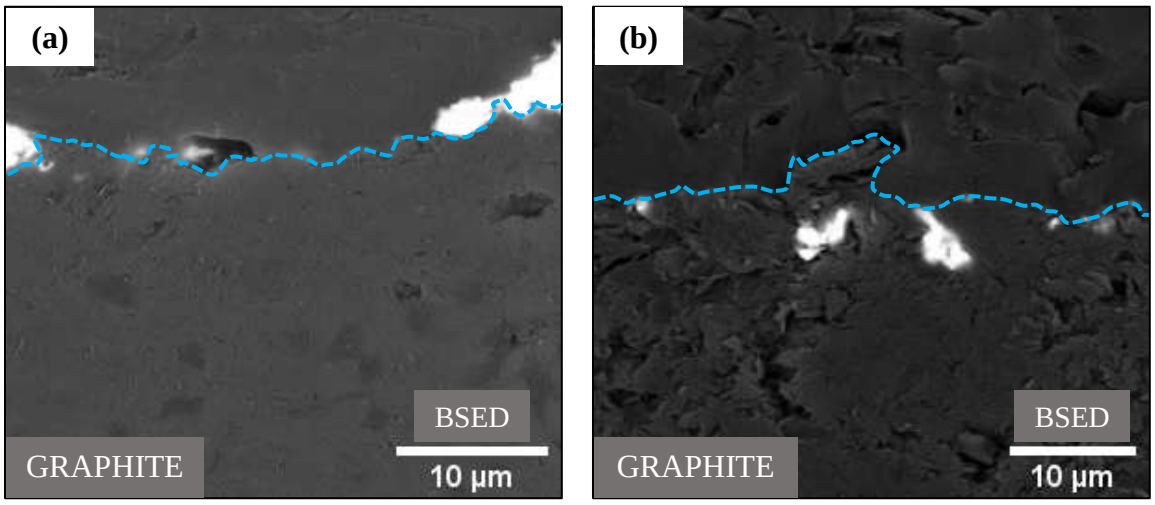

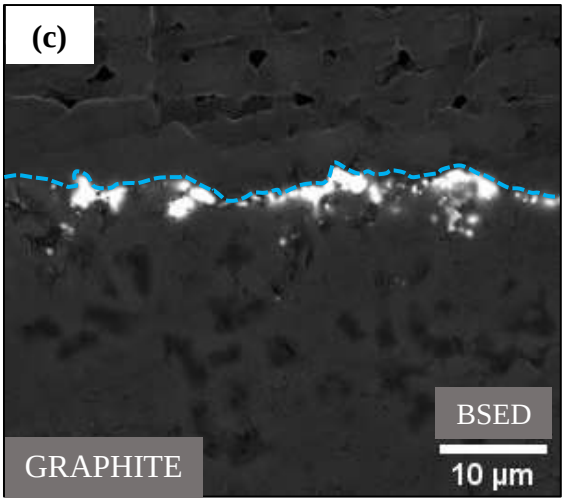

Figure 69. SEM cross-sectional characterization of the infiltrated graphites, SGL R7710 after **(a)** 24 hours **(b)** 100 hours, and Toyo Tanso HPG830 after **(c)** 200 hours, by the molten KF-UF_4-NaF salt at 700 °C and 6 bar (abs).

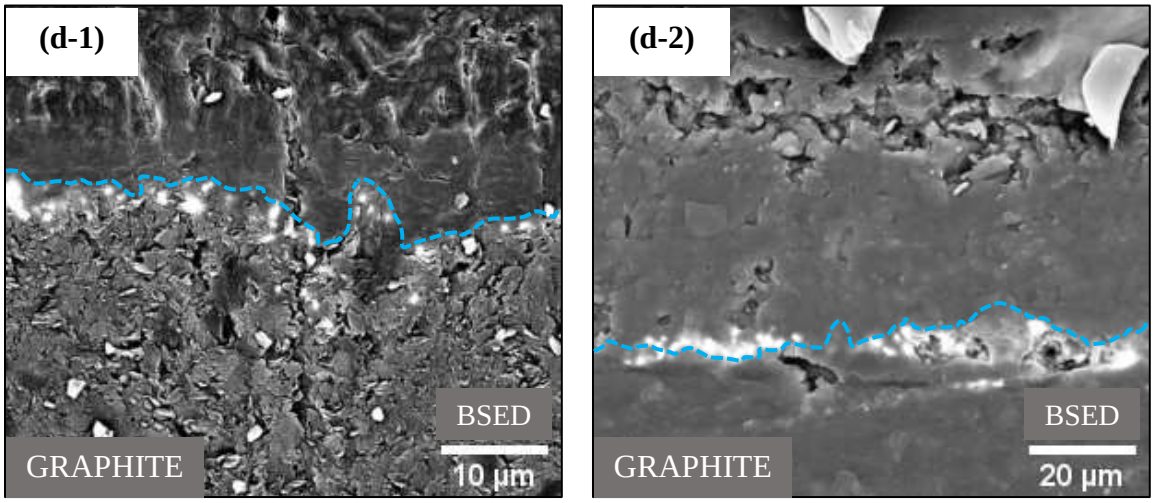

Figure 69d. SEM cross-sectional characterization of the infiltrated graphites, Mersen 2175P after 100 hours by the molten KF-UF_4-NaF salt at 850 °C and 10 bar (abs).

Table 13 provides the molten salt infiltration data for the graphite grades, SGL R7710, Toyo Tanso HPG-830 and Mersen 2175P, at the required conditions.

Table 13. Molten salt infiltration data for SGL R7710, HPG830 at 700 °C and 6 bar (abs), and Mersen 2175P at 850 °C and 10 bar (abs).

Graphite Details					Time (Hours)	Infiltration Depth Range (μm)
Grade	Pore-Size (μm)	Porosity (%)	Raw Material	Process		
SGL R7710	0.6	10	Coke	Iso-Moulding	24	No Infiltration
SGL R7710	0.6	10	Coke	Iso-Moulding	100	1.91–9.12
Toyo Tanso HPG-830	0.6	16	Not Available to Public	Iso-Moulding	200	2.53–10.44
Mersen 2175P	0.9	13.5	Pitch	Iso-Moulding	100	4.39–13.24
Mersen 2175P	0.9	13.5	Pitch	Iso-Moulding	200	6.95–21.03

Based on this data, it can be inferred that the infiltration process is time-dependent, where for shorter time duration there is no infiltration, but as time progresses the infiltration commences, and continues until it reaches equilibrium i.e. graphite is saturated with the molten salt. It must be also be noted that other factors like applied pressure, graphite's microstructure (i.e. porosity and pore-size, manufacturing defects), temperature, etc. will also influence the infiltration rate. As shown in **Figure 70**, the average weight-gain in SGL R7710 after 24 hours was 0.27 ± 0.01%, which is due to the salts that adhered on the graphite surface , while the average weight-loss in SGL R7710 after 100 hours and Toyo Tanso HPG-830 after 200 hours was 0.04 ± 0.01% and 0.05 ± 0.01%, and in Mersen 2175P after 100 and 200 hours was 0.53 ± 0.01% and 2.86 ± 0.00%., which is mainly due to the degradation of the graphite samples.

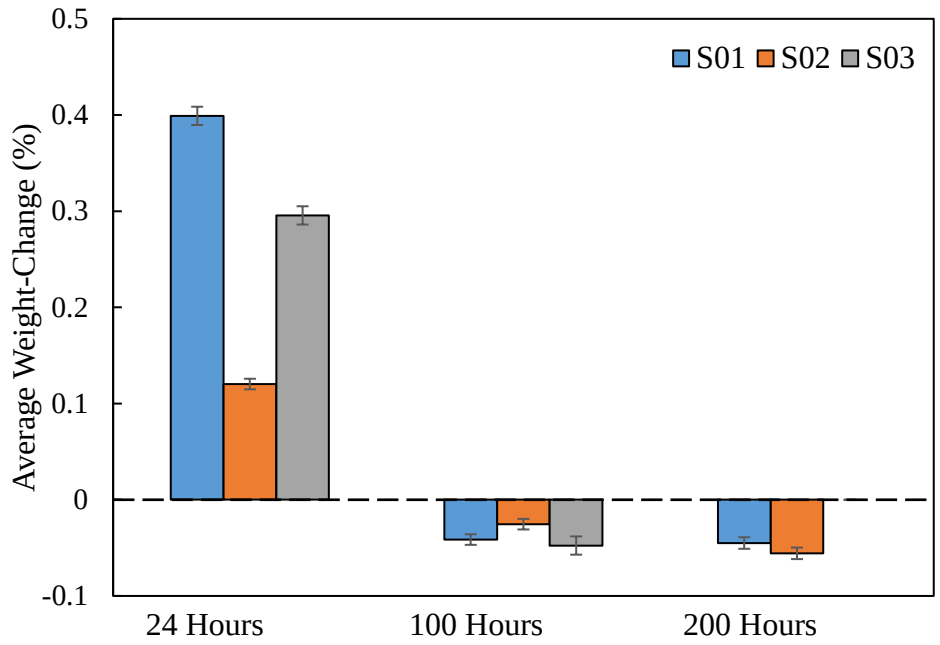

Figure 70a. Weight-change in SGL R7710 after 24 and 100 hours, Toyo Tanso HPG-830 after 200 hours due to infiltration by the molten KF-UF_4-NaF salt at 700 ºC and 6 bar (abs).

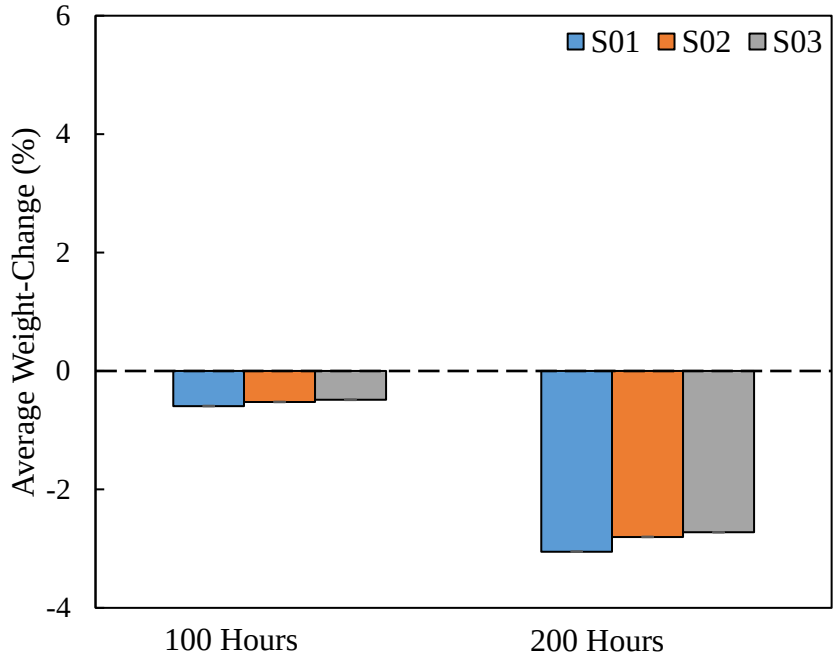

Figure 70b. Weight-change in Mersen 2175P after 100 and 200 hours at 850 ºC and 10 bar (abs), due to infiltration by the molten KF-UF_4-NaF salt.

It must be noted that the infiltrated graphite specimens exhibited weight-loss even after salt infiltration, thus indicating possible break-down, and/or degradation, and/or disintegration of graphite's structure because of internal and external induced stresses.

4.9 Effects of Applied Pressure on Molten Salt Infiltration in Graphite

The effects of applied pressure on molten salt infiltration was evaluated by testing Mersen 2175P with pore-size 0.9 µm in the molten KF-UF_4-NaF salt for 200 hours at 850 °C, and 10 and 11 bar (abs) respectively. **Figure 71** and **Figure 72** show the SEM-EDS surface and cross-sectional characterization of the infiltrated graphite specimens.

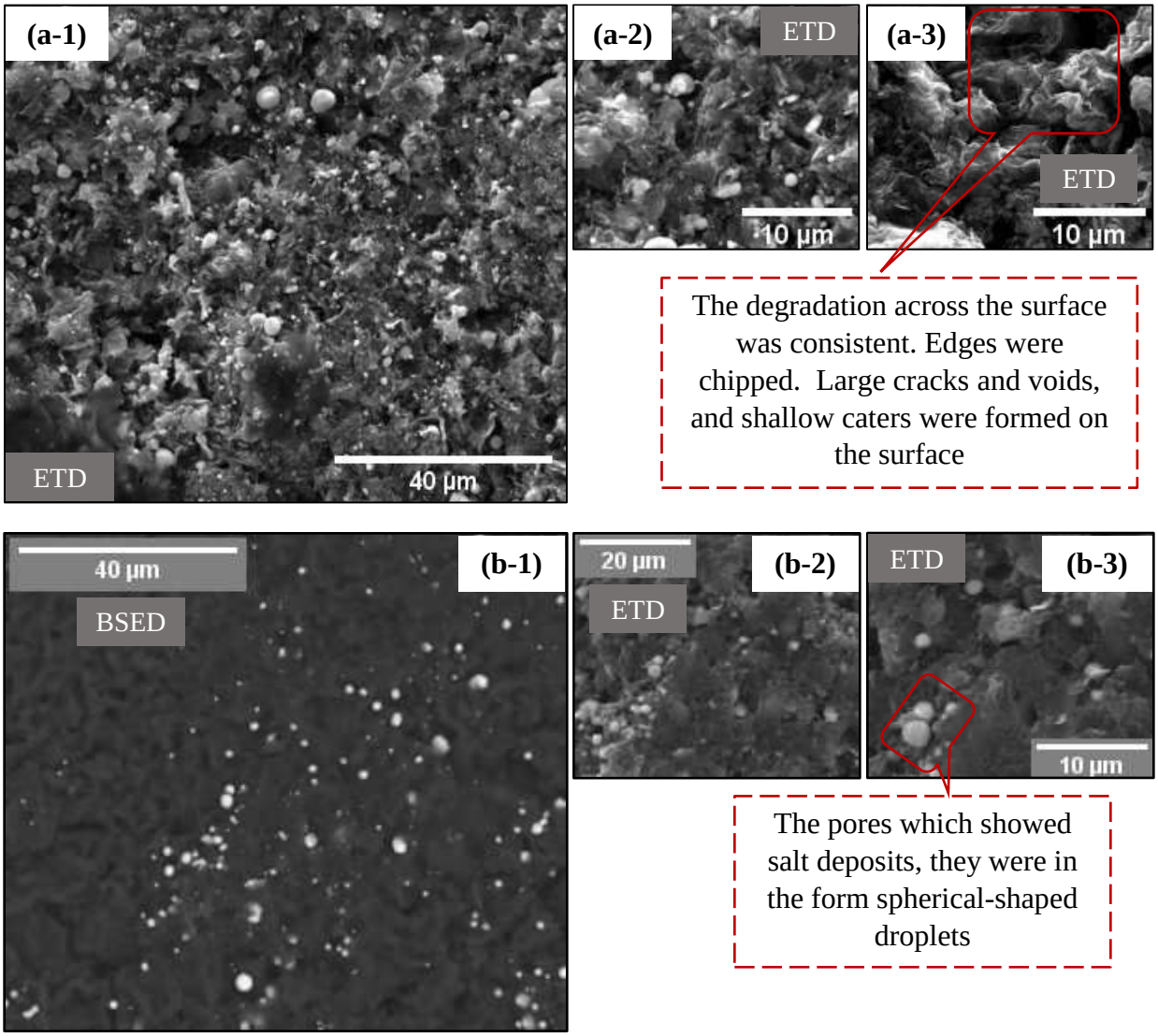

Figure 71. SEM surface characterization of the infiltrated graphite grade, Mersen 2175P by the molten KF-UF_4-NaF salt after 200 hours at 850 °C, and **(a)** 10 bar (abs), and **(b)** 11 bar (abs).

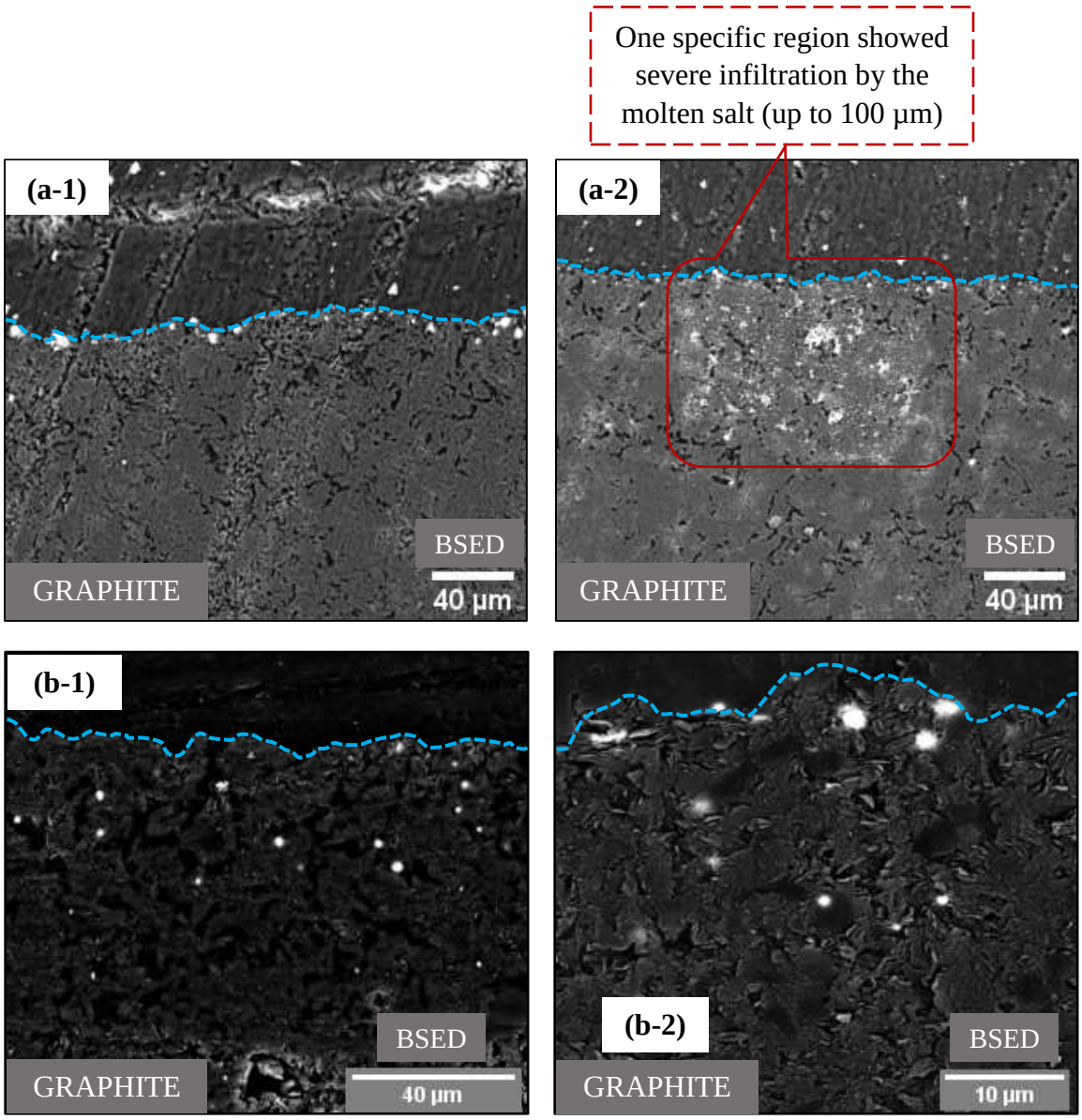

Figure 72. SEM cross-sectional characterization of the infiltrated graphite grade, Mersen 2175P by the molten KF-UF_4-NaF salt after 200 hours at 850 °C, and **(a)** 10 bar (abs), and **(b)** 11 bar (abs).

Table 14 provides the molten salt infiltration data for the graphite grade, Mersen 2175P, at the required conditions.

Table 14. Molten KF-UF_4-NaF salt infiltration data for Mersen 2175P after 200 hours at 850 ºC.

Graphite Details					Applied Pressure (bar (abs))	Infiltration Depth Range (µm)
Grade	Pore-Size (µm)	Porosity (%)	Raw Material	Process		
Mersen 2175P	0.9	13.5	Pitch	Iso-Moulding	10	6.95–101.04*
					11	10.22–146.99

* The infiltration was severe (i.e. up to 100 µm) only in one specific region as shown in **Figure 72(a-2)**, however it cannot be confirmed whether it was due to molten salt infiltration, or polishing when preparing the specimen for the SEM analysis.

It was found that after 200 hours, the infiltration-rate in Mersen 2175P at 11 bar (abs) was greater than at 10 bar (abs). It can be inferred that the infiltration-rate increases with applied pressure, where the maximum molten salt infiltration at 11 bar (abs) was seven folds higher than at 10 bar (abs). Here also, the graphite specimens exhibited weight-loss even after molten salt infiltration possibly due to break-down, and/or degradation, and/disintegration of graphite's structure caused because of salt infiltration, and/or temperature, and/or applied pressure. This is confirmed from the SEM surface images (refer **Figure 71a-1**, **Figure 71a-3**, **Figure 71b-1** and **Figure 71b-3**) of the infiltrated graphite specimens which show chipped edges, formation of large cracks or voids, and shallow caters. The average weight loss in Mersen 2175P at 10 and 11 bar (abs) was measured as 2.86 ± 0.00% and 0.11 ± 0.00% respectively. The large difference in the weight loss can also be attributed to other factors like irregularities in the microstructure (i.e. pore-size and shape, and pores exposed on the surface), and manufacturing defects (pre-existing cracks and caters) in the supplied graphites.

4.10 Effects of Graphite's Microstructure on Molten Salt Infiltration

The effects of graphite's microstructure on the infiltration-rate was evaluated by testing different graphite grades like Mersen 2175P, Ibiden T6 and SGL R7650 with pore-sizes 0.9 µm, 0.6 µm and 1.1 µm at 850 ºC and 11 bar (abs), and Entegris TM, Ibiden FGM19 and Toyo Tanso HPG-510 with pore-sizes 1.5 µm, 1.02 µm and 1.2 µm at 850 ºC and 8 bar (abs), in the molten KF-UF_4-NaF salt for 200 hours. **Figure 71b**, **Figure 72b**, **Figure 73**, **Figure 74**, **Figure 75** and **Figure 76** shows the SEM surface and cross-sectional characterization of the infiltrated graphite specimens.

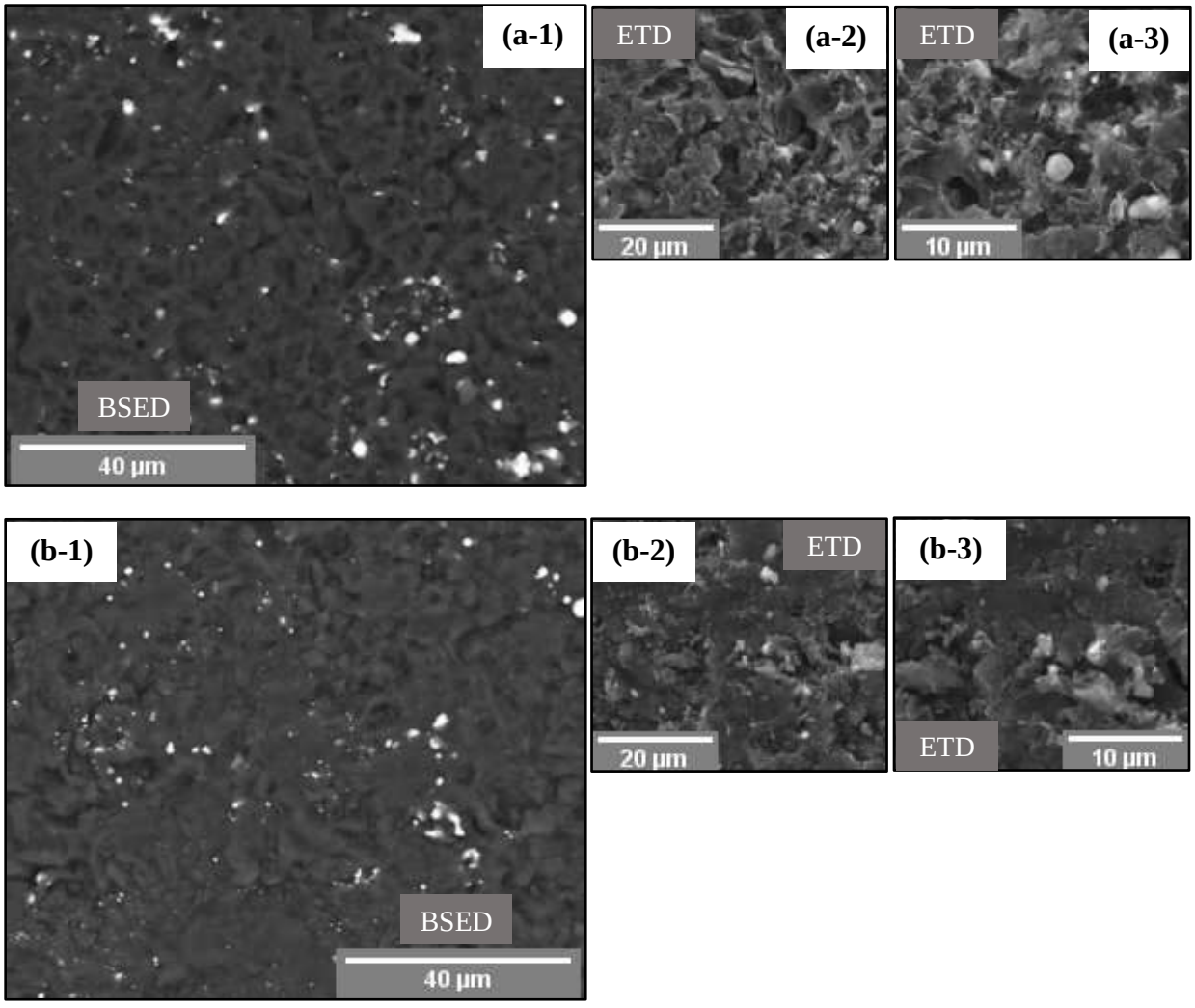

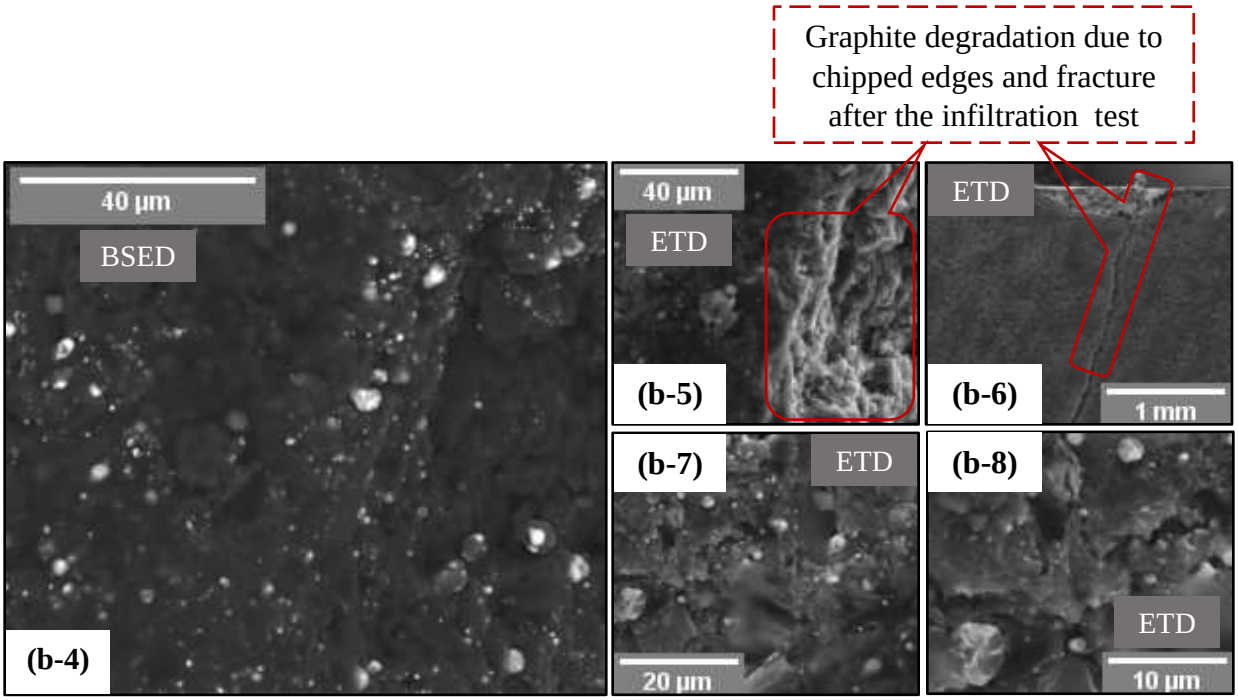

Figure 73. SEM surface characterization of the infiltrated graphite grades, **(a)** Ibiden T6, and **(b)** SGL R7650, by the molten KF-UF_4-NaF salt after 200 hours at 850 °C and 11 bar.

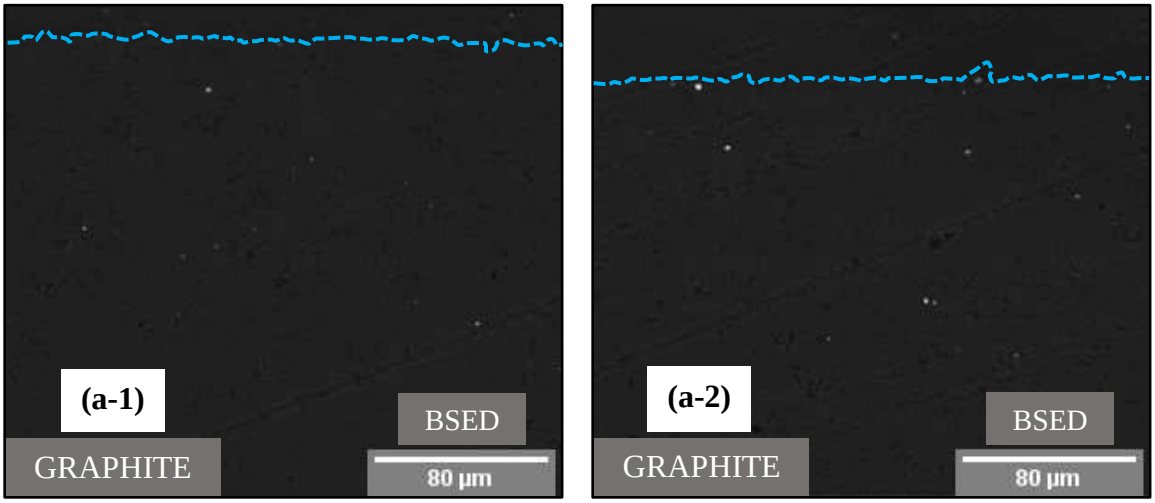

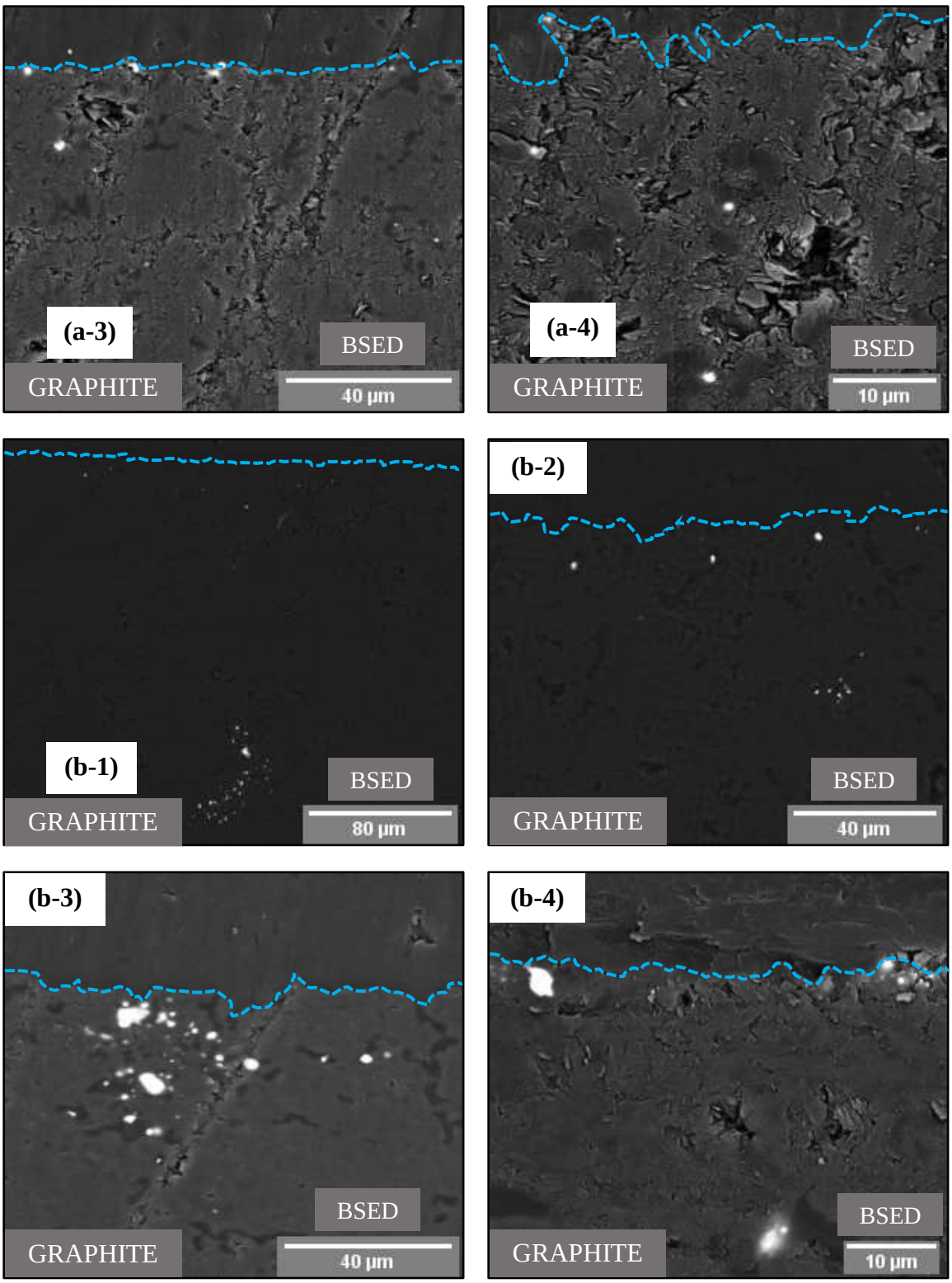

Figure 74. SEM cross-sectional characterization of the infiltrated graphites, **(a)** Ibiden T6, and **(b)** SGL R7650, by the molten KF-UF_4-NaF salt after 200 hours at 850 °C and 11 bar (abs).

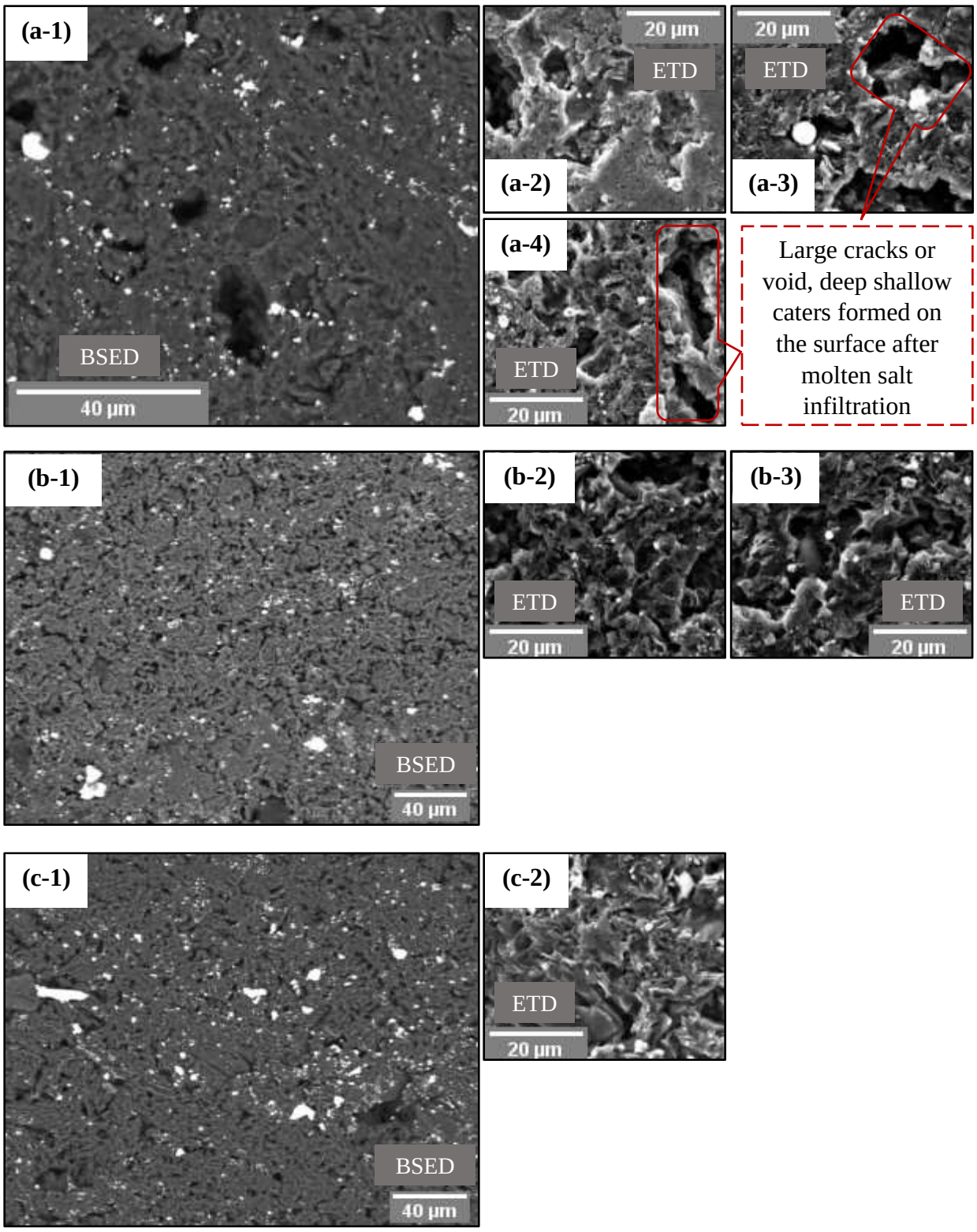

Figure 75. SEM surface characterization of the infiltrated graphite grades, **(a)** Entegris TM, **(b)** Ibiden FGM19, and **(c)** Toyo Tanso HPG510, by the molten KF-UF_4-NaF salt after 200 hours at 850 °C and 8 bar (abs).

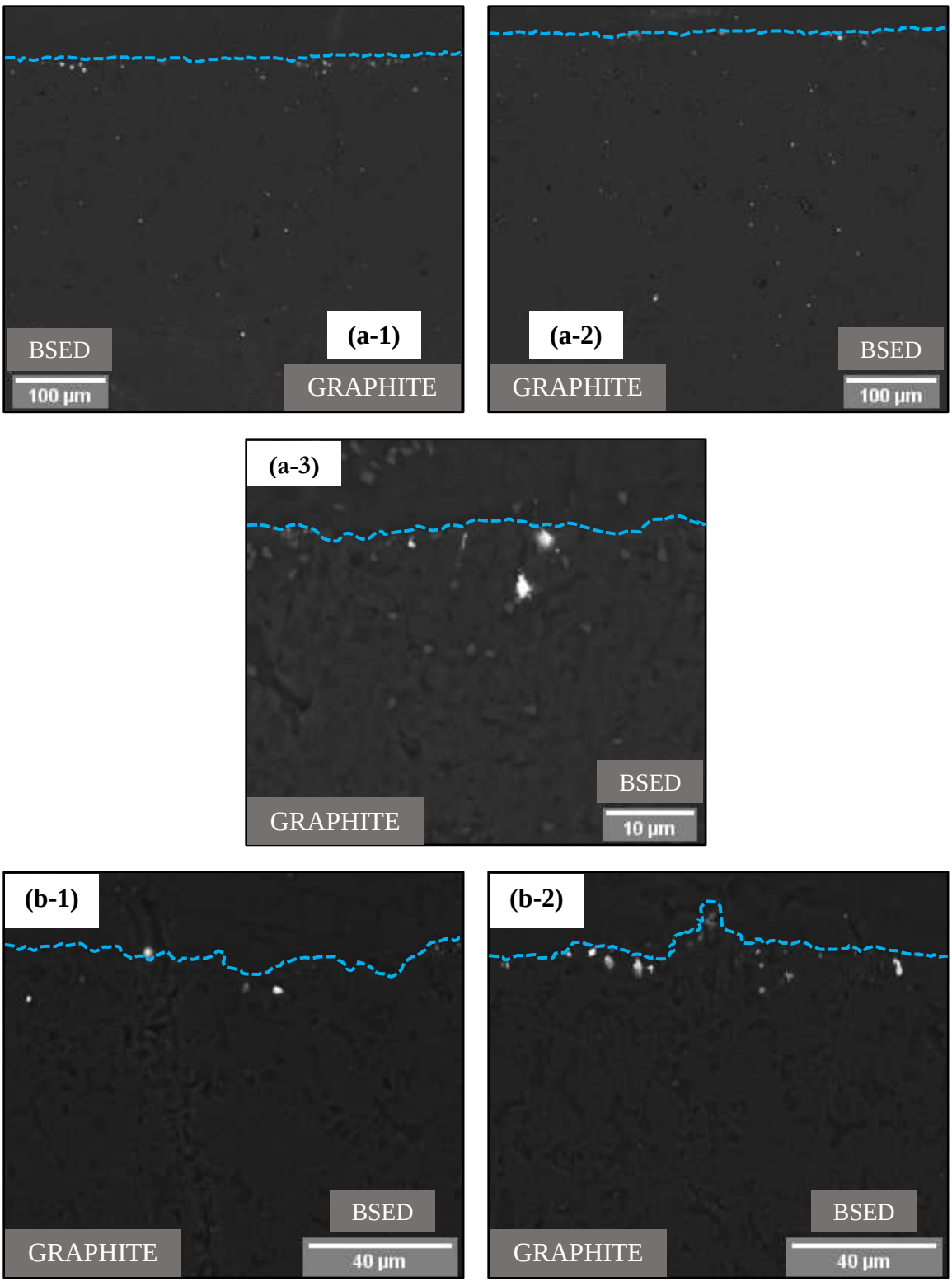
(a-1)
BSED
100 μm
GRAPHITE
(a-2)
GRAPHITE
BSED
100 μm
(a-3)
GRAPHITE
BSED
10 μm
(b-1)
GRAPHITE
BSED
40 μm
(b-2)
GRAPHITE
BSED
40 μm

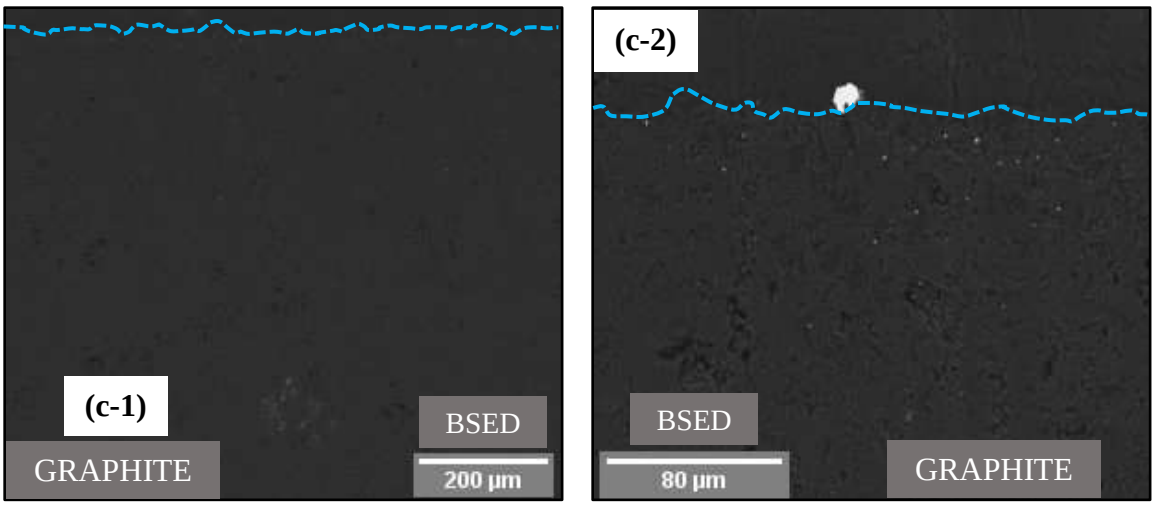

Figure 76. SEM cross-sectional characterization of the infiltrated graphites, **(a)** Entegris TM, **(b)** Ibiden FGM19, and **(c)** Toyo Tanso HPG510, by the molten KF-UF_4-NaF salt after 200 hours at 850 °C and 8 bar (abs).

Table 15 provides the molten salt infiltration data for graphite grades, Mersen 2175P, Ibiden T6, SGL R7650, Entegris TM, Ibiden FGM19 and Toyo Tanso HPG-510, at the required conditions.

Table 15. Molten KF-UF_4-NaF salt infiltration data for graphite grades, Mersen 2175P, Ibiden T6, SGL R7650, Entegris TM, Ibiden FGM19 and Toyo Tanso HPG-510, at 850 °C after 200 hours.

Graphite Details					Applied Pressure (bar (abs))	Infiltration Depth Range (µm)
Grade	Pore-Size (µm)	Porosity (%)	Raw Material	Process		
Mersen 2175P	0.9	13.5	Pitch	Iso-Moulding	10	10.22–146.99
Ibiden T6	0.6	9	Coal	CIP	10	14.37–189.08
SGL R7650	1.1	10	Coke	Iso-Moulding	10	4.78–338.16
Entegris TM	1.5	85	Pet Coke	Iso-Moulding	8	25.70–647.54
Ibiden FGM19	1.02	12	Coal	CIP	8	8.56–400.00
Toyo Tanso HPG-510	1.2	16	Not Available to Public	Iso-Moulding	8	8.12–39.71

The infiltration-rate was found in the increasing order of Mersen 2175P (0.9 µm pore-size; 13.5% porosity) < SGL R7650 (1.1 µm pore-size; 10% porosity) < Ibiden T6 (0.6 µm pore-size; 9% porosity) at 850 °C and 10 bar (abs), and after 200 hours; and Toyo Tanso HPG-510 (1.2 µm pore-

size; 16% porosity) < Ibiden FGM19 (1.02 µm pore-size; 12% porosity) < Entegris TM (1.5 µm pore-size; 85% porosity) at 850 °C and 8 bar (abs), and after 200 hours. The graphite grades, Mersen 2175P, Ibiden T6 and SGL R7650 exhibited weight-loss after molten salt infiltration, which was measured (average weight-loss) as $0.11 \pm 0.00\%$, $0.14 \pm 0.00\%$ and $0.14 \pm 0.00\%$ respectively. The infiltrated graphite specimens showed chipped edges (refer **Figure 73b-4** and **Figure 73b-5**), formation of large cracks or voids, and deep shallow caters (refer **Figure 73a**, **Figure 73b**, **Figure 75a**, **Figure 75b** and **Figure 75c**). As shown in **Figure 73b-7** and **Figure 73b-8**, the salt infiltration in the chipped edges was severe possibly caused by the change in the graphite's microstructure. SGL R7650 was also fractured after the infiltration test (refer **Figure 73b-6**). This cannot be confirmed because it is not possible to predict whether the infiltration intensifies before or after the edges are chipped.

Unlike these graphite grades, Entegris TM, Ibiden FGM19 and Toyo Tanso HPG-510 showed weight-gain after molten salt infiltration, which was measured (average weight-gain) as $0.018 \pm 0.00\%$, $0.06 \pm 0.00\%$, $0.01 \pm 0.00\%$ respectively. The weight-gain was minimal, and indicated that the break-down, and/or degradation and/or disintegration of graphite could have been less severe or less intense. Furthermore, it could also be because of increased molten salt infiltration due to differences in the graphite's original microstructure (refer **Table 15**). It was observed that even among these three graphite grades, the molten salt infiltration in Toyo Tanso, HPG-510 with pore-size 1.2 µm was comparatively lower than in Ibiden, FGM19 with pore-size 1.02 µm, thus indicating that apart from pore-size, other factors like porosity (i.e. number of pores in graphite), non-uniformity in the pore-size (i.e. irregular shaped pores) and its distribution (i.e. number of open pores available on the surface that will be exposed to molten salt during the infiltration test), microstructure (i.e. defects in non-infiltrated graphite due to manufacturing process), etc. could also influence molten salt infiltration in graphite.

Based on the current tests, it is not possible to identify the reason that leads to break-down of graphite. The break-down of graphite could be due to thermal-induced stresses, or/and external stresses caused by the exerted pressure, or/and internal stresses caused by salt infiltration, or/and machining induced residual stresses, or/and salt-graphite interaction. It should also be noted that some of the "virgin" graphites already showed the presence of large cracks on its surface (refer **Figure 77** and **Figure 78**). These cracks also known as "Mrozowshi" cracks are formed during the

graphite's manufacturing processes such as baking or graphitization (which involves heating the graphites to high temperatures). These cracks mostly form during cool-down from the graphitization temperatures [[103]]. Generally, these cracks increase the graphite's thermal shock resistance by accommodating the thermal expansion without destroying its structure. However, they can also create new pore-entrances and ultimately pathways for molten salt infiltration. This along with other irregularities such as inconsistent porosity and pore-sizes in the graphite can result in increased molten salt infiltration and eventually lead to the total destruction or failure of the graphite component Generally, smaller and uniformly distributed pores are known to exhibit better resistance to degradation due to their enhanced capabilities to accommodate internal stresses among the neighboring pores.

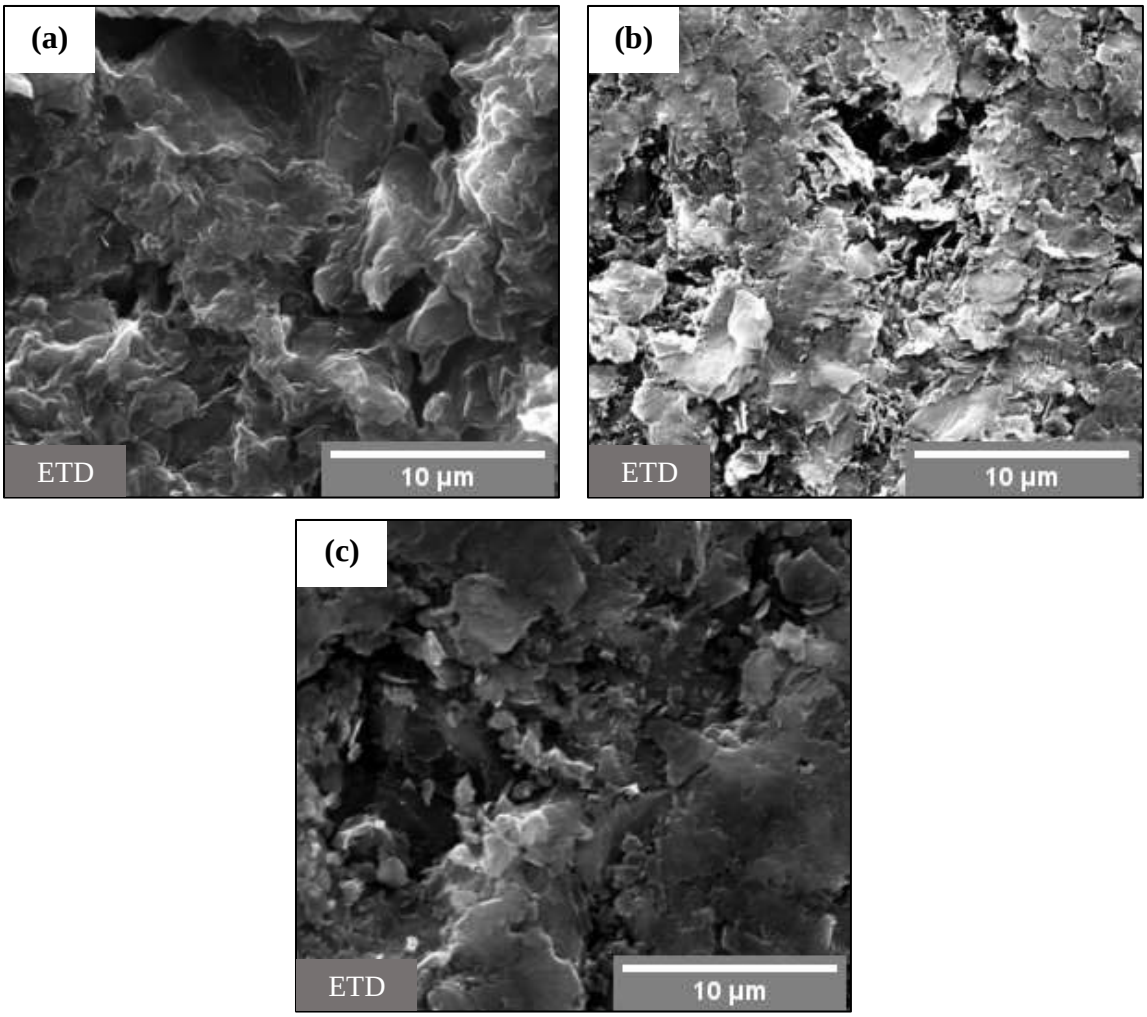

Figure 77. SEM-EDS surface characterization of "virgin" graphite grades, **(a)** Mersen 2175P, (**b)** Ibiden T6, and **(c)** SGL R7650.

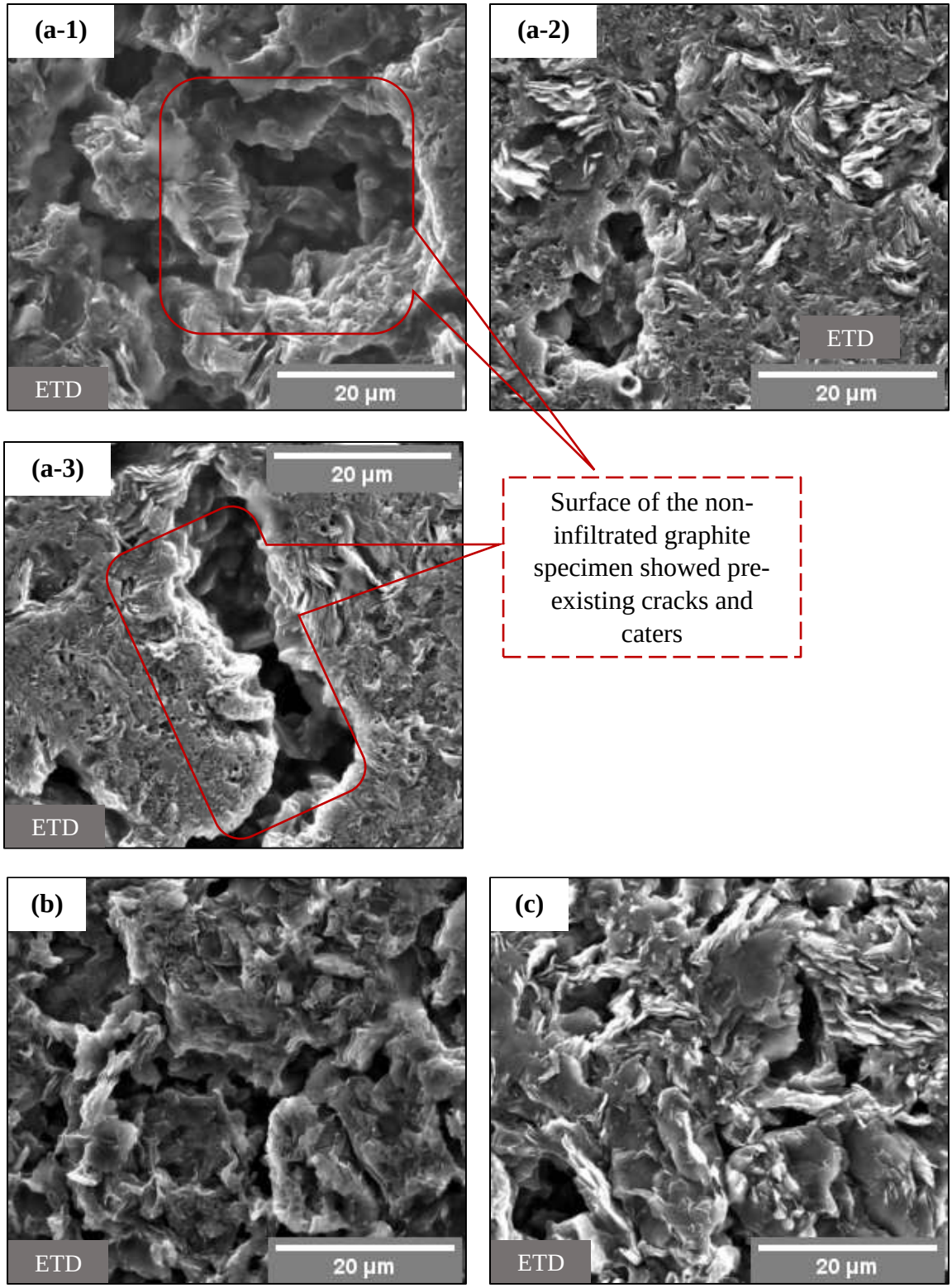

Figure 78. SEM-EDS surface characterization of "virgin" graphite grades, **(a)** Ibiden FGM19, (**b)** Toyo Tanso HPG-510, and **(c)** Entegris TM.

Another possibility of degradation or disintegration is the molten salt-graphite interaction. Though graphite is chemically inert in molten fluoride salts, studies [36] have still shown possible fluorination by replacement of certain C-H bonds (viz. a residual from its manufacturing process) with C-F bonds, thus forming organic compounds like C-F_x, where x is 2, 3 and 4. The high-resolution XPS spectrum (refer **Figure 79**) obtained for the F (1s) peaks also showed presence of C-F (CF_2) compounds at the salt-graphite interface.

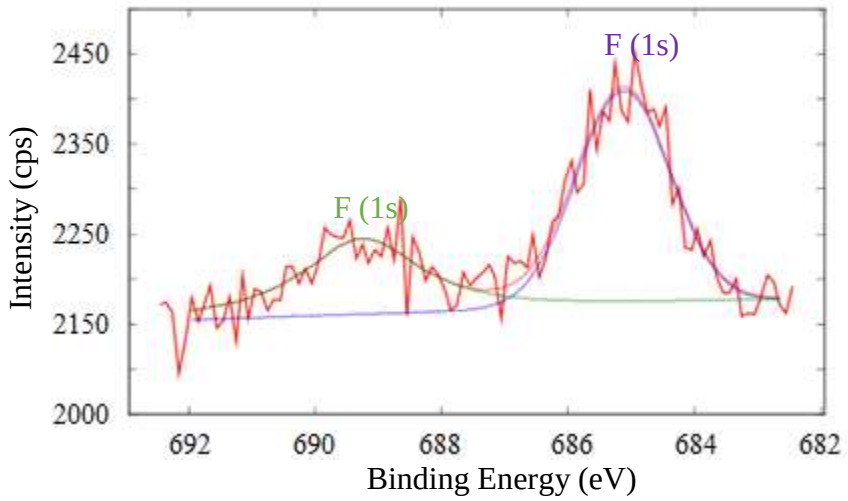

Peak Details	Measured Position (eV)	NIST Database (eV)	Peak Assignment
F (1s)	685.2	685.4 [123]	Metal-F (UF_4)
F (1s)	689.0	689.0 [124]	CF_x (CF_2)

Figure 79. XPS high-resolution spectra for F (1s) peaks from the non-sputtered Toyo Tanso HPG-830 graphite specimen after 200 hours of infiltration by molten KF-UF_4-NaF salt at 700 °C and 6 bar (abs).

However, as shown in **Figure 80**, the only thermodynamically favorable reactions that can form the C-F compounds are the graphite-F_2 reactions in the temperature range of 500 to 900 °C. There should not be any F_2 gas produced during the infiltration test as the fluoride salts cannot thermally decompose to produce the fluorine gas. The only fluorine-based gas that can be produced is the hydrogen fluoride (HF) gas from the hydrolysis of the fluoride salt in the presence of moisture and the salt is purified to remove/reduce this moisture, but even if it is present in the salt it will still not react with graphite as the HF-graphite interactions are non-spontaneous for the selected temperatures (i.e. not thermodynamically favorable).

4.11 Metallic Effects on Molten Salt-Graphite Interaction

Metallic inclusions/contaminants were observed floating on the liquid salt-mixture after the infiltration test (refer **Figure 81**). The SEM-EDS analysis showed that these inclusions were mainly nickel, nickel and tungsten, or nickel with trace amounts of silicon, aluminum, and iron. The source of these inclusions/contaminants were from the degradation of nickel crucible (Ni) and nickel wire (Ni)/tungsten wire (W) (refer **Figure 82**)/graphite rod and washers (i.e. Si, Al and Fe) that were used to hold the graphite specimens during the infiltration test. In the absence (trace amounts) of chromium and iron, nickel is the most active element which can react with the fluoride salt to form nickel-fluoride (NiF_2) compounds. If UF_3 is present or formed in the salt during the infiltration test then NiF_2 can react with UF_3 to form UF_4 and liberate Ni metal (refer **Figure 80**). The nickel metal being less dense will float and accumulate on the liquid salt.

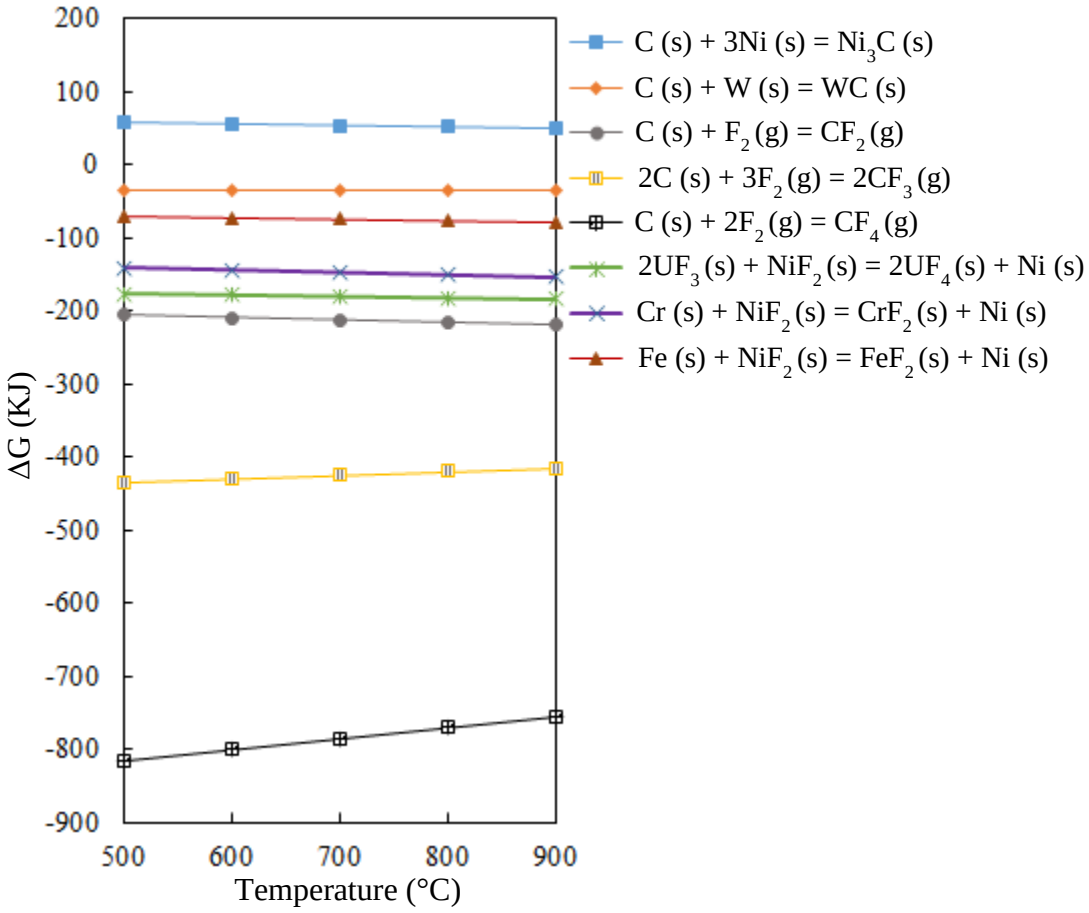

Figure 80. Gibbs free energy of formation for all possible graphite reactions in molten KF-UF_4-NaF salt [HSC Chemistry® 10 Software].

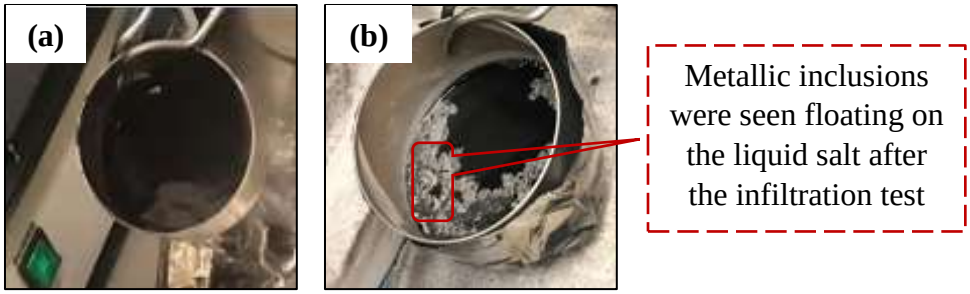

Figure 81. The KF-UF_4-NaF salt **(a)** before, and **(b)** after infiltration test.

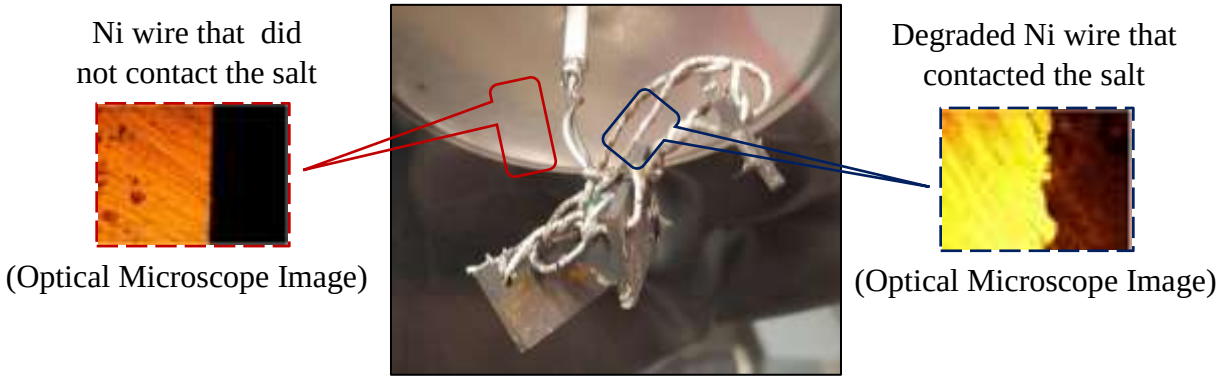

Figure 82. Ni and molten KF-UF_4-NaF salt interaction at 700 ºC.

Some studies have shown carburization of nickel and tungsten is only possible at high temperatures above 900°C, which is also supported by the thermodynamic data (refer **Figure 80**) obtained for nickel and tungsten carburization as a function of temperature [[125], [126]]. So, since carburization is not possible, then the only possibility that caused the degradation of nickel and tungsten wires could have been galvanic corrosion due to dissimilar metal contact with the graphite specimens in the electrolytic molten KF-UF_4-NaF salt medium. However, based on the current tests this cannot be confirmed and will require more understanding on this degradation mechanism.

CHAPTER 5

5 CONCLUSION AND FUTURE WORKS

Different purification processes were used to purify the molten halide salts, where the chloride salt (KCl-$MgCl_2$-NaCl) was purified using thermal purification process (i.e. heat-treatment), and chemical purification process (viz. heat-treatment with Mg addition), while the fluoride salt (KF-UF_4-NaF) was purified only using thermal purification process (i.e. heat-treatment). The purification processes were effective in reducing the corrosive contaminants (moisture and oxygen-based) in the salt without compromising its chemistry.

The influence of salt impurities on the corrosion behavior of nickel-based alloy was investigated by conducting static corrosion tests for the H230 alloy in the molten KCl-$MgCl_2$-NaCl salt with different purity conditions at 800 ºC for 100 hours. It was found that the H230 alloy exhibited excellent corrosion resistance (i.e. no mass-loss was observed) in the salt with very low concentration of impurities (viz. salt condition (b), high-purity salt that was thermally and chemically purified using Mg), while the corrosion in the salt with the highest concentration of impurities (viz. salt condition (c): ICL salt without any purification) was severe (i.e. higher mass-loss observed) even though the specimens were did not contact the molten salt. This also indicates that the moisture in the salt along with its own vaporization at higher temperatures does not only intensifies corrosion but also corrodes the non-exposed alloys. The corroded alloys showed extensive pitting across the surface and a porous corrosion layer along its cross-section because of chromium depletion. Furthermore, appending the purified salt with Mg as a corrosion inhibitor resulted in an even higher mass-loss possibly because of interaction between nickel (nickel-based alloy) and Mg pieces.

Additionally, various different alloys (i.e. nickel-based alloys such as Inconel® 718, Hastelloy® C276, Haynes® 230® and ferrous-based alloys such as stainless steel 316L and 709-4B2, 709-RBB and 709-RBB*) were studied for their corrosion characteristics in the molten KCl-$MgCl_2$-NaCl salt (ICL salt, thermally and chemically purified using Mg) at 800 ºC for 100 hours. The mass-loss (mg/cm^2) was in the increasing order of C276 < 316L < 709-RBB* < IN718 < H230 < 709-RBB < 709-4B2. The corrosion in these alloys was attributed to the Cr content and presence of inert elements like Mo and W. However, their usefulness is restricted because of their non-uniform

distribution in the alloy. Furthermore, the less corrosion in 316L also indicates that molten salt corrosion is not only influenced by the alloy composition but also on other factors like impurity concentration in the salt and the microstructure of the alloy, which depends on the manufacturing or refining and heat-treatment processes. Additionally, Mg and O presence in the pits (created by the outward diffusion of Cr) indicated that the salt infiltrates into the pores and should continue its attack on the alloy until it reaches equilibrium i.e. either the impurities in the salt are completely exhausted or the molten salt is saturated with the respective oxide or chloride compounds.

To mitigate molten salt corrosion, the various nickel-based alloys and ferrous-based alloy were boronized, and studied for their compatibility in the molten KCl-$MgCl_2$-NaCl salt at 800 ºC for 100 hours. Both these alloys were boronized in the same agent and at the same temperature and time. Both these alloys showed a different morphology of the boride layer. The boride layer composition and its properties depends on the alloy composition, while its thickness depends on the boronizing time and temperature. The boride layer also consisted of thin undesirable silicide layer or structures, which easily cracked and/or peeled under mechanical and thermal stresses. The boride layer in both these alloys comprised of either single or multiple solid "compound" layer/s, the outermost solid silicide composite structures or layer, and an innermost solid "dispersed" layer or "diffusion" zone. The boride layers were non-porous thus indicating a strong adhesion between the coating and the substrate. The borided alloys exhibited better resistance to molten salt corrosion than the non-borided alloys, where the mass-loss (mg/cm^2) was in the increasing order of boronized C276 < boronized IN718 < C276 < IN718 among the nickel-based alloys, and boronized 316L < 316L among the ferrous-based alloy. Unlike

For the boronized alloys, the boride layer (after exposure to molten salt) was still intact, solid (non-porous and no cracking or peeling), and strongly adhered to the substrate, thus protecting the alloy. This shows the compatibility of boride layer in molten salt, and also its stability at high temperatures. The mass-loss in some of the boronized alloys (IN718) was attributed to the depletion of the outermost silicide layer or structures, which can easily break because of thermal mismatch owing to the differences in the thermal expansion coefficient. For 316L, the boronization process still needs to be developed to consider proper surface preparation, boronizing agent, temperature and time as the boride layer in some of specimens spalled after the boronization process. The properties (hardness) measured for the boronized and non-boronized alloys before

and after exposure to molten salt showed that there was no significant change in the hardness of the boronized alloys after exposure to molten salts. The corroded non-boronized alloys showed an increase in the hardness value due to change in the microstructure (corrosion layer, Cr depletion and Ni or Fe enrichment) of the alloy. However, the corrosion layer is porous and weak, and will not provide any protection even with its increased hardness value against induced stresses. The boronized alloys can be considered as a promising candidate material for CSP plant technologies and molten salt reactors. It can also retain most of its physical and mechanical properties. If they exhibit good sustainability in molten salts then they can be applied to critical components like valve balls and seats, pump impellors, etc. in the power plants and reactors. The candidate material selected from the static corrosion tests needs to be further studied in non-conventional flow-conditions for longer time duration. A forced circulation molten salt loop was designed and built to achieve these objectives.

Static tests were conducted for several grades of nuclear graphites in the molten KF-UF_4-NaF salt. It was found that the molten fluoride salt exhibits poor wettability with the graphite. However, at higher applied pressures, it infiltrates into the graphite pores. The infiltration also depends on other factors such as microstructure of "virgin" graphites, pore-size and porosity. At higher pressures (9 bar (abs)) and temperatures (>800 °C), degradation and/or disintegration of graphite's structure was also observed possibly caused due molten salt-graphite interaction (fluorination), thermal stresses, internal stresses (due to salt crystallization), external stresses (applied pressures), and/or residual stresses (due to machining, drilling and polishing).

The Ni and W wires which were used initially to hold the graphite specimens in the molten salt showed severe degradation possibly due to galvanic corrosion or other material degradation mechanism which needs more investigation. Metallic inclusions were seen floating on the liquid salt which were mainly Ni (wire and/or crucible) and/or W (wire) and trace amounts of other impurities like Si, Al and Fe. The Ni presence indicates there could be a possible interaction between the nickel crucible and the molten KF-UF_4-NaF salt, which produces NiF_2 compounds. The NiF_2 then reacts with UF_3, Fe and/or Cr depending on their presence in the molten salt to liberate Ni metal. Though, more detailed investigation is needed to understand this phenomenon.

However, there are several more studies that should be pursued in the future which include,

1. Refine the boronization process for ferrous-based alloys to ensure the boride layer exhibits the same level of stability as of nickel-based alloys.
2. Conduct flow corrosion studies for the selected materials.
3. Examining molten salt infiltration in irradiated graphite grades.
4. Examining the infiltrated graphite specimens for their characteristics and mechanical properties.
5. Studying the effects of impurities and fission products in the fluoride salt-mixture on the graphite infiltration.
6. Determining the threshold temperature and applied pressure for infiltration in the selected graphite grades and pore-sizes.
7. Determining the infiltration rate as a function of time (≥500 hours) in the selected graphite grades and pore-sizes.
8. Shim testing for different candidate materials with a higher anodic potential than the graphite and the contacting metals or alloys in KF-UF_4-NaF salt-mixture to mitigate the effects of galvanic corrosion.
9. Studying the flow-induced effects on the infiltration and degradation of graphite by the liquid KF-UF_4-NaF salt-mixture.

MSRs are the next generation advanced reactors, which uses molten halide salts to enhance its efficiency and safety. As discussed, material selection is a challenge for these reactors considering the (lower) economics of nuclear reactors. This study will assist in creating a database for various commercially available materials that may or may not be compatible with molten salts. Furthermore, this study also emphasizes on the causes (impurities, alloy composition and microstructure) of corrosion in molten salts and solutions to mitigate them (boronization). The loss of alloying elements not only weakens the alloy structure, but also compromises on the alloy properties (i.e. physical and chemical resistance), hence, this collective information could assist in the development of new materials, or expedite the process of materials selection for critical components of the MSRs.

REFERENCES

[1] International Atomic Energy Agency. Energy, Electricity and Nuclear Power Estimates for the Period up to 2050, Reference Data Series No. 1. *IAEA*, Vienna, (2019).

[2] International Atomic Energy Agency. The Fukushima Daiichi Accident, GC(59)/14. *IAEA*, Vienna, (2015).

[3] International Atomic Energy Agency, Nuclear Power Technology Development Section and INPRO Section. *IAEA*, Vienna, (2012)

[4] Sheil, R.J., Evans, R. B., and Watson, G. I. Molten Salt-Graphite Compatibility Test. Results of Physical and Chemical Measurements. *Oak Ridge National Lab*, (1959).

[5] Williams, D.F., Toth, L.M., and Clarno, K.T. Assessment of Candidate Molten Salt Coolant for Advanced High-Temperature Reactor (AHTR). *Oak Ridge National Lab*, (2006).

[6] Vignarooban, K., Arvay, A., Hsu, K., and Kanan, A.M. Heat Transfer Fluids for Concentrating Solar Power Systems-A Review. *Appl. Energy* 146, 383–396, (2015).

[7] Ding, W. Bank, A., and Bauer, T. Molten Chloride Salts for Next Generation CSP Plants: Selection of Promising Chloride Salts & Study on Corrosion of Alloys in Molten Chloride Salts. *AIP Conference Proceedings*. vol. 2126, issue 1, (2019).

[8] Ding, W., Shi, H, et.al. Molten Chloride Salts for Next Generation Concentrated Solar Power Plants: Mitigation Strategies against Corrosion of Structural Materials. *Sol. Energy Mater. Sol. Cells*. vol. 193, 298–313, (2019).

[9] Laird, W. J. Salt Bath Heat Treatment and Equipment. ASM Handbook, *ASM International*, (2014).

[10] Hoglund, B. Construction Materials for Molten-Salt Reactors. *Fluid Fuel Reactors*, Addison-Wesley (1958), chapter 13, p. 595.

[11] Sarvghad, M., Maher, S. D., Collard, D., Tassan, M., and Will, G. Materials Compatibility for the Next Generation of Concentrated Solar Power Plants. *Energy Storage Mater.* 14, 179–198, (2018).

[12] Liu, B., Wei, X. L., Wang, W. L., Lu, J. F., and Ding, J. Corrosion Behavior of Ni- Based Alloys in Molten NaCl-CaCl2-MgCl2 Eutectic Salt for Concentrating Solar Power. *Sol. Energy Mater. Sol. Cells* 170, 77–86, (2017).

[13] Ding, W., Shi, H., Xiu, Y., Bonk, A., Weisenburger, A., and Jianu, A. Hot Corrosion Behavior of Commercial Alloys in Thermal Energy Storage Material of Molten $MgCl_2$/KCl/NaCl under Inert Atmosphere. *Sol. Energy Mater. Sol. Cells* 184, 22–30, (2018).

[14] Hofmeister, M., Klein, L., Miran, H., Rettig, R., Virtanen, S., and Singer, R.F. Corrosion Behavior of Stainless Steels and a Single Crystal Superalloy in a Ternary LiCl-KCl-CsCl Molten Salt. *Corros. Sci.* 90, 46–53, (2015).

[15] Hosoya, Y., Terai, T., Yoneoka, T., and Tanaka, S. Compatibility of Structural Materials with Molten Chloride Mixture at High Temperature. *J. Nucl. Mater.* 248, 348–353, (1997).

[16] Liu, B., Wei, X. L., Wang, W. L., Lu, J. F., and Ding, J. Corrosion Behavior of Ni-Based Alloys in Molten NaCl-$CaCl_2$-$MgCl_2$ Eutectic Salt for Concentrating Solar Power. *Sol. Energy Mater. Sol. Cells* 170, 77–86, (2017).
[17] Logier, J., Wang, J., Villalpando, O., Jalbuena, A., and Ravi, V. Corrosion of Ferrous Alloys in a Molten Chloride Salt for Solar Thermal Energy Storage. *NACE, Corros*, No. 9562, (2017).
[18] Olson, L., Ambrosek, J. W., Sridharan, K., Anderson, M. H., and Allen, T. R. Materials Corrosion in Molten LiF-NaF-KF Salt. *J. Fluorine Chem.* 130, 67–73, (2009).
[19] Gomez-Vidal, J. C. Corrosion Resistance of MCrAlX Coatings in a Molten Chloride for Thermal Storage in Concentrating Solar Power Applications. *Materials Degradation*, (2017).
[20] Gomez-Vidal, J. C., and Morton, E. Castable Cements to prevent Corrosion of Metals in Molten Salts. *Solar Energy Materials and Solar Cells*, Volume 153, 44–51, (2016).
[21] Porcayo-Calderon, J. et al. Electrochemical Performance of Ni20Cr Coatings applied by Combustion Powder Spray in $ZnCl_2$-KCl Molten Salts. *Int. J. Electrochem. Sci.* 7, 1134–1148, (2012).
[22] Tristancho-Reyes, J. L., Chacón-Nava1, J. G. et. al. Hot Corrosion Behaviour of NiCrFeNbMoTiAl Coating in Molten Salts at 700 °C by Electrochemical Techniques. *Int. J. Electrochem. Sci.* 6, 432–441, (2011).
[23] Şahin, S. Effects of Boronizing Process on the Surface Roughness And Dimensions of AISI 1020, AISI 1040 and AISI 2714. *Journal of Materials Processing Technology*. 209, (2009).
[24] Matsuda, F., Nakata, K., and Nishio, Y. Surface Hardening of Ni-Base Alloys with Boronizing Technique. *Tans of JWRI.* 16(1) 145–157, (1987).
[25] Luo, W., Selvadurai, U., and Tillmann, W. Effect of Residual Stress on the Wear Resistance of Thermal Spray Coatings. *J Therm Spray Tech* 25, 321–330 (2016).
[26] Burchell, T. D., Fuller, E. L., et. al. Graphite for the Nuclear Industry. *Oak Ridge National Lab*, CONF-9105220-1, (1991).
[27] Virgil, T. S., and Kalyana, I. P. Reactor Graphite. *Inorg Mater*, 39: S46–S58, (2003).
[28] Nightingale, R. E. Graphite: Advantages, Limitations, and Applications. *Pacific Northwest Laboratories*, (1962).
[29] Morel, C.F. Surface Tensions of Molten Salts and Contact Angle Measurements of Molten Salts on Solids. *EURATOM*, EUR 4482 e, (1970).
[30] Zhoutong, H., Lina, G., et. al. Molten FLiNaK Salt Infiltration into Degassed Nuclear Graphite under Inert Gas Pressure. *Carbon* 84, 511–518, (2015).
[31] MacPherson, H. G. Molten-Salt Reactor Project: Quarterly Progress Report. *Oak Ridge National Laboratory*, ORNL-2723, (1959).
[32] Briggs, R. B. Molten-Salt Reactor Program Progress Report. *Oak Ridge National Laboratory*, ORNL-3122, (1961).
[33] He, Z., Gao, L., Wang, X., Zhang, B., et. al. Improvement of Stacking Order in Graphite by Molten Fluoride Salt Infiltration. *Carbon* 72:304–311, (2014).

[34] Kasten P. R., Bettis E. S., Cook W. H., et. al. Graphite Behavior and its Effects on MSBR Performance. *Nucl Eng Des* 9(2):157–195, (1969).
[35] Jeon, K. J., Lee, Z., et. al. Fluorographene: A Wide Bandgap Semiconductor with Ultraviolet Luminescence. *ACS Nano*; 5(2):1042-6, (2011).
[36] Yang, X., Feng, S., et al. Interaction between Nuclear Graphite and Molten Fluoride Salts: A Synchrotron Radiation Study of the Substitution of Graphitic Hydrogen by Fluoride Ion, *J. Phys. Chem. A*, 116 985–989, (2012).
[37] Scherer, G. W. Stress from Crystallization of Salt. *Cem Concr Res* 34 (9), 1613–1624, (2004).
[38] Scherer, G. W. Crystallization in Pores. *Cem Concr Res* 29 (8), 1347–1358, (1999).
[39] Koger, J. W. A Forced-Circulation Loop for Corrosion Studies: Hastelloy N Compatibility with $NaBF_4$-NaF (92-8 mole %). *Oak Ridge National Lab*, ORNL-TM-4221, (1972).
[40] Sabharwall, P., Ebner, M., Sohal, M., Sharpe, P., and Thermal Hydraulics Group. Molten Salts for High Temperature Reactors: University of Wisconsin Molten Salt Corrosion and Flow Loop Experiments - Issues Identified and Path Forward. *Idaho National Lab*, (2010).
[41] Indacochea, J. E., et.al. Corrosion Performance of Ferrous and Refractory Metals in Molten Salts under Reducing Conditions. *J Mater Res*; 14(5): 1990-1995, (1999).
[42] Joo, C. G., et al. Spectrophotometric Study of the Corrosion Behaviour of Chromium in Molten Alkali Carbonates. *Journal of Power Sources*, 72(2): 211–214, (1998).
[43] Bell, S., Steinberg, T., and Will, G. Corrosion Mechanisms in Molten Salt Thermal Energy Storage for Concentrating Solar Power. *Renewable and Sustainable Energy Reviews*, (2019).
[44] Powers, W. D., Cohen, S. I., and Greene, N. D. Physical Properties of Molten Reactor Fuels and Coolants. *Nuclear Science and Engineering*, 17:2, 200–211, (1963).
[45] Hosova, Y., Terai, T., Yoneoka, T., and Tanaka, S. Compatibility of Structural Materials with Molten Chloride Mixture at High Temperature. *J. Nucl. Mater.*, 248, 348–353. (1997).
[46] Inoue, T., and Koch, L. Development of Pyro-Processing and its Future Directions. *Nucl. Eng. Technol.*, 40, 183–190, (2008).
[47] Holcomb, D. E., Flanagan, G. F., et. al. Fast Spectrum Molten Salt Reactor Options. *Oak Ridge National Lab*, ORNL/TM-2011/105, (2011).
[48] Taube, M. Fast Reactors using Molten Chloride Salts as Fuel. *Swiss Federal Institute for Research Reactor*, EIR-Bericht Nr. 332. (1978).
[49] Kipouros, G. J., and Sadoway, D. R. The Chemistry and Electrochemistry of Magnesium Production. *Advances in Molten Salt Chemistry*, vol. 6, Elsevier, Amsterdam, pp. 127–209, (1987).
[50] Huang, Q., Lu, G., Wang, J, and Yu, J. Thermal Decomposition Mechanisms of $MgCl_2 \cdot 6H_2O$ and $MgCl_2 \cdot H_2O$. *Journal of Analytical and Applied Pyrolysis* 91, 159–164, (2011).
[51] Koger J. W. Fundamentals of High-Temperature Corrosion in Molten Salts. ASM Metals Handbook, vol. 13. *ASM International*, 98–111. Corrosion, (1987).

[52] Sun, H, Wang, J., et. al. Corrosion Behavior of 316SS and Ni-Based Alloys in a Ternary NaCl-KCl-$MgCl_2$ Molten Salt. *Solar Energy*, 171, 320–329, (2018).
[53] ASTM G1-03, Standard Practice for Preparing, Cleaning, and Evaluating Corrosion Test Specimens. 20030.10.
[54] Hamer. W. J., Malmberg, M. S., Rubin, B. Theoretical Electromotive Forces for Cells containing a Single Solid or Molten Chloride Electrolyte. *J. Electrochem. Soc.*, 103(1), pp. 8–16, (1956).
[55] Ishitsuka, T., and Nose, K. Stability of Protective Oxide Films in Waste Incineration Environment-Solubility Measurement of Oxides in Molten Chlorides. *Corros. Sci.*, vol. 44, no. 2, 247–263, (2002).
[56] Lorimer, J. W. Solubility Data Series-Gases in Molten Salts. *International Union of Pure and Applied Chemistry*, Canada, vol. 45/46, p. 555, (1992).
[57] Goods, S. H., and Bradshaw, R. W. Corrosion of Stainless Steels and Carbon Steel by Molten Mixtures of Commercial Nitrate Salts. *J. Mater. Eng. Perform.*, vol. 13, no. 1, 78–87, (2004).
[58] Oryshich, I.V., and Kostyrko, O.S. Influence of Molybdenum, Tungsten, and Cobalt on the Corrosion of High-Temperature Strength Nickel Alloys in Molten Salts. *Met. Sci. Heat Treat.* 27, 740–745, (1985).
[59] Quyang, F. Y., Chang, C. H., and Kai, J. J. Long-Term Corrosion Behaviors of Hastelloy-N and Hastelloy-B3 in Moisture-Containing Molten FliNaK Salt Environments. *J. Nucl. Mater*. 446, 81–89, (2014).
[60] Veverkova, J., Strang, A., Marchant, G. R., McColvin, G. M., and Atkinson, H. V. High Temperature Microstructural Degradation of Haynes Alloy 230. *TMS (Miner. Met. Mater. Soc.)* 479–488, (2008).
[61] Vignarooban, K., Pugazhendhi, P., Tucker, C., Gervasio, D., and Kannan, A. M. Corrosion Resistance of Hastelloys in Molten Metal-Chloride Heat-Transfer Fluids for Concentrating Solar Power Applications. *Sol. Energy* 103, 62–69, (2014).
[62] Sridharan, K., and Allen, T. R. Corrosion in Molten Salts. *Molten salts chemistry*, From Labs to Application, chapter 12, (2013).
[63] Paul, C. S., et. al. Sensitization, Intergrannular Attack, Stress Corrosion Cracking, and Irradiation Effects on the Corrosion of Iron-Chromium-Nickel Alloys. *Oak Ridge National Lab*. ORNL/TM-6311, (2013).
[64] Mishra, A. Sensitization Study of Corrosion-Resistant Nickel-Alloys. *NACE International*, NACE-2018-11329, (2018).
[65] Sun, H., Zhang, P., and Wang, J. Effects of Alloying Elements on the Corrosion Behavior of Ni-Based Alloys in Molten NaCl-KCl-$MgCl_2$ Salt at Different Temperatures. *Corrosion Science*, 143, 187–199, (2018).
[66] Olson, L., Sridharan, K., et. al. Intergrannular Corrosion of High Temperature Alloys in Molten Fluoride Salts. *Materials At High Temperatures*, 27 (2), 145–149, (2010).
[67] Chen, T. F., Tiwari, G. P., Iijima, Y. and Yamauchi, Y. K. Volume and Grain Boundary Diffusion of Chromium in Ni-Base Ni-Cr-Fe Alloys. *Mater. Trans.*, 44, 40–46, (2003).

[68] Heitz, E. Chemo-Mechanical Effects of Flow on Corrosion. *Corrosion Engineering*, vol. 47, No. 2, (1991).
[69] Shemilt, L. W., and Shoukry, E. I. Modelling Electrochemical Processes at Rough Surfaces under Mass Transfer Control. *70th Ann. Meeting of A ICh E*, New York, 1–14, (1977).
[70] David, S., and Ting, K. Wall Turbulence. *Basics of Engineering Turbulence*, chapter 6, 119–138, (2016).
[71] Kashani-Nejad, S., Ng, K. W., and Harris, R. MgOHCl Thermal Decomposition Kinetics. *Metallurgical and Materials Transaction B*, vol. 36B, 153–157, (2005).
[72] Young, J. P., Mamantov, G., Coffield, J. E., and Dai, S. In-line Sensors for Electrolytic Magnesium Cells. *Oak Ridge National Lab*, ORNL/M/3003, (1993).
[73] Mayes, R. T., Kurley, J. M., et. al. Purification of Chloride Salts for Concentrated Solar Power Applications. *Oak Ridge National Lab*, ORNL/LTR-2018/1052, (2018).
[74] Handbook of Preparative Inorganic Chemistry; *Academic Press Inc.: New York*, (1963).
[75] Sun, I. W., Sienerth, K. D., and Mamantov, G. The Use of Phosgene for the Removal of Oxide Impurities from a Sodium Chloroaluminate Melt Saturated with Sodium-Chloride. *J. Electrochem. Soc.*, 138, 2850-2852, (1991).
[76] Chen, G. S., Sun, I. W., Sienerth, K. D., Edwards, A. G., and Mamantov, G. Removal of Oxide Impurities from Alkali Haloaluminate Melts Using Carbon-Tetrachloride. *J. Electrochem. Soc.*, 140, 1523-1526, (1993).
[77] Urguhart, R., Deshko, R., and Mourad, S. Process for Purification of Molten Salt Electrolytes. *Hatch Associates Ltd.* US20030015434 A1, (2003).
[78] Morss, L. R., Fuger, J., and Katz, J. J. The Chemistry of the Actinide and Transactinide Elements. 3rd Ed., vol. 1–5, chapter 5, p. 486-487, (2006).
[79] Shamberger, P. J., and Reid, T. Thermophysical Properties of Potassium Fluoride Tetrahydrate from 243 to 348 K. *J. Chemical & Engineering Data*, (2013).
[80] Figueroa, J., and Williamson, M. A. Uranium Dioxide Conversion. *Argonne National Lab*. ANL/CSE-13/25, (2008).
[81] Perkins, B. L. Evaluation of Environmental Control Technologies for Commercial Nuclear Fuel Conversion (UF6) Facilities, *Los Alamos National Laboratory*, LA-9397-MS, UC-70, (1982).
[82] Dussoubsa, B., Jourdeb J., Patissona F., Houzelotc J. L., Ablitzera, D. Modelling of a Moving Bed Furnace for the Production of Uranium Tetrafluoride. Part 1: Formulation of the Model. *Chemical Engineering Science*, 58:2617–2627, (2003).
[83] Joly, F., Simon, P., et. al. Direct Conversion of Uranium Dioxide UO_2 to Uranium Tetrafluoride UF_4 using the Fluorinated Ionic Liquid [Bmim][PF_6]. *Dalton Trans.*, 49, 274–278, (2020).
[84] Mahdavi, A., Medvedovski, E. et. al. Corrosion Resistance of Boronized, Aluminized, and Chromized Thermal Diffusion-Coated Steels in Simulated High-Temperature Recovery Boiler Conditions. *Coatings*, (2018).
[85] Ueda, N., Mizukoshi, T., Demizu, K., Sone, T., Ikenaga, A., and Kawamoto, M. Boriding of Nickel by the Powder-Pack Method. *Surf. Coatings Technol.*, vol. 126, no. 1, 25–30, (2000).

[86] Makuch, N., Kulka, M., and Piasecki, A. The Effects of Chemical Composition of Nimonic 80A-Alloy on the Microstructure and Properties of Gas-Borided Layer. *Surf. Coatings Technol.*, vol. 276, 440–455, (2015).
[87] Khalili, A. Effective Boronizing Process for Age Hardened Inconel 718. *Electronic Thesis and Dissertation Repository*. 4507, (2017).
[88] Joshi, A. A., Singh, R. P., and Hosmani, S. S. Microstructure Evolution in Boronized Inconel 718 Superalloy. *J. Metallurgy and Materials Science.* Vol. 59, 11–21, (2017).
[89] Alias, S. K., Abdullah, B., et. al. Boron Dispersion Layer of Paste Boronized 304 Stainless Steel Before and After Shot Blasting Process. *Applied Mechanics and Materials*. vol. 393, 217–221, (2013.
[90] Campos-Silva, I., Contla-Pacheco, A. D., et. al. Sliding Wear Resistance of Nickel Boride Layers on an Inconel 718 Superalloy. *Surface & Coatings Technology*, 378 124862, (2019).
[91] Mu, D., Shen, B. L., Yang, C., and Zhao, X. Microstructure Analysis of Boronized Pure Nickel using Boronizing Powders with SiC as Diluent. *Vacuum*, vol. 83, no. 12, 1481–1484, (2009).
[92] Mebarek, B., Benguelloula, A., and Zanoun, A. Effect of Boride Incubation Time During the Formation of Fe_2B Phase. *Materials Research*, 21(1): e20170647, (2018).
[93] Deng, D., Wang, C., Liu, Q., and Niu, T. Effect of Standard Heat Treatment on Microstructure and Properties of Borided Inconel 718. *Trans. Nonferrous Met. Soc. China*, 25, 437–443, (2015).
[94] Yuan, Y., and Lee, T. R. Contact Angle and Wetting Properties. G. Bracco, B. Holst (eds.). *Surface Science Techniques*, chapter 01, (2013).
[95] Zhang, W., Zhang, B., et. al. Microstructure and Molten Salt Impregnation Characteristics of a Micro-Fine Grain Graphite for Use in Molten Salt Reactors. *New Carbon Materials*, vol. 31, Issue 6, 585–593, (2016).
[96] Washburn, E. W. The Dynamics of Capillary Flow. *Phys. Rev.* 117(3), 273–283, (1921).
[97] Xu, H., Lin, J., et. al. Characterization of Molten 2LiF-BeF_2 Salt Impregnated into Graphite Matrix of Fuel Elements for Thorium Molten Salt Reactor. *Nuclear Science and Techniques*, (2019).
[98] Tang, H., Qi, W., et. al. Infiltration of Graphite by Molten 2LiF-BeF_2 Salt. *J. mater Sci*, 52:11346–11359, (2017).
[99] He, Z., Song, J., et. al. Excluding Molten Fluoride Salt from Nuclear Graphite by Sic/Glassy Carbon Composite Coating. *Nuclear Energy and Technology*, 51, 1390–1397, (2019).
[100] O' Hagan, D. Understanding Organofluorine Chemistry. An Introduction to the C–F Bond. *Chem. Soc. Rev.*, 37, 308–319, (2008).
[101] Delhaes, P. Graphite and Precursors. *Gordon and Beach Science Publishers*, Amsterdam, Netherlands, (2001).
[102] Mohanty, S., and Majumdar, S. HTGR Graphite Core Component Stress Analysis Research Program - Task 1 Technical Letter Report. *Argonne National Lab*, ANL-11/04, (2011).

[103] Marsden, B. J., Fok, S. L., and Li, H. Irradiation Behavior and Structural Analysis of HTR/VHTR Graphite Core Components. *18th International Conference on Structural Mechanics in Reactor Technology (SMiRT 18)*, Beijing, China, (2005).

[104] Burchell, T. D., and Snead, L. L. The Effect of Neutron Irradiation Damage on the Properties of Grade NBG-10 Graphite. *Journal of Nuclear Materials*, vol. 371, No. 1-3, 18–27, (2007).

[105] Galwey, A. K., Laverty, G. M. The thermal decomposition of magnesium chloride dihydrate. *Thermochimica Acta*, 138, 115-127, (1989).

[106] Kashani-Nejad, S., Ng, K.W., Harris, R. Chlorination of MgOHCl with HCl gas. *Mineral Processing and Extractive Metallurgy*, 115:3, 121-122, (2006).

[107] Vasquez, R. P. Magnesium (II) Oxide. *Surf. Sci. Spectra*, 2, 13. (1993). NIST XPS Database.

[108] Morss, L. R., Fuger, J., Katz, J. J. The chemistry of the actinide and transactinide elements. 3rd Ed., Volumes 1–5, (2006), Chapter 5, pp. 486-487.

[109] Trowbridge, L.D., Richards, H.L. X-Ray Photoelectron Spectra of the U 4f Levels in UF_4, UF_5 and UF_6. *Surface and Interface Analysis*, Vol. 4, No. 3, (1982).

[110] McIntyre, N.S., Sunder, S., Shoesmith, D.W., Stanchell F.W. *J. Vac. Sci. Technol.* 18, 714 (1981). NIST XPS Database.

[111] Nefedov, V. I., Gati, D., Dzhurinskii, B.F., Sergushin, N.P., Salyn, Y.V. *Zh. Neorg. Khimii* 20, 2307 (1975). NIST XPS Database.

[112] Reactor Fuel Processing: Volumes 5–6. *U.S. Argonne National Laboratory* (1962), Section III, pp. 31–35.

[113] Peterson, D. E. The Ni-U (Nickel-Uranium) System. *Bulletin of Alloy Phase Diagrams* 9, 490–493 (1988).

[114] Galetz, M. C., Rammer, B., Schutze, M. Refractory metals and nickel in high temperature chlorine-containing environments-thermodynamic prediction of volatile corrosion products and surface reaction mechanisms: a review. *Mater. Corrros.* 66, pp. 1206-121, (2015).

[115] Nayeb-Hashemi, A. A., Clark, J. B. The Mg−Ni (Magnesium-Nickel) system. *Bulletin of Alloy Phase Diagrams* 6, 238–244, (1985).

[116] Kruizenga, A. M. Corrosion Mechanism in Chloride and Carbonate Salts. *Sandia National Laboratories*. SAND2012-7594. (2012).

[117] Gurvich, L., Veyts, I., Alcock, C. Thermodynamic Properties of Individual Substances: Elements and Compounds. *CRC Press.* (1990).

[118] Pokhmurskii, V. et. al. Structure-Phase Transformation in Electrochemical Boron containing Coatings by Thermal Treatment. *WTK* 2005, pp. 29-30 (2015).

[119] Banerjee, S., Mukhopadhyay, P. Phase Transformations: Examples from Titanium and Zirconium Alloys. *Elsevier Science*, Chapter 7 (2007).

[120] Targhi, V. T., Omidvar, H., et. al. Microstructure and Hot Corrosion Behavior of Hot Dip Siliconized Coating on Ni-base Superalloy IN718LC. *Mater. Res. Express*, (2020).

[121] Markovsk, Y. L. The Chemical Stability and Structure of Borides. *Institute of Applied Chemistry* 4(10), pp. 39-45 (1962).

[122] Sahin, S. Effects of boronizing process on the surface roughness and dimensions of AISI 1020, AISI 1040 and AISI 2714. *J. Materials Processing Technology*. 209, 1736 1741. (2009).

[123] Hayes, R. G., Edelstein, N. Electron Spectroscopy, *D. A. Shirley*, Editor, North-Holland, Publishing Company, Amsterdam, 771 (1972).

[124] Wagner, C. D. 'Handbook of X-Ray and Ultraviolet Photoelectron Spectroscopy', *D. Briggs*, Editor (1977), Chapter 7.

[125] Okoli, S., Haubner, R., Lux, B. Carburization of tungsten and tantalum filaments during low-pressure diamond deposition. *Surface and Coatings Technology*, Volume 47, Issues 1-3, 1991. Pages 585-599.

[126] Becker, P., Young, D. J. Carburization resistance of nickel-base, heat-resisting alloys. *Oxidation of Metals* 67, 267-277(2007).